# Spatiotemporal coordination of collective activity in neuronal ensembles

Ph. D. THESIS


**Alessandro Barardi**

A thesis presented to obtain the degree of Doctor of Philosophy from the

Universitat Politecnica de Catalunya
Department of Physics

Director: Jordi Garcia-Ojalvo
Tutor: Antonio Javier Pons-Rivero

Barcelona June 2016

UNIVERSITAT POLITÈCNICA DE CATALUNYA
BARCELONATECH
Escola de Doctorat

## Acta de calificación de tesis doctoral

**Curso académico:**

Nombre y apellidos

Programa de doctorado

Unidad estructural responsable del programa

## Resolución del Tribunal

Reunido el Tribunal designado a tal efecto, el doctorando / la doctoranda expone el tema de la su tesis doctoral titulada _____

_____.

Acabada la lectura y después de dar respuesta a las cuestiones formuladas por los miembros titulares del tribunal, éste otorga la calificación:

☐ NO APTO ☐ APROBADO ☐ NOTABLE ☐ SOBRESALIENTE

| | |
|---|---|
| (Nombre, apellidos y firma)<br>Presidente/a | (Nombre, apellidos y firma)<br>Secretario/a |

| | | |
|---|---|---|
| (Nombre, apellidos y firma)<br>Vocal | (Nombre, apellidos y firma)<br>Vocal | (Nombre, apellidos y firma)<br>Vocal |

_____, _____ de _____ de _____

El resultado del escrutinio de los votos emitidos por los miembros titulares del tribunal, efectuado por la Escuela de Doctorado, a instancia de la Comisión de Doctorado de la UPC, otorga la MENCIÓN CUM LAUDE:

☐ SÍ ☐ NO

| | |
|---|---|
| (Nombre, apellidos y firma)<br>Presidente de la Comisión Permanente de la Escuela de Doctorado | (Nombre, apellidos y firma)<br>Secretario de la Comisión Permanente de la Escuela de Doctorado |

Barcelona a _____ de _____ de _____

I dedicate this Thesis to my parents Rita and Oronzo, my brother Emanuele, my girlfriend Dafne and all my family for their constant support and unconditional love.
A thought gets through to all young people whose dream has been broken …

# ACKNOWLEDGEMENTS

This PhD Thesis is the last photograph of a challenging journey, which it has been a truly life-changing experience for me and it would not have been possible to do without the support and guidance that I received from many people.

First and foremost I want to thank my advisor Prof. Jordi Garcia-Ojalvo. I am extremely grateful to him for his valuable guidance, insightful discussions about the research, his patience and immense knowledge of biological system dynamics. The joy, enthusiasm, and sensible optimism he has for his research was contagious and motivational for me, even during tough times in the PhD pursuit. Jordi has supported me not only by providing a research assistantship over the last three years, but also academically and emotionally through the rough road to finish this Thesis. And during the most difficult times, he taught me to laugh and work. And try again. And again. I am also thankful for the excellent example he has provided as a successful physicist and professor. It has been an honor to be his PhD student. Thank you Jordi, for all your help and support.

I thank Prof. Antonio Javier Pons-Rivero, co-supervisor and tutor, for his scientific advice and knowledge and many insightful discussions and suggestions. I really appreciate his willingness to meet me at short notice every time and going through several steps of my research. Antonio has been very encouraging and supportive, as a longtime friend.

I gratefully acknowledge Prof. Stephen Coombes, coordinator of Neural Engineering Transformative Technologies (NETT), and the committee for selecting me to be a member of this Europe-wide consortium during these three years that has been made possible by a grant by the European Commission through its Marie Curie Initial Training Network scheme. I would like to thank the NETT Consortium not only for providing the funding that allowed me to undertake this research, but also for giving me the opportunity to attend conferences and meet so many interesting people. I was honored to be a ITN Marie Curie Fellow during the last three years.

My gratitude is reserved for Prof. Evgueniy (Eugene) V. Lubenov and Prof. Athanassios (Thanos) G. Siapas from the Division of Biology and Biological Engineering at Californian Institute of Technology (Caltech), where I spent part of my PhD. I have appreciated their

scientific collaboration and their impressive ability to do research. My time at Caltech was made enjoyable in large part due to Eugene and Thanos and their families, which became a part of my life. I am grateful for time spent together doing research, meetings and Skype calls during countless nights, football matches, lunches with *Charlie Bread* and dinners at *Settebello*, and long walks on the campus among trees and squirrels and through the streets of Pasadena talking about everything. I also remain indebted for their understanding and support during the times when I was really down due to personal family problems.

I would like to acknowledge Belén Sancristóbal, former PhD student of Jordi Garcia-Ojalvo and currently postdoc at the University of Ottawa, because she helped me during my first part of the PhD. I gained a lot from her, through her personal and scholarly interactions, her suggestions at various points of my research programme, and through a scientific collaboration that has been very productive. I would like to acknowledge Dr Alberto Mazzoni from Scuola Sant'Anna Superiore of Pisa for the fruitful scientific collaboration, and Daniel Malagarriga, PhD student at the Universitat Politecnica de Catalunya, for the time spent together doing research. I thank all the other collaborators for sharing their knowledge that influenced the work and resulted in cooperative joint publications.

I am also very grateful to all those at the Dynamical Systems Biology lab at the Universitat Pompeu Fabra directed by Jordi Garcia-Ojalvo. I am grateful to Elena, postdoc in the lab, for her wise advice, experience and long conversations about everything related to science, Marçal for his willingness to solve any kind of problem, Pau for having provided all his knowledge, Marta, Rosa, Leticia and Carlos for being so passionate and active in doing research. It was easy working hard with all of them everyday. I want to thank all the other past and present group members that I have had the pleasure to work with, and the numerous summer and rotation students who have come through the lab. Very special thanks you to Maciej for his advice and feedback on my research, and for always being so supportive of my work. I shared with him the organization of the International Conference on Systems Level Engineering held in Barcelona in September 2015. It was an intense job, but I learnt a lot from him and our interactions.

I would like to thank Prof. David Liley, for being my first advisor during my master at Swinburne University of Technology in Melbourne, Australia. David is a great scientist with exceptional skills, who guided me through my master thesis on the nonlinear analysis of EEG time series, and made it possible for me to obtain an important PhD grant. I still think fondly of my time as an undergraduate student in his lab. David was the reason why I decided to go to pursue a career in research. His enthusiasm and love for teaching is contagious.

I will forever be thankful to my former advisor Prof. Lamberto Rondoni from Politecnico di Torino, great scientist and great person, who first introduced me to the world of research and

supported me during the first steps in my career. He was and remains a model for a scientist, mentor, and teacher. I would like to thank Federico Frascoli, currently professor at Swinburne University of Technology in Melbourne, who helped me to start my master thesis in Australia. He has been helpful in providing advice many times during my career. He is an inspiration.

Thank you to Prof. Stephen Coombes and Prof. Lamberto Rondoni for being part of the international committee, and Cristina Masoller, David Liley and Ruben Moreno-Bote for being part of my oral defense committee.

I would like to thank my best friends Luca, Mario, Federico, Rosa and many others (too many to list here but you know who you are!) for providing the support and friendship that I needed during this journey. Special thanks to Jinq Chen, currently postdoc at Harvard University, exceptional mate in Turin and in Pasadena for all the help, support and immense friendship. Lastly, I would like to thank my family for all their love and encouragement in all my pursuits. And I need to thank them in Italian now...

Grazie a Mamma e Papà per avermi trasmesso il piacere e la gioia nel raggiungere traguardi importanti dopo tanti sacrifici e piacevoli rinunce. Grazie perchè mi avete insegnato a cercare la felicità che si prova quando si superano ostacoli insormontabili con le proprie mani. Senza fermarsi mai. Grazie per la forza che mi avete trasmesso lontano da casa durante questi anni, quando la nostra vita è stata messa a dura prova. Senza di voi non avrei potuto raccontare questo intenso viaggio. Grazie a mio fratello Emanuele perchè è stato e sempre sarà la guida e l'esempio più stimolante di una vita piena di successi e sua moglie Ilenia. Sebbene spesso in continenti diversi porto il vostro esempio e l'orgoglio di essere parte della vostra nuova famiglia che cresce: un caloroso benvenuto a Giorgia venuta alla luce in questi istanti. Grazie a zia Anna, zio Fernando, Tonio, Luca, Valentina, Maria Antonietta e Maristella perchè non mi avete mai fatto sentire solo ovunque sia andato.

Finally, I would like to acknowledge my girlfriend Dafne and her wonderful family who all have been supportive and caring. She has been a constant source of strength and inspiration by my side throughout this PhD, living every single minute of it. Dafne is the only person who can appreciate all my efforts and commitments of these years, my fears and weaknesses. She has been a true and great supporter and has unconditionally loved me during every moment. I feel that what we both learned a lot about life and strengthened our commitment and determination to each other and to live life to the fullest. I cannot forget her visit to Pasadena and our memorable trips in the Monument Valley, Antelope Canyon, Death Valley, and our breaks in Paris, Madrid, Valencia, Barcelona, Rome and Florence. This Thesis would not have been written without your immense support, Dafne. Thank you for your invaluable loving help and your patience. Enjoying a wonderful life with you, I am looking forward to many more happy and exciting years together.

# SUMMARY

The brain is a complex multi-scale dynamical system, made of more than $10^{11}$ nerve cells, the *neurons*, which are connected by $10^{15}$ chemical and electrical synaptic connections, and many more *neuroglial cells* recently discovered to provide support and protection for neurons. Neurons themselves are multidimensional nonlinear systems able to exhibit various dynamical activities and processes happening at different temporal and spatial scales, from local microcircuits to brain-wide networks. The correct operation of the brain requires a carefully orchestrated activity across these scales, which includes the establishment of synchronized behavior within and among multiple neuronal populations, from which different spatiotemporal patterns transiently arise. As a matter of fact, information processing underlying brain cognitive functions such as action, perception and cognition relies on the coordinated interaction between large groups of interconnected neurons distributed within and across different specialized brain areas. In this Thesis we study a diverse range of collective dynamical phenomena in brain networks that reveal exquisite coordination, by means of different models of cortical neuronal networks. We explore how neurons are dynamically and transiently engaged in functional assemblies, resulting in a periodic synchronization of neuronal spiking (*neuronal oscillations*) in a brain area or between distant brain areas (*long-range oscillatory synchronization*), and the consequences for *information* processing. Synchronous oscillations are usually observed to be coherent in space, meaning that the temporal progression of activity has identical phase across recording sites. However, out-of-phase synchronous oscillations also exist, and occasionally they give rise to complex spatiotemporal patterns of activity in the form of traveling waves. Therefore, we investigate as well how neurons engage in *traveling wave* patterns through self-organizing dynamics.

In Part I we introduce the different spatiotemporal phenomena motivating our studies (Chapter 1) and the computational models used in this work (Chapter 2).

In Part II we present the main results of this study. In Chapter 3 we study temporally-coordinated patterns in the thalamus, a key brain structure in the processing of sensory information. During the sleep and awake states, this brain area is characterized by the presence of two distinct dynamical regimes: in the sleep state the activity is dominated by *spindle os-*

*cillations* ($7-15$ Hz) that is weakly affected by external stimuli, while in the awake state the activity is primarily driven by external stimuli. We have developed a simple and computationally efficient model of the thalamus that exhibits two dynamical regimes with different information-processing capabilities, and study the transition between them. Our results reveal a range of connectivity conditions under which the thalamic network composed by different type of neurons displays the two aforementioned dynamical regimes, such as spindle-like oscillations in the alpha range. Overall, our model gives a novel and clear description of the role that the two different types of neurons, thalamocortical and reticular thalamic cells, and their connectivity, play in the dynamical regimes observed in the thalamus, and in the transition between them.

In Chapter 4 we study other temporal regimes such as neuronal oscillations in the gamma range, and in particular how temporally synchronized patterns of oscillatory gamma activity between neuronal populations could provide preferential communication channels. In fact, synchronization between neuronal populations plays an important role in information transmission between brain areas. In particular, collective oscillations emerging from the synchronized activity of thousands of neurons can increase the functional connectivity between neural assemblies by coherently coordinating their phases and controlling information flow among connected regions. This mechanism allows the brain's connectivity topology to be flexibly reconfigured in response to changing task demands. This synchrony of neuronal activity can take place within a cortical patch or between different cortical regions. While short-range interactions between neurons involve just a few milliseconds, communication through long-range projections between different regions could take up to tens of milliseconds. How these heterogeneous transmission delays affect communication between neuronal populations is not well known. To address this question, we study the dynamics of two bidirectionally delayed-coupled neuronal populations using conductance-based spiking models, examining how different synaptic delays give rise to in-phase/anti-phase transitions at particular frequencies within the gamma range, and how this behavior is related to the phase coherence between the two populations at different frequencies. We use spectral analysis and information theory to quantify the information exchanged between the two networks. The results confirm that zero-lag synchronization maximizes information transmission, although out-of-phase synchronization allows for efficient communication provided the coupling delay, the phase lag between the populations, and the frequency of the oscillations are properly matched.

As these results show, the brain self-organizes in different spatiotemporal highly organized patterns across not only temporal, but also spatial scales. How the brain reaches this required level of coordination is not well known yet. A full understanding depends on our knowledge of large-scale brain organization. It is known that the mammalian brain operates in multiple

spatial scales simultaneously, ranging from the microscopic scale of single neurons through the mesoscopic scale of cortical columns, to the macroscopic scale of brain areas. These levels of description are associated with distinct temporal scales, ranging from milliseconds in the case of neurons to tens of seconds in the case of brain areas. In Chapter 5 we examine theoretically how these spatial and temporal scales interact in the functioning brain, by considering the coupled behavior of two mesoscopic neural masses that communicate with each other through a microscopic neuronal network. We use the synchronization between the two neural mass models as a tool to probe the interaction between the mesoscopic scales of those neural populations and the microscopic scale of the mediating neuronal network. Our results show that the neuronal network, which operates at a fast temporal scale, is indeed sufficient to mediate coupling between the two mesoscopic oscillators, which evolve dynamically at a slower scale. We also establish how this synchronization depends on the topological properties of the microscopic neuronal network, on its size and on its oscillation frequency.

When synchronized neuronal oscillations exhibit a consistent phase pattern across recording sites (e.g. a continuous progression of phase at each location), complex spatiotemporal phenomena arise in the form of brain waves. Chapter 6 focuses on the mathematical properties of traveling waves, emerging from a one-dimensional network of inhibitory neurons with asymmetric synaptic coupling. Our results show that these networks behave as excitable media that exhibit anomalous dispersion, and therefore have counter-intuitive wave-propagation properties. In particular, when neurons at the head of the chain are periodically forced traveling waves emerge, with the wavefronts moving from the tail to the head of the chain, in a direction opposite to that of the synaptic connectivity. To mathematically explore this dynamics, we first develop a continuum model with topology similar to the HH model to study the existence of these backward waves. Secondly we investigate the generality of this phenomenon across different systems by studying an integrate-and-fire continuum approximation that is analytically tractable, and derive a self-consistency condition for the existence of traveling waves which allows the calculation of the dispersion curve. The analysis of the latter model reveals how wave-propagation depends on a variety of neuronal properties.

Finally, in Part III we summarize the results of this Thesis and discuss future perspectives.

# TABLE OF CONTENTS

**Summary** vii

**List of figures** xiv

**List of tables** xvii

**I Introduction** 1

**1 From single neuron dynamics to neural collective phenomena** 2

1.1 Organized activity of neuronal ensembles . . . 2

1.1.1 Neurons and neuronal assemblies . . . 2

1.1.2 Temporal coordination of neuronal oscillations . . . 4

1.1.3 Spatiotemporal coordination: large-scale synchrony and wave propagation . . . 6

1.2 Temporally organized patterns in the thalamus: spindle oscillations . . . 8

1.2.1 Thalamic dynamical regimes: bursting vs tonic . . . 8

1.2.2 Functional role of the thalamus . . . 10

1.3 Synchronization of neuronal oscillations . . . 15

1.3.1 Local mechanisms of zero-lag synchronization . . . 16

1.3.2 Zero-lag synchronization of distant coupled populations . . . 17

1.3.3 Gamma-band synchronization . . . 19

1.3.4 Communication through coherence between coupled gamma oscillating populations . . . 19

1.4 Synchronization as a mechanism of large-scale integration . . . 22

1.4.1 Local and large-scale integration . . . 22

1.4.2 Evidence for large-scale synchronization . . . 23

1.4.3 Multi-scale approach . . . 27

1.5 Propagation of neuronal oscillations . . . 32

1.5.1 Mechanisms of traveling waves and computational role . . . . . 33
1.5.2 Propagating waves: experimental findings . . . . . 35
1.5.3 Cerebellar waves in early development . . . . . 37
1.5.4 Hippocampal theta oscillations . . . . . 38

**2 Computational Models 42**
2.1 Microscopic models . . . . . 43
2.1.1 Integrate-and-fire models (IF) . . . . . 43
2.1.2 Adaptive exponential integrate-and-fire models (aEIF) . . . . . 44
2.1.3 Hodgkin-Huxley-type conductance-based models (HH) . . . . . 45
2.2 Modeling synapses . . . . . 48
2.3 Mesoscopic models . . . . . 53
2.3.1 Neural mass models . . . . . 53

**II Results 57**

**3 Transition between functional regimes in an integrate-and-fire network model of the thalamus 58**
3.1 Dynamical properties of the thalamus . . . . . 59
3.2 Network model of aEIF . . . . . 61
3.3 Dynamics of the aEIF network with increasing size . . . . . 64
3.3.1 Dynamics of single neurons . . . . . 64
3.3.2 Two-neuron loops . . . . . 65
3.3.3 Four-neuron motifs . . . . . 70
3.3.4 Full thalamic network . . . . . 73
3.4 Conclusion . . . . . 79

**4 Phase-coherence transitions and communication in the gamma band between delay-coupled neuronal populations 82**
4.1 Oscillatory-based coordination of coupled neuronal populations . . . . . 83
4.2 Network model of Hodgkin-Huxley conductance-based neurons . . . . . 85
4.3 Dynamics of populations of HH neurons . . . . . 87
4.4 In-phase synchronization of collective oscillations under instantaneous coupling 89
4.5 Phase-coherence transitions for increasing coupling delay . . . . . 92
4.6 From phase coherence to communication . . . . . 98
4.6.1 In-phase and anti-phase coherence transitions under external stimulation 98

4.6.2 Information transmission between coherent delay-coupled neuronal populations . . . 101
4.7 Conclusion . . . 107

**5 Probing scale interaction in brain dynamics through synchronization 113**
5.1 Towards a multi-scale approach . . . 114
5.2 Dynamical model . . . 115
5.2.1 Inter-scale coupling terms . . . 117
5.3 Probing scales interaction . . . 118
5.4 Conclusion . . . 125

**6 Wave propagation in inhibition-dominated neuronal chains 128**
6.1 Wave propagation . . . 129
6.2 Phenomenological analysis . . . 132
6.2.1 Computational model . . . 132
6.2.2 Backward wave propagation . . . 134
6.3 Continuum model approximation starting from Hodgkin-Huxley model . . . 138
6.4 Integrate-and-fire model continuum approximation . . . 146
6.5 Conclusion . . . 158

**III Conclusions 161**

**7 Conclusions 162**
7.1 Transition between functional regimes in an IF network model of the thalamus 163
7.2 Phase-coherence and communication between neuronal populations . . . 166
7.3 Probing scale interaction in brain dynamics through synchronization . . . 170
7.4 Wave propagation in inhibition-dominated neuronal chains . . . 173
7.5 Perspectives . . . 174

**IV Appendices 176**

**Appendix A Methods 177**
A.1 Local field potential and multi-unit activity . . . 177
A.2 Spectral analysis . . . 177
A.3 Phase coherence . . . 178

A.4 Mutual information . . . . . 178
A.5 Clustering coefficient . . . . . 180

**Appendix B Continuum model approximation starting from HH model 181**
B.1 Forward waves . . . . . 181
B.2 Backward waves . . . . . 183

**List of publications and research activities 184**

**Glossary 189**

**References 194**

# List of figures


1.1 Mechanisms of action potentials . . . 3
1.2 Schematic representation of transient distributed neural assemblies . . . 4
1.3 Structural connectivity of the thalamocortical system . . . 9
1.4 Tonic and bursting responses of relay TC neurons to visual stimulation from the LGN in the cat brain . . . 11
1.5 Contribution to sensory-evoked cortical activity: cortex versus thalamus . . . 13
1.6 Dynamics of three neuronal populations interacting through dynamical relaying. 18
1.7 Communication through coherence hypothesis . . . 21
1.8 Neural synchrony as a multi-scale phenomenon . . . 24
1.9 Functional role of long-range neural oscillatory synchronization . . . 26
1.10 Multi-scale approach for recording of brain activity . . . 31
1.11 Illustrative plots of different one-dimensional configurations supporting traveling waves . . . 34
1.12 Propagating waves in thalamic slices . . . 36
1.13 Propagating waves in a network of Purkinje cells . . . 39
1.14 Theta traveling waves and distribution parameters . . . 40

2.1 Firing patterns produced by an adaptive exponential integrate-and-fire model 46
2.2 Electrical circuit representing the membrane potential dynamics of HH neurons 47
2.3 Time course of an action potential in the HH model . . . 49
2.4 Waveforms for synaptic conductances . . . 52
2.5 Illustrative scheme of a neural mass model of a cortical column . . . 55

3.1 Dynamical properties of single RE and TC neurons as a function of input current 66
3.2 Dynamical properties of two-neuron loops . . . 68
3.3 Effect of the GABA decay time on the two-neuron TC-RE loop . . . 69
3.4 Effect of the synaptic strength on the two-neuron TC-RE loop . . . 70
3.5 Effect of the synaptic strengths on the two-neuron RE-RE motif . . . 71

3.6 Four-neuron motifs in the form of coupled pairs of TC-RE loops . . . . . 72
3.7 Spindle activity generated by a full network of TC-RE neurons depending on RE-RE clustering . . . . . 74
3.8 Bursting and tonic modes displayed by a TC-RE network with RE-RE clustering as a function of external input on TC neurons . . . . . 76
3.9 Bursting and tonic modes displayed by the TC-RE network with RE-RE clustering as a function of external input on TC neurons for different corticothalamic inputs . . . . . 78
3.10 Influence of corticothalamic input on a full TC-RE network . . . . . 79

4.1 Collective oscillations of a population of 2000 neurons . . . . . 89
4.2 Phase locking between LFP and MUA of a network . . . . . 90
4.3 Phase coherence of the uncoupled neuronal populations . . . . . 91
4.4 Collective oscillations of two coupled bidirectionally neural populations . . . 92
4.5 Phase coherence of two coupled bidirectionally neural populations for three different values of the inter-areal axonal delays $\tau_{axo}$ . . . . . 93
4.6 Phase coherence and time shift behavior in the case of bidirectional symmetric coupling for increasing inter-areal axonal delays $\tau_{axo}$ . . . . . 95
4.7 Phase coherence for constant inter-areal delay . . . . . 97
4.8 Effect of external stimulation for increasing coupling delay . . . . . 99
4.9 Time shift behavior at the peak of power spectrum for increasing inter-areal axonal delays for different extra inputs . . . . . 100
4.10 Phase coherence in the case of bidirectional asymmetric coupling for increasing extra inputs . . . . . 101
4.11 Time shift in the case of bidirectional asymmetric coupling for increasing extra inputs . . . . . 102
4.12 Effect of external stimulation for increasing coupling delay . . . . . 103
4.13 Phase coherence and time shift in the case of unidirectional coupling . . . . . 104
4.14 Phase coherence for constant inter-areal delay . . . . . 105
4.15 Mutual information carried by LFP and MUA power spectrum of the receiver 106
4.16 Mutual information in the case of unidirectional coupling . . . . . 108
4.17 Carriers of information and signals . . . . . 112

5.1 Diagram representing the coupling between different scale-based models . . . 116
5.2 Collective dynamics of the coupled system . . . . . 119
5.3 Effect of coupling on the power spectra of the three neuronal populations . . 121
5.4 Coupling of NMs through dynamically evolving NN vs constant input . . . . 122

5.5 Influence of the topological and dynamical properties of the neuronal network on the interaction between the NMs . . . 123
5.6 Dynamics of coupled NMs . . . 125

6.1 Illustrative plot of chain of inhibitory neurons asymmetrically connected . . . 133
6.2 Firing dynamical patterns of the chain at its horizontal attractor . . . 134
6.3 Zoom of propagation of backward waves in inhibition-dominated chains . . . 135
6.4 Propagation of backward waves in inhibition-dominated chains . . . 136
6.5 Dispersion relation of waves arising from a chain of inhibitory HH neurons receiving an excitatory input . . . 137
6.6 Numerical results of a chain of inhibitory HH neurons under different conditions 138
6.7 Dispersion relation for forward waves . . . 142
6.8 Local field temporal derivative for forward waves . . . 143
6.9 Local field temporal derivative for backward waves . . . 146
6.10 Dispersion relation for backward waves . . . 147
6.11 Dispersion relation derived from IF continuum approximation . . . 156
6.12 Dispersion relations under different ratios of excitation to inhibition . . . 157
6.13 Dispersion relations under different levels of connection asymmetry . . . 158
6.14 Dispersion relations under different axonal delays . . . 159
6.15 Dispersion relations under different synaptic decay . . . 160

# LIST OF TABLES


1.1 Neural oscillations in cortical networks . . . . . 5

3.1 Values of temporal rise and decay constants for RE and TC. . . . . 63
3.2 Values of synaptic strengths for a network of 500 neurons. . . . . 63

4.1 Synaptic time constants. . . . . 86
4.2 Synaptic conductances and synaptic reversal potentials. . . . . 87

6.1 Synaptic time constants. . . . . 133
6.2 Synaptic conductances and synaptic reversal potentials. . . . . 134

A.1 Parameters for spectral analysis and phase coherence . . . . . 178

# Part I

# Introduction

# CHAPTER 1

# FROM SINGLE NEURON DYNAMICS TO NEURAL COLLECTIVE PHENOMENA

## 1.1 Organized activity of neuronal ensembles

In order to accomplish a cognitive task, the brain requires a spatiotemporal organization of different brain areas. Cognitive tasks are not carried out by single neurons, but they result from the dynamical transient coordination of neuronal discharges between different neurons, which are engaged in specialized *functional assemblies* and contribute to highly-coordinated collective patterns at multiple spatial and temporal scales. In what follows we review the main features of the dynamics of single neurons, and the mechanisms and consequences of their coordination.

### 1.1.1 Neurons and neuronal assemblies

Neurons are the basic data-processing units of the brain. They encode, transmit, and integrate signals originating inside or outside the nervous system. Signals between neurons occur via synapses. The transmission of information is due to changes in the electrical potential of the neurons with respect to the extracellular space. One neuron receives inputs from other neurons through intercellular contacts called *synapses*, causing a transient change in its resting membrane potential, called *postsynaptic potential* (PSP). This transient change is due to the flux of different ions between the intracellular and extracellular spaces through of ion channels present in the membrane. The opening and closing of these ion channels depends on the membrane voltage and on the neurotransmitters released by the presynaptic neuron, which bind to receptors on the cell's membrane and hyperpolarize or depolarize the cell, through what is known as an inhibitory or an excitatory PSP respectively (Figure 1.1A). If the PSP reaches a certain threshold, the neuron produces an action potential (*spike*), which is characterized by a

certain amplitude and duration (Figure 1.1B). Spikes are essential units of information transmission at the interneuronal level (Izhikevich, 2006; Kandel et al., 2000). Information can be encoded by the spiking activity frequency or firing rate (commonly named rate coding) or by the precise timing of the discharges of action potentials (temporal coding).

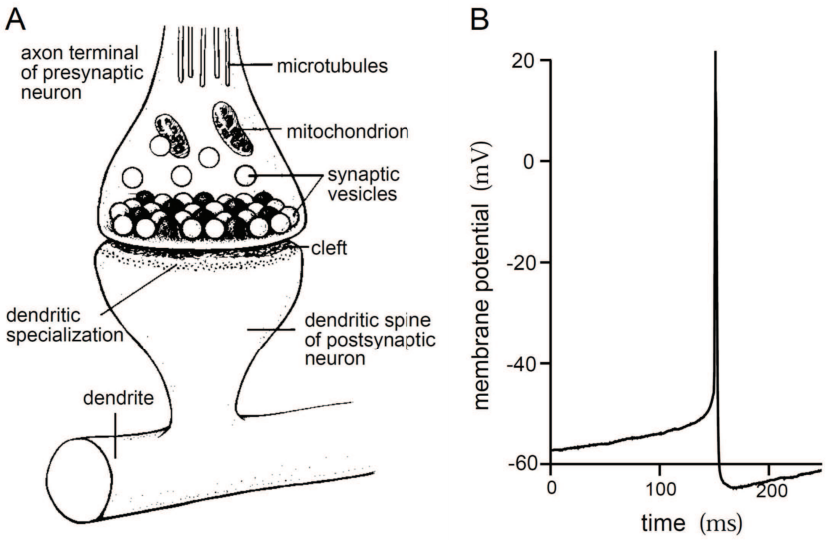


Fig. 1.1 **Action potential and synapses.** (A) Diagram of a synapse. The axon terminal is at the end of the axonal branch (top left of the figure). It has synaptic vesicles containing neurotransmitters, which are released when an action potential arrives from the presynaptic neuron. The neurotransmitter molecules cross the synaptic cleft and bind to receptors on the dendritic spine in the postsynaptic neuron. (B) Action potential recorded intracellularly from a cultured rat neocortical pyramidal cell. From Dayan and Abbott (2005).

The brain is made of more than $10^{11}$ neurons which are connected by $10^{15}$ chemical and electrical synaptic connections. Neurons are anatomically interconnected to form functionally specialized neural assemblies. Neural assemblies are distributed local networks of neurons transiently synchronized by reciprocal dynamic connections (Buzsáki and Draguhn, 2004; Llinas et al., 1998; Shadlen and Movshon, 1999; Varela, 1995). The large density of local short-range connections in the brain subserves the development of local functional populations, and a small percentage of long-range connections reduces the minimal path length between any two neurons (see Figure 1.2). This pattern of structural connectivity can foster a selective bias of the communication within local and global networks. Spatiotemporal dynamic coordination of these neuronal ensembles is the core of neural communication, because it can provide flexible neural communication pathways.

Functionally, temporally organized patterns such as *neuronal oscillations*, which will be introduced in Section 1.1.2, could be a signature of the collective activity of large groups of cells (Buzsáki and Draguhn, 2004; Buzsáki and Wang, 2012) and play an important role for cortical processes that control the flow of information in the brain (Fries, 2005; Salinas and Sejnowski, 2001). Furthermore spatiotemporal collective phenomena such as large-scale synchronization of neuronal oscillations (Varela et al., 2001) or wave propagation (Lubenov and Siapas, 2009) arising from neuronal ensembles could provide a mechanism for neural communication, and contribute to the accomplishment of a specific task (Schnitzler and Gross, 2005). These phenomena will be presented in Section 1.1.3.

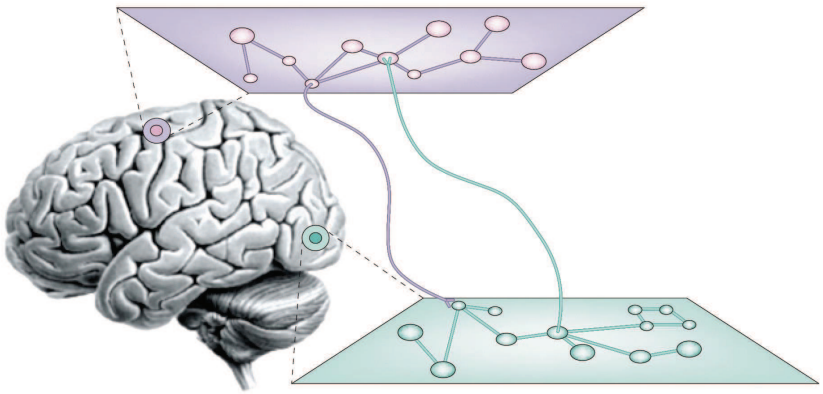

Fig. 1.2 **Schematic representation of transient distributed neural assemblies.** Distributed neural assemblies in different brain areas are connected by long-range dynamic connections. From Varela et al. (2001).

### 1.1.2 Temporal coordination of neuronal oscillations

A prominent property of neural ensembles is the tendency to engage in oscillatory dynamics. Hans Berger (Berger, 1929) observed this activity in the form of brain rhythms from recorded electrical potentials on the scalp of healthy subjects, and categorized this electroencephalographic (EEG) activity in different frequency bands: delta ($0-3$ Hz), theta ($4-7$ Hz), alpha ($8-12$ Hz), beta ($13-30$ Hz) and gamma ($30-200$ Hz).

In general, neuronal oscillations arise collectively from the temporal coordinated activity of anatomically connected circuits. They lead to periodic variations in the recordings of neural activity such as local field potential (LFP), a population measure (spatial average across many neurons, see Appendix A.1) that highlights temporally correlated activity within a local population. At the network level, these oscillatory patterns are commonly attributable to

either spike-to-spike synchrony, where neurons spike regularly and synchronize due to chemical/electrical synapses, or sparse synchronization, where neurons spike irregularly, possibly with different frequencies, but a collective rhythmicity emerges at the population level (synchronous irregular state) (Brunel and Hakim, 2008; Wang, 2010a). The frequency and the emergence of these oscillations depend on cellular pacemaker mechanisms and neuronal network properties: a smaller recruitment of cells leads to higher frequencies (e.g. gamma band), while lower frequencies originate from larger neuronal populations (Bibbig et al., 2007). Neuronal oscillations have been found in several brain areas, including the cortex, the thalamus and the hippocampus. The range of frequencies of these oscillatory patterns are associated with distinct cognitive processes and behavioral tasks (Salinas and Sejnowski, 2001; Ward, 2003) (see Table 1.1). The functional role of these oscillations has remained obscure for several years, but recent experimental and theoretical results indicate that neural oscillations can subserve cognitive processes (such as sensory representation, attentional selection) and might subserve dynamic gating and routing of information (Buzsáki and Draguhn, 2004; Salinas and Sejnowski, 2001; Schyns et al., 2011; Singer, 1999). In this Thesis we will focus on different

| | Theta (4 – 7 Hz) | Alpha (8 – 12 Hz) | Beta (13 – 30 Hz) | Gamma (30 – 200 Hz) |
|---|---|---|---|---|
| Anatomical origin | Hippocampus, prefrontal cortex, sensory cortex | Thalamus, Hippocampus, reticular formation, sensory cortex, motor cortex | All cortical structures, subthalamic nucleus, hippocampus, basal ganglia, olfactory bulb | All brain structures, retina, olfactory bulb |
| Functions | Memory, synaptic plasticity, top-down control, long-range synchronization | Inhibition, attention, consciousness, top-down control, long-range synchronization | Sensory gating, attention, perception, motor control, long-range synchronization | Perception, attention, memory, consciousness, synaptic plasticity, motor control |

Table 1.1 Neural oscillations in cortical networks. Adapted from Uhlhaas et al. (2009).

patterns of oscillatory activity at different frequencies (e.g. gamma band in the cortex) and associated with different cognitive states and functions (e.g. activity in the thalamus during sleep). Perhaps one of the most studied rhythms is the thalamic *spindle oscillation*, present in all mammals during sleep or anesthesia. This is a rhythmic oscillation at $7 - 15$ Hz orig-

inated in the thalamus during slow-wave sleep. The generation of this rhythm is due to the temporal interaction and coordination of thalamocortical relay (TC) cells, which are mutually connected with thalamic reticular (RE) neurons.

In Section 1.2 we will emphasize the functional role of the thalamus, focusing on diverse dynamical activities during different cognitive states, specifically during sleep and wakefulness. In particular, we will describe the mechanisms responsible for the generation of spindle oscillations during slow-wave sleep and how changes in dynamical organization patterns in the thalamus subserve a switch from sleep to the awake state, resulting in different information-processing capabilities. By reviewing new interesting results about the functional role of the thalamus, we will motivate our work in Chapter 3 aimed at shedding light on the different dynamical regimes that allow the thalamus to be not only a simple relay station, but interestingly a gate for information transmission towards the cortex and back.

### 1.1.3 Spatiotemporal coordination: large-scale synchrony and wave propagation

Neuronal oscillations emerge at many different spatial scales: they can arise from synchronization between individual neurons, larger assemblies of neurons, cortical areas, or even between hemispheres (global brain synchronization). Transient synchronization of neuronal discharges has been proposed as a possible mechanism to dynamically bind widely distributed sets of neurons into functionally coherent ensembles that represent the neural correlates of a cognitive content or a motor program (*binding-by-synchronization* hypothesis) (Singer, 1999). Beyond that, long-range synchronization has been proposed as a general mechanism for selectively routing the flow of information between brain areas.

In particular, gamma-band synchronization has been suggested as a mechanism to spatiotemporally coordinate the transmission of information between brain areas (*communication through coherence* hypothesis of Fries, 2005). In Section 1.3 we will introduce how synchronization of gamma oscillations can subserve neural communication. We will review the possible synchronization mechanisms in a large group of neurons and between distant populations even in presence of large synaptic delays, in particular focusing on gamma-band synchronization between coupled neural populations. This will be introductory and will offer the chance to motivate our study in Chapter 4.

Brain activity reveals exquisite coordination across not only temporal, but also spatial scales: from local microcircuits to brain-wide networks. Therefore synchronization, as a mechanism of large-scale integration, requires the study of different spatial and temporal scales simultaneously. We will deal briefly with this issue in Section 1.4, exploring the new advances

in the simultaneous multi-scale study of collective brain phenomena, that is preliminary to our work in Chapter 5.

Experimental tools such as voltage-sensitive dye (VSD) imaging (Shoham et al., 1999) and multielectrode arrays (MEAs) (Maynard et al., 1997) routinely allow nowadays measurements of large-scale spatio-temporally coherent population dynamics, revealing the existence of propagating waves in the visual, somatosensory, auditory and motor cortices under different cognitive conditions both *in vitro* (Buonomano, 2003; Pinto et al., 2005) and *in vivo* (Jancke et al., 2004; Lubenov and Siapas, 2009; Nauhaus et al., 2009; Watt et al., 2009). Propagating waves reveal a large-scale spatiotemporal coordination in the activity of neuronal ensembles at different spatial and temporal scales. In Section 1.5 we will briefly review experimental evidences of propagation activity in different brain areas, and focus on the possible functional role of propagating waves in the awake brain, that is propaedeutic to the study that will be presented in Chapter 6.

## 1.2 Temporally organized patterns in the thalamus: spindle oscillations

The thalamus is located near the center of the brain and it is made of two major components: the dorsal thalamus, composed of several thalamic nuclei and containing the gluatammatergic thalamocortical relay (TC) neurons that project to the neocortex, and the ventral thalamus, mainly composed by the reticular nucleus and containing GABAergic reticular thalamic (RE) neurons that inhibit TC neurons in the dorsal thalamus (Sherman, 2006). The thalamus is identified as a relay station between subcortical and cortical areas: sensory inputs from visual, auditory and somato-sensory receptors reach the cortex through TC neurons in specific regions of the thalamus, which project onto the corresponding areas in the primary sensory cortex. Along with these forward projections, there are feedback fibers from cortical layer 6 to the corresponding thalamic nucleus (see Figure 1.3) (Destexhe and Sejnowski, 2003). These large-scale thalamocortical interactions produce different rhythms in the thalamus according to the different cognitive states. One of the most studied rhythms are the spindle oscillations.

Spindle oscillations are rhythmic oscillations at $7-15$ Hz resulting from the coordinated temporal activity of neurons within the thalamus during slow-wave sleep. They originate in the thalamus and not from its connections with the cortex (Adrian, 1941; Bishop, 1936; Bremer, 1938; Morison and Bassett, 1945; Steriade and Deschenes, 1984; von Krosigk et al., 1993a), although their triggering and large-scale synchrony could rely on the cooperation with the cerebral cortex through the above-mentioned thalamocortical interactions (Destexhe, 2014). The generation of this rhythm is due to the rebound-bursting properties of the TC cells, which are mutually connected with the RE neurons. Spindles can be originated in TC cells with a burst of spikes, which can elicit PSPs that activate RE cells. In turn RE cells produce bursts at the spindle frequency, entraining TC cells to follow this oscillation and feeding back to the RE cells in order to sustain this rhythmicity. Therefore spindle generation is due to an interplay between TC and RE cells (Andersen and Eccles, 1962; Destexhe et al., 1993; Destexhe and Sejnowski, 2003; McCormick, 1992).

### 1.2.1 Thalamic dynamical regimes: bursting vs tonic

This oscillatory dynamical regime at the spindle frequency is defined as *bursting* because of the form of the response of thalamic relay cells to incoming inputs, and depends on the status of the corresponding intrinsic voltage-dependent membrane conductance (Sherman, 2001). This regime mainly dominates during slow-wave sleep, drowsiness and certain pathological conditions. On the other hand, during normal waking behavior, thalamic relay cells present

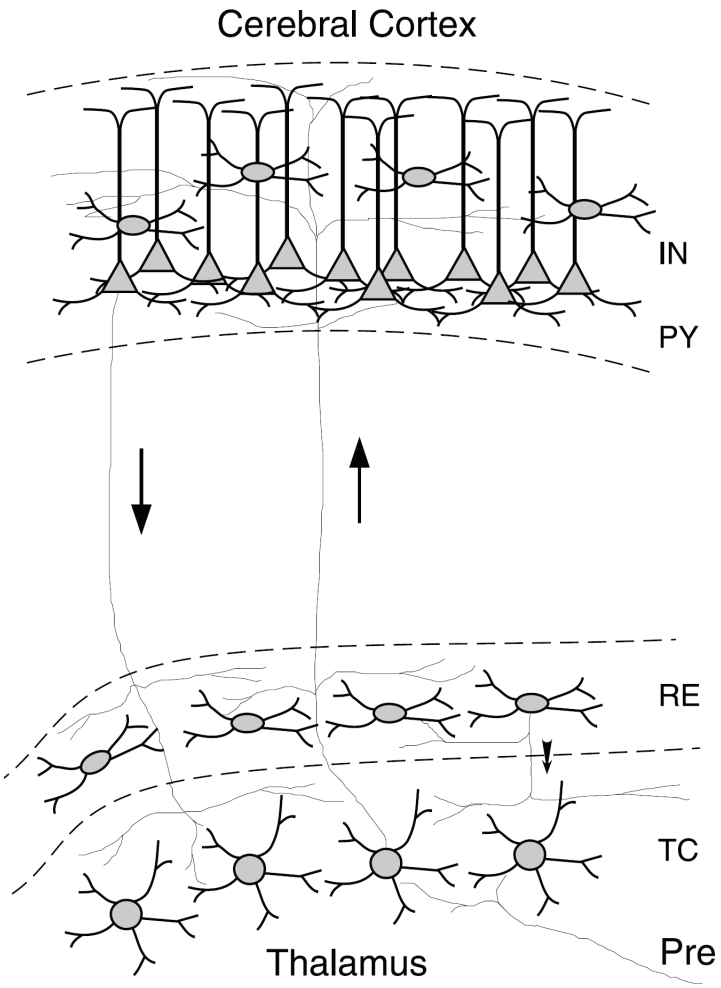


Fig. 1.3 **Structural connectivity of thalamocortical system.** Map of thalamocortical interactions between the thalamus and the cerebral cortex. The cortex receives its primary source of sensory input from the thalamus via thalamic afferents to the cortex, and the cortex projects back to the thalamus. This reciprocal interaction between thalamus and cortex could alter the cortical representation of sensory activity in time. Excitatory TC cells receive sensory inputs directly from subcortical areas, project mainly to pyramidal neurons and to interneurons of the corresponding sensory cortical area, and make excitatory synapses with RE neurons. RE neurons make collaterals with TC neurons. Along with feedforward thalamocortical projections, pyramidal neurons from the cortical area feed back to thalamic neurons. Adapted from Destexhe and Sejnowski (2003).

a different dynamical mode known as *tonic*. The two different dynamic modes, bursting and tonic, reflect the status of the voltage-dependent, intrinsic membrane conductance of TC cells and affect how TC neurons respond to incoming sensory inputs, with important effects on the process of relaying information to the cortex (Sherman, 2001).

During tonic firing, the spikes of a TC neuron are directly linked to an excitatory postsynaptic potentials (EPSP) in that cell, in such a way that larger EPSPs could elicit higher spiking rates. In a bursting regime there is no direct relation between an EPSP and an action potential, thus larger EPSPs do not generate higher firing rates. The quality of the information differs between modes (Sherman, 2001). The analysis of Sherman summarized in Figure 1.4 suggests that (i) the neural response profile to a sinusoidal input is more sinusoidal during tonic than during bursting mode (Figure 1.4C,D), and this reflects better linear summation (Figure 1.4E); (ii) spontaneous activity is higher during tonic firing (Figure 1.4A,B), which contributes to maintain linearity by minimizing rectification of the response (Sherman, 2001). Therefore the spontaneous activity represents the noise against which the visual response has to be detected. Figure 1.4 suggests that the signal-to-noise ratio or detectability is higher during bursting than during tonic regime. This has been confirmed directly by appropriate detectability measures in Figure 1.4F.

The understanding of how thalamic neurons are engaged in these dynamical modes depending on the cognitive states, and how these dynamics influences the information processing from thalamus to cortex and vice versa, could help elucidate what is the real functional role of the thalamus, which is still quite obscure.

### 1.2.2 Functional role of the thalamus

During the last decades, the idea of a thalamus as a simply relay to the cortex has been strongly debated. For instance, the discovery that feedback cortical projections represent the majority of afferent modulatory inputs on the thalamus led scientists to think that the thalamus plays a stronger role in the transmission of information to the cortex. In other words, the thalamus does not limit its activity to faithfully transmit information to the cortex, but it might play an active role in thalamocortical communication, acting as a dynamic control of the information that is passing through the thalamus. In that perspective, it might dynamically alter the information relayed in a manner that reflects various behavioral states such as attention and drowsiness, corresponding to different temporal organized patterns and dynamical regimes (Sherman and Guillery, 2002).

Moreover, the appearance of new technologies for the measurement and manipulation of intracellular activity sheds light on the functional role of thalamus in the processing of information. In this direction, Reinhold et al. (2015) performed exquisite experimental studies

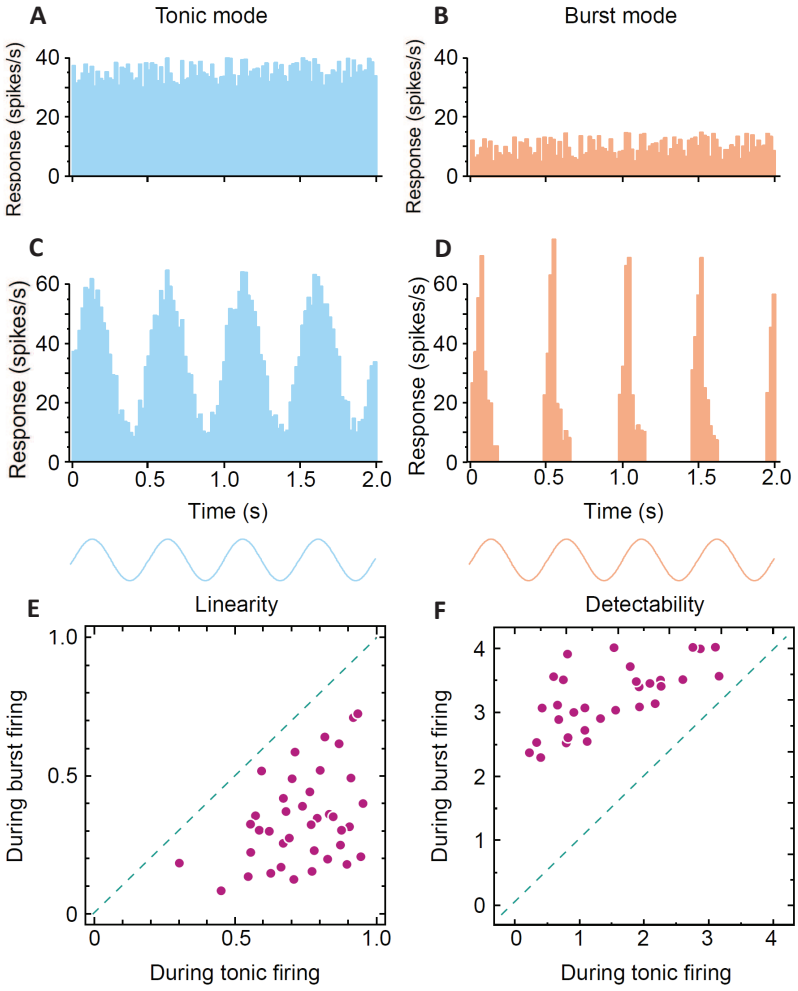


Fig. 1.4 **Tonic and bursting responses of relay TC neurons to visual stimulation from the LGN in the cat brain.** Tonic and bursting responses to visual stimulation of thalamic relay (TC) neurons from the lateral geniculate nucleus (LGN) of a cat (recorded *in vitro*). (A-D) Average response histograms of responses, recorded intracellularly, of one cell to four-cycles of drifting sinusoidal grating (C,D) and during spontaneous activity (A,B). Current was injected through the recording electrode to bias membrane potential towards depolarization (65 mV), which produces tonic firing (A,C), or towards increasing hyperpolarization (75 mV), producing burst firing (B,D). (E) Response linearity and (F) signal detectability during tonic and burst firing. Each point in the scatter plots reflects data from one relay cell of the cat's LGN recorded *in vivo* during visual stimulation. The dashed line in each plot has a slope of 1. To obtain a measure of linearity, responses to sine wave gratings were Fourier-analyzed and a linearity index was computed. The larger this index, the more linear the response. Note that every single cell shows more linearity during tonic firing. For detectability, values were determined by receiver operating characteristic (ROC) analysis. From Sherman (2001).

and obtained very interesting results about the role of the thalamus in clocking the recurrent cortical dynamics. They found that the sensory-evoked activity in visual cortex upon the appearance of a stimulus does not simply reflect a self-sustaining activity due to intracortical recurrent circuits (with the important contribution of cortical inhibition), but it is entrained and amplified by the direct thalamocortical communication pathway. In particular they designed an optogenetic method able to silence, with millisecond precision, the cortical circuits and the direct thalamic input, and identified what are the relative contributions of the intracortical circuits versus the thalamic afferents on the sensory-evoked cortical activity. These experiments have been carried out in awake and under anesthesia conditions (Reinhold et al., 2015). First, they silenced the cortex (Figure 1.5A), and found that during the first 40 ms the thalamic excitation is dominant, after what the contribution of the cortical recurrent circuits grows progressively, and after 250 ms, cortical recurrent circuits amplify the thalamic input by more than a factor of 3 (Figure 1.5C) (Reinhold et al., 2015). Second, they silenced the thalamic afferents once the visual cortical response is enhanced (Figure 1.5B) to study the timescale of intra-cortical self-sustaining activity when the thalamic input is removed. By silencing the thalamus without visual stimulation, intracortical self-sustaining dynamics lasts up to hundreds of milliseconds. Upon sensory stimulation, if the thalamus is silenced, cortical response decays with a time constant of 10 ms, which corresponds to the integration time window of a single cortical neuron and is more than two orders of magnitude faster than when the thalamus is on (Figure 1.5D). Silencing the thalamus reduces the visual cortical responses and the spontaneous cortical activity of the awake primary visual cortex, meaning that the thalamus temporally constraints cortical responses and drives cortical spontaneous activity (Alonso and Swadlow, 2015). The fast sensory-evoked recurrent intracortical activity (without direct thalamic input) could be due to cortical inhibition, which is proposed to regulate the dynamics of recurrent circuits (Constantinople and Bruno, 2011; Sanchez-Vives and McCormick, 2000; Timofeev et al., 2000). Thus, intracortical inhibition enforces the fast decay time of cortical recurrent networks and allows them to follow the fast temporal frequencies of thalamic inputs during the awake state (Alonso and Swadlow, 2015).

Additionally it is known that by passing from anesthesia and drowsiness to awake and alert state there is an increased spiking activity in the thalamus. Given that thalamocortical synapses exhibit depression (Gil et al., 1997), higher firing rates in alert subjects lead to chronic depression at the thalamocortical synapses (Alonso and Swadlow, 2015; Castro-Alamancos and Oldford, 2002). According to the results of Reinhold et al., this activity-dependent depression of thalamocortical synapses could explain the lack of response of the cortex to high temporal frequencies in the anesthetized brain (Figure 1.5E). Indeed, self-sustained activity under anesthesia or with absence of sensory stimulation is prolonged for several tens of milliseconds.

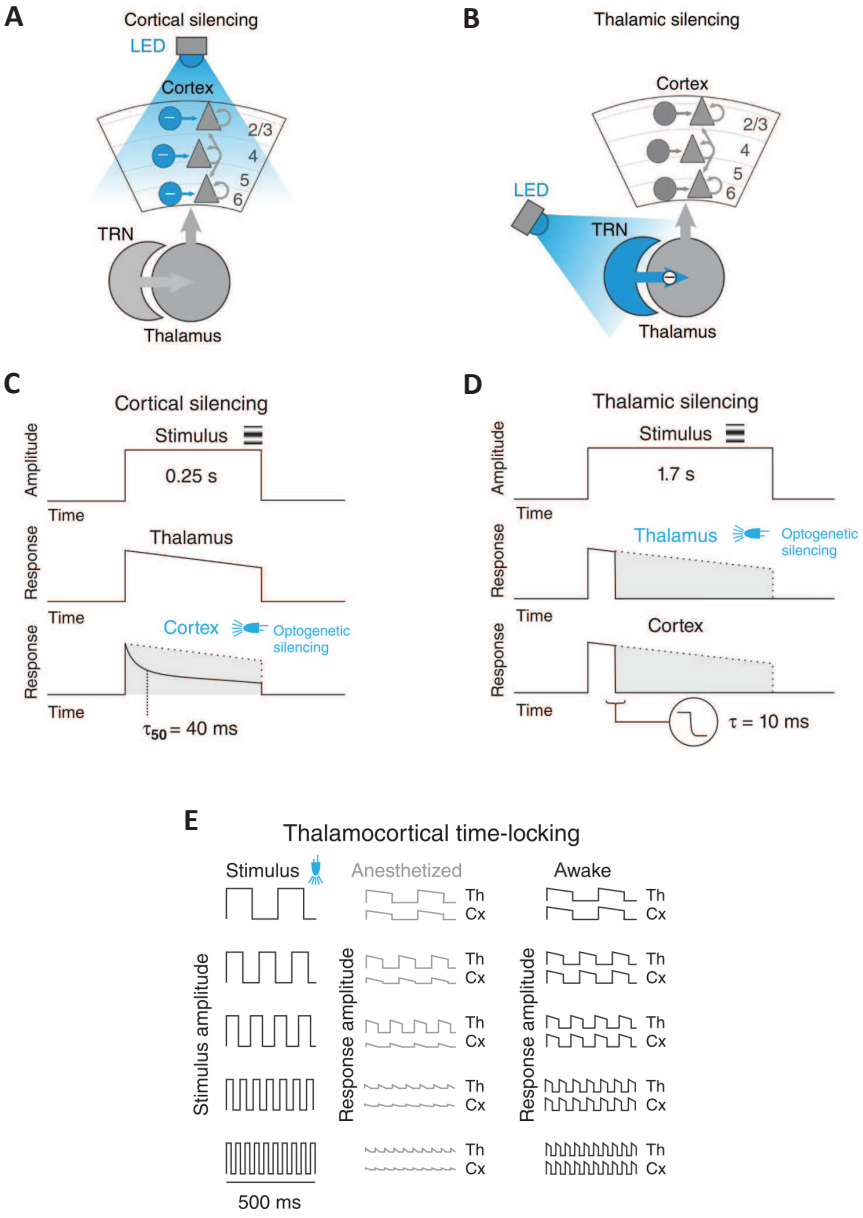


Fig. 1.5 **Contribution to sensory-evoked cortical activity: cortex versus thalamus.** (A,B) Optogenetic tool developed by Reinhold et al. (2015) to silence the thalamus by activating inhibitory reticular neurons (A) and to silence the cortical neurons in layer 4 by activating cortical inhibition (B). (C) By optogenetically silencing the visual cortex in mice, Reinhold et al. (2015) recorded the response of layer-4 neurons to a visual stimulus. They found that the thalamus mainly contributes to the total excitatory response during the first 40 ms ($\tau_{50}$). (D) By optogenetically silencing the thalamus, the cortical response rapidly decays with a characteristic time of 10 ms, corresponding to the integration time of a single cortical neuron. (E) Due to the fast decay dynamics, the cortex is able to follow high-frequency stimulation (transmitted by the thalamus when the animal is awake). When the animal undergoes anesthesia, the high-frequency transmission is not possible due to weaker thalamic responses and thalamocortical synaptic depression. Panels (A,B) adapted from Reinhold et al. (2015), panels (C,D,E) adapted from Alonso and Swadlow (2015).

These results shed light on the possible functional role of the thalamus, which cannot be a simple relay station in every cognitive state, but it transiently and functionally switches from a dynamical mode to another, to gate and elaborate the flow of information according to the specific cognitive state. These results could also call for the design of new experimental studies to understand the effective modulatory role of corticothalamic feedback on the thalamus.

The results discussed above show that understanding how the different types of thalamic neurons are engaged in different temporal motifs, and how they switch from one mode to the other depending on the cognitive state, could give crucial insights on the dynamical role of the thalamus in transmitting information to the cortex. Guided by this need, in Chapter 3 we will address the general question of how the thalamus changes its dynamical behavior (which is associated with different information-processing regimes, corresponding broadly to wakefulness and sleep) as a function of both its internal state and external inputs. In particular, we will show that a simple yet biologically realistic model of the thalamus can exhibit two dynamical regimes with different information processing capabilities, and study the transition between them. Furthermore we will investigate how the network architecture of the thalamus influences the occurrence of these two regimes, and how the transition between them is controlled.

## 1.3 Synchronization of neuronal oscillations

As the spindle oscillations in the thalamus, neuronal oscillations in general are a signature of the temporal coordination of neuronal discharges of a large group of neurons. They are associated with different cognitive functions and brain areas according to their frequency and intrinsic properties. Understanding how and when oscillations arise at the population level and give rise to oscillatory synchronized patterns at large scale might provide interesting insights on how the brain reaches the required level of spatiotemporal coordination between brain regions that seems to be essential for the accomplishment of cognitive tasks. Functionally a challenging hypothesis is that synchronization of neuronal oscillations at different spatiotemporal scales is a possible candidate for neural communication (Fries, 2005; Schnitzler and Gross, 2005).

Neuronal synchronization is different from other widely studied natural synchronization phenomena because (i) the brain is a complex nonlinear system, (ii) neurons themselves are nonlinear multidimensional systems displaying a range of dynamics in various spatiotemporal scales and finally (iii) neurons are connected by means of synapses, which are dynamical elements that influence the process of synchronization (Rabinovich et al., 2012). Local neuronal synchronization results from a temporally precise coordination of neurons in a certain population, while long-range oscillatory synchronization stems from a spatiotemporal coordination of neural activities of distant populations. Oscillation-based synchrony is considered the most energy-efficient physical mechanism for temporal coordination (Buzsáki and Draguhn, 2004; Mirollo and Strogatz, 1990).

The establishment of local and long-range synchronization relies on the topology of complex neuronal networks. In cortical networks, the topology of the connectivity recalls some properties of the small-world networks characterized by areas densely connected more than others with no singular center working as coordinator where all information converges. These local circuits are supplemented by a smaller percentage of long-range connections (with respect to the local ones) (Braitenberg and Schüz, 1998), and this drastically reduces the synaptic connections between distant neuronal assemblies (Buzsáki et al., 2004). It is thus natural to ask how the different computations taking places simultaneously in spatially segregated areas, e.g. underlying different features of an object, are coordinated to give rise to a unified perception (Uhlhaas et al., 2009). A solution could lie in the emerging synchronized behavior of the involved areas. Despite the smaller number of long-range connections, the synchronization of local and distant areas might be accomplished by oscillators due to the low energy costs involved in coherent neuronal oscillations, which provide temporal opportunities for preferential communication pathways, by tuning the fluctuations of the membrane voltage of neurons par-

ticipating in the collective oscillatory dynamics (Buzsáki and Draguhn, 2004; Fries, 2005). In this Section we will mainly concentrate on synchronization and phase locking as coordinating mechanisms based on the temporal patterning of neuronal activity.

### 1.3.1 Local mechanisms of zero-lag synchronization

Several experiments have shown that neuronal circuits can synchronize either at zero time lag or with a time lag much smaller than the conduction delay (near zero phase) (Roelfsema et al., 1997). We focus mostly on the first mechanism, known as zero-lag synchronization. Given the complexity of the phenomenon, several mechanisms have been proposed to be responsible for sustaining synchrony at different scales and different cerebral structures.

A first mechanism supporting a zero-lag synchronization scenario in cortical neuronal networks is entrainment via a common drive from a single source. The source could be located in another cortical area, or in a sub-cortical area like the thalamus (Steriade et al., 1993). Locally, intrinsic oscillating cells or pacemaker cells could entrain the network activity at a specific frequency. An example are the chattering cells likely involved in the generation of stimulus-driven gamma oscillations (Gray and McCormick, 1996). This entrainment influences the rhythm and the synchronization among the target cells. Although the mechanism is quite simple, the synchronization can be dynamic and depends on the strength of the entrainment, on the internal coupling and on the intrinsic properties of the neurons (Uhlhaas et al., 2009).

A second mechanism compatible with the generation of zero-phase synchrony is based on local network effects. A single neuron cannot entrain the network, but the interaction between neurons in the network can give rise to emerging synchronous oscillations with small phase-lag. This mechanism is different from entrainment, because emerging patterns are a feature of the interactions between neurons. Network effects responsible for this synchronization are for instance recurrent inhibition, mutual excitation, mutual inhibition and gap junction coupling (Kopell et al., 2000b; Ritz and Sejnowski, 1997; Van Vreeswijk et al., 1994).

Furthermore in complex heterogeneous networks with non-instantaneous coupling, the recurrent inhibition between excitatory and inhibitory balanced sub-networks plays a crucial role in inducing zero-phase synchronization (Kopell et al., 2000b; Van Vreeswijk et al., 1994). In this synchronization via recurrent inhibition, neuronal networks can synchronize their activity at zero lags without necessarily altering the average firing rate of the neurons (Buia and Tiesinga, 2006; Tiesinga and Sejnowski, 2004). The same is not true for instantaneous excitatory coupling, which seems to favor desynchronization rather than synchronization for a broad class of models and parameter regimes (Kopell et al., 2000b; Ritz and Sejnowski, 1997). Electrical gap junctions are often neglected in many computational models, however they are important for generating oscillatory synchronized activity. A proof was provided by experi-

mental studies where chemical coupling is blocked and thus oscillatory activity is entrained by gap junctions (Buzsáki and Draguhn, 2004).

These mechanisms cannot be adopted to explain zero-phase synchrony findings between distant brain regions, e.g. between areas located in different hemispheres where synaptic delays are not negligible (Singer, 1999; Varela et al., 2001) and are due to conduction times, synaptic delays and electrotonic propagation. By way of example, the aforementioned zero-lag synchronization induced by recurrent inhibition, with or without gap junctions, is only plausible for networks dominated by local neuronal coupling (Uhlhaas et al., 2009). A unique mechanism to explain local and global zero-lag synchronization has not been found yet.

### 1.3.2 Zero-lag synchronization of distant coupled populations

A network topology that can exhibit zero-lag synchronization of distant populations of neurons is made of two dynamical elements bidirectionally coupled with a central mediator, which redistributes symmetrically identical information to the outer two (Fischer et al., 2006) (Figure 1.6). In this configuration, zero-lag synchrony is preserved even when the fibers connecting the networks have a diversity of conduction delays (Vicente et al., 2008). The mediator role could be played for instance by the thalamus, given its simple topology of bidirectional and radial connectivity to the neo-cortex as a mechanism to support distributed cortical processing (Jones, 2002; Sherman and Guillery, 2002). In this scheme, thalamic nuclei have the cortex as the input and the output at the same time, and could play an important role for the mediation of zero phase solutions, enhancing cortical coherence (Shipp, 2003b). This long-range oscillatory activity could be extended to different motifs whose senders populations share the relay network (*hub*) (Sporns et al., 2007). Therefore, provided that there is a constant temporal latency between the relay and the outer populations, which is true between thalamic nuclei and any area in the mammalian cortex (Salami et al., 2003), self-organized lag-free synchronization can emerge in all three networks (Figure 1.6B-E). Thus, dynamical relaying-based synchronization might induce and sustain the establishment of long range neuronal synchrony, with the relay being the thalamus or other cortical areas through corticothalamic or purely cortico-cortical connections, respectively. In what follows we concentrate on synchronization between neuronal populations oscillating in the gamma range and possible consequences for neural communication, because gamma-band synchronization might subserve various cognitive functions.

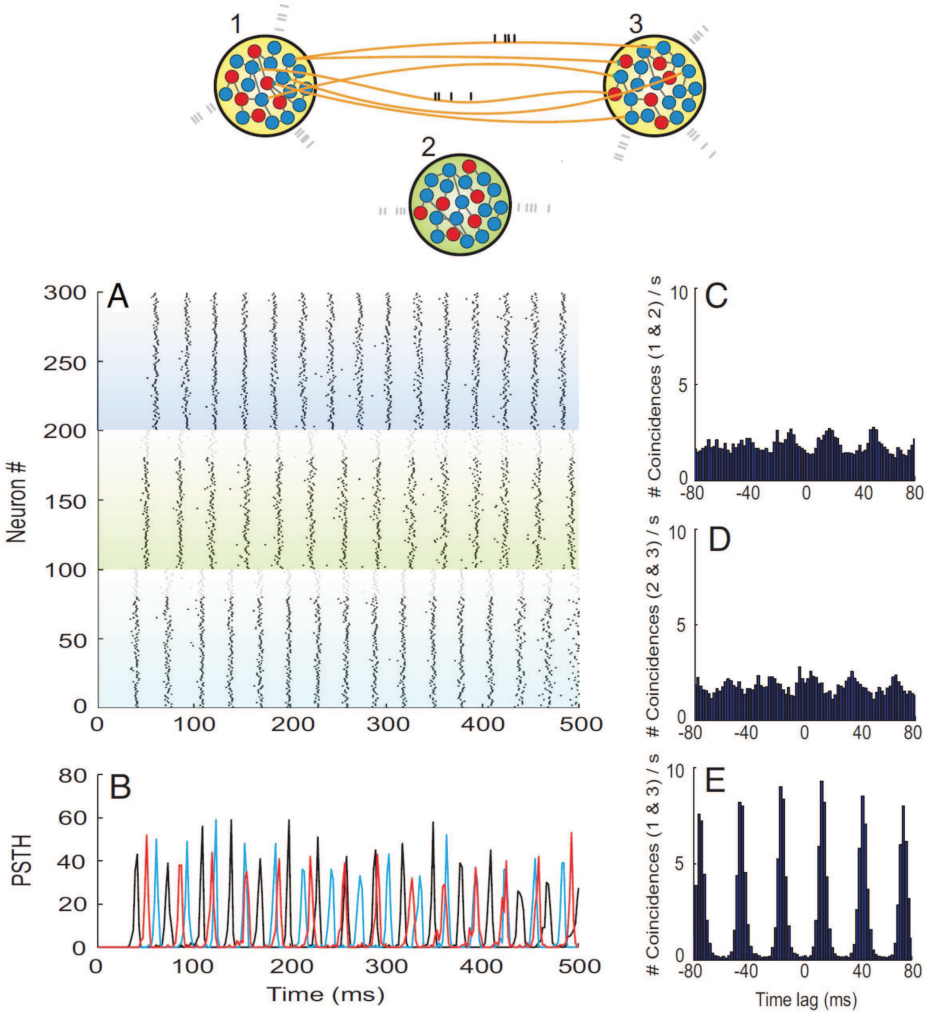


Fig. 1.6 **Dynamics of three neuronal populations interacting through dynamical relaying.** Topology of three large-scale networks of excitatory and inhibitory neurons receiving external poissonian excitatory input interacting through dynamical relaying. Axonal delays are set to 12 ms. (A) Raster plot of the activity of each neuron of population 1 (neurons 1–100), population 2 (neurons 101–200) and population 3 (neurons 201–300). The top 20 neurons of each subpopulation (plotted in gray) are inhibitory, and the rest are excitatory (black). (B) Firing histogram of each subpopulation of 100 randomly selected neurons (black, red, and blue colors code for populations 1, 2, and 3, respectively). (C) Average cross-correlation between population 1 and 2. (D) Average cross-correlation between population 2 and 3. (E) Average cross correlation between the outer populations 1 and 3. The size of histogram bins is set to 2 ms. From Vicente et al. (2008).

### 1.3.3 Gamma-band synchronization

Numerous experimental and computational findings have described activated neuronal groups engaging in rhythmic synchronization in the gamma-frequency band (broadly 30 – 100 Hz). These studies have been performed in many brain areas, including the visual cortex (Eckhorn et al., 1988; Engel et al., 1991; Gray et al., 1989), the auditory cortex (Brosch et al., 2002; Edwards et al., 2005), the somatosensory cortex (Bauer et al., 2006), the motor cortex (Brown et al., 1998; Schoffelen et al., 2005), the retina and lateral geniculate nucleus of anesthetized cats (Neuenschwander and Singer, 1996), and the hippocampus of awake behaving rats (Bragin et al., 1995). Moreover gamma-band synchronization has been observed across different species, including cats, monkeys, rats and mice (Bragin et al., 1995; Csicsvari et al., 2003; Montgomery and Buzsáki, 2007; Montgomery et al., 2008), in different invertebrates (Stopfer et al., 1997; Wehr and Laurent, 1996), and in the visual cortex of human subjects (Fries et al., 2007, 2008). This mechanism has been associated with cognitive functions such as attention, arousal, object recognition and top-down modulation of sensory processes (Engel et al., 2001; Singer, 1999).

Pioneering studies mainly focused on testing the proposal that gamma-band synchronization subserves perceptual binding, known as the *binding-by-synchronization hypothesis*. This hypothesis states that neurons forming a functional assembly are bound together by synchronization of their action potentials. Emerging oscillations then allow activated neuronal groups in distant cortical regions with sparse interconnections to become temporally linked, and subsequently activate unique sets of downstream assemblies (Eckhorn et al., 1988; Gray et al., 1989; Singer, 1999; Singer and Gray, 1995).

New experimental observations have extended the concept of gamma-band synchronization beyond being exclusively a mechanism for binding (Schnitzler and Gross, 2005). The time span required to bring together transient cell assemblies (Harris et al., 2003) approximately matches the gamma cycle, and the induced oscillation is long enough to allow for an elementary cognitive act (Engel et al., 2001; Llinas and Ribary, 1993; Varela et al., 2001).

### 1.3.4 Communication through coherence between coupled gamma oscillating populations

When the neurons in a target group are synchronized in the gamma-frequency band, they are under the dominant influence of gamma-rhythmic inhibitory inputs (Hasenstaub et al., 2005). Consequentially, synaptic excitatory inputs are more efficient if they impinge on the network out of phase and vice versa. The implication of this statement is that rhythmic local inhibitory synchronization leads to periodic modulation of excitatory input gain (Fries, 2009). The input

gain is modulated cyclically with short windows (around 12 ms, corresponding to half the gamma period), and affects the average gain of rhythmic excitatory input across multiple cycles. The average gain across cycles is determined by the precision and phase of the synchronization between rhythmic input and rhythmic gain. Therefore, synchronization provides a more consistent phase relation between the rhythms than lack of synchronization, and the input gain can be maximized or minimized according to this phase relation (Figure 1.7A,B). Therefore interactions among rhythmically active neuronal groups could depend on neuronal synchronization. This is behind the hypothesis called *communication through coherence* (Fries, 2005) (Figure 1.7). This hypothesis establishes that if two neuronal populations oscillate with a constant phase difference, then an effective transmission of information is possible provided that spikes sent by one population reach the other one at its peak of excitability.

However, temporal coordination between spatially separated populations (connected by long-range axon collaterals) might be destabilized by the presence of conduction delays (Ermentrout and Kopell, 1998). If the conduction delays are of the order of $4-8$ ms, reciprocally coupled oscillators in the two hemispheres might still synchronize at zero-phase. However, given that conduction delays can take up to several tens of milliseconds, how does the brain reaches the required level of coordination in order to establish efficient communication channels between different brain areas?

In Chapter 4 we will address the general question of how communication is established between physically separate brain areas, using neuronal oscillations as information carriers. In particular, we will examine whether and how effective communication between cortical areas arises even when the time taken by neuronal signals to go from one area to another is comparable to, or larger than, the typical time scales of the underlying neuronal networks. To do so, we used a biophysically realistic computational model of two synaptically coupled neuronal populations working in the gamma regime. Our model reproduces quantitative features of experimental observations of communication through coherence (Bosman et al., 2012; Womelsdorf et al., 2007), and provides a mechanism to explain why the experimental observation of this strategy of information transmission is so pervasive.

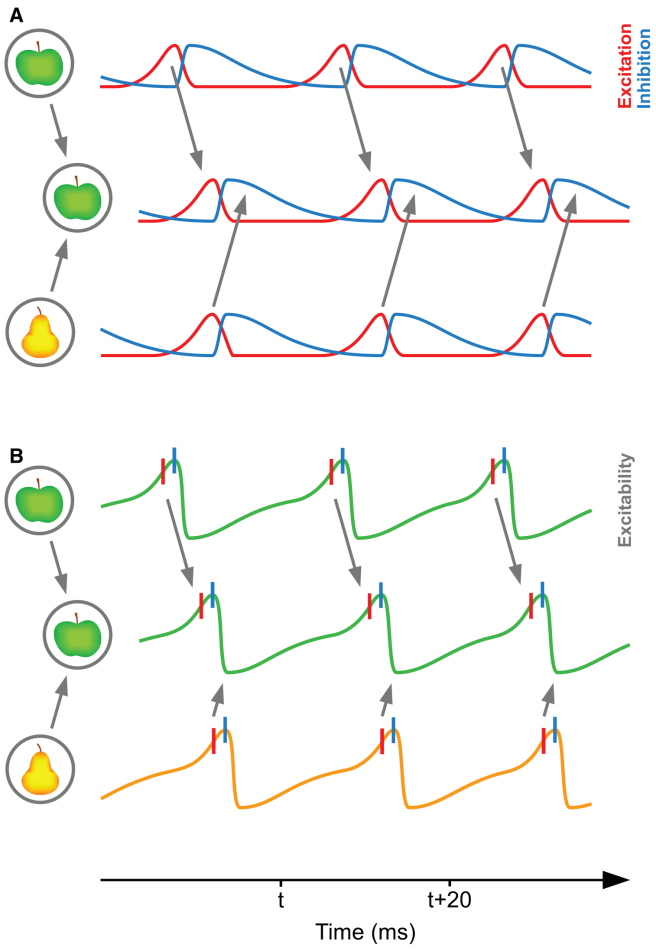


Fig. 1.7 **Communication through coherence hypothesis.** (A) Two presynaptic neuronal groups in a lower visual area send two inputs (an apple and a pear) to a postsynaptic neuronal group in a higher visual area. In each neuronal group, excitation (red) triggers inhibition (blue), which inhibits the local network. When inhibition wears off, excitation starts again along the gamma cycle. The gamma rhythm of the presynaptic group representing the apple reaches the postsynaptic group in antiphase, and is therefore able to engage it. Thereby, the apple-representing presynaptic group can optimally transmit its representation. On the other hand the pear-representing presynaptic group cannot transmit its representation (Fries, 2005). (B) Illustrative plot of network excitation and inhibition combined into network excitability. Red vertical lines indicate excitatory neuron spiking and blue vertical lines inhibitory neuron spiking. From Fries (2005).

## 1.4 Synchronization as a mechanism of large-scale integration

The mammalian brain is composed of a myriad of coupled neurons that interact dynamically and exhibit various dynamical activities and processes happening at different timescales, including sub-milliseconds (gating of ionic channels), milliseconds (action potentials), seconds (flow of slow ionic currents), minutes (synaptic conductances variation), days (growth and development of new synaptic connections) and decades (death of neurons). The same applies with respect to space. In fact neuronal dynamical processes cover a wide range of spatial scales, from micrometers (molecular and biochemical processes within neurons), to millimeters (synaptic interaction in local neuronal ensembles) and centimeters (interaction between different areas of the brain). Owing to a complex functional hierarchy between cell groups, the brain is able to process multiple sensory inputs efficiently and simultaneously and produce coherent output in the form of actions and thoughts. Therefore information processing relies on the coordinated interaction between large groups of interconnected neurons distributed within and across different specialized brain areas (Bressler and Kelso, 2001; Jirsa, 2004; McIntosh, 2000). How does the brain coordinate all the perceptions, thoughts and actions that result from neural processes happening at different temporal scales and distributed across the brain? What are the neural mechanisms that select and coordinate this distributed neural activity to accomplish a certain cognitive task? This is the large-scale integration problem (Varela et al., 2001).

### 1.4.1 Local and large-scale integration

In the brain, the emergence of a neural assembly (see Section 1.1) underlies the operation of each cognitive act. These functional neuronal ensembles have a transient existence that spans the time necessary to accomplish a cognitive act (which can be as short as a fraction of a second), but their existence is long enough to allow the activity to propagate throughout the assembly, propagation that requires cycles of reciprocal spike exchanges with delays of transmission up to tens of milliseconds. Therefore the relevant variable to describe these neural assemblies is the dynamic nature of the links between them, rather than the individual activity of single component. In fact each neuronal integration mechanism is based on the local interaction between the participating networks (Damasio, 1990; Mesulam, 1990). While some authors thought that, due to the hierarchical organization of the brain, the associative areas between motor and sensory regions allow for integration, the hypothesis most widely accepted nowadays is that networks with their respective interactions provide the basis for in-

tegration (Damasio, 1990; Mesulam, 1990). Between the various modes of mutual interaction, one of the most experimentally studied is integration through phase synchronization (Varela et al., 2001).

Phase synchrony is a basic mechanism for brain integration, and direct evidence is provided by the visual binding hypothesis (see Section 1.1.3). This hypothesis states that different features of a visual object, which are processed separately in specific visual areas, bind together to give a unified percept through the synchronization of local discharges of cell assemblies (Roskies, 1999). Therefore, visual binding refers to *local* integration of neuronal properties at the level of neighboring cortical areas, specialized in the same modality. In contrast, Varela et al. (2001) proposed that synchronization of neural assemblies is a process spanning multiple spatial and temporal scales in the nervous system (see Figure 1.8), and not just a local mechanism.

Local integration takes place over a local network of the size order of $\approx 1$ cm (Figure 1.8A) by making direct reciprocal connections (in the same cortical area) with conduction delays of typically $4-6$ ms (Girard et al., 2001). In contrast, large-scale synchronization involves neural assemblies that are located in distant parts of the brain, even in different hemispheres ($> 1$ cm) (Figure 1.8B). Consequently signal transmission along indirect connections (usually named feedforward or feedback, connecting different brain regions) could take up to several tens of milliseconds due to conduction delays (Phillips and Singer, 1997; Varela et al., 2001).

### 1.4.2 Evidence for large-scale synchronization

In the last years several experiments have been designed to illustrate the existence of large-scale oscillatory synchronization and test its potential functional role, as one of the mechanisms that might implement coordinated communication across different neural subsystems (Bressler et al., 1993; Roelfsema et al., 1997; Schnitzler and Gross, 2005; Varela, 1995), going beyond the binding hypothesis. Three main observations support the functional relevance of large-scale oscillatory synchronization: (i) the fact that beta oscillations are functionally involved in long-range synchronization (Baudry et al., 2001; Kopell et al., 2000b; Tallon-Baudry et al., 2004), (ii) the importance of the spatiotemporal balance of synchronization and desynchronization (Friston, 2000; Hanslmayr et al., 2016; Rodriguez et al., 1999), and (iii) the discovery that synchronization patterns are directly related to behavior (Fell et al., 2001; Fries et al., 2002b; Tallon-Baudry et al., 2004).

Significant evidence for large-scale synchronization has been provided by experiments with EEG and MEG, among others. A significant experiment conducted by Rodriguez et al. (1999) provides direct support for long-range synchrony and represents one of the first signatures of the functional significance of long-distance synchronization in human brain activ-

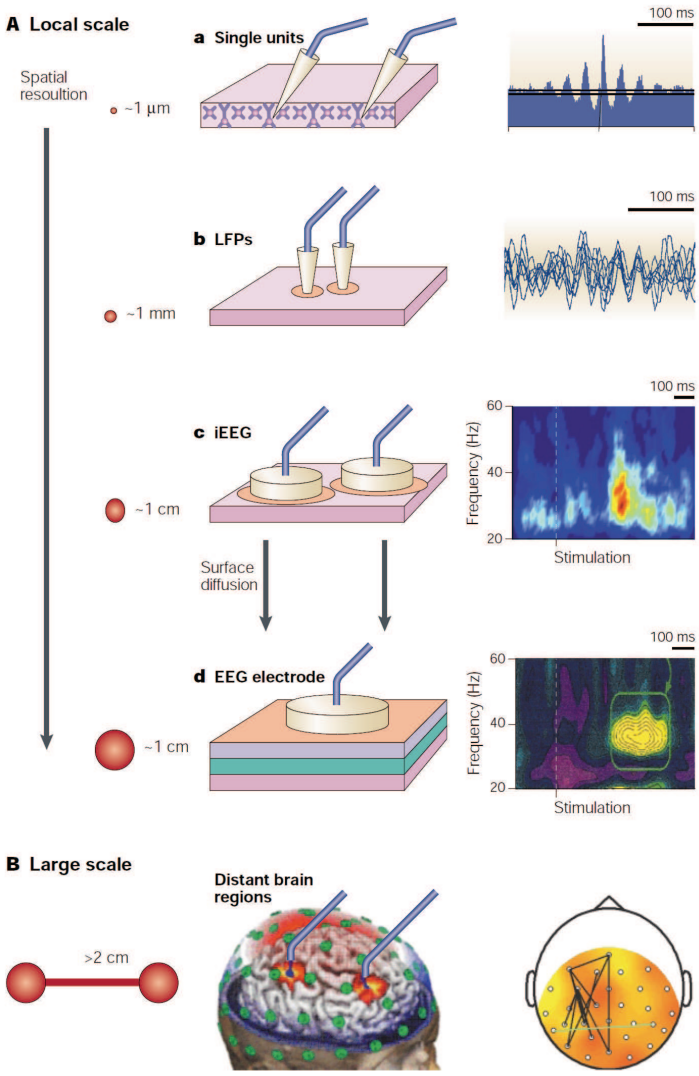


Fig. 1.8 **Neural synchrony as a multi-scale phenomenon.** Synchronization of neural assemblies is a process spanning multiple spatial and temporal scales in the nervous system. (A) Local scale. In a small region or a local network three different levels of analysis can be considered: (a) Synchronization between single cells under specific stimulus as measured by cross-correlogram. (b) Local field potentials from recording electrodes (separated maximum 7 mm). The traces represent fast oscillations synchronization episodes. (c) Transient synchronized patterns within a population of neurons measured intracranially. Populations are most transiently synchronized in the gamma range after the appearance of a stimulus. (d) Activity from recording electrodes on the surface: synchronous patches appear as spatial summation of cortical responses that account for the increase in the gamma range. (B) Large scale. Patches of local synchrony in distant brain areas can synchronize during the accomplishment of a cognitive task. Black lines identify electrodes that are synchronized during a stimulus recognition task. From Varela et al. (2001).

ity. The authors recorded electrical brain activity from subjects who had to discern among ambiguous visual stimuli perceived either as faces (Figure 1.9A) or as meaningless shapes (Figure 1.9B). Figures 1.9C and 1.9D show two induced gamma-activity peaks, with the second likely involved in post-perceptual processes. The two peaks correspond to the moment of perception of the face itself and to the ensuing motor response. It does seems there is not too much difference in the power spectrum between the perception and no perception cases. On the other hand phase synchrony analysis, that quantifies effective synchrony between the activities recorded in different electrodes (Figure 1.9E), shows that during the perception condition, there is an increase in phase synchrony soon after the stimulus (around 230 ms), which is temporally correlated with the increase in power spectrum in Figure 1.9C. Given that there is no evident pattern in the case of no perception, it is reasonable to think that this sharp increase of phase synchrony at the power spectrum peak is functionally relevant in the perception itself. There is another peak of phase synchrony around 645 ms associated with the motor response in both conditions, because the subject was asked to respond to the two stimuli. The transition between these two cognitive states, i.e. face perception and motor response, is characterized by a sharp decrease in phase coherence, or desynchronization, probably driven by an active uncoupling of the underlying neural ensembles. The authors also mapped the areas of long-distance synchronization, verifying that they effectively correspond to regions devoted to visual perception and motor task according to previous experiments. This result supports as well the idea that long-distance phase synchronization and desynchronization play an essential role in large-scale cognitive integration (Bressler et al., 1993; Roelfsema et al., 1997; Varela, 1995; Von Stein et al., 2000), and not just in local visual-feature binding. There are other results (Perez-Orive et al., 2002; Salmelin and Kujala, 2006) supporting the functional role of oscillatory synchrony in perception.

If large-scale synchrony subserves normal brain functioning, then synchrony disruption should be the cause of abnormal functionalities (Varela et al., 2001). Important advances in the study of neurological disorders provide further relevance to oscillatory synchronization and its involvement in cognitive functions. In fact many experimental studies showed a sharp correlation between abnormalities in neural synchronization and cognitive dysfunctions. Evidences are related to brain disorders, such as schizophrenia (Friston, 1999; Phillips and Silverstein, 2003; Schnitzler and Gross, 2005), epilepsy (Penfield and Jasper, 1954), autism (Hussman, 2001; Rubenstein and Merzenich, 2003), Alzheimer's disease (Montez et al., 2009; Pons et al., 2010; Stam et al., 2007), and Parkinson's disease (Levy et al., 2000; Limousin et al., 1995; Lyons and Pahwa, 2008; Schnitzler and Gross, 2005) (see table 1 of Uhlhaas and Singer, 2006). These findings reveal that disorders of these diseases are related to local and long-range synchronization, and concurrently the cognitive functions that are impaired in these diseases

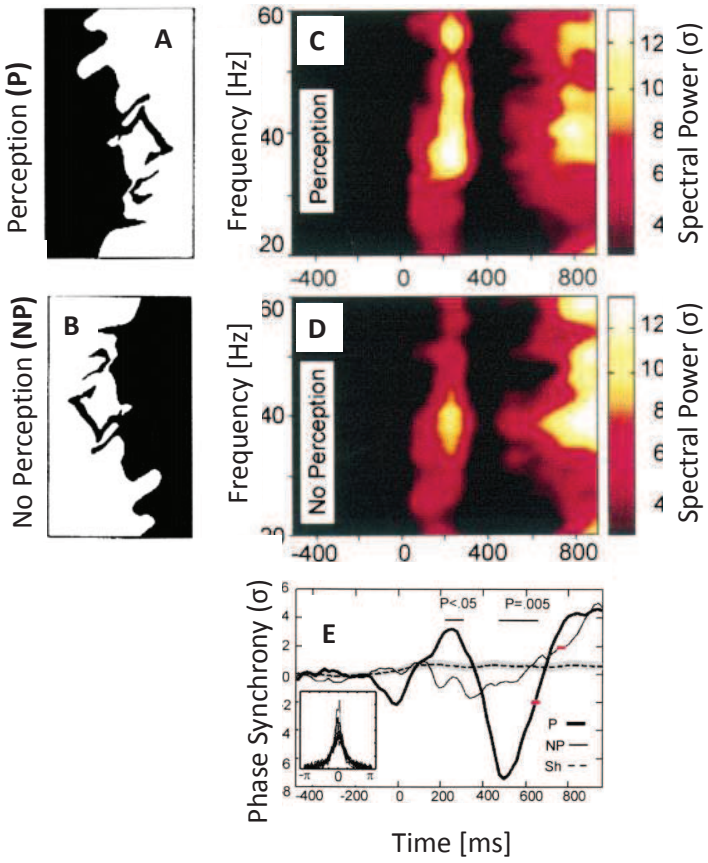


Fig. 1.9 **Functional role of long-range neural oscillatory synchronization.** (A,B) Examples of *Mooney* faces, high-contrast pictures of a human face. These pictures look like a human face when seen upright (A) but have no clear meaning when inverted (B). (C,D) Time-resolved power spectral density after the appearance of the two different stimuli: (A) as perception and (B) as no-perception. The color plots focus on the gamma range and exhibit two periods of increased gamma power emission between $20-60$ Hz. A first power peak is recorded at 230 ms after stimulus onset. The power emission in the perception (P) condition is higher than in the no-perception (NP) condition. (E) Phase synchrony for the P and NP conditions. NP synchrony remains stable until 700 ms. Phase synchrony for the P condition increases at 230 ms ($P < 0:05$), decreases sharply at 500 ms ($P = 0.005$), and ends with a second increase. Adapted from Rodriguez et al. (1999).

have all been associated with neural synchronization. These experimental results support the hypothesis that abnormal synchrony is one of the causes of cognitive dysfunction, and consequently that temporal and spatial coordination of distributed neuronal activity through precise synchronization plays an important role in normal brain functions.

### 1.4.3 Multi-scale approach

An answer to the large-scale integration problem has not been found yet, because a full theoretical description of the normal and pathological functioning of the brain is still missing. Its study is usually partitioned into different research fields devoted to distinct brain structures (such as the thalamus, amygdala, hippocampus, etc.), cortical functional areas (motor, visual, auditory cortex, etc.) or particular microscopic circuits, from the level of cortical columns down to single-neuron responses. Moreover, studies of the global activity of the brain usually focus for convenience on specific cognitive or motor tasks, in order to compare them with a control state such as spontaneous activity at rest.

Further the advent of neuroimaging methods has led to the study of functional localization, focusing on a one-to-one mapping between regions of the brain and physiological processes. Using these approaches, neuroscientists have been working to link brain dynamics to behavior by correlating increases or decreases of some measure of brain activity with the cognitive status of a human subject undergoing a certain task. Under the assumptions that the cognitive processes can be localized in specific regions of the brain (functional localization) and at the same time can be measured by the average increase in activity levels, the complexity of these cognitive processes is reduced to two dimensions: their location in space and their activation state. But can these two dimensions fully characterize cognitive processes? The typical scale of functional localization (of the order of a few cubic centimeters) is large compared to the amount of neurons that possess similar physiological, neurochemical, morphological and structural properties contained in each MRI voxel. Moreover, it is doubted that a one-to-one mapping exists between cognition and brain regions (Price and Friston, 2005). In fact, given the diversity and flexibility of the various cognitive processes, some of them may activate the same region and inversely, the activation of different brain regions may reflect the same cognitive process. These evidences may be an indication of the physically separated but functionally linked networks that underlie neurocognitive function (Bullmore and Sporns, 2009; Cohen, 2011; Varela et al., 2001). As mentioned above, in the brain there are different spatial scales which differ by several orders of magnitude, from single neurons at the microscopic level to cortical columns at the mesoscopic and macroscopic levels. It is not clear what is the appropriate spatial for the study of functional localization or if several neurocognitive processes can be localized at different scales. It is plausible that some brain dynamics might be relevant at certain scales and not at others. Therefore, functional localization has been a useful approach to understand the theories and experiments of cognitive neuroscience. However it has some limitations. There is evidence that the brain uses multiple dimensions for information processing, in addition to activation and space. Another dimension, time, may be equally important, or even more important than space in terms of the neurocomputational mecha-

nisms (Cohen, 2011), namely for coding, processing and information transmission. There are several observations that emphasize the rich landscape of temporal dynamics:

- First, the information can be transmitted in the precise timing of activities within and across physically separated areas of the brain. In this case, information can be lost by averaging over larger periods of time.

- Second, time provides a rich source of complex multi-dimensional data where information can be represented and processed. This large amount of information embedded in the temporal patterns of neuronal activity comes in part because the electrophysiological activity in the brain is strongly oscillatory. As introduced in Section 1.3, neuronal oscillations represent periodic modulation of the excitability of populations of neurons (Tiesinga et al., 2008; Wang, 2010a). They occur in multiple temporal and spatial scales in the form of ultra-slow oscillations with a periodicity of tens of seconds in the cortex during deep sleep (Steriade, 2006) or ultra-fast oscillations with a periodicity of a few milliseconds in patches of somatosensory cortex (Curio, 2000). In fact different frequency bands are functionally related to a diversity of cognitive processes (Traub et al., 2004; Varela et al., 2001). Activities at a certain frequency can be performed independently or in parallel with activities at other frequencies, therefore it is natural to think of the wide band of frequencies in which information can be processed. In this context, several functionally distinct neural networks can spatially coexist and be dissociated according to their frequency band or spatiotemporal patterns (Cohen, 2011), thus constituting a mechanism supporting flexible signal routing (*multiplexing* hypothesis, see Akam and Kullmann, 2010). At the same time, space can increase the potential for information processing: interactions can occur through physically separated networks on different frequency bands, and between power and phase.

- Third, the timeframes of neuronal processes are linked to those of the cognitive and behavioral processes. Simply, a fast neural process implies a rapid cognitive process. On the contrary, the spatial organization of neuronal processes is arbitrarily linked to cognitive processes. There are no implications for the corresponding (location of) behavior if a neural process takes place in one region or another, except if the physical location constrains the temporal dynamics (Cohen, 2011). Therefore time can be highly informative about cognitive behaviorally relevant mechanisms.

By way of example, in the auditory world, time is a key variable in the processing of information, spanning from microseconds up to tens of seconds. In contrast with the visual system, where the retina is like the screen of the exterior world, spatial information is not

embedded in the information captured by the ears. Thus the organization in the auditory system is based on frequencies and not space, and spatial information has to be computed in the brain by comparing time and intensity differences of the sound that reaches the ears, somehow representing the spatial information through a computational process (Klug and Albrecht, 2015). In fact a sound reaches the ears with different time or intensity depending on the location of its source: it will arrive earlier and louder to the ear closer to the source than the other. There are two different neural pathways devoted to the computation of time and intensity in the auditory system, but both require high-precision timing of the order of tens of microseconds (Grothe, 2003). This is why the lower auditory system is highly specialized in detecting and processing this information at temporal scales that are smaller than the width of a single action potential (Taschenberger et al., 2002).

### Cross-frequency coupling

Cross-frequency coupling is a significant mechanism that could underlie time-embedded information. This phenomenon refers to a relationship between activities occurring in different frequency bands for instance when the power of gamma cycles ($30-80$ Hz) varies according to the phase of theta ($4-8$ Hz). Cross-frequency coupling could be used to encode the information if the lower frequency oscillations coordinate the activity of sub-populations of neurons that oscillate at higher frequencies. This phenomenon is seen as a neural mechanism for information processing (Jensen and Colgin, 2007), where spatially overlapping but functionally heterogeneous neural networks can be activated and coordinated in a rapid timescale. Standard localization- and hemodynamic-based methods such as fMRI with a low temporal resolution cannot monitor these brain dynamics, but this information can be extracted non-invasively in humans using EEG and MEG. This is an example of the importance to use methods with high temporal resolution to highlight brain dynamics that go beyond what one can study human through fMRI or time-domain averaged ERP.

Furthermore, in addition to frequency-based mechanisms such as cross-frequency coupling occurring in the same spatial region, information may also be contained in the temporal relationship of brain activity over the space. Indeed inter-regional oscillatory synchronization (see Section 1.4.2) may underlie information transfer and co-processing (Womelsdorf et al., 2007). For instance, given that changes in phase synchronization could emerge without any changes in power, information can be embedded in the temporal relationship between areas. Although some measurements of phase synchronization are non-directional (namely do not reveal the direction in which the oscillations are traveling), the temporal precision of EEGs can lead to an estimate of the activity flow, and therefore to a relevant information that is not localized to either region alone (Granger, 1969).

Temporal information is thus embedded in the rich framework of the neural electrophysiological dynamics, and much of this information may be lost if only an analysis of spatial dimensions is performed. Examining the temporal dynamics of brain electrical activity, along with the spatial-based approaches, represents an important next step in the development of theoretical and empirical human neuroscience.

**Novel methods to bridge scales**

The switch from the modular (reductionist) approach to the large-scale network paradigm is nowadays being supported as well by the advent of new advanced methodologies. Current methodologies overcome several limitations in the study of different spatial scales simultaneously such as the identification of which areas are interacting and communicating without an exhaustive mapping or the computationally and statistically high-demanding analysis of recordings from many channels. New approaches aim at mapping behaviors and cognitive variables into physiology by sampling and monitoring the brain activity at each relevant scale (see Figure 1.10). Lewis et al. (2015a), for instance, are carrying on an ambitious project with the help of different recordings methods: with electrocorticography they map specific regions involved in a cognitive task (Figure 1.10A), with dense surface recordings with higher resolution they further map the areas involved in the task thus localizing specific neuronal populations (Figure 1.10B), then with the implantation of laminar arrays in specific points in the cortical area they record the activity of interacting neuronal groups at a certain distance (Figure 1.10C) and finally with penetrating arrays they operate dense mapping of local populations to monitor targeted local circuits (Figure 1.10D). These approaches, along with similar new technologies, will enable to relate single cells with local populations in terms of their activity, areal dynamics and inter-areal communication across brain-wide networks.

From the computational point of view different mathematical models have been developed to account for the activity at each scale, from single neurons to the mesoscopic level of neuronal ensembles. Recently, large-scale models of the brain have received special attention. So far, global brain activity has been modeled by dividing the brain into discrete volume elements, or voxels, and coupling them according to statistical correlations and structural information (Deco et al., 2013; Pons et al., 2010; Sotero et al., 2007). Both the Human Brain Project and the Brain Activity Map project propose integrated views to bridge the gap between the behavior of single neurons and the functions of the full brain (Alivisatos et al., 2012), but this quest is still in its infancy. In Chapter 5, we will propose an alternative approach to explore scale interaction, by considering a system formed by two neural masses (mesoscopic description of neuronal activity) that are coupled exclusively via an intermediate population described by a spiking NN model (microscopic description). In that way, we use synchroniza-

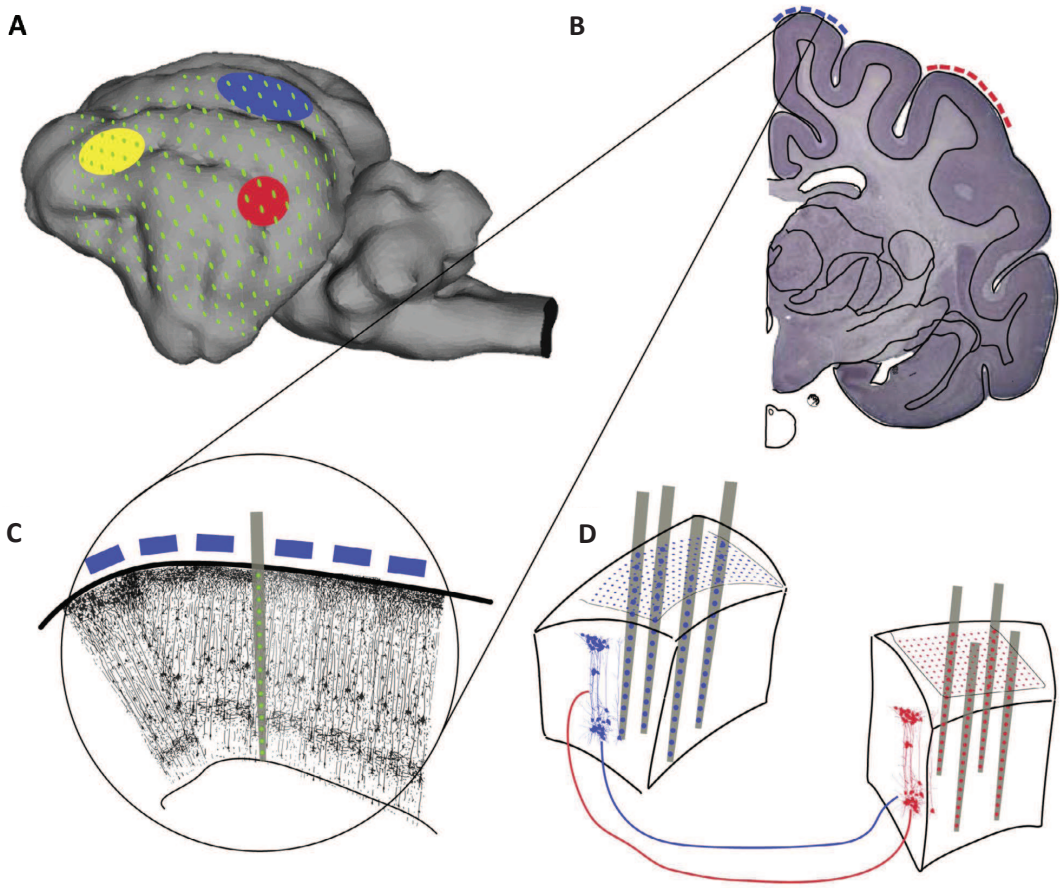


Fig. 1.10 **Multi-scale approach for recording of brain activity.** (A) Using electrocorticography (ECoG) allows mapping of distributed areas involved in a cognitive task. Identified regions can then be targeted for higher-resolution recording. Green dots represent sites on an ECoG array and colored areas represent regions participating in a functional network, identified by ECoG. (B) Refined high resolution ECoG mapping of specific areas of interests engaged in the cognitive task. Dense mapping of these areas allow to target neuronal groups that cooperate across long distances or share selectivity. (C) Targeted ensemble recording across laminar circuits from identified coupled populations. Laminar arrays can be inserted at specific points in the cortical area that correspond to interacting populations (Lewis et al., 2015a). (D) Dense mapping of interacting populations through laminar arrays to analyze the propagation of information through local and distributed circuits. From Lewis et al. (2015a).

tion as a tool to probe the interaction between the two scales of description and determine which are the microscopic features that modulate the mesocopic activity.

## 1.5 Propagation of neuronal oscillations

The introduction of voltage-sensitive dyes (VSD) [1] (Shoham et al., 1999), of multielectrode array (MEA) [2] (Maynard et al., 1997) and other optical imaging techniques offers the opportunity to explore spatiotemporal structure of activity in mesoscopic regions in the neocortex and other brain areas. Many results provided evidence of the tendency of neuronal populations to self-organize in spatiotemporal patterns that resemble traveling waves. In fact stimulus-evoked propagating waves have been observed in several sensory cortices of anesthetized animals (Ahmed et al., 2008; Gao et al., 2012; Grinvald et al., 1994; Han et al., 2008; Huang et al., 2004; Stroh et al., 2013). In awake conditions, MEA recordings have reported the existence of traveling high-frequency gamma- and beta-band oscillations propagating across the primary visual cortex (Gabriel and Eckhorn, 2003), the motor cortex (Rubino et al., 2006) of the monkey under both spontaneous and evoked conditions, and fast wave propagation in the auditory cortex of the awake cat (Witte et al., 2007). Moreover, VSD imaging studies have revealed propagating waves spanning large parts of the cerebral cortex in freely moving mice (Ferezou et al., 2006).

The existence of traveling waves in the brain has been highly debated in recent years. However the advent of technologies with better signal-to-noise ratio and new methodological approaches (Muller et al., 2014) allows to carry out data analysis on the single-trial level, because trial-to-trial variability may in fact preclude specific measurements due to average effects. These innovative tests confirm that traveling waves occur systematically in the awake, behaving animals and are consistent across trials and thus the wave propagation is a general phenomena in the large-scale dynamics of the neocortex and other brain areas (Lubenov and Siapas, 2009; Muller and Destexhe, 2012; Muller et al., 2014).

In what follows we briefly introduce some mechanisms behind the propagation of neuronal oscillations and discuss the potential benefits for the brain to develop these coordinated patterns of activity. Then we briefly review the main experimental results focusing on cerebellar

[1] Voltage-sensitive dyes (VSD) are organic molecules which change their optical properties in response to a change in membrane potential. They have been widely used (i) in combination with fast cameras to monitor membrane potential in processes of individual neurons in localized brain regions and (ii) to follow population changes in membrane potential over large regions of the brain and the heart. Differently from other optical techniques, voltage-sensitive dyes are optical measurements that relate directly to electrical activity, because dyes change their absorption or emission spectra in a manner depending upon membrane potential (Frostig et al., 2009).

[2] Microelectrode arrays (MEA) are devices with fixed geometry arrangements of microelectrodes for the purpose of multisite, parallel electrophysiological recording. They essentially serve as neural interfaces that connect neurons to electronic circuitry. There are two general classes of MEAs: implantable MEAs, used *in vivo*, and non-implantable MEAs, used *in vitro* (Spira and Hai, 2013).

and hippocampal waves, which provide important insights for our work that will be presented in Chapter 6.

### 1.5.1 Mechanisms of traveling waves and computational role

Many theoretical studies on networks of neuronal oscillators demonstrated the existence of traveling oscillatory waves in networks with spatially restricted connectivity (Bressloff and Coombes, 1998; Bressloff, 2000, 2001; Ermentrout and Kleinfeld, 2001; Osan and Ermentrout, 2002). There are different mechanisms underlying the generation of traveling electrical waves (Ermentrout and Kleinfeld, 2001). The simplest one requires a single neuronal oscillator, e.g. a pacemaker. This oscillator excites progressively neighboring cortical regions with increasing synaptic delays (see Figure 1.11A). In the case of hippocampal traveling waves, this role could be played by the medial septum, which is considered the main pacemaker of theta oscillations. Another case is waves generated by a single neuronal oscillator whose output propagates unidirectionally in chain-like configuration or in consecutive connected groups of neurons (see Figure 1.11B). The third mechanism is due to a gradient of natural frequencies in a network of weakly coupled oscillators. This mechanism does not rely on a single pacemaker but instead on the stabilization of phase differences between all the rhythms intrinsically originated in each single neuronal oscillator (see Figure 1.11C). By way of example, neurons in the entorhinal cortex have intrinsically oscillating membranes with natural frequencies in the theta range, which progressively decrease in the dorsoventral direction (Giocomo et al., 2007), providing opportunities for intrinsic traveling waves. In the same way, neurons in *CA*1 exhibit resonances at theta frequencies (Leung and Yu, 1998), which decreases along the septo-temporal axis as well.

With the development of theoretical models and the design of precise and systematic experiments revealing traveling wave patterns, neuroscientists started to investigate the possible role of neuronal waves and their implications in information processing. In Section 1.1.3 we discussed about the functional significance of synchronous neuronal oscillations, because oscillating membrane potentials could offer windows of opportunity for neurons to spike, thus modulating the sensitivity of neurons to incoming dynamical inputs. A potential benefit is that the spiking output of a neuron is tuned according to the peak of depolarized oscillation phase. In contrast, waves originated from propagation in networks with local short-range connections might subserve different processes. First, the emergence of traveling waves allows that only a part of sensory field is made unresponsive during each period of the oscillation cycle, in contrast with the periodic windows of opportunity for spiking (namely when inhibition is low) in the presence of synchronous oscillations. The second potential role derives from the finding that neurons are most sensitive to changes in their input that occur one-half period before

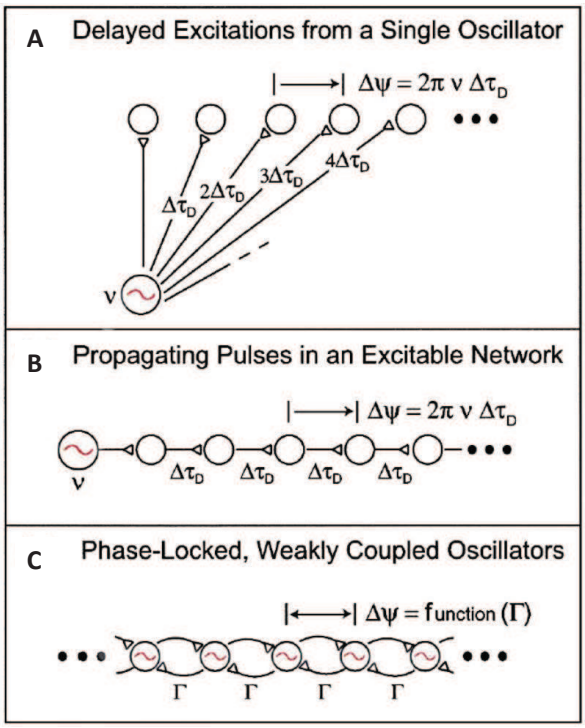


Fig. 1.11 **Illustrative plots of different one-dimensional configurations supporting traveling waves.** Open circles stand for excitable but not necessarily oscillatory neurons or neuronal tissue, while circles with $\sim$ represent local oscillators with frequency $\nu$. (A) A single oscillator drives neighboring neurons or neuronal groups through increasing time delays of $\tau_D$, thus generating a fictitious wave pattern. (B) Wave patterns take place from the transmission of periodic signals along a chain of cortical neurons. Here the delay between neurons is f $\tau_D$. (C) Wave propagation relies on stabilization of phase differences among neuronal oscillators in a network with nearest neighbor coupling. From Ermentrout and Kleinfeld (2001).

firing an action potential. Indeed in this perspective traveling waves might allow sensory areas to work as *bar code scanner*, where only a fraction of the total sensory input is scanned at each instance (Ermentrout and Kleinfeld, 2001). Furthermore, based on the idea that cortical regions are mapped according to their respective sensory field, traveling waves may serve to label perceived features in the stimulus stream with a unique phase. It is still not clear if the switch from traveling waves to synchronous purely oscillations due to the sensory stimulation is computationally relevant, however some findings reveal that it might serve to gate synaptic plasticity (Feldman, 2000; Markram et al., 1997). In the last decades, next to theoretical studies, the introduction and development of multichannel recording techniques and imaging techniques make the spatiotemporal structure of traveling waves in cortical regions a prime subject of study.

### 1.5.2 Propagating waves: experimental findings

#### *In vitro* experiments

Many *in vitro* studies have reported propagating activity by the application of electrical stimulation to cortical areas or to thalamocortical afferents (Buonomano, 2003; Pinto et al., 2005) or stimulated by local application of glutamate (Sanchez-Vives and McCormick, 2000). These stimuli, although different from the ones induced by the sensory stimulation delivered *in vivo*, induce strong EPSPs on these neuronal cortical networks which are in a quiescent state, and synchronously drive many neurons close to the firing threshold, thus eliciting propagation of activity through the network (Muller and Destexhe, 2012). Interestingly, recent findings suggest a critical role for the infragranular layers in contributing to the horizontal spread of this activity across the cortex (Wester and Contreras, 2012). Furthermore VSD and MEA studies *in vitro* provided first approximations of the speed of horizontal propagation of neuronal populations across the cortex (Fukuda et al., 1998), confirming other estimations made by studies *in vivo* (Jancke et al., 2004; Nauhaus et al., 2009), although some differences have been identified in anesthetized rats and slice preparations (see Muller and Destexhe (2012) for a review).

The wave-like propagation of neuronal activity has been observed in *in vitro* studies in slices of the visual thalamus of ferrets (Kim et al., 1995). Spontaneous spindle waves (see Section 1.2) have been recorded in slices of the LGN. These spindle oscillations (i) initiate at one side of the slice and propagate in the ventro-dorsal axis (von Krosigk et al., 1993b), (ii) are generated in control conditions (while under specific pharmacological conditions slow waves have been observed), and (iii) present different speeds of propagation (see Figure 1.12). Interestingly, while spatiotemporal wave-like organization in the cortex is mainly due to the excitatory connections between pyramidal neurons, in thalamic slices these patterns arise from the mutual interaction of excitatory TC and inhibitory RE neurons (Muller and Destexhe, 2012).

#### *In vivo* experiments

Multichannel recordings under anesthesia have reported many examples of large, low-frequency spreading depolarization in the visual cortex of the rat (Han et al., 2008; Xu et al., 2007), cat (Nauhaus et al., 2012) and macaque (Grinvald et al., 1994) that spreads across the cortical areas. The spreading depolarization takes place where visual stimuli activate peaks of activity with a center of mass that remains stationary during the response and the level of activation decreases with increasing distances (Muller and Destexhe, 2012). However, the wave propagation of activity, differently from the spreading depolarization, refers to oscillations propagating through the network. Large, low-frequency propagating waves of activity spreading through the entire cortical area under anesthesia have been observed in several studies, and the results

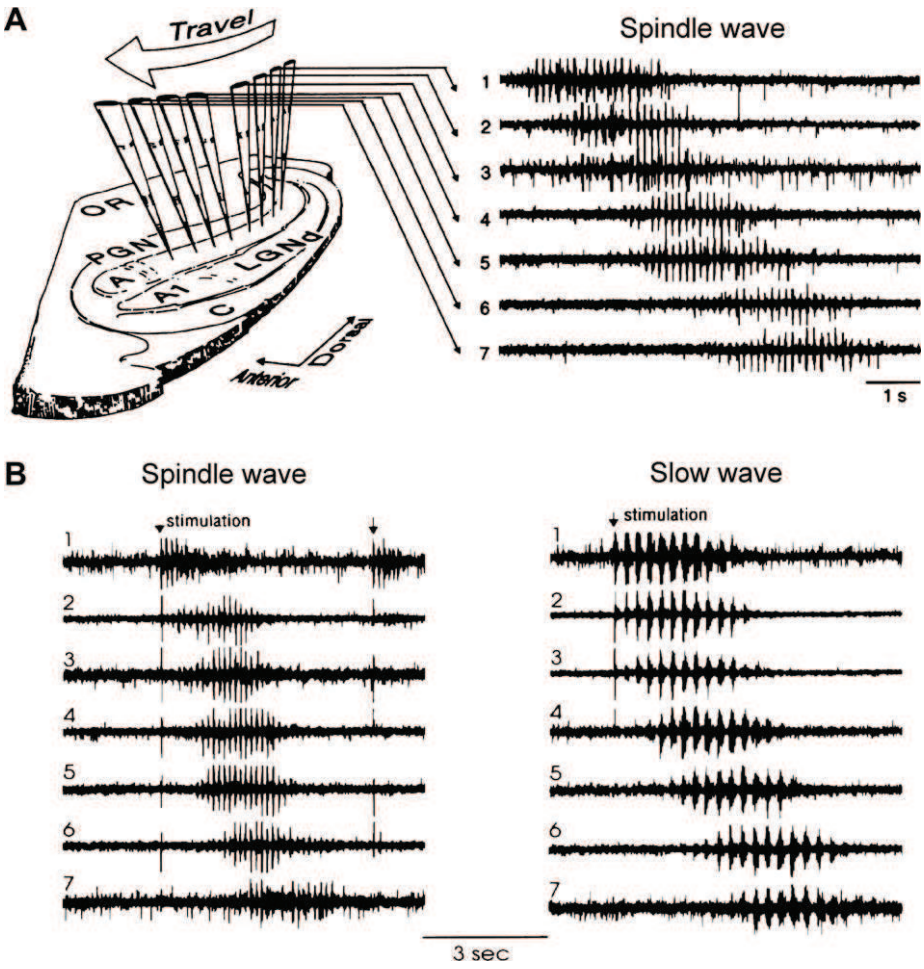


Fig. 1.12 **Propagating waves in thalamic slices.** (A) Illustrative plot of propagation of spindle waves in multisite extracellular recordings in ferret thalamic slices (left) and spontaneous spindle waves along the ventral-dorsal axis of the slice (right). (B) Refined high resolution ECoG mapping of specific areas of interests engaged in the cognitive task. Dense mapping of these areas allow to target neuronal groups that cooperate across long distances or share selectivity. Adapted from Kim et al. (1995).

strongly depend on the specific anesthetic used during the analysis (Ferezou et al., 2006; Han et al., 2008; Reimer et al., 2010).

VSD recordings in awake monkeys have suggested that spreading depolarization is an emerging feature in the cortical response of awake animals, confirming the results obtained in anesthetized animals (Ayzenshtat et al., 2010; Slovin et al., 2002). However, the results of these first studies in the awake monkey were based on trial-averaged data and, given the well-known sensitivity of propagating waves *in vivo* to trial averaging, it is possible that waves on the single-trial level were attenuated by the averaging procedure (Muller et al., 2014; Xu et al.,

2007). Thanks to the advent of new techniques in VSDI denoising (with an improved signal-to-noise ratio), Muller and co-authors applied a new method to single-trial voltage-sensitive dye imaging data in order to clearly detect spontaneous propagating waves and stimulus-evoked propagating events. Their results showed that in response to a visual stimulus, propagating waves systematically emerge in several visual areas (Muller et al., 2014). At the same time, propagating waves of activity have been observed in MEA recordings of the awake cat auditory cortex (Witte et al., 2007), and in the spontaneous background activity of the awake state in MEA recordings of the monkey primary visual cortex (Nauhaus et al., 2012). In contrast to the low-frequency propagating waves observed during anesthesia (Sanchez-Vives and McCormick, 2000), traveling high-frequency oscillations have been detected in MEA recordings of the primary visual cortex (Gabriel and Eckhorn, 2003) and in motor cortex of the awake monkey (Rubino et al., 2006) and human (Takahashi et al., 2011). In what follows we present two significant examples of wave patterns whose peculiar properties will be explored with spiking models in Chapter 6.

### 1.5.3 Cerebellar waves in early development

In several CNS regions, including the visual system, the hippocampus and the spinal cord, spontaneous traveling waves of activity in early development are critical for establishing the accurate synaptic connectivity of mature circuits (Feller, 1999; Katz and Shatz, 1996). Watt et al. (2009) have first reported the existence of wave-like activity in the developing cerebellum using two-photon laser scanning microscopy to guide patch-clamp recordings in slices of transgenic mice. Purkinje cells, a class of GABAergic neurons in the cerebellum, provide the output of the cerebellar cortex and project to the deep nuclei of cerebellum (DCN), where they form GABergic synapses. Watt and co-authors found that the asymmetric projection structure of Purkinje-Purkinje synapses is behind the mechanism of waves propagation in the developing (not adult) cerebellum (Figure 1.13A). From these studies it emerges that Purkinje-Purkinje connections can enhance synchronization of Purkinje cells, with the phase of entrainment depending on the driving force at GABAergic synapses (Watt et al., 2009), with consequential effect on the direction of the wave propagation with respect to the direction of connectivity.

To characterize their experimental results, they built a simple model of integrate-and-fire neurons where cells were connected in a chain-like manner according to the directional asymmetry. Specifically, each neuron was connected with the neighboring 5 neurons asymmetrically (Figure 1.13B) and two reversal potential values were studied corresponding to depolarizing and hyperpolarizing synapses respectively. That model with that specific structural connectivity supported the spontaneous propagation of waves of activity: in particular depending

on the type of synapses (if excitatory or inhibitory) it changes the neuron in the chain leading all the other neurons, indeed providing two distinct propagation's direction (Figures 1.13C,D). Propagating waves have been characterized by calculating spatial wavelength and speed propagation (Figures 1.13E-G). Functionally, these cerebellar waves in the early development could contribute to the formation of functional maps and local subnetworks (Watt et al., 2009).

### 1.5.4 Hippocampal theta oscillations

Theta oscillations $4-10$ Hz are typical in hippocampal LFPs of mammals and humans (Arnolds et al., 1980; Green and Arduini, 1954; Vanderwolf, 1969; Winson, 1972), emerging during wakefulness under specific conditions and invariably present during REM sleep. From experimental studies in rats, it turns out that theta oscillations are associated with voluntary movement and active exploration (O'Keefe and Nadel, 1978). Furthermore theta oscillations clock hippocampal activity during awake behavior and REM sleep, and this is essential for the temporal coding of spatial information by place cells, according to the mechanism of theta phase precession [3] (Lubenov and Siapas, 2009).

A few years ago, it was common belief that theta oscillations are synchronized within each layer across the anatomical extent of the hippocampus (Buzsáki, 2002). According to this view, theta oscillations were a global clock, and the anatomical extent of the hippocampus was synchronized with zero delay or figuratively speaking contained in a single time zone (Lubenov and Siapas, 2009). However, exquisite experiments by Lubenov and Siapas (2009) revealed that in freely behaving rats theta hippocampal oscillations in area *CA*1 are actually traveling waves that roughly propagate along the septo-temporal axis of the hippocampus, and consequently these wave patterns modulate the firing activity of *CA*1 pyramidal cells. These important results showed that theta oscillations pattern hippocampal activity not only in time but also across anatomical space (Figure 1.14). The presence of traveling waves indicates that the instantaneous output of the hippocampus is topographically organized and represents a segment, and not a point of physical space, as the mapping of time on Earth in a progression of local time zones (Lubenov and Siapas, 2009).

[3] **Theta phase precession**. Mechanism by which hippocampal neurons fire during a specific phase of the oscillation cycle (theta range), whereby the relative phase of discharge generation varies in a context-dependent way. The encoding of information about the amplitude of the stimulus into the phase values of the discharges response has been proposed in the hippocampus to explain the phenomenon of theta-phase precession (O'Keefe and Recce, 1993): pyramidal neurons also called *place fields* fire preferentially when the animal moves through the corresponding place field of firing pyramidal neurons and they phase-lock to the theta rhythm. As the animal moves and proceeds in that place field, neurons fire earlier and earlier along the theta cycle. It is a quite well explained phenomenon due to the interaction between excitatory drive on pyramidal neurons and rhythmic inhibition in the theta range imposed by inhibitory neurons to whole network (O'Keefe, 1976). The functional

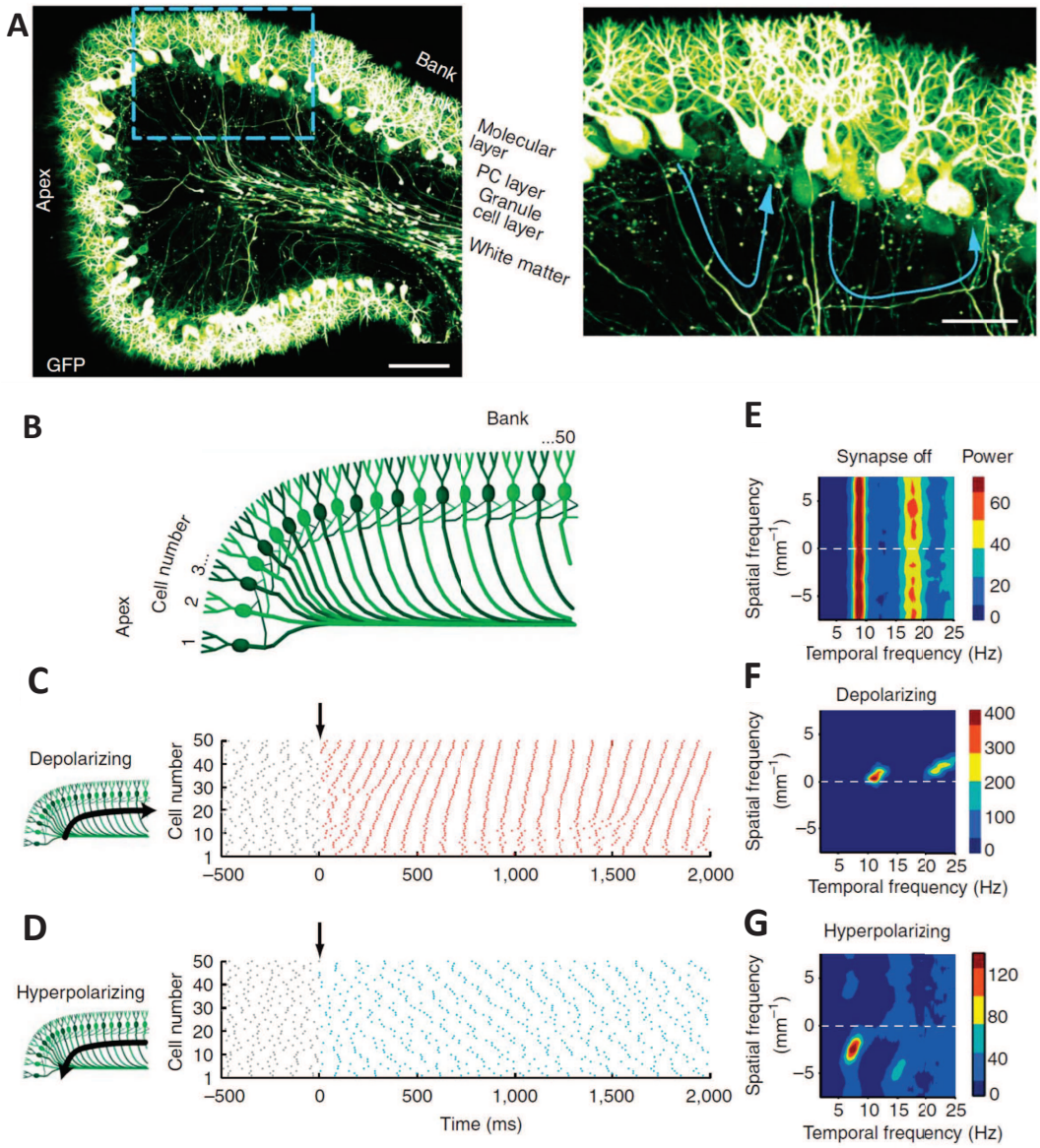


Fig. 1.13 **Propagating waves in a network of Purkinje cells.** (A) Image of the anatomical distribution of Purkinje cell axon collaterals in case of a lobule from a P9 mouse (left) and an image of the region indicated by the blue square (right) with two axon collaterals highlighted with blue arrows. (B) Illustrative plot of the Purkinje cell axon collateral network model. The connectivity is regular and asymmetric. (C) Raster plot from the network model showing action potentials of Purkinje cells (points) versus time. The presence of depolarizing synapses gives rise to waves propagating from the apex to the base of the folium (black arrow). (D) Hyperpolarizing synapses generate activity waves traveling in the opposite direction with respect to the depolarizing synapses. (E-G) Two-dimensional Fourier transformation corresponding to the angular spectrum of the raster plots when the synapse is off (E), depolarizing (F) or hyperpolarizing (G) (Watt et al., 2009). The peaks of Figures (F-G) correspond to the traveling waves features. Adapted from Watt et al. (2009).

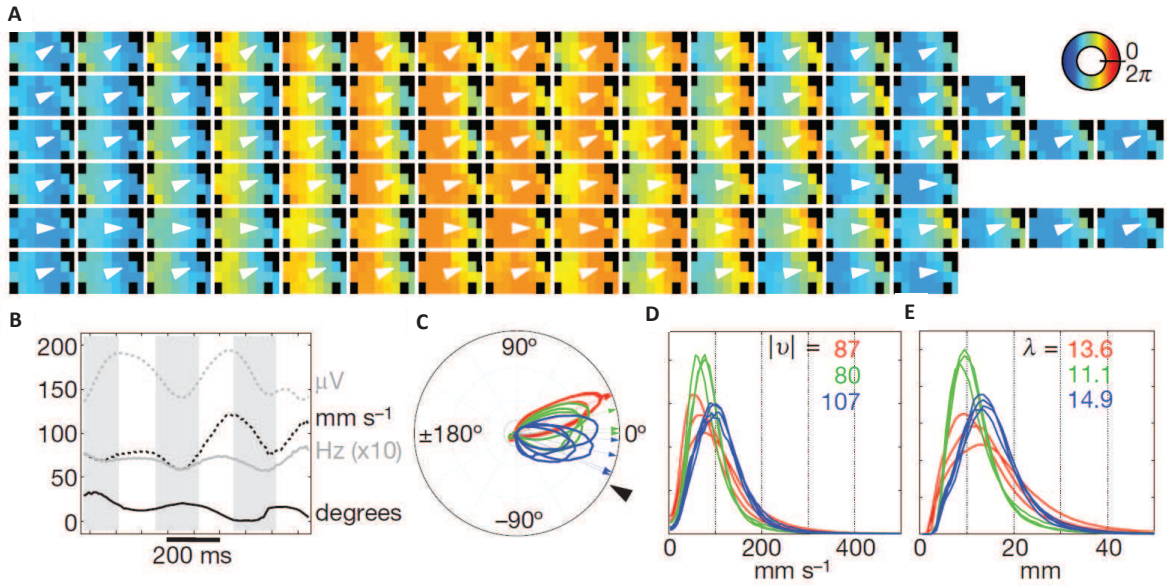


Fig. 1.14 **Theta traveling waves and waves distribution parameters.** (A) Consecutive snapshots of theta oscillations across the recording grid places in stratum oriens of *CA*1. Colors correspond to the phase of the theta wave at each grid location according with the circular color map on the right, and arrows stand for the direction of the propagation; (B) instantaneous properties of the waves shown in A: amplitude (dashed gray line), frequency (solid gray line), speed (dashed black line) and direction (solid black line) of wave propagation; (C) wave propagation direction; (D) wave propagation speed; (E) spatial wavelength. Different colors correspond to different animals and the number to the median for each animal. From Lubenov and Siapas (2009).

The understanding of the mechanisms of wave propagation in the hippocampus and other brain regions could elucidate the global properties of information representation and the direction and nature of the flow and process of information. It is also interesting to determine whether anatomical asymmetries in axonal projections found in brain regions can also support waves and the extent to which waves documented experimentally in other brain areas are linked to possible asymmetries in axonal projections (as cerebellar waves). In Chapter 6, starting from experimental findings of Lubenov and Siapas (2009) and in collaboration with them, we will first propose a biophysically plausible spiking model to reproduce traveling waves, and secondly investigate the mechanisms generating this wave-like behavior and study the topological determinants by means of a continnum approximation model that is analytically tractable.

importance of theta phase precession is given by the fact that firing temporal sequence of pyramidal neurons gives insights on the position and trajectory of the animal and information recorded about the past.

The next Chapter provides an introductory overview of computational models at the microscale, e.g. modified integrate-and-fire and conductance-based models, and at the mesoscale, e.g. neural mass models, that will be used to obtain the main important results in Part II.

# Chapter 2

# Computational Models

In order to understand the basic principles of brain function it is essential to consider the different scales involved (from single neurons to behavior) via the study and exploration of different computational models able to capture with a certain degree of approximation a variety of spatiotemporal phenomena. At the microscale, the *Hodgkin–Huxley* (HH) model (Hodgkin and Huxley, 1952) and related conductance-based models were developed to describe in a quite detailed electrophysiological framework the spiking properties (action potentials) of an individual neuron embedded in a larger network. Simpler models like *leaky integrate-and-fire* (LIF) (Lapicque, 1907; Stein, 1967; Tuckwell, 2005) and the *Izhikevich* (Izhikevich, 2004) models have been widely exploited because they are able to reproduce some spiking properties of neurons under certain regimes, while being analytically tractable and computationally efficient in comparison with conductance-based models.

Another set of models, named *neural mass* (NM) models (Coombes, 2010; David and Friston, 2003; Grimbert and Faugeras, 2006b; Jansen and Rit, 1995), avoid the single-neuron perspective and consider instead the averaged behavior of the neuronal population. This mesoscopic description is more phenomenological than the single-neuron models, in the sense that it represents directly the collective behavior of the network, without singling out individual cells. NM models provide a direct link from neural activity to EEG and fMRI data (Bojak et al., 2010) by unifying data from different imaging techniques. In fact based on the NM model, several studies have been carried out at the scale of a whole cortical column by studying the interaction of several NMs using bifurcation theory (Coombes, 2010), and the scale of the whole brain using a realistic distribution of neural masses and their short- and long-range connectivity (Pons et al., 2010; Sotero et al., 2007).

These mesoscopic models revealed to be successful in generating alpha oscillations consistent with those found in the human EEG spectrum. In this direction a successful study of Liley and colleagues proposed a mesoscopic model where cortical activity is locally de-

scribed by the mean membrane potentials of populations of excitatory and inhibitory neurons interacting with each other (Liley et al., 2002). Modeling approaches based on NMs have been extended (Moran et al., 2013; Rennie et al., 2000; Wright and Liley, 1996) as well to explore several neurobiological processes (Jedynak et al., 2015; Malagarriga et al., 2015) such as anesthesia (Steyn-Ross et al., 1999) and epilepsy (Breakspear et al., 2006) among others.

This Chapter briefly introduces different models that have been explored in this Thesis, and is structured as follows. In the first Section, microscopic models are introduced. In particular LIF models are briefly described and an extension of them, the *adaptive exponential integrate-and-fire* (aEIF) model will be introduced. That model will be used in Chapter 3, where we will address the dynamical properties of collective temporal phenomena in the thalamus. The more electrophysiologically detailed HH model will be explained next, since it is the mathematical framework where synchronization and communication between delayed-coupled populations has been studied (Chapter 4). A network with HH neurons with structural connectivity inspired by hippocampal experiments will be used to study spatio-temporal wave-like patterns in populations of neurons (Chapter 6). In the last Section, a brief description of NMs will be provided, since in Chapter 5 we will study the interaction of populations described at different scales, namely at the level of single neurons (HH model) and cortical columns (NM model).

## 2.1 Microscopic models

### 2.1.1 Integrate-and-fire models (IF)

A simple model that faithfully reproduces the main neurocomputational properties of neurons is the so-called integrate-and-fire model (IF). It is often referred to as a spiking model, although it lacks any spike generation mechanism. It combines linear filtering of input currents with a strict voltage threshold: once the voltage of the neuron goes above that threshold the neuron is considered to generate a spike. The model produces all-or-none spikes, because the shape of the spikes is not simulated and all spikes have the same temporal duration and size.

The LIF model (Izhikevich, 2006; Lapicque, 1907; Stein, 1967; Tuckwell, 2005) reproduces the subthreshold behavior of a neuron having ohmic leakage current, and other voltage-gated currents that are deactivated at rest. The dynamical evolution is described by the differential equation:

$$C_m \frac{dV}{dt} = I - g_L(V - E_L), \tag{2.1}$$

where $C_m$ is the capacitive current, $V(t)$ is the voltage variable and $-g_L(V-E_L)$ represents the ohmic leakage current. In particular $g_L$ is the leak membrane conductance and $E_L$ is the Nerst equilibrium potential of the leakage current, i.e. is the value of the membrane potential where

all inward and outward currents balance each other and the net current flux is zero. When the membrane voltage $V$ reaches the threshold value $E_{thresh}$, the neuron produces an action potential, and $V$ is reset automatically to $V_r$. When the current input is excitatory ($I > 0$), it depolarizes the neuron, whilst when $I < 0$ the input is inhibitory and hyperpolarizes the membrane voltage. Further mathematical analysis and comments on this model can be found in Izhikevich (2006).

This model is very simple, computationally efficient but at the same time it has obvious limitations. Ermentrout (1996) and Latham et al. (2000) proposed an extension to a quadratic IF and Fourcaud-Trocmé et al. (2003) to an exponential IF model to replace the strict threshold with a smooth spike initiation zone. Additionally, the original IF was enriched by a second variable to take into consideration subthreshold resonances or adaptation (Izhikevich et al., 2003; Richardson et al., 2003).

An extended model that takes into consideration these different additions of original IF model was developed by Brette and Gerstner (2005) and is called adaptive exponential integrate-and-fire model (aEIF). We introduce this model because it has been used in Chapter 3 to explore spindle oscillations mechanisms in the lateral geniculate nucleus (LGN).

### 2.1.2 Adaptive exponential integrate-and-fire models (aEIF)

As said above, this model is an evolution of a two-variable IF model proposed by Izhikevich (2004), and it is enriched by an exponential non-linearity around the spike threshold, as in the exponential IF model of Fourcaud-Trocmé et al. (2003). The combination of these two models leads to the aEIF formulated by Brette and Gerstner (2005). A detailed analysis of the dynamics of this system can be found in Touboul and Brette (2008). In this model, the equations describing the evolution of membrane voltage of neurons are:

$$C_m \frac{dV}{dt} = -g_L(V - E_L) + g_L \Delta \exp\left(\frac{V - E_{thresh}}{\Delta}\right) - w + I \tag{2.2}$$

$$\frac{dw}{dt} = \frac{1}{\tau_w}[a(V - E_L) - w], \tag{2.3}$$

$$\text{if } V \geq E_{thresh}, \begin{cases} V = V_r \\ w = w + b. \end{cases} \tag{2.4}$$

The Equation (2.2) describes the evolution of the membrane voltage: the capacitive current through the membrane equals the sum of the ionic currents, the adaptation current $w$ and the input current $I$. The ionic currents are the ohmic leak current defined by the resting leak con-

ductance $g_L$ and the resting voltage potential $E_L$, and the exponential term which reproduces the $Na^+-$ current that is responsible for the generation of spikes. With this term we assume that the activation of $Na^+-$channels is instantaneous (thus neglecting their activation), with $\Delta$ denoting the steepness of the exponential approach to threshold, and $E_{thresh}$ representing the threshold potential. The membrane time constant is $\tau_m = C_m/g_L$. The Equation (2.3) describes the dynamics of the adaptation variable $w$, with a time constant $\tau_w$. The parameter $a$ quantifies the conductance that mediates subthreshold adaptation. When $V$ is pushed over the threshold, the exponential term provides a positive feedback and a spike is emitted. The voltage is then instantaneously reset to $V_r$, and the adaptation variable $w$ is increased a value $b$, which accounts for spike-triggering adaptation and regulates the strength of adaptation itself (Equation (2.4)). After the spike, the neuron cannot spike again during a refractory period $\tau_{ref}$ (imposed manually in the model).

When the input current $I$ applied to the neuron at rest reaches a critical value, the resting state is destabilized, leading to repetitive spiking for large regions of parameter space (Ladenbauer et al., 2012). For a complete analysis of different firing patterns achievable with the aEIF model and phase plane analysis see Naud et al. (2008). Figure 2.1 shows a variety of spiking patterns that can be achieved by tuning $a$ and $b$. The simplest firing pattern is the *tonic firing*, a regular discharge of action potentials without adaptation obtained for $a = b = 0$ (Figure 2.1A). However, many neurons present a certain level of spike-frequency adaptation (SFA), meaning that the inter-spike interval (ISI) grows during a sustained stimulus (*adaptation* firing pattern, Figure 2.1B). With the aEIF model, an increase of $a$ or $b$ leads to SFA, characterized by a gradual increase in the ISI until a steady-state spike frequency is reached. *Initial bursting* refers to events when groups of spikes are emitted at a frequency considerably greater than the steady-state frequency (Figure 2.1C). Finally, this model is able to reproduce the *rebound bursting* capabilities of thalamic neurons (*regular bursting*, Figure 2.1D), namely their ability to trigger high-frequency bursts of action potentials (300 Hz) in response to hyperpolarization. The aEIF model will be used in Chapter 3 to study dynamical properties of thalamic spindle oscillations.

### 2.1.3 Hodgkin-Huxley-type conductance-based models (HH)

A more physiologically detailed model than the IF model is the Hodgkin-Huxley model initially developed for the squid's giant axon (Hodgkin and Huxley, 1952). Hodgkin and Huxley performed a series of experiments on that axon (1000 times thicker than a typical mammalian axon) and they were able to find the time and voltage dependence of the sodium and potassium conductances. Their equations faithfully reproduced the generation of action potential. Differently from IF models, in HH conductance-based models each variable and parameter have a

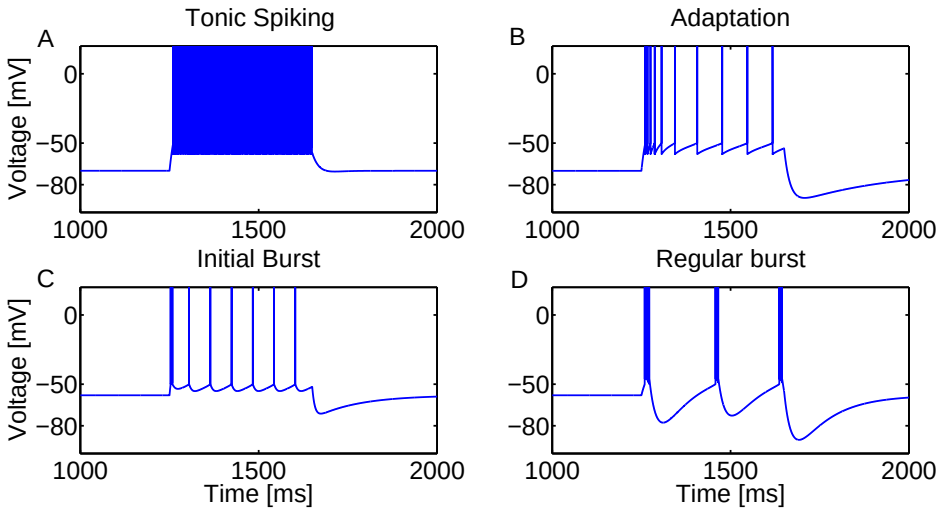


Fig. 2.1 **Firing patterns produced by an adaptive exponential integrate-and-fire model.** Firing patterns of adaptive exponential integrate-and-fire model during a step current stimulation: (A) tonic spiking, (B) adaptation, (C) initial burst, (D) regular bursting. These different regimes are achieved by tuning the parameter $a$ that regulates the dynamics of adaptation and parameter $b$, which regulates the strength of adaptation. Parameters values can be found in Naud et al. (2008).

well-defined biophysical meaning, that have been measured experimentally. The drawback is that these parameters are usually measured in different neurons, then averaged and fine-tuned and therefore measurements might be not accurate for specific case. They also require a larger computational effort. However they still provide a higher level of detail from the physiological point of view.

In the light of their model, Hodgkin and Huxley proposed an equivalent representation of the membrane potential as an electrical circuit (Figure 2.2), in which the total current passing through the membrane potential is given by the sum of ionic currents ($I_{ionic}$) and the capacitive current accounting for the storage of charges in the inner and outer surfaces of the membrane:

$$I = I_{ionic}(t) + C_m \frac{dV}{dt}. \tag{2.5}$$

Hence, voltage changes reflect the storage and release of ionic changes on the two surfaces of the neuronal membrane. Equation (2.5) is a nonlinear differential equation describing the membrane voltage. $I_{ionic}$ represents the sum of sodium and potassium conductance currents plus a leak current with a constant resistance primarily carried by chloride ions. Each of these currents, $I_{Na}, I_K$ and $I_L$ (Figure 2.2), represents the behavior of a large population of microscopic ionic currents of the same type, and is modeled following Ohm's law: $I_i = g_i(V_m - E_i)$ where $i$ is the ionic species and $E_i$ is the equilibrium potential, as in the IF model. The ionic

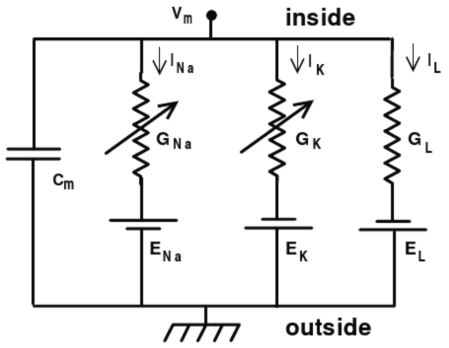


Fig. 2.2 **Electrical circuit representing the membrane potential dynamics of HH neurons.** The capacitor represents the dielectric properties of the membrane, and the other branches containing the resistors represent its conductive properties. The arrows designate variable conductances due to the opening and closing of ionic channels. The batteries represent the electrochemical forces caused by the different ionic concentrations inside and outside the cell body. From Nelson and Rinzel (1998).

conductances $g_i$ vary due to the opening and closing of the ion channels, which are regulated by gates. Each gate can be in one of two possible states, permissive or non-permissive, with a probability that depends on the membrane potential. Considering the large number of ion channels of a ionic species $i$, we can introduce a probability $p_i$ for the fraction of gates of that population that are in the permissive state, with $1-p_i$ being the fraction of gates in the non-permissive state. When all the gates of species $i$ are in the permissive state, $p_i = 1$ and the channel of $i$ is open. The transition between these two states is governed by a linear first-order differential equation:

$$\frac{dp_i}{dt} = \alpha_i(V)(1-p_i) - \beta_i(V)p_i \tag{2.6}$$

where $\alpha_i$ and $\beta_i$ are voltage-dependent rate constants for the non-permissive-to-permissive and permissive-to-non-permissive transitions, respectively. Hodgkin and Huxley considered three different kinds of gates, $m$, $n$ and $h$:

$$G_{Na} = \overline{g_{Na}} p_m^3 p_h \equiv \overline{g_{Na}} m^3 h \tag{2.7}$$

$$G_K = \overline{g_K} p_n^4 \equiv \overline{g_K} n^4 \tag{2.8}$$

in which the powers of $m$, $n$ and $h$ are obtained by adjusting the functions to the experimental data. In summary, the dynamics of the membrane voltage is given by:

$$C_m \frac{dV_m}{dt} = -\overline{g_{Na}} m^3 h(V_m - E_{Na}) - \overline{g_k} n^4 (V_m - E_k) - \overline{g_L}(V_m - E_L) + I, \tag{2.9}$$

where the constants $\overline{g_{Na}}$, $\overline{g_K}$, and $\overline{g_L}$ are the maximal conductances of the sodium, potassium, and leakage channels, respectively, and $E_{Na}$, $E_K$, and $E_L$ stand for the corresponding reversal potentials. Other variables have the same meaning as in the IF model presented in the Section 2.1.1. According to the HH formulation, the voltage-gated ion channels are described by the following set of differential equations

$$\begin{aligned} \frac{dm}{dt} &= \alpha_m(V)(1-m) - \beta_m(V)m, \\ \frac{dh}{dt} &= \alpha_h(V)(1-h) - \beta_h(V)h, \\ \frac{dn}{dt} &= \alpha_h(V)(1-n) - \beta_n(V)n, \end{aligned} \tag{2.10}$$

where the gating variables $m(t)$, $h(t)$ and $n(t)$ represent the activation and inactivation of the sodium channels, and the activation of the potassium channels, respectively. The voltage-dependent transition rates are:

$$\begin{aligned} \alpha_m(V) &= \frac{0.1(V+40)}{1-\exp(-(V+40)/10)}, \\ \beta_m(V) &= 4\exp(-(V+65)/18), \\ \alpha_h(V) &= 0.07\exp(-(V+65)/20), \\ \beta_h(V) &= [1+\exp(-(V+35)/10)]^{-1}, \\ \alpha_n(V) &= \frac{(V+55)/10}{1-\exp(-0.1(V+55))}, \\ \beta_n(V) &= 0.125\exp(-(V+65)/80). \end{aligned} \tag{2.11}$$

These equations have to be solved numerically, due to the nonlinear relationship between the conductances and the voltage. The time course of the generation of an action potential is represented in the illustrative plot of Figure 2.3. Others models use this formalism to describe a larger variety of ionic conductances, and are all referred to as conductance-based models. The HH model will be used in Chapter 4 to study the oscillatory activity of neuronal populations.

## 2.2 Modeling synapses

The equations representing the membrane potentials of two neurons can be coupled in a way that mimics synaptic communication between them. Synapses are highly specialized structures that enable neurons to exchange signals with other neurons, or to send signals to non-neural cells such as muscle fibres. Presynaptic signals are emitted via release of neurotransmit-

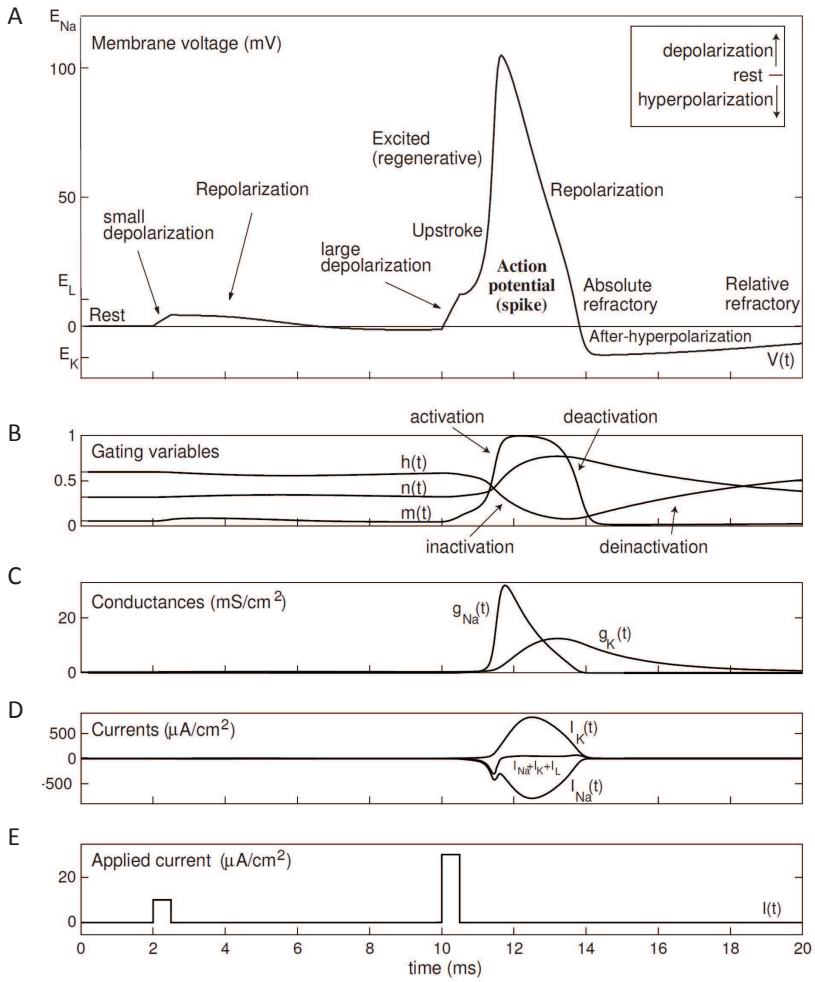


Fig. 2.3 **Typical time course of an action potential in the HH model**. Illustrative plots of time courses of the (A) membrane voltage $V$, (B) gating variables $h(t), n(t), m(t)$, (C) conductances $g_{Na}(t), g_K(t)$, (D) related currents $I_{Na}(t), I_K(t)$ and resulting $I_L(t)$ and (E) the applied current $I(t)$. Strong depolarizing inputs (panel E) increase activation variables $m$ and $n$ and decreases inactivation variable $h$ (panel B). Since $\tau_m(V)$ is relatively small (not shown), the variable $m$ is relatively fast (panel B). Consequentially fast activation of $Na^+$ conductance (panel C) drives $V$ toward $E_{Na}$ (panel A) with favored depolarization and activation of $g_{Na}$. This loop leads to the upstroke of $V$ (panel A). While $V$ gets closer to $E_{Na}$, $h \Rightarrow 0$ causes inactivation of $Na^+$ current and $n \Rightarrow 1$ causes slow activation of outward $K^+$ current (panel D), thus V moves toward $V_r$. After the action potential, the recovery of variables $n$ and $h$ is slow (panel B), because their voltage-sensitive time constants are relatively large. In particular, outward $K^+$ current is still activated (because of large $n$) after the action potential (panel D), therefore $V$ moves toward $E_K$, below the resting potential (*afterhyperpolarization*). Since the $Na^+$ current is still inactivated due to $h$ being small (panels B and D), the HH neuron cannot spike during a temporal window, named *absolute refractory period* ($\tau_{ref}$); as $I_{Na}$ is deinactivated, the HH system is able to generate a new action potential if a strong current is applied (*relative refractory period*). Adapted from Izhikevich (2006).

ters from the presynaptic neuron, which binds to receptors at the postsynaptic neuron. The type of transmitter released by a neuron determines the action on the postsynaptic neuron. This can be either excitatory (e.g. glutamate, acetylcholine) or inhibitory (e.g. GABA, glycine). Therefore a synaptic input to a dendrite can be excitatory or inhibitory, meaning that the triggered electrical signal is a transient increase (excitatory postsynaptic potential, EPSP) or decrease (inhibitory postsynaptic potential, IPSP) of the membrane potential of the postsynaptic dendrite. All the synapses made by a neuron onto others are of the same type, either excitatory or inhibitory, so it is straightforward to divide neurons into those that are excitatory and those that are inhibitory. The current generated by a receptor channel can be described using Ohm's law in a conductance-based formalism:

$$I_{syn}(t) = g_{syn}(t)(V(t) - E_{syn}), \tag{2.12}$$

where $V$ is the membrane potential, $g_{syn}$ is the synaptic conductance and $E_{syn}$ is the reversal potential of the synapse, in agreement with the definitions above. If $E_{syn}$ is negative, the synapse is depolarizing, hence excitatory ($E_{syn} = 0$ mV for glutamate receptors). If positive, it is hyperpolarizing, hence inhibitory. For positive values of $E_{syn}$ the synapse is depolarizing or excitatory ($E_{syn} = -70$ mV for GABA receptors).

Deterministic models of synaptic dynamics give a description of the averaged behavior of the system. For instance, the basic model for a receptor has a closed and an open state and the average state can be described by a rate equation:

$$\frac{d\sigma}{dt} = \alpha T(t)(1-\sigma) - \beta\sigma, \tag{2.13}$$

where $\sigma(t)$ is the number of open receptors relative to the total number of receptors (bounded between $[0,1]$), $T(t)$ is the time-varying neurotransmitter concentration, $\alpha$ is the rate of opening and $\beta$ the rate of closing. The synaptic conductance can be expressed as $g_{syn}(t) = g_{max}\sigma(t)$, where $g_{max}$ is the peak conductance. If $T(t)$ is considered to be a Dirac delta function $\delta(t-t_j)$ occurring at every presynaptic spike time $t_j$, a solution for $\sigma(t)$ is obtained (Destexhe and Rudolph, 2004):

$$\sigma(t) = \alpha \sum_j \left|1 - \sigma(t_j)\right| \exp(-\beta(t-t_j)), \tag{2.14}$$

where the rise of $\sigma(t)$ is instantaneous and its amplitude depends on the concentration of closing receptors at that time, $1-\sigma(t_j)$ (Figure 2.4A). This solution implements a saturation, because the rise of $\sigma$ at $t_j$ due to the delta-pulse release of neurotransmitters depends on the state of $\sigma$ at that time, then decaying at $t > t_j$.

A more realistic option is to consider that $T$ occurs as a pulse (Destexhe et al., 1994b), such that $|T| = T_{max}$ for $t_0 < t < t_1$. Solving Equations (2.13) we obtain:

$$\sigma(t - t_0) = \sigma_{\text{inf}} + (\sigma(t_0) - \sigma_{\text{inf}}) \exp(-\beta(t - t_j)) \tag{2.15}$$

where

$$\sigma_{\text{inf}} = \frac{\alpha T_{max}}{\alpha T_{max} + \beta} \tag{2.16}$$

and

$$\tau_{sigma} = \frac{1}{\alpha T_{max} + \beta} \tag{2.17}$$

for a general initial condition $\sigma(t_0)$. After the pulse $t > t_1$, when $|T| = 0$:

$$\sigma(t - t_0) = \sigma(t_1) \exp(-\beta(t - t_1)) \text{ for } t > t_1. \tag{2.18}$$

A simple model for postsynaptic conductance changes is the alpha function (Rall, 1967):

$$\sigma(t) = \sum_j \frac{t - t_j}{t_{peak}} \exp\left(-\frac{t - t_j - t_{peak}}{t_{peak}}\right) \tag{2.19}$$

which reaches its maximum at $t - t_j = t_{peak}$. The parameter $t_{peak}$ specifies the duration of the response, and can be used to distinguish for instance between fast and slow transmission, but it is not possible to define independently the rise and decay time (Figure 2.4B). Instead we can use a sum of two exponentials, which allows for the independent definition of the rise and decay dynamics(Figure 2.4C):

$$\sigma(t) = f \sum_j \left(\exp\left(-\frac{t - t_j}{\tau_{decay}}\right) - \exp\left(-\frac{t - t_j}{\tau_{rise}}\right)\right). \tag{2.20}$$

Here $\sigma$ reaches its maximum at $t_{peak} = t_j + \frac{\tau_{decay}\tau_{rise}}{\tau_{decay} - \tau_{rise}} ln(\frac{\tau_{decay}}{\tau_{rise}})$. $f$ normalizes $\sigma$ to take values between 0 and 1:

$$f = \frac{1}{\exp\left(-\frac{t_{peak} - t_j}{\tau_{decay}}\right) - \exp\left(-\frac{t_{peak} - t_j}{\tau_{rise}}\right)}. \tag{2.21}$$

The neuron sums the excitatory and inhibitory inputs arriving from different sites of the dendritic arbor, and an action potential can be generated if the integration of all the inputs brings the membrane potential above threshold. Whether or not the summation of several postsynaptic potentials results in an action potential depends on the balance of excitation and inhibition.

Additionally the activation of a synapse is delayed a certain time after the presynaptic spike is fired, and this depends on the transmission delays of neuronal signals through axons and dendrites. Note that the conductance $g_{max}$ is not constant in reality, but varies according to the type of synaptic coupling and on the location of synapses. In fact GABAergic terminals outnumber non-GABAergic terminals at the soma, while the opposite is true at the dendrites (Benson and Cohen, 1996). Given that synapses located at the dendrites trigger an inward current that travels through the dendrite to the soma, the postsynaptic potential elicited locally at the dendrite spreads passively into the soma reducing its amplitude. Therefore single inhibitory postsynaptic potentials are stronger than single excitatory potentials, and this accounts for an essential balance between excitation and inhibition.

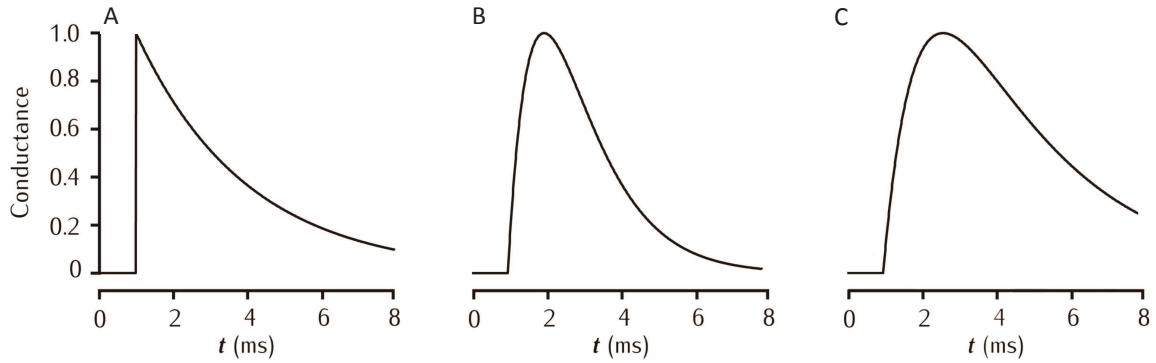


Fig. 2.4 **Waveforms for synaptic conductances.** (A) exponential decay, Equation (2.14), (B) alpha function, Equation (2.19), (C) dual exponential, Equation (2.20). From Sterratt et al. (2011).

Differently from the chemical synapses introduced above, electrical synapses or gap junctions are to date probably still under-appreciated because they have been only directly seen between inhibitory neurons in the neocortex (Gibson et al., 1999). These synapses are very fast transmission channels leading to synchronization of membrane voltages of larger populations of neurons (Velazquez and Carlen, 2000). Electrical junctions are permanently active, do not need an activation threshold and do not distinguish between pre- and postsynaptic neurons.

In Part II for each Chapter, we will describe the neuronal networks built starting from its individual components, represented by single-neuron equations introduced above, where the signal transmission between neurons is made by means of chemical synapses modeled with bi-exponential alpha functions (Equation (2.20)). We move now to phenomenological models at the mesoscopic scale.

## 2.3 Mesoscopic models

### 2.3.1 Neural mass models

Mountcastle (1957) discovered a columnar organization in the cortex by moving an electrode perpendicularly to the cortex surface, which revealed neurons with similar electrical activities grouped locally across the cortex. He first showed the existence of columns $300-500$ $\mu$m wide in the cortex which he named *cortical columns*. The most well known neural mass model aimed at modeling cortical columns is that of Jansen and Rit (1995) based on the original work of Da Silva et al. (1974). Jansen and Rit (1995) developed a biologically inspired mathematical framework to simulate spontaneous electrical activities of neuronal assemblies as observed in EEG, with a particular interest for alpha activity. But these lumped parameter models are also capable to produce evoked potentials, i.e. EEG activities observed after a sensory stimulation (Jansen et al., 1993) and more complex rhythms ranging from delta to gamma seen in EEG and MEG recordings (Coombes, 2010; David and Friston, 2003).

Jansen's model characterizes the dynamics of a cortical column by using a mean field approximation, describing the average activity of three cortical populations; excitatory and inhibitory neurons and pyramidal cells. All three populations form a feedback circuit (Figure 2.5A). The main pyramidal population excites both interneuronal populations in a feed-forward manner, and the excitatory (inhibitory) interneurons feed back in an excitatory (inhibitory) manner into the pyramidal population. The dynamical evolution of these three populations is introduced considering two different transformations. Each population transforms the total average density of action potentials reaching their afferent synapses from different origins, $\sum_m p_m(t)$, into an average postsynaptic excitatory or inhibitory membrane potential $y_i(t)$ (see Figure 2.5B). This transformation can be introduced in the model using the differential operator

$$L(y_i(t);a_{NM}) = \frac{d^2y_i(t)}{dt^2} + 2a_{NM}\frac{dy_i(t)}{dt} + a_{NM}^2 y_i(t) = Aa_{NM}\left[\sum_m p_m(t)\right], \tag{2.22}$$

and correspondingly $L(y_i(t);b)$ for the inhibitory integration of the average density of action potentials, with $b_{NM}$ and $B$ substituting $a_{NM}$ and $A$ above. $A$ and $B$ are related with the maximum heights of the excitatory and inhibitory postsynaptic potentials (EPSP and IPSP, respectively), whereas $a_{NM}$ and $b_{NM}$ represent the inverse of the membrane time constants and the dendritic delays (see Figure 2.5B). Explicitly, the equivalent impulse responses resulting from

the second order differential linear transformation (2.22) are given by:

$$h_e(t) = \begin{cases} Aa_{NM}te^{-a_{NM}t} & \text{if } t \geq 0 \\ 0 & \text{if } t \leq 0 \end{cases}$$

in the excitatory case and

$$h_i(t) = \begin{cases} Bb_{NM}te^{-b_{NM}t} & \text{if } t \geq 0 \\ 0 & \text{if } t \leq 0 \end{cases}$$

in the inhibitory case.

The second dynamical transformation in the model is the conversion of the net average membrane potential into an average density of spikes (see Figure 2.5B). This conversion is done at the somas of the neurons that form the population, and is described mathematically by a sigmoidal function

$$S(m(t)) = \frac{2e_0}{1+e^{r(v_0-m(t))}}. \tag{2.23}$$

Here $e_0$ determines the maximum firing rate of the neural population, $v_0$ sets the net PSP for which a 50% firing rate is achieved, $r$ is the steepness of the sigmoidal transformation, and $m(t)$ corresponds to the net PSP input into the population being considered. The average density of action potentials produced by the presynaptic population acting upon the postsynaptic population, $p_i(t)$, turns out to be proportional to $S(m(t))$, where the proportionality constant weights the contact between the populations, and gives the range of efficiency of the synaptic interaction. Combining Equations (2.22)-(2.23) we obtain the complete model for the NMs:

$$\begin{aligned}
\dot{y}_0(t) &= y_3(t) \\
\dot{y}_1(t) &= y_4(t) \\
\dot{y}_2(t) &= y_5(t) \\
\dot{y}_3(t) &= Aa_{NM}S[y_1(t)-y_2(t)] - 2a_{NM}y_3(t) - a_{NM}^2y_0(t) \\
\dot{y}_4(t) &= Aa_{NM}(p_e(t)+C_2S[C_1y_0(t)]) - 2a_{NM}y_4(t) - a_{NM}^2y_1(t) \\
\dot{y}_5(t) &= Bb_{NM}(p_i(t)+C_4S[C_3y_0(t)]) - 2b_{NM}y_5(t) - b_{NM}^2y_2(t),
\end{aligned} \tag{2.24}$$

where $y_0(t)$ is the excitatory postsynaptic potential (EPSP) produced by the pyramidal population on the interneuron populations, and $y_1(t)$ is the EPSP acting upon the pyramidal population and arriving from (i) the excitatory interneurons, (ii) other areas of the brain. Finally, $y_2(t)$ is the IPSP acting upon the pyramidal population and arriving from the inhibitory interneurons. The intra-columnar connectivity constants values are defined in terms of $C_i$, with $i = 1,\ldots,4$. We use the values given in Jansen and Rit (1995), but we refer the reader to Chapter 5 for fur-

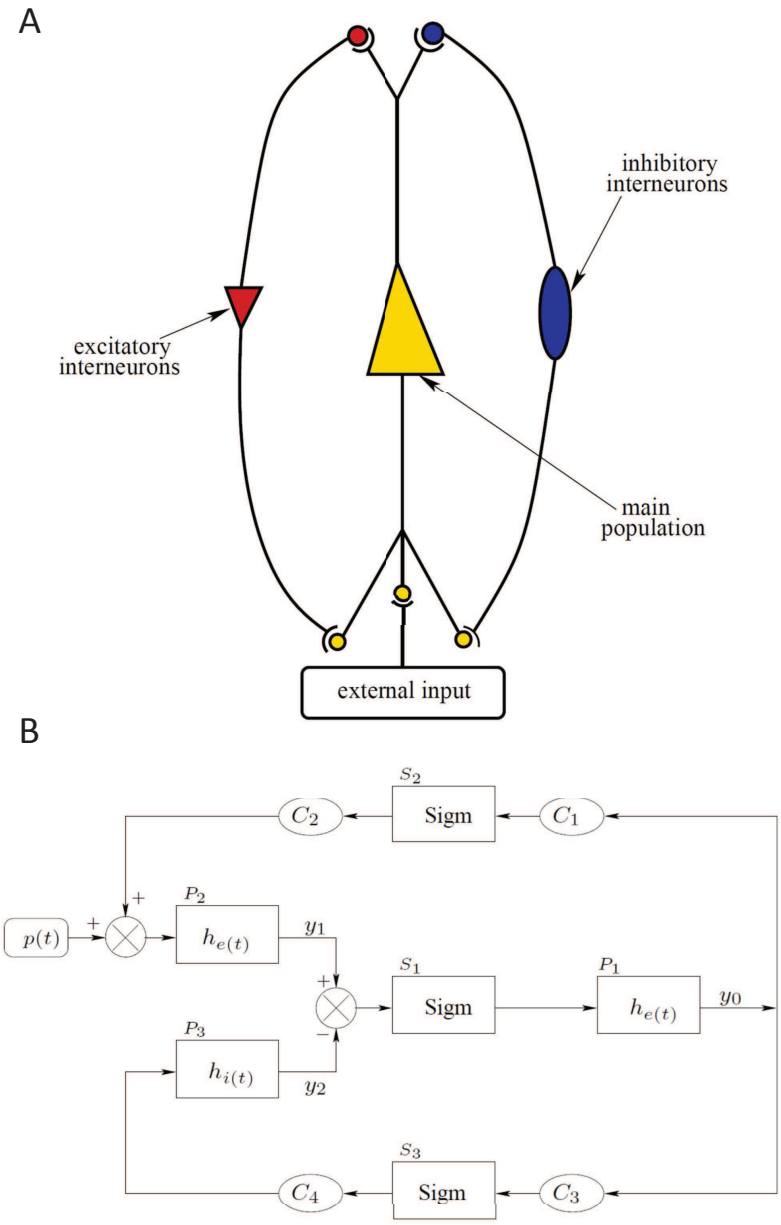


Fig. 2.5 **Illustrative scheme of a neural mass model of a cortical column.** (A) A population of pyramidal neurons interacting with two populations of interneurons, one excitatory (left branch) and the other inhibitory (right branch). (B) Flowchart representation of operations performed inside a column. The boxes labeled $h_e$ and $h_i$ represent the effect of synapses between populations, which is modeled mathematically as a second order differential linear transformation from the average firing rate of the presynaptic population to the membrane potential of the postsynaptic one. The boxes labeled *Sigm* represent the nonlinear transformation of the membrane potential of a population into an output firing rate. The constants $C_i$ account for the strength of the synaptic connections between populations. Adapted from Grimbert and Faugeras (2006a).

ther details about the parameters, where we will propose a multi-scale approach made of NM and HH models simultaneously. We use and explore these computational approaches at different scales to characterize a diversity of spatio-temporal phenomena, which will be described in Part II.

# Part II

# Results

# Chapter 3

# Transition between functional regimes in an integrate-and-fire network model of the thalamus

The thalamus is a key brain structure in the processing of sensory information. Transient temporal coordination of distributed neuronal activity of thalamic cells through precise synchronization allows this structure to dynamically process information, in a way that it reflects different behavioral states. This Chapter addresses the general question of how the thalamus changes its dynamical behavior (which is associated with different information-processing regimes, corresponding broadly to wakefulness and sleep) as a function of both its internal state and external inputs. To that end we implement a simple yet biologically realistic neuronal network model of adaptive exponential integrate-and-fire neurons, which exhibits two dynamical regimes with different information processing capabilities. The model includes two prominent types of thalamic neurons, namely thalamocortical relay cells (TC) and reticular neurons (RE). We investigate how the network architecture of the thalamus influences the occurrence of these two regimes, and how the transition between them is controlled.

In Section 3.1, we introduce the main dynamical properties of thalamic neurons depending on the behavioral state. Next we present in Section 3.2 the neuronal network model adopted for the analysis. In Section 3.3 we build our network progressively. In Section 3.3.1, we show how our aEIF neurons reproduce the two activity modes of TC and RE neurons: the standard depolarizing regime (Jahnsen and Llinás, 1984) and the rebound from hyperpolarization (Halassa et al., 2014). In Section 3.3.2 and 3.3.3 we investigate how spindle oscillations are generated through the TC-RE interaction as a function of their coupling and of the presence of external inputs, and how heterogeneity can be tamed by the interaction of different TC-RE loops. The analysis extends up to full networks in the presence of cortical inputs impinging on the reticular neurons from the periphery and the cortical areas (Section 3.3.4). Finally, in Section 3.4, we summarize the main results of this study. These results are reported in Barardi et al. (2016) (under revision).

## 3.1 Dynamical properties of the thalamus

The thalamus is often identified as a relay station between subcortical and cortical areas, since all sensory pathways of the nervous system pass through it before reaching the cortex. Indeed, sensory inputs from visual, auditory and somato-sensory receptors reach the cortex through synapses on thalamocortical relay neurons in a specific region of the thalamus, which in turn projects into the corresponding area in the primary cortex. It is thus reasonable to think that thalamus does not limit its activity to faithfully transmitting information to the cortex, but it might play a role in gating and modulating the flow of information towards the cortex (Crick, 1984; Reinhold et al., 2015; Sherman and Guillery, 2002), i.e. in selecting which external information is supposed to reach the cortex and when. In particular, this view is coherent with the important role found to be played by the thalamus in the sleep/arousal/wake processes (Dang-Vu et al., 2008; Llinás and Paré, 1991; Steriade et al., 1993), and attention (Guillery et al., 1998; McAlonan et al., 2008; Wimmer et al., 2015).

The main kind of excitatory neurons in the thalamus are the above-mentioned TC neurons. *In vitro* studies (Jahnsen and Llinás, 1984; Llinás and Jahnsen, 1982) have revealed that these neurons can operate in different firing modes depending on their voltage level. Near the resting membrane potential, TC neurons can produce trains of spikes with frequency proportional to the amplitude of the injected current, due to voltage-dependent currents that generate action potentials (Destexhe and Sejnowski, 2003). This is usually called *tonic mode*. Alternatively, when TC neurons are hyperpolarized they can operate in a *bursting mode*, characterized by high-frequency bursts of action potentials (300 Hz) in response to hyperpolarization.

During slow-wave sleep, TC neurons display strong spindle oscillations ($7-15$ Hz) independently from external stimuli (Andersen and Eccles, 1962; Destexhe and Sejnowski, 2003). In contrast, in the awake state TC neurons are known to vary their activity according to inputs coming from the associated receptor layers, and to affect in turn the activity of the associated primary sensory cortex. For instance, TC neurons belonging to the lateral geniculate nucleus (LGN) and the ventral posterior nucleus (VPN) are modulated by the retina (Butts et al., 2007) and by the tactile afferents (Land et al., 1995), respectively, and modulate in turn the activity of primary visual and somatosensory cortical areas (Gilbert and Wiesel, 1992; Pais-Vieira et al., 2015; Reinhold et al., 2015). TC neurons are also key components of the above-mentioned gating role of the thalamus, contributing to the selection of salient information during selective attention (Wimmer et al., 2015).

As suggested by Crick in his seminal paper (Crick, 1984), the role of modulating the efficacy of sensory transmission of TC neurons is mainly played by the neurons of the reticular nucleus of the thalamus (RE neurons). In particular, the activation of RE neurons can strongly

hyperpolarize TC neurons, which consequently undergo inhibitory rebounds that give rise to an endogenous oscillatory activity (Halassa et al., 2014). Specifically, spindles can be originated by TC bursts eliciting firing activity in RE cells. In turn RE bursts hyperpolarize TC cells, which consequently stop firing. When RE cells, lacking excitatory drive, stop firing too, the rebound of TC cells from hyperpolarization causes them to emit a burst of spikes and the cycle starts again. The overall process takes about 100 ms and generates rhythmic spindle oscillations. Therefore spindle generation is due to an interplay between TC and RE cells (Destexhe et al., 1993; McCormick, 1992). Coherently with this fact, manipulating the activity of RE neurons was found to have behavioral consequences in attention tasks (Lewis et al., 2015b; Wimmer et al., 2015).

During the awake state, TC cells undergo a transition and alternate this bursting mode with a tonic mode. As mentioned above, both modes are typical of TC neurons, and they could provide different frameworks for information processing, since during the bursting mode action potentials in the TC cell are not linked directly to EPSPs in that cell, whereas the opposite is true in the tonic mode. Therefore we expect that the bursting mode transmits information less efficiently than the tonic mode, in which an increase in the extra-thalamic inputs on TC neurons leads to a direct increase in the response of TC neurons (Sherman and Guillery, 2002). How the thalamus exhibits the functional transition between the two regimes is not clear. In fact, a coherent view accounting for both TC and RE interactions and the resulting functional behavior of the thalamic network is still missing, due in particular to the relative paucity of simultaneous neurophysiological recordings of the two neuron types *in vivo*. In this context, the role of modeling becomes very relevant, due to its capacity to suggest candidate mechanisms for the generation of the observed behavior. Modeling of thalamic networks has been pursued for more than 20 years (Destexhe et al., 1994a; Golomb et al., 1996), during which network models have been developed that capture a wealth of thalamic phenomena (Muller and Destexhe, 2012). However, almost all studies to date have adopted neuron models at least as complex as the Hodgkin-Huxley model (Destexhe et al., 1994a; Willis et al., 2015), probably due to the aforementioned role of rebound currents. We are aware of one attempt to model realistically thalamic interactions with integrate-and-fire (IF) neurons (Destexhe, 2009). Other relevant work on this topic has been done by Smith and colleagues (see e.g. Huertas et al. 2005, based on an earlier model of Smith et al. 2001) and also by Coombes (2003), whose work is based on a firing rate reduction of IF networks with slow T-type calcium currents in RE and TC cell networks.

In this Chapter we focus on a single property of the thalamic network as a whole, namely its above-mentioned ability to switch between two dynamical regimes that display different external input sensitivity. We also study the role played in this phenomenon by the network archi-

tecture (connectivity and synaptic strength), ranging from loops of two neurons to the effect of sensory and cortical input on the whole thalamic network. To that end we develop a thalamus TC-RE network model based on a particularly simple spiking neuron model, namely a different suited version of the adaptive exponential integrate-and-fire (aEIF) neuron model (Brette and Gerstner, 2005) for each neuron type (see Section 2.1.2). The choice of this neuron model allowed us to focus on a restricted number of parameters, specifically those related to physiological quantities influencing the rebound-driven oscillations and the tonic state (Touboul and Brette, 2008). Moreover, our aEIF thalamic model will be particularly suited to be interfaced with cortical column LIF models (e.g. Potjans and Diesmann, 2014) to model accurately the whole thalamocortical loop (see Perspectives section 7.5).

## 3.2 Network model of adaptive exponential integrate-and-fire neurons

We build the thalamic network based on the single-neuron adaptive exponential integrate-and-fire (aEIF) model (Brette and Gerstner, 2005), described in Section 2.1.2. The network is made of TC and RE cells, endowed with intrinsic properties and topographic connectivity specific to the thalamus (Destexhe, 2009). Here we consider a network of 500 neurons, half of which are TC neurons and the other half being RE neurons. Given that thalamic interneurons do not contribute to the development of internal dynamics such as oscillations, they are neglected. Axonal projections within the thalamic circuitry are local but sparse. The excitatory projections from TC to RE have a connection probability of 1%, while RE to TC inhibitory projections are more dense, with a connection probability of 4%. The same density is assumed from inhibitory connections between RE cells. The structural connectivity is built starting from a ring network and then randomly rewiring with probability *RP*. This process allows us to control the clustering coefficient, which quantifies the connectedness or local connectivity of the network (in terms of the probability that two nodes that are connected to a common node are also connected between them). According to the Watts and Strogatz algorithm Watts and Strogatz (1998), a pure regular network can be turned into a small-world network, in which few edges separate any two nodes, by rewiring the connections. A rewiring probability equal to 0 implies a regular network with large clustering (provided the coupling extends beyond nearest neighbors), whereas a rewiring probability equal to 1 implies a completely random network with small clustering. The network model is constructed based on the Equations (2.2)-(2.3) of

the aEIF, which we reproduce here for clarity:

$$C_m \frac{dV_i}{dt} = -g_L(V_i - E_L) + g_L \Delta_i \exp\left(\frac{V - V_{T_i}}{\Delta_i}\right) - w_i - \sum_j g_{ij}(V_i - E_j) \tag{3.1}$$

$$\frac{dw_i}{dt} = \frac{1}{t_{w_i}}[a_i(V_i - E_L) - w_i], \tag{3.2}$$

$$\text{if } V \geq E_{thresh}, \begin{cases} V_i = V_r \\ w_i = w_i + b, \end{cases} \tag{3.3}$$

where the first equation describes the evolution of the membrane voltage $V_i$ of neuron $i$ and $C_m = 1$ nF is the capacitance. The ionic currents are the ohmic leak current defined by the resting leak conductance $g_L = 0.05\ \mu$S and the resting voltage potential $E_L = -60$ mV, and the exponential term that reproduces the $Na^+-$ current responsible for the generation of spikes. $\Delta$ denotes the steepness of the exponential approach to threshold, taken equal to $\Delta = 2.5$ mV, and $V_T = -50$ mV is the threshold potential. The membrane time constant is $\tau_m = C_m/g_L$. When $V$ is pushed over the threshold, the exponential term provides a positive feedback and a spike is emitted, at which point the voltage is instantaneously reset to $V_r = -60$ mV and the adaptation variable $w$ is increased a value $b$. After the spike, the neuron cannot spike again during a refractory period (2.5 ms). The second equation describes the dynamics of the adaptation variable $w$, with time constant $\tau_w = 600$ ms. The parameter $a$ (in $\mu$S) quantifies a conductance that mediates subthreshold adaptation, while the increment $b$ (in $n$A) at each spike takes into account spike-triggering adaptation (it regulates the strength of adaptation). In order to reproduce the peculiar properties of TC and RE when operating in bursting mode, we adopt specific values of $a$ and $b$. With $a = 0.4\ \mu$S, $b = 0.02\ \mu$A, neurons display bursting activity in response to both depolarizing and hyperpolarizing stimuli typical of RE neurons. In contrast, with $a = 0.2\ \mu$S, $b = 0.0\ \mu$A, neurons display responses with moderate adaptation and strong rebound bursts, like TC neurons. RE and TC neurons can display different regimes (beyond bursting and tonic, fast spiking, regular spiking) by tuning the parameters $a$ and $b$ (Izhikevich, 2004; Ladenbauer et al., 2012; Naud et al., 2008). In both cases, since $a/g_L > \tau_m/\tau_w$ we are in the parameter regime in which rebound firing is possible, as demonstrated by Touboul and Brette (2008).

The term $\sum_j g_{ij}(V_i - E_j)$ accounts for the synaptic current coming from the neighboring neurons impinging on a neuronal cell, where $g_{ij}$ is the conductance of the synapse from neuron $j$ to neuron $i$ (which can be zero), and $E_j$ is the reversal potential of the synapse ($E_j = 0$ mV for excitatory synapses and $-80$ mV for inhibitory synapses). Synaptic conductances are

described by:

$$g_{ij}(t) = \frac{\hat{g}_{syn}}{\tau_{decay} - \tau_{rise}} \left[ e^{\frac{-t-t_j}{\tau_{decay}}} - e^{\frac{-t-t_j}{\tau_{rise}}} \right], \tag{3.4}$$

where $\tau_{decay}$ and $\tau_{rise}$ are the decay and rise synaptic time, respectively, and $\hat{g}_{syn}$ is constant and depends on the type of synapses and network (see Table 3.1). Once the presynaptic cell fires, $g_{ij}$ exponentially increases up to a certain value, after which it decays exponentially with a fixed time constant (5 ms for excitation and 10 ms for inhibition). Different synaptic strengths are considered (see Table 3.2), depending on the network type. If different values are considered, they are indicated in the captions of each figure. Note that the conductance values use here are higher than the ones observed experimentally. This is done to compensate for the unrealistically low amount of incoming inputs, due to the fact that we are considering small networks. This synaptic strength rescaling is a common practice in computational neuroscience (Destexhe, 2009). Synaptic delays are equal to 1 ms.

| | AMPA $\tau_{rise}$ | AMPA $\tau_{decay}$ | GABA $\tau_{rise}$ | GABA $\tau_{decay}$ |
|---|---|---|---|---|
| Network 2 neurons | 0.4 *ms* | 5 *ms* | 0.4 *ms* | 20 *ms* |
| Network 4 neurons | 0.4 *ms* | 5 *ms* | 0.4 *ms* | $\mu = 20$ *ms*, $\sigma = 5$ *ms* |
| Network 500 neurons | 0.4 *ms* | 5 *ms* | 0.4 *ms* | 10 *ms* |

Table 3.1 Values of temporal rise and decay constants for RE and TC.

| | $g_{RE\to TC}$ | $g_{TC\to RE}$ | $g_{RE\to RE}$ | $g_{ext\to TC}$ | $g_{CX\to RE}$ |
|---|---|---|---|---|---|
| Network 2 neurons | $200-800$ $\mu$S | $10-60$ $\mu$S | $200-800$ $\mu$S | 1 $\mu$S | 1 $\mu$S |
| Network 4 neurons | 550 $\mu$S | 32 $\mu$S | 20 $\mu$S | 1 $\mu$S | 1 $\mu$S |
| Network 500 neurons | 300 $\mu$S | 200 $\mu$S | 300 $\mu$S | 5 $\mu$S | 1 $\mu$S |

Table 3.2 Values of synaptic strengths for a network of 500 neurons.

To initiate activity, during the first 50 ms a number of randomly-chosen neurons are stimulated by an incoming current (with synaptic strength g= 40 $\mu$S), representing an heterogeneous Poisson train of excitatory presynaptic potential with an instantaneous event rate $\lambda(t)$ that varies following an Ornstein-Uhlenbeck process:

$$\frac{d\lambda}{dt} = -\lambda(t) + \sigma(t)\sqrt{\frac{2}{\tau}}\eta(t) \tag{3.5}$$

where $\sigma(t)$ is the standard deviation of the noise and is set to 0.6 spikes/s. $\tau$ is set to 16 ms, leading to a power spectrum for the $\lambda$ time series that is approximately flat up to a cut-off frequency $f = \frac{1}{2\pi\tau} = 9.9$ Hz. $\eta(t)$ is a Gaussian white noise of mean zero and intensity unity. The only source of noise is the random connectivity. In simulations in which we take into

account external sensory inputs, after 5 s of self-sustained activity we inject for 10 s homogeneous Poisson processes with rate comprised between 10 and 150 spikes/s. In simulations in which we did not take into account external input after 50 ms, and thus the activity states described here are self-sustained.

## 3.3 Dynamics of the aEIF network with increasing size

The presence of two different dynamical regimes in the thalamus has been known for decades (Livingstone and Hubel, 1981; Steriade and McCarley, 2005; Steriade et al., 1993). This behavior can be linked to a specific property of the two main kinds of neurons in the thalamus, described above, glutamatergic thalamocortical relay (TC) neurons and GABAergic thalamic reticular (RE) neurons. Both types of neurons can fire either as a result of depolarizing driving or as a rebound due to hyperpolarizing driving. In what follows we show how the aEIF model defined above reproduces the two types of responses for both kinds of neurons (Figure 3.1). We investigate how and when the connectivity between the neurons displaying these properties induces a regime dominated by spindle oscillations, or responding to stimuli in a tonic-like mode. The analysis starts from two-neuron loops and extends up to full networks receiving input from the periphery and the cortical areas.

### 3.3.1 Dynamics of single neurons

The first step towards reproducing the two dynamical regimes of the thalamus described above, and the transition between them, is to choose a single-neuron model able to capture the peculiar properties of thalamic neurons, and in particular the firing induced by hyperpolarization-driven rebound. To that end we select a properly tuned adaptive exponential integrate-and-fire (aEIF) spiking neuron model (Brette and Gerstner, 2005; Fourcaud-Trocmé et al., 2003; Izhikevich, 2004) (see Section 3.2) for each of the two thalamic neuron types considered. By tuning the key parameters of the aEIF model it is possible to adjust the dynamics and the strength of adaptation (parameters $a$ and $b$ in Equations (3.2)-(3.3), respectively) to reproduce the intrinsic dynamical modes typical of thalamic neurons. For $a = 0.4$ $\mu$S and $b = 0.02$ nA, the RE aEIF neuron models (RE neuron from now on) exhibits regular firing activity in response to depolarizing stimuli (Figures 3.1A,B), while they display bursting activity in response to hyperpolarizing stimuli (Figure 3.1C,D), consistently with experimental findings (Contreras et al., 1993; Domich et al., 1986; Steriade, 2003). In particular, in response to a depolarizing stimulus (Figure 3.1A), RE neurons display firing activity with a certain degree of spike-frequency adaptation that saturates before the end of the stimulus and stops neuronal firing.

For large enough applied currents, the response extends for the whole duration of the stimulus (Figure 3.1B). In response to a hyperpolarizing stimulus (Figures 3.1C,D), and due to the relatively large value of $a$, the neuron exhibits rebound bursting activity, also with spike-frequency adaptation, for the same spike threshold used in the depolarizing case.

TC neurons generally show a more robust bursting activity and a negligible level of spike-frequency adaptation (Llinás and Jahnsen, 1982) (see (Destexhe and Sejnowski, 2003) for a review). This is achieved in the model by imposing a larger value of $a = 0.2$ $\mu$S and $b = 0$ nA, thus making the adaptation strength negligible. In particular, in response to a depolarizing stimulus the TC neurons produce patterns of firing activity (Figure 3.1E) with negligible spike-frequency adaptation (Figure 3.1F) (leading thereby to high firing activity for all the duration of the stimulus). In contrast, a hyperpolarizing stimulus leads to rebound bursting (Figure 3.1G) and moderate spike-frequency adaptation (larger than in RE neurons) (Figure 3.1H). In the case of depolarizing stimuli, characterized by negligible adaptation and regular firing activity, TC neurons exhibit an effective increase of activity (Figure 3.1F) according to the increasing external input and compatibly with the refractory period, where neuron is not allowed to fire. Therefore the firing activity increases proportionally with larger external sensory inputs. This is consistent with the linear input-output relation in the tonic mode (Figure 3.1E,F), in contrast with the bursting mode where there is no direct link between the EPSP and spike generation, which thus corresponds to a nonlinear input-output relation (Sherman, 2001). Relevant works have been recently done showing that bursts may also be important in the encoding of sensory information (Elijah et al., 2015; Samengo et al., 2013).

Overall these results show that the aEIF models properly capture the two firing modes (depolarizing-driven and hyperpolarization-driven) for both TC and RE neurons. In the following we show the transition between the two modes for TC neurons due to external inputs, and how recurrent activity drives a transition at the network level from stimulus-insensitive to stimulus-sensitive behavior.

### 3.3.2 Two-neuron loops

Before moving to large, structured networks we carefully analyze the properties of the mutual interaction between TC and RE neurons. Specifically, we study different simple two-neuron loops formed by TC-RE and RE-RE neurons, and examine how self-sustained oscillatory patterns originated in these networks are modulated by synaptic strengths regulating the internal recurrent activity. We also study the effect of GABA temporal decay dynamics on the frequency of oscillation, and the input-driven oscillatory pattern of a TC-RE loop. This analysis is informative towards the building of a full network. We first build a minimal model of two bidirectionally coupled neurons, a RE neuron and a TC neuron (Figure 3.2A). Activating this

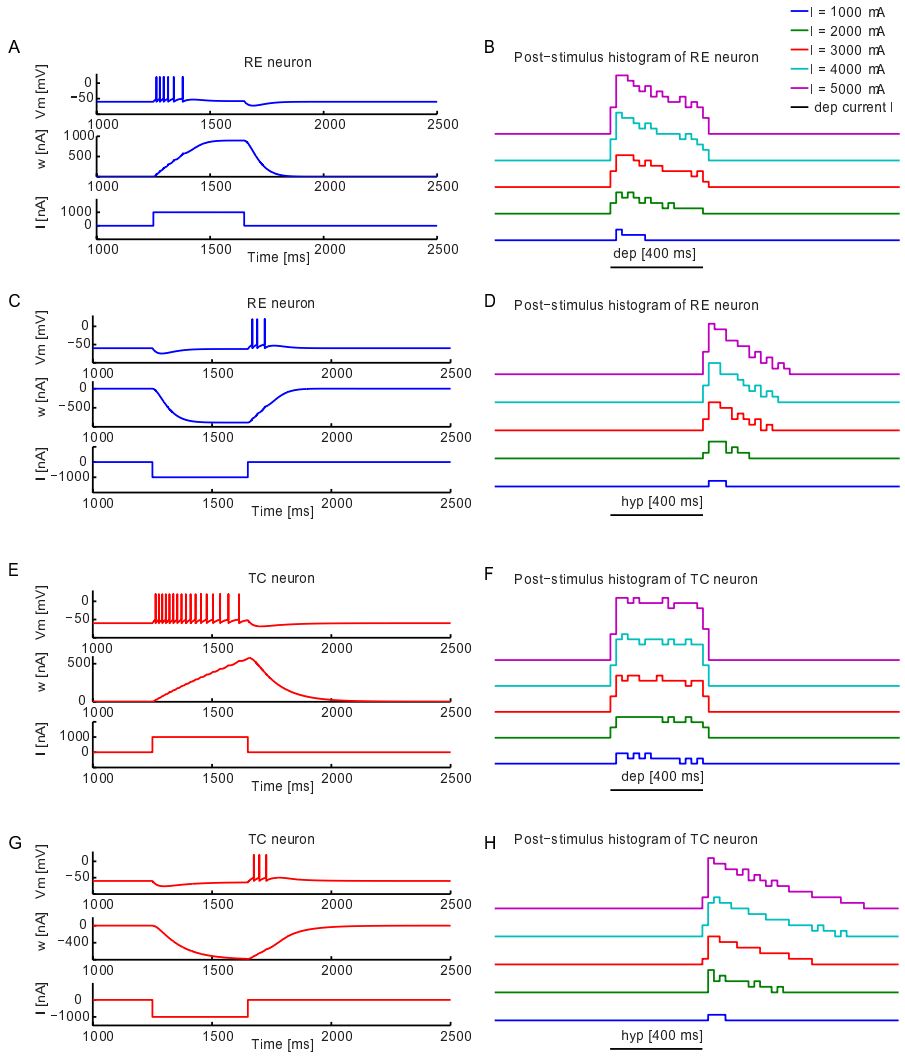


Fig. 3.1 **Dynamical properties of single RE and TC neurons as a function of input current.** (A) Depolarization activity of a RE neuron. Membrane voltage (top) and adaptation variable (middle) of a RE neuron in response to a depolarizing current (bottom). (B) Corresponding post-stimulus time histograms for increasing depolarizing currents. (C) Hyperpolarization-rebound activity of a RE neuron and (D) corresponding post-stimulus time histograms for increasing hyperpolarizing currents. Parameters $a$ and $b$, representing respectively the dynamics and the strength of adaptation (see Equations (3.2)-(3.3)) of RE neurons are defined in this way: $a = 0.4$ $\mu$S and $b = 0.02$ nA. (E) Depolarization activity of a TC neuron and (F) corresponding post-stimulus time histograms for increasing depolarizing currents. (G) Hyperpolarization-rebound activity of a TC neuron and (H) corresponding post-stimulus time histograms for increasing hyperpolarizing currents. The values $a$ and $b$ are 0.2 $\mu$S and 0 nA. The current intensity in (A,C,E,G) is 1000 mA, while it varies between 1000 mA and 5000 mA in panels (B,D,F,H). $V_T = -50$ mV is the threshold potential for both types of neurons.

RE-TC loop for 50 ms leads to oscillations that persist stably after the stimulus termination (Figure 3.2B). These oscillations are due to the rebound bursting properties of the TC relay cell, which is mutually connected with the RE neuron: the TC neuron provides depolarizing input to the RE neuron, which displays bursting activity that generates strong hyperpolarization, followed by rebound firing activity in TC neurons. Consequently, in this configuration the RE neuron fires in response to depolarizing currents, while the TC neuron fires only in response to hyperpolarizing inputs.

Next we investigate how these oscillatory patterns vary as a function of the synaptic strength $g_{TC\to RE}$, keeping $g_{RE\to TC}$ constant at a reference value of 550 $\mu$S. By increasing $g_{TC\to RE}$, both the TC and RE neurons oscillate with higher frequency, as can be seen from the decrease of the inter-spike interval (ISI) in Figure 3.2C (bottom). Stronger synaptic strengths enhance the firing activity of the RE neuron, which fires in advance along the oscillation cycle and thus leads the TC neuron to spike at an earlier phase. The net effect is an increase in the oscillation frequency. The RE neuron (Figure 3.2C, top) displays bursting activity in response to depolarizing input above a threshold value of $g_{TC\to RE} = 29$ $\mu$S. It oscillates at around 11 Hz (inter-burst ISI $\approx$ 90 ms) with two spikes per burst with an intra-burst ISI $\approx$ 5 ms. By increasing the synaptic strength $g_{TC\to RE}$, the neuron passes a second threshold $g_{TC\to RE} = 40$ $\mu$S and presents three spikes per burst (three ISIs are present), eventually entering a regime in which the ISI approaches the intrinsic refractory period of the neuron (2.5 ms).

Subsequently we perform the complementary analysis by fixing $g_{TC\to RE}$ to 32 $\mu$S (which leads to two-spike bursting in the preceding analysis) and varying $g_{RE\to TC}$. Figure 3.2D shows that as $g_{RE\to TC}$ is increased, the TC neuron oscillates with a gradually increasing frequency that stabilizes around 10.5 Hz (Figure 3.2D, bottom), while the RE neuron displays bursting activity with the same inter-burst ISI as the TC neuron and an intra-burst ISI of $\approx$ 3 ms (two-spikes-per-second scenario of previous analysis) (Figure 3.2D, top). Note that the brief hyperpolarization induced in the TC cell by the firing of a single RE cell is able to trigger only one rebound spike, and consequently the number of spikes/burst in the RE cell remains constant. This is consistent with the results reported by Destexhe and Sejnowski (2003), where spindle activity required at least a four-neuron network (see next Section).

Next we explore the dynamics of a purely GABAergic reticular RE-RE loop (Figure 3.2E) as a function of the synaptic strength $g_{RE\to RE}$. As Figure 3.2F shows, the RE neurons present a sustained strong and adapting bursting activity (corresponding to a wide range of intra-burst ISI) and for increasing values of the synaptic strength, the inter-burst ISI decreases. Importantly, unlike in previous studies, here the decreasing inter-burst ISI does not entail an increase in oscillation frequency, since in this case bursts last much longer (with more than 10 spikes per burst). This result shows that RE-RE synapses strengthen the rebound bursting properties

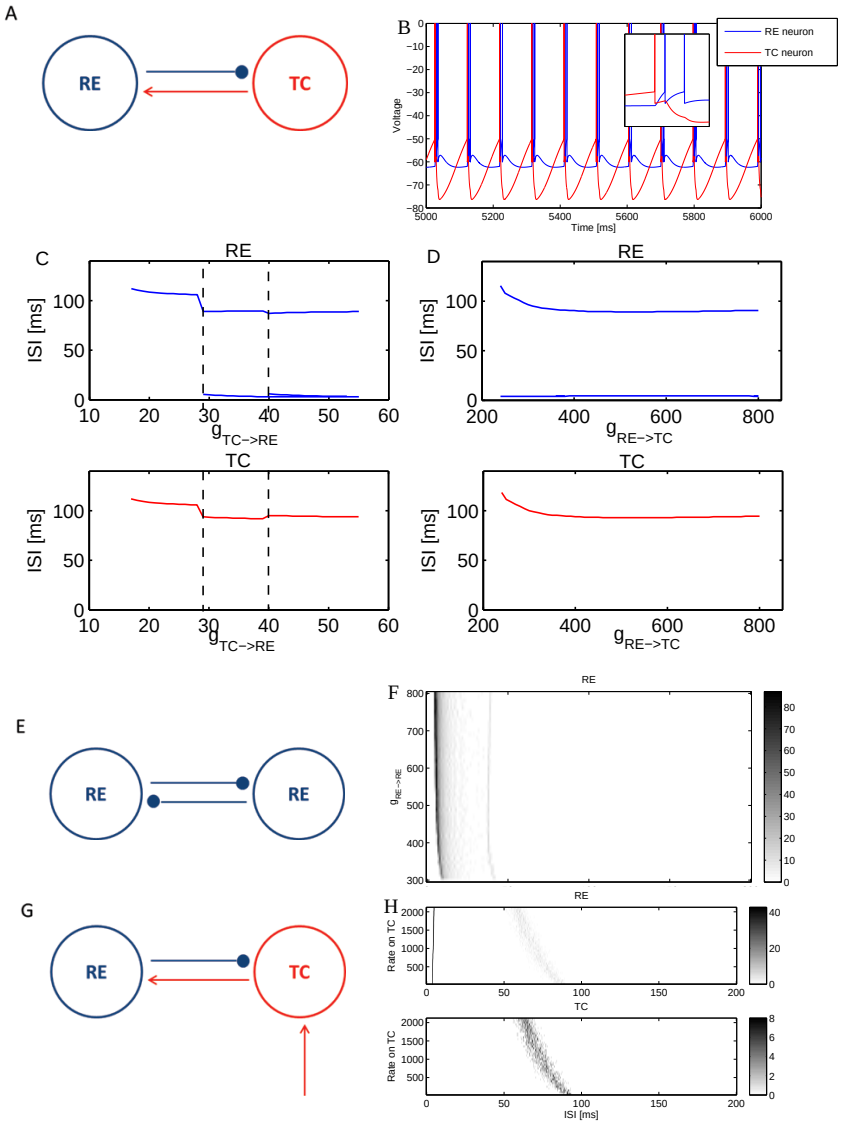


Fig. 3.2 **Dynamical properties of two-neuron loops.** (A) Scheme of a two-neuron TC-RE loop. (B) Membrane voltage traces of the TC and RE neurons generated by this minimal TC-RE loop. (C) Interspike interval (ISI) distribution of the TC-RE loop as a function of the synaptic strength $g_{TC\to RE}$. The value of $g_{RE\to TC}$ is appropriately set to 550 $\mu$S in order to support self-sustained activity, while $g_{TC\to RE}$ varies between 10 $\mu$S and 60 $\mu$S. RE and TC ISI distributions are shown in the top and bottom plots, respectively. (D) ISI distribution of a TC-RE loop as a function of the synaptic strength $g_{RE\to TC}$. The value of $g_{TC\to RE}$ is chosen equal to 32 $\mu$S to reproduce the two-spike bursting dynamical regime of panel B while $g_{RE\to TC}$ varies between 200 $\mu$S and 800 $\mu$S. RE and TC ISI distributions are shown in the top and bottom plots, respectively. (E) Scheme of a minimal purely reticular RE-RE loop. (F) ISI distribution of this loop as a function of the synaptic strength $g_{RE\to RE}$. $g_{RE\to RE}$ varies between 200 $\mu$S and 800 $\mu$S. (G) Scheme of an input-driven two-neuron TC-RE loop. (H) ISI distribution of this loop as a function of external sensory input strength. RE and TC ISI distributions are shown in the top and bottom plots, respectively. The synaptic strengths are respectively: $g_{RE\to TC} = 550$ $\mu$S, $g_{TC\to RE} = 32$ $\mu$S and $g_{EXT\to TC} = 1$ $\mu$S.

and can be expected to enhance the bursting activity in a larger network. In the simple TC-RE loop motif, the oscillation frequency can be tuned by the GABA decay time constant. For instance, by varying $\tau_{decay}$ from 5 to 35 ms in the minimal model of Figure 3.2D, the frequency of the two neurons oscillates between $\sim$ 25 and 6 Hz (Figure 3.3). This leads to corresponding changes in the ISI distributions (Figures 3.4- 3.5), without qualitative variations with respect to the behavior shown in Figure 3.2. The key role played by the GABA decay time constant in modulating the frequency of spindle oscillations is qualitatively similar to the way it affects gamma-range oscillation frequencies in LIF networks where rebound oscillations are not present (Brunel and Wang, 2003).

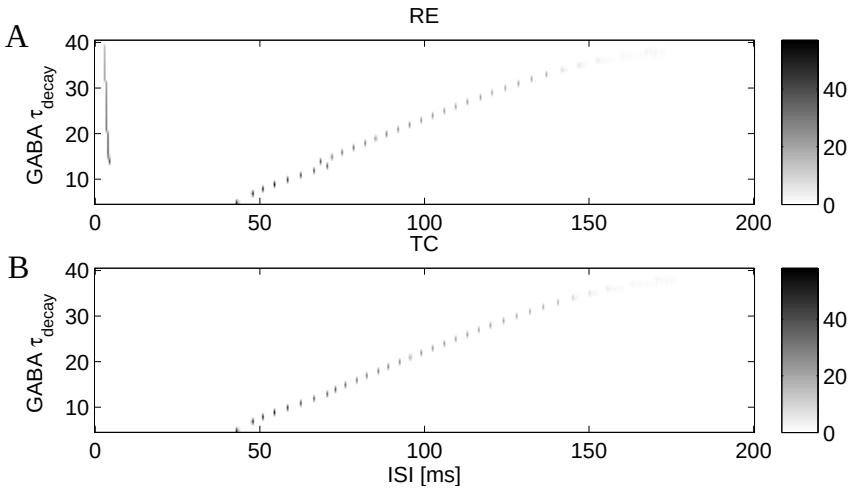


Fig. 3.3 **Effect of the GABA decay time on the two-neuron TC-RE loop.** Interspike Interval (ISI) distribution of a TC-RE loop as a function of the GABA decay time $\tau_{decay}$ for RE (A) and TC (B) neurons. $\tau_{decay}$ varies between 5 and 40 ms. The synaptic strengths are respectively: $g_{RE\to TC} = 550\ \mu$S, $g_{TC\to RE} = 32\ \mu$S.

After investigating the properties of stand-alone RE-TC loops, we move to analyze an input-driven loop in which the TC neuron receives an external sensory input modeled as a Poisson distribution with increasing amplitude (Figure 3.2G). We only consider inputs to TC, mimicking the sensory stimuli coming from the retina or the peripheral nervous system. We set reference values of $g_{TC\to RE} = 32\ \mu$S , $g_{RE\to TC} = 550\ \mu$S and GABA $\tau_{decay} = 20$ms, for which the spontaneous activity (in the absence of external input) takes the form of low-frequency bursting with two spikes per burst. The value of GABA $\tau_{decay}$ is lower in the full population model. When we increase the external input rate (Figure 3.2H) the ISI distribution is significantly different from the one observed in the absence of external stimulus (Figure 3.2D): both neurons show a strong variation in the bursting frequency due to the external stimulus, and the ISI displays a large variance due to the introduction of noise. On the other hand, and con-

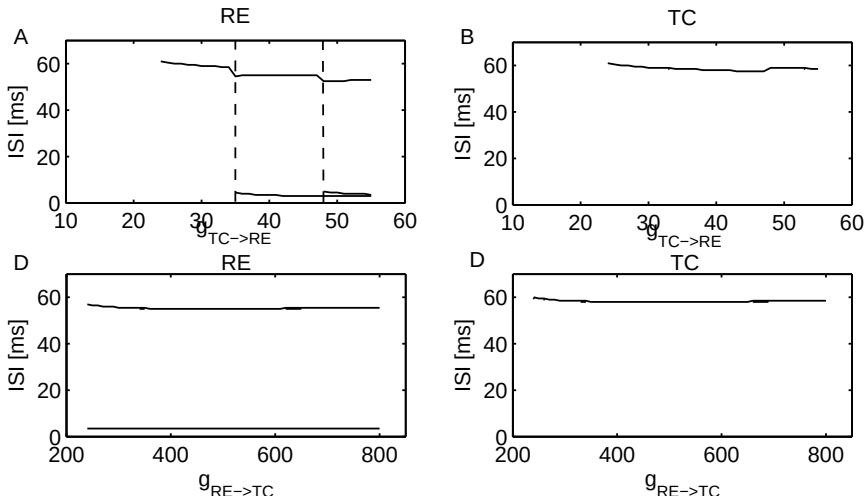


Fig. 3.4 **Effect of the synaptic strength on the two-neuron TC-RE loop.** Interspike Interval (ISI) distribution of a TC-RE loop as a function of the synaptic strength for RE (A,C) and TC (B,D) neurons. As in Figure 3.2C, in A and B the value of $g_{RE\rightarrow TC}$ is appropriately set to 550 $\mu$S in order to support self-sustained activity, while $g_{TC\rightarrow RE}$ varies between 10 $\mu$S and 60 $\mu$S. In C and D, the value of $g_{TC\rightarrow RE}$ is chosen equal to 40 $\mu$S to reproduce the two-spike bursting dynamical regime, while $g_{RE\rightarrow TC}$ varies between 200 $\mu$S and 800 $\mu$S. GABA decay $\tau_{decay}$ is set equal to 10 ms in the two cases.

sistently with Figure 3.2D, the RE neuron is in bursting mode for all values of external input, with the ISI approaching the refractory period.

### 3.3.3 Four-neuron motifs

As a last step before moving to the full network, we investigate several four-neuron motifs, made of two RE and two TC neurons, to understand what are the structural connectivity features more suitable to explain large oscillatory synchronization phenomena, namely spindle oscillations, in the bursting regime, even in presence of heterogeneity between neurons that leads to different oscillation frequencies. Previous work has shown (Destexhe, 2009) that aEIF models are able to reproduce this self-sustained oscillatory behavior in the form of periodic bursting, and that the minimal circuit reproducing the phenomenon is a circuit of two TC and two RE neurons fully connected with each other, with the exception of TC-TC connections, which are not present in the thalamus (Izhikevich and Edelman, 2008). As in the case of the two-neuron loop, bursting is mainly due to the rebound bursting properties of TC cells and RE (Figure 3.6F) (Destexhe and Sejnowski, 2003), and the oscillation frequency depends on the GABA temporal decay constant.

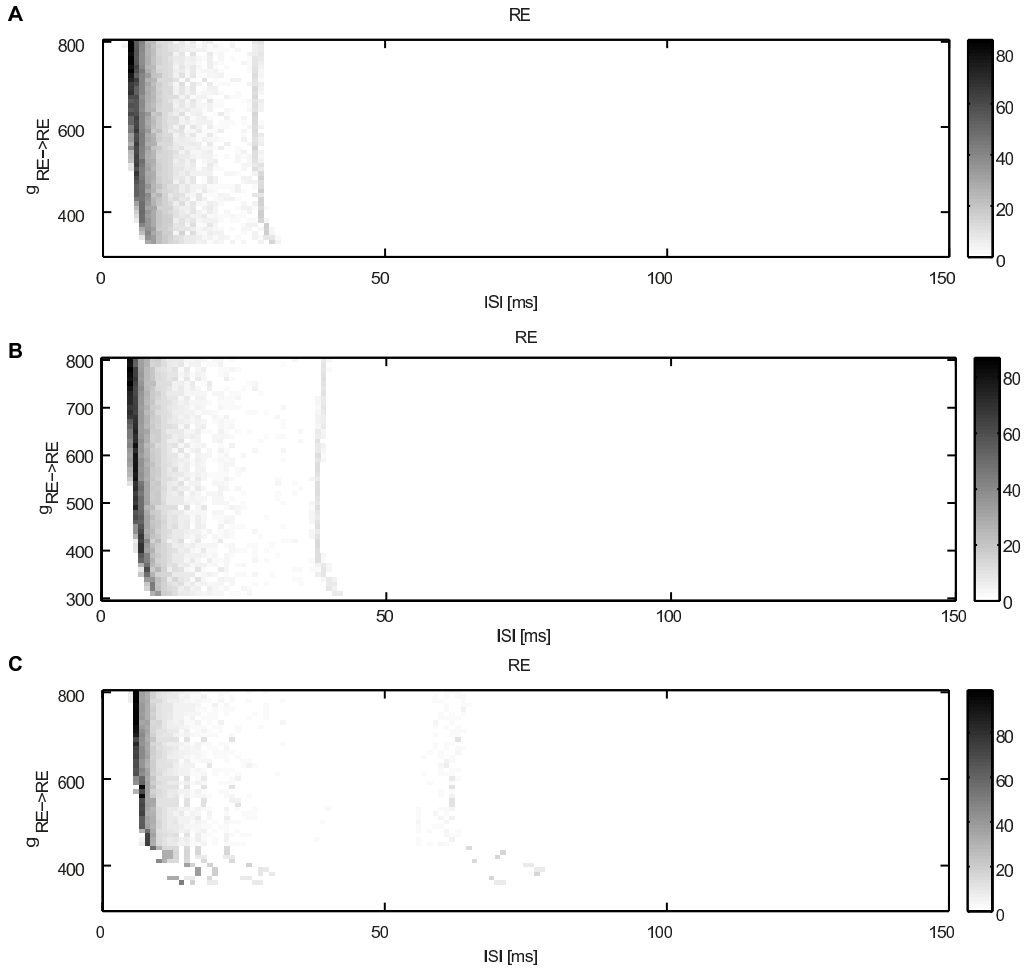


Fig. 3.5 **Effect of the synaptic strengths on the two-neuron RE-RE motif.** Interspike interval (ISI) distribution of a minimal purely reticular RE-RE motif as a function of the synaptic strength $g_{RE\rightarrow RE}$ for three different values of the GABA decay time: (A) 5 ms, (B) 10 ms, (C) 20 ms. $g_{RE\rightarrow RE}$ varies between 300 $\mu$S and 800 $\mu$S.

Since the oscillation frequency might vary slightly between loops, we checked the conditions for the onset of coherent oscillations. In particular, we studied different couplings between pairs of two-neuron TC-RE loops (which are equivalent to two bidirectionally coupled oscillators) with different intrinsic oscillation frequencies, and analyzed which coupling configuration leads more readily to oscillatory spindle patterns by examining the power spectrum of TC neurons and the phase coherence between them. Figure 3.6 shows the schemes of the different circuits explored depending on the coupling links being considered: TC-RE connections (Figure 3.6A), RE-TC connections (Figure 3.6B), RE-RE connections (Figure 3.6C) and all three types of connections (Figure 3.6D). For each circuit, we calculate the power spectral density and phase coherence between the two loops (see Sections A.2- A.3 in Appendix

A) by using the activity of TC neurons. The phase coherence is calculated by averaging 50 trials each with a different GABA $\tau_{decay}$ drawn from a Gaussian distribution with mean 20 ms and standard deviation 5 ms, which leads to variability in the frequencies of the two TC-RE loops being coupled.

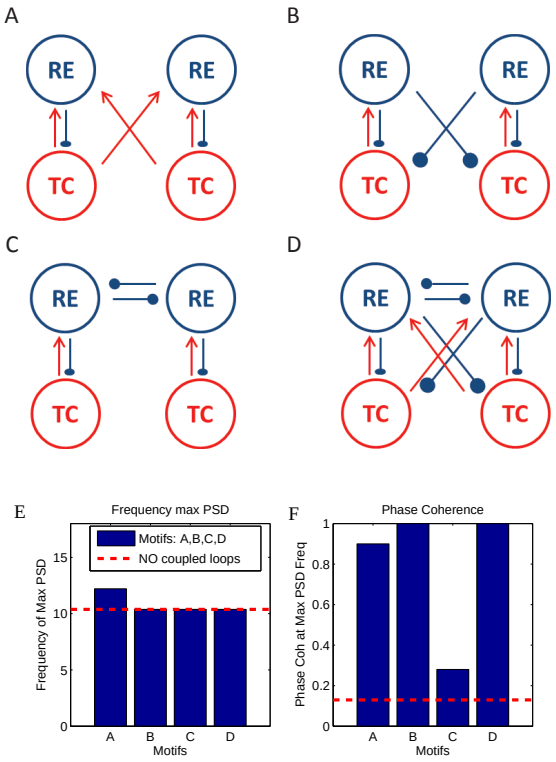


Fig. 3.6 **Four-neuron motifs in the form of coupled pairs of TC-RE loops.** The two TC-RE oscillators are bidirectionally coupled through (A) TC-RE connections, (B) RE-TC connections, (C) RE-RE connections, and (D) all three connections. (E) Frequency of the power spectral peak and (F) phase coherence at that frequency for the four different motifs. The power spectral density and phase coherence were averaged across 50 trials for random values of the GABA decay time (see text). GABA rise time and AMPA rise and decay times are set constant (see Section 3.2). When the corresponding connections exist in the motifs, the synaptic strengths are respectively: $g_{RE\to TC} = 550\ \mu$S, $g_{TC\to RE} = 32\ \mu$S, and $g_{RE\to RE} = 20\ \mu$S.

Figure 3.6E shows the frequency at which the power spectrum of the TC neuron activity has its maximum, and Figure 3.6F the corresponding phase coherence at that frequency. The horizontal dashed red lines represent the corresponding values in the case of uncoupled loops. In the uncoupled case, the oscillation frequency is $\approx 10.4$Hz and the loops are weakly synchronized (the phase coherence being $\approx 0.12$). The two TC-RE oscillators strongly synchronize with a zero-lag phase (corresponding time lag is $\approx 0$, not shown) with respect to the uncoupled case, while the loops are poorly zero-lag synchronized when only RE-RE connections

are present. Therefore this result supports the idea that spindle generation is mainly due to an interplay between TC and RE cells (Destexhe et al., 1993; McCormick, 1992), which is enhanced by RE-RE connections.

### 3.3.4 Full thalamic network

We finally extend the size of the network to 500 neurons to capture the dynamics of a complex thalamic structure. Following experimental indications (FitzGibbon et al., 1995; Kim et al., 1997; Minderhoud, 1971), we consider that each RE projects four connections to TC neurons and to RE neurons themselves, while TC neurons have only on average one connection with RE neurons only. Starting from these numbers we considered two network configurations, in order to investigate how the spindle oscillations are affected by network architecture. The first configuration was a purely random one (Fig. 3.7A) with rewiring probability $RP = 1$ (see Methods), while the second favored RE-RE clustering with rewiring probability $RP = 0.25$ (Fig. 3.7B).

We find that in the random network (Figure 3.7A), temporally irregular bursting is dominant (Figure 3.7C). On the other hand, in the presence of RE-RE clustering (Figure 3.7B) the network shows quite regular and synchronized spindle oscillations at 8 Hz (Figure 3.7D). In order to characterize and quantify the bursting regular state (or spindle rhythm) and distinguish it from irregular tonic activity, we study the inter-burst interval distribution (in particular the probability of a peak of ISI distribution above 50 ms) as a function of the rewiring probability $RP$ of the architecture (see Section 3.2). Our results, shown in Figure 3.7E, reveal that fully regular networks ($RP = 0$, each neuron projects regularly to a fixed number of adjacent neurons) cannot support regular bursting activity and are often almost silent (with a firing rate of around 0.4 spikes/s, results not shown). At the other extreme, fully random networks ($RP = 1$) show sustained activity with temporally irregular bursting of TC and RE neurons. Between these two conditions, there is an optimum rewiring probability ($RP \sim 0.25$) showing a relatively large ISI peak corresponding to frequency $\sim 8.5$ Hz. The fraction of neurons displaying a large inter-burst ISI peak decreases substantially for increasing rewiring probability, namely when going towards fully random networks. Intuitively, given that connections between thalamic circuits are local but sparse (FitzGibbon et al., 1995; Kim et al., 1997; Minderhoud, 1971), excitatory synapses are very sparse and they are more effective when they impinge on small clusters of RE-RE neurons, enhancing and modulating the oscillatory spindle rhythm.

Given the results obtained above, we decide to study a network with the critical degree of clustering ($RP = 0.25$), and simulate constant external sensory input of different intensities impinging on TC neurons. We test if by increasing the external input on these neurons the network shows a transition from bursting to tonic mode, which could be associated with the

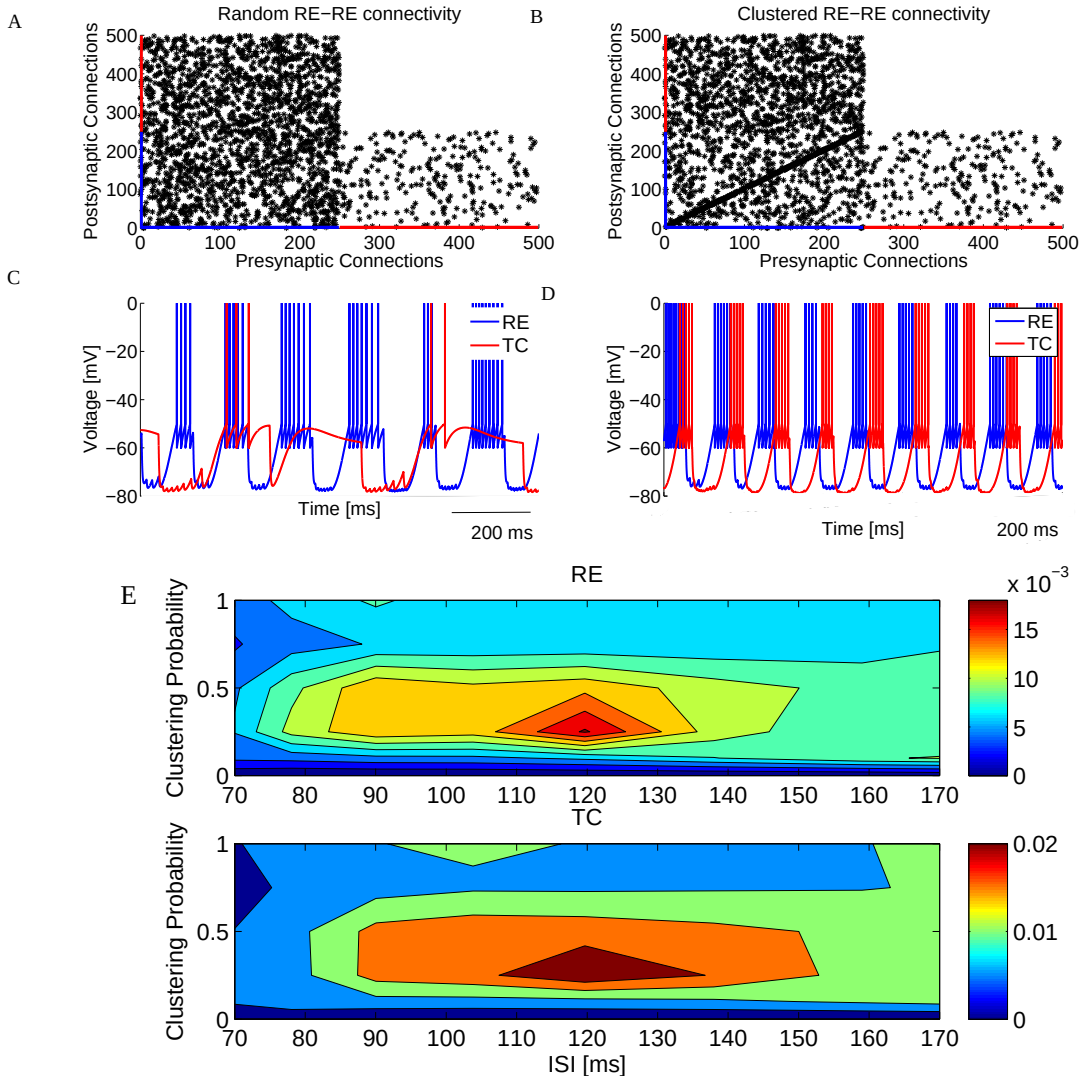


Fig. 3.7 **Spindle activity generated by a full network of TC-RE neurons depending on RE-RE clustering.** (A) Connectivity matrix of a random TC-RE network. The presynaptic neurons are represented in the x axis and the postsynaptic neurons in the y axis. The network is made of 500 neurons, of which the first 250 are RE neurons and the remaining ones are TC neurons. (B) Connectivity matrix in the presence of RE-RE clustering (rewiring probability $RP = 0.25$) (C) Membrane voltage dynamics of a couple of arbitrarily chosen TC and RE neurons in the case of random network. (D) Membrane voltage dynamics of a couple of arbitrarily chosen TC and RE neurons in the presence of clustering: evidence of typical spindle oscillations. (E) ISI distribution (color-coded) as a function of the rewiring probability for RE (left) and TC (right) neurons. The synaptic strengths are respectively: $g_{RE\to TC} = 300\ \mu$S, $g_{TC\to RE} = 200\ \mu$S and $g_{RE\to RE} = 300\ \mu$S.

switch from sleep to awake state (Livingstone and Hubel, 1981; Steriade and McCarley, 2005; Steriade et al., 1993). Given the nonlinear relation between input and output in the bursting mode (Sherman, 2001), we expect to see a change in the firing rate trend of TC neurons (the neurons that project to the cortex) only when the network goes from bursting to tonic, through which the firing rate should increase with the input. Figure 3.8A shows the firing rate of TC (red) and RE (blue) neurons for increasing external sensory input on TC neurons. The case of input $S = 0$ spikes/s corresponds to the self-sustained condition discussed above. By increasing the input amplitude, the network displays a transition in the firing rate of TC neurons at around $S = 50$ spikes/s, after which the response of the thalamus increases sub-linearly with the external input. We interpret this as an indication of the switch from a purely bursting mode to a temporally irregular state. Note that the driver of this transition is the response of the recurrent activity to the external sensory input, since we do not change the intrinsic parameters of the model.

In order to explore this scenario further, we calculate the ISI distribution of RE and TC neurons by averaging over 100 trials for each different stimulus $S$. The RE neurons are the most insensitive to increasing external input, as can be seen in Figure 3.8B. On the other hand the fraction of TC neurons displaying a large inter-burst ISI decreased as the stimulus intensity surpasses a critical value (going from region S1 to region S2 in Figure 3.8A), and a corresponding increase of the intra-burst ISI peak approaching the refractory period (2.5 ms). We classify this as a further signature of a transition between a bursting mode and an irregular firing regime.

Next we calculate the information about the stimuli carried by the firing rates of the TC and RE neurons in the two different regimes. To that end we use the mutual information (see Section A.4 in Appendix A), which quantifies the reduction of the uncertainty in predicting the applied stimulus given a single observation of the triggered response. Here we estimate the mutual information $I(\mathbf{FR}, S)$ between the set of stimuli $S$ given by the external Poisson inputs with different rates and the response **FR**, firing rate. Given that we were interested in how the specific neurons encode and carry information, in this case we have selected as response the average firing rate **FR** over the whole stimulation. We have considered as stimuli different inputs with increasing amplitude (from 0 to 150 spikes/s) impinging on TC neurons. This measure allows us to evaluate how well the firing rate $\mathbf{r}$ of both type of neurons (namely TCs and REs) encodes the stimulus $s$.

Figure 3.8C compares $I(S1; FR)$ and $I(S2; FR)$ between the firing rates of TC (red) and RE (blue) neurons and the set of stimuli $S1$ and $S2$, where $S1$ ranges between 0 and 50 spikes/s, while $S2$ varies from 60 to 150 spikes/s, corresponding to the two dynamical regimes of Figure 3.8A. The figure clearly shows that in the bursting mode both the RE and TC neurons

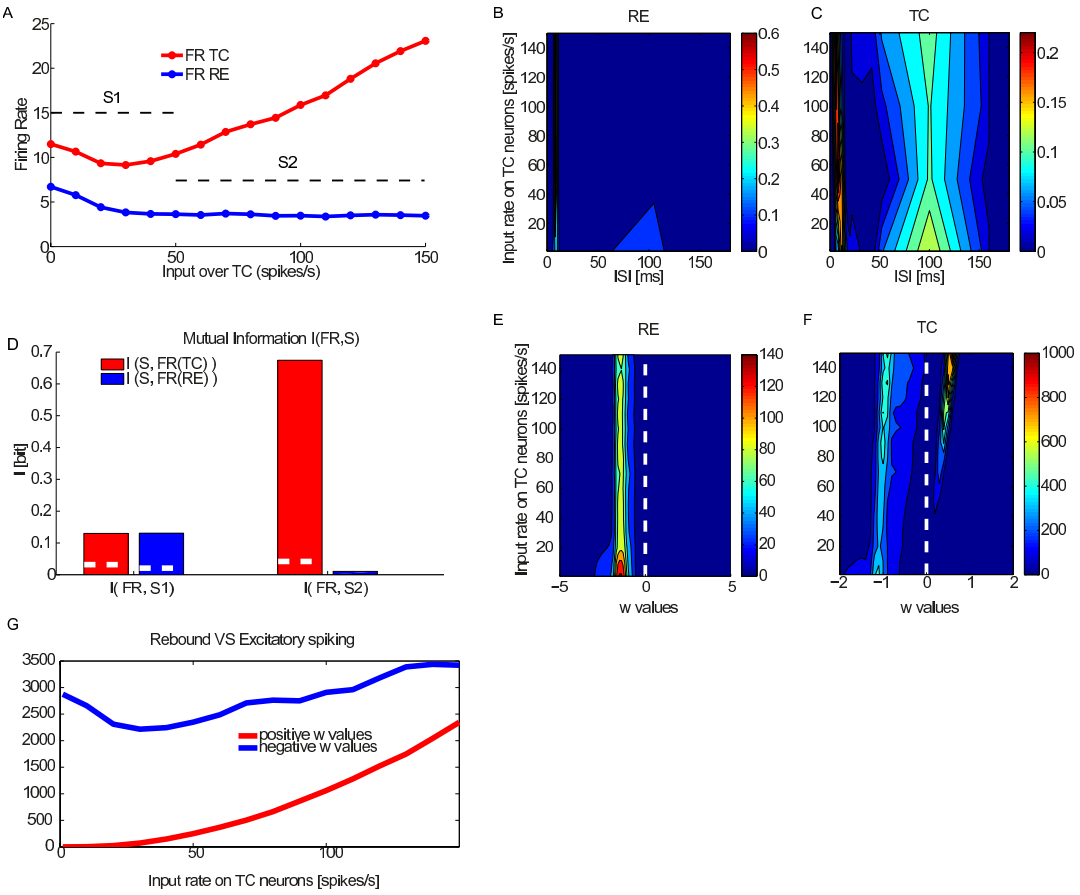


Fig. 3.8 **Bursting and tonic modes displayed by a TC-RE network with RE-RE clustering as a function of external input on TC neurons.** (A) Firing rate of TC (red) and RE (blue) neurons as a function of external driving input impinging on TC neurons. (B,C) ISI distribution as a function of external driving input on TC neurons of RE (B) and TC (C) neurons. (D) Mutual Information between the set of increasing external stimulus (0-150 spikes/s) and the neural response given by the firing rate of TC and RE neurons. Different external sensory inputs are considered for the two regimes, following panel A: 0-50 spikes/s for the bursting mode and 60-150 spikes/s for the tonic mode. The white dashed line in the bar plots refers to significance threshold ($p < 0.05$, bootstrap test). The measures are averaged over 100 trials for each external stimulus. (E,F) Adaptation variable $w$ of RE (E) and TC (F) neurons (color coded) as a function of the external input on TC neurons, averaged across 100 trials for each external stimulus. (G) Number of positive $w$ values (depolarizing events) and negative $w$ values (rebound events) of TC neurons. The synaptic strengths are respectively: $g_{RE\to TC} = 300\ \mu$S, $g_{TC\to RE} = 200\ \mu$S and $g_{RE\to RE} = 300\ \mu$S.

carry a lower information (0.13 bit, $p < 0.05$: bootstrap test), in comparison with the information encoded by TC neurons during the tonic mode ($\approx 0.7$ bit, $p < 0.05$: bootstrap test). RE neurons during the tonic mode do not encode significant information, in fact their firing rate decreases with respect to the bursting regime and after that remains constant for all inputs. These results show that the information about the stimulus that the thalamus carries (and is then potentially able to convey to the cortex) is much higher in the tonic mode, since in that regime spontaneous activity is enhanced and this contributes to keeping an almost linear relation between input and output and thus to minimizing rectification of the response (Sherman, 2001).

In order to further interpret this transition, we examine the nature of each TC and RE spike by checking the sign of the adaptation variable $w$ at the spiking time of each neuron. A positive value of $w$ indicates that neuron fires via a depolarizing input (see Figure 3.1), while if negative we classify it is as a rebound spike. Figure 3.8E shows that RE neurons spike mostly due to a rebound in response to hyperpolarizing inputs (coming only from internal RE-RE clustered connections) for all the range of sensory input over TC neurons. TC neurons, in turn, also fire mainly in response to incoming hyperpolarizing currents (in this case coming from RE neurons) during the burst mode (Figure 3.8F), and after the transition from bursting to tonic mode a fraction of the spikes occur in response to depolarizing external inputs. Thus the transition occurring at around $S = 50$ spikes/s, shown in Figure 3.8A, underlies a shift in the spiking mechanism profile. This is confirmed in Figure 3.8G, which shows a quantitative estimation of the effective number of excitatory-driven spikes (blue) and inhibitory-rebound spikes (red) as the external input increases.

So far we have considered a thalamic network receiving an external sensory input impinging on TC neurons. We complete the picture including also a corticothalamic input (Destexhe, 2000) projecting to RE neurons. Figure 3.9A shows that the transition dynamics is not altered by the addition of a constant input from the cortex, which results only on an increase of the firing rate for both kind of neurons. The appearance and the increase of depolarization spikes occur for similar levels of inputs (Figure 3.9B). The amount of information carried by RE and TC neurons in the two different regimes is relatively unaltered (Figure 3.9C,D), supporting the hypothesis that the information carried by projecting neurons during the tonic mode is higher than in the bursting mode. Interestingly, by increasing the amplitude of the cortical input on RE (from 1000 to 2000 spikes/s), the information encoded by TC neurons is increased for the tonic mode (from 0.6 to 0.66 bits, $p < 0.05$, bootstrap test) (Figure 3.9D).

This result highlights the role of the intrinsic rebound bursting properties of TC neurons, which are essential in the generation of the spindle rhythm. They could also reinforce the role of corticothalamic feedback in information processing, for instance by recruiting TC neurons

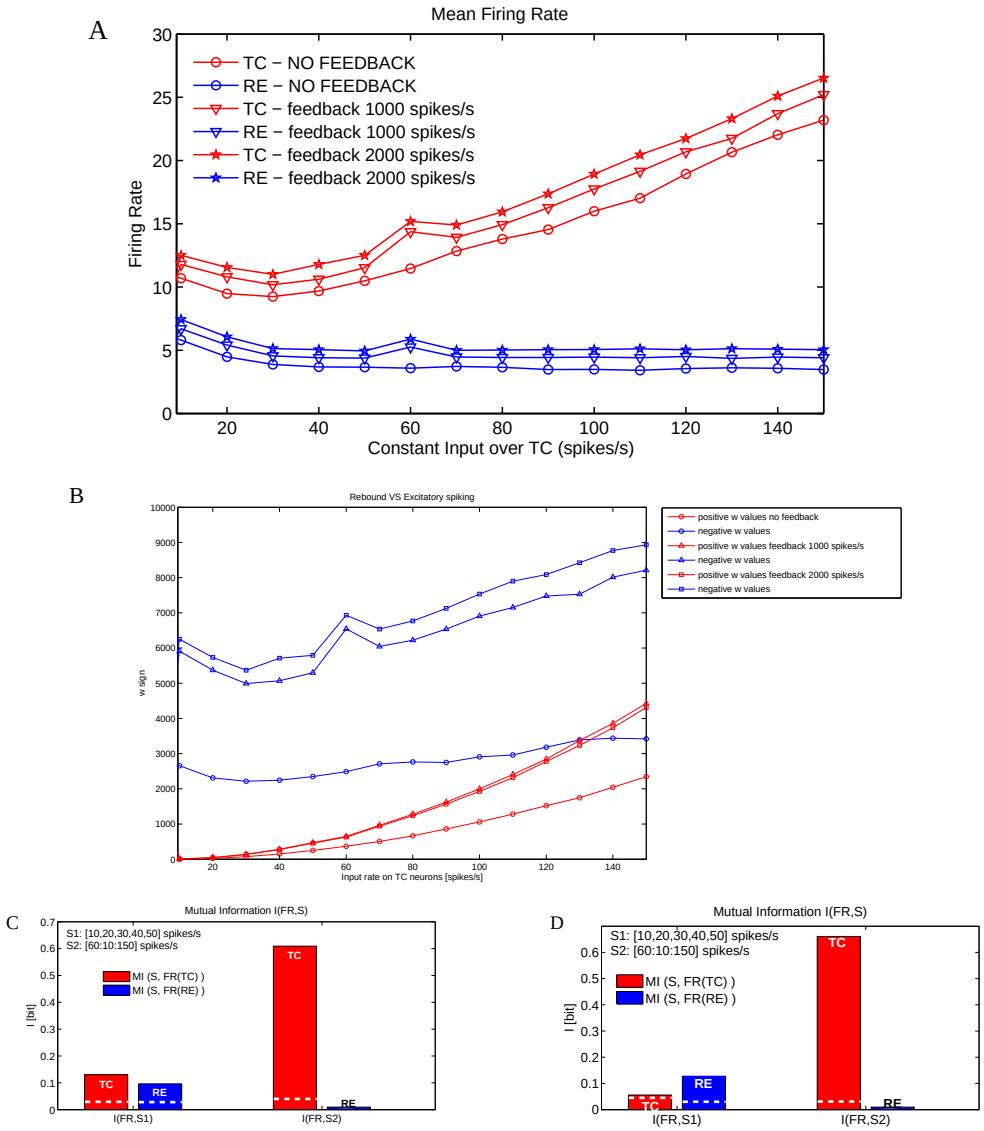


Fig. 3.9 **Bursting and tonic modes displayed by the TC-RE network with RE-RE clustering as a function of external input on TC neurons for different corticothalamic inputs.** (A) Firing rate of TC (red) and RE (blue) neurons as a function of the external driving input impinging on TC neurons for different corticothalamic input amplitudes. (B) Number of positive (depolarizing, red) and negative (rebound, blue) $w$ values of TC spikes for different corticothalamic inputs. The $w$ values are averaged across 100 trials for each external stimulus. (C,D) Mutual Information carried by the firing rate of TC (red) and RE (blue) neurons with a cortico-thalamic input of (C) 1000 spikes/s and (D) 2000 spikes/s. I is calculated between the set of increasing sensory stimuli ($10-150$ spikes/s) and the neural response given by the firing rate. The white dashed lines in the bars refer to the significance threshold ($p < 0.05$, bootstrap test). Measures are averaged over 100 trials for each external stimulus. The synaptic strengths are respectively: $g_{RE\to TC} = 300\ \mu$S, $g_{TC\to RE} = 200\ \mu$S and $g_{RE\to RE} = 300\ \mu$S.

through inhibition and thus modulating TC firing rate (Destexhe, 2000). To support the importance of rebound bursting properties of TC neurons, we plot in Figure 3.10 the firing rate of TC and RE neurons, the ISI distribution and the $w$ distribution at a fixed rate of external sensory input on TC neurons (150 spikes/s), for different levels of cortical input.

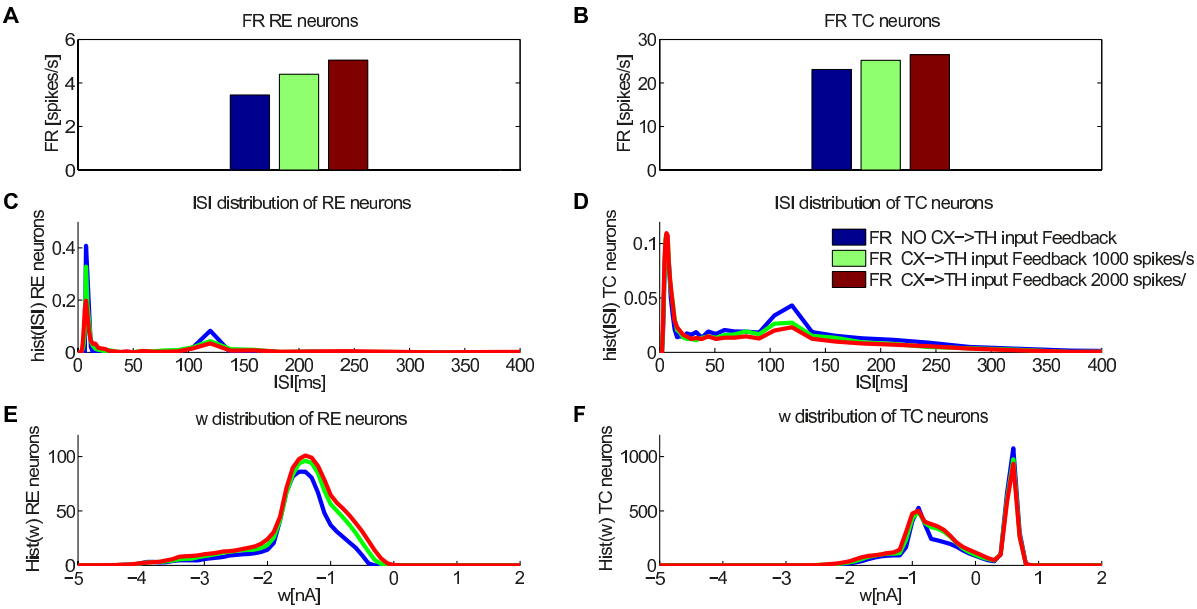


Fig. 3.10 **Influence of corticothalamic input on a full TC-RE network.** (A) Firing rate, (B) ISI distribution, and (C) distribution of the adaptation variable $w$ of RE and TC neurons as a function of corticothalamic input. The external sensory input it set to 150 spikes/s. The synaptic strengths are respectively: $g_{RE\to TC} = 300\ \mu$S, $g_{TC\to RE} = 200\ \mu$S and $g_{RE\to RE} = 300\ \mu$S. Bars colors in panels (A) and (B) coincide with the lines colors in the other panels.

## 3.4 Conclusion

In this Chapter we have presented an adaptive exponential integrate-and-fire (aEIF) network model that is able to reproduce the spindle oscillations and the transition between a stimulus-insensitive and a stimulus-sensitive state of the thalamus. In agreement with experimental observations based on direct optogenetic stimulation (Halassa et al., 2014), spindle oscillations are generated in our model by RE activation leading to TC bursts as rebound from inhibition. Our results suggest that (i) a critical value of RE-RE clustering favors the presence of large-scale spindle oscillations, (ii) for external stimuli below a given threshold the network is in a purely rebound-bursting state insensitive to external stimuli, while (iii) when this threshold

is crossed there is a non-zero contribution of the spikes due to depolarization, and this makes the TC neurons (and not the RE neurons) of the network sensitive to the stimulus intensity coherently with experimental observation. These conclusions hold in the presence of cortical inputs impinging on the reticular neurons.

A recent computational paper (Willis et al., 2015) investigated the role of TC-RE interactions from a perspective complementary to the one discussed in this Chapter, using a Hodgkin-Huxley model much more detailed than the aEIF adopted here, and limiting the investigation only to minimal loops such as those we described in Section 3.3.2 and 3.3.3 (Figure 3.2). Notwithstanding the higher realism of their model, the functional properties at the single-neuron level are similar to those described here (compare our Figure 3.1 with Figure 1 of their paper). Moreover, Willis et al. (2015) highlighted the fact that open-loops between TC and RE neurons might play a functional role in the thalamus, and indeed in our full network (Figure 3.7 and following) both open and closed TC-RE loops are taken into account. In a recent paper (Lewis et al., 2015b), Brown and collaborators stimulated optogenetically RE neurons, simultaneously recording from them. They found that the majority of those neurons ($10/17$) decreased significantly their firing rate, and only a minority of them ($4/17$) displayed a significant increase. At the same time they found that the activity of the TC neurons was inhibited, with functional consequences on the cortex. The interpretation of the authors was that a small increase in RE activity was sufficient to inhibit TC activity. Our model offers a simpler explanation: since most TC neurons fire due to hyperpolarization rebound, a decrease in RE activity can be associated to a decrease in TC firing (see Figure 3.9). Indeed, stimulating RE neurons has been shown to alter the temporal structure of TC neuron firing, without changing their average firing rate (Halassa et al., 2014).

Our model reproduces qualitative features of experimental observations, and provides a mechanism to explain the factors that contribute to the gating role of the thalamus in the processing of sensory information toward the cortex. A future model will include the cortex (see Perspectives section 7.5), thus it will be possible to explore the role of thalamocortical circuits in the switch between the two dynamical modes that account for different behavioral states and transmission of information dynamics. These thalamocortical circuits are made of bidirectional excitatory projections between thalamus and cortex and inhibitory interactions given by collaterals of ascending and descending fibers to GABAergic neurons (RE neurons). The latter inhibitory circuits are essential to explain large-scale synchronization of thalamocortical oscillations. To this regard, in the next Chapter, we will study how two neuronal populations, which are bidirectionally coupled through long-range excitatory projections and oscillate in the gamma range due to internal inhibitory circuits, engage in large scale oscillatory synchro-

nization, thus providing a system by which information can be transmitted efficiently even at long distances.

# Chapter 4

# Phase-coherence transitions and communication in the gamma band between delay-coupled neuronal populations

Spatiotemporal coordination of functional neural assemblies could subserve information processing. In the previous Chapter we have described the mechanisms responsible for the generation of thalamic spindle oscillations during slow-wave sleep, revealing that the temporal coordination between TC and RE neurons is essential, and how changes in dynamical organization patterns in the thalamus underlie a switch from sleep to the awake state, resulting in different information-processing capabilities. This Chapter addresses the general question of how communication is established between physically separate brain areas, using neuronal oscillations as information carriers. In particular, we examine whether and how effective communication between cortical areas arises even when the time taken by neuronal signals to go from one area to another is comparable, or larger than, the typical time scales of the underlying neuronal networks. To do so, we use a biophysically realistic computational model of two synaptically coupled neuronal populations working in a collective gamma regime. The Chapter is structured as follows. In Section 4.1 we focus on the importance of the spatiotemporal coordination of the activities of coupled neuronal populations (modeled as described in Section 4.2) as introduced in Section 1.3, and in particular we describe the dynamics of populations of HH neurons oscillating in the gamma range involved in this coupling (Section 4.3). Then we report how these two populations can synchronize with instantaneous coupling (Section 4.4) and in presence of large axonal delays (Section 4.5) by means of phase coherence measures. In Section 4.6 we use information theory to quantify the information exchanged between the two networks for different transmission delays and external inputs. Finally in Section 4.7 we summarize the main achievements of this study. These results have been reported in Barardi et al. (2014b).

## 4.1 Oscillatory-based coordination of coupled neuronal populations

In Section 1.3 we emphasized that brain function emerges from the collective dynamics of coupled neurons, the structural connectivity among which enables correlations between their firing activities. As a result of these correlations, effective neuronal networks function collectively on a mesoscopic scale, comprising thousands of coupled neurons that operate together, giving rise to emergent behavior. In awake animals, this collective dynamics takes the form of recurrent series of high and low network activity, corresponding with repetitive epochs of increased excitation over inhibition followed by boosts of inhibition. This leads to the appearance of rhythmicity at certain frequency bands. As introduced in Section 1.3.3, oscillations in the gamma-band (30 Hz−90 Hz) are observed in several cortical areas in relation with cognitive tasks (Buzsáki and Wang, 2012).

Synchronized oscillations can increase the functional connectivity between neural assemblies by coherently coordinating their firing dynamics. This hypothesis, known as communication through coherence (CTC), was proposed (Fries, 2005) as a mechanism by which gamma-band synchronization could regulate routing of information between brain areas (see Section 1.3.4). Since neuronal oscillations are associated with the dynamics of the excitatory-inhibitory balance, they represent periodic modulations of the excitability of neurons, which are more likely to spike within specific time windows (i.e. when inhibition is low). If two neuronal populations oscillate with a constant phase difference, then an effective transmission of information between the two groups of neurons is achieved provided the spikes sent by a population reach systematically the other population at the peaks of excitability. In that way, modulation of the relative phases of the emerging rhythms might dynamically generate functional cell assemblies (Fries et al., 2002a, 2008; Womelsdorf et al., 2006).

A key requirement of the CTC mechanism is the existence of a constant phase difference between the two neuronal networks that reliably allows their binding, favoring communication. This coordination can be expected to arise from the synaptic coupling between the neurons of the two populations. But this coupling is not instantaneous, since propagation times between different cortical regions can reach up to several tens of milliseconds (Ringo et al., 1994). Previous CTC studies have mainly concentrated on describing the dependence of the coherence on the phase lag between the neuronal populations (Buehlmann and Deco, 2010; Fries, 2005; Womelsdorf et al., 2006), without examining systematically the relationship between the actual coupling delay and the phase lag at which the coherence is maximal. In fact, coupled nonlinear oscillators are known to adjust their phases upon frequency locking, leading under certain conditions to either in-phase (zero phase lag) or anti-phase synchronization ($\pi$-

phase lag) (Pikovsky et al., 2003). Anti-phase patterns in cortical networks, for instance, have been widely studied (Li and Zhou, 2011). Zero-lag synchronization, in turn, has been experimentally observed between gamma oscillations emerging from separated brain areas (Castelo-Branco et al., 1998; Engel et al., 1991; Frien et al., 1994; Gross et al., 2004; Roelfsema et al., 1997). The conditions leading to zero-lag synchronization in neuronal oscillations are however somewhat stringent, requiring non-trivial spiking dynamics (Traub et al., 1996) or complex network architectures (Bibbig et al., 2002; Vicente et al., 2008). In particular, zero-lag synchronization between two cortical areas has been shown to be possible even with long axonal delays (Vicente et al., 2008; Viriyopase et al., 2012), provided the two areas interact through a third oscillator (Fischer et al., 2006), which could correspond to the thalamus (Gollo et al., 2010; Theyel et al., 2010) (see Section 1.3.2).

But in contrast with most nonlinear oscillators, neuronal populations are highly complex, since they contain a very large number of degrees of freedom (corresponding to the individual neurons), their oscillations are a pure collective phenomenon (the individual neurons in the population do not oscillate), and they operate in a broad frequency range. Additionally, neuronal populations are connected by a large number of axons, and inhomogeneities in the properties of those axons affect differentially the propagation speed of action potentials and lead to a wide spectrum of axonal delays rather than a uniform distribution (Aboitiz et al., 1992). It thus becomes necessary to study systematically (i) the conditions under which two such complex oscillators synchronize (i.e. lock their frequencies), (ii) what is the resulting phase difference between them, how does this phase difference relate with the coupling delay (and with the frequency band being considered), and (iii) how is the efficiency of the communication between the two cortical areas affected by the delayed coupling.

As mentioned above, within the CTC scenario effective communication arises when spikes from the emitting neuronal population reach the receiver population during the windows of maximum excitability. For this to happen two conditions have to be met: (1) the two coupled oscillators should be frequency locked, and (2) the transmission delay, the oscillation frequency, and the phase difference between the two oscillations should match. In particular, if the networks and the inter-connectivity are symmetric the second condition should hold in the two directions of spike propagation. The time delay (or rather, the distribution of time delays) is fixed as given by the anatomical connectivity. Therefore, it is the frequency of the oscillation spectrum what determines the particular phase lag that meets the matching condition. We investigate whether this condition only occurs at specific rhythms, or if it holds at all frequencies. To do so, we implement a conductance-based network model based on the single-neuron HH model described in Section 2.1.3 (Barardi et al., 2014b).

## 4.2 Network model of Hodgkin-Huxley conductance-based neurons

We consider two populations of 2000 neurons, 80% of which are excitatory while the remaining 20% are inhibitory (Soriano et al., 2008). Each neuron connects on average with 200 other cells through only chemical synapses. The structural connectivity is built according with the Watts-Strogatz small-world algorithm (Watts and Strogatz, 1998). The rewiring probability $r_p$ is set to 0.5, so that the connectivity shows a certain degree of clustering, which favors the connections between neighboring neurons (see the definition of clustering coefficient in Appendix A.5). Coupling between the two networks is mediated by 60% of the neurons of one population making random long-range excitatory projections with 10% of the neurons belonging to the other population. Here we assume that the connectivity within a network is 2-fold the connectivity across networks, neglecting heterogeneity across neurons. Moreover, in order to obtain a certain amount of phase coherence between the two networks, we consider that the majority of excitatory neurons project onto the other network. A stronger (weaker) coupling will lead to unrealistically higher (lower) phase coherence values (Womelsdorf et al., 2007). We introduce a synaptic transmission delay within and among the networks, assuming that internal delays (taken from a gamma distribution whose scale and shape parameters are fixed to 1) are smaller than the inter-area delays. The axonal delays, termed $\tau_{axo}$, stand for the time between the generation of a spike in a presynaptic neuron from one network and the elicitation of a postsynaptic potential in the other network. These delays are taken from a gamma distribution whose mean and variance increase with increasing $\tau_{axo}$. We choose the scale parameter of the distribution equal to unity, so that the shape parameter equals $\tau_{axo}$. In this way the coefficient of variation (CV) decreases for increasing mean as $1/\sqrt{\text{mean}}$. In our analysis we systematically vary $\tau_{axo}$ between 0 ms and 30 ms. Both inhibitory and excitatory neurons were modeled as HH neurons. The dynamics of the membrane voltage of the single neuron are given by Equation (2.9) introduced in Chapter 2.1.3. The equation of the membrane potential of i-th neuron embedded in a neuronal network has the following form:

$$C\frac{dV_i}{dt} = -g_{Na}m^3h(V_i(t)-E_{Na}) - g_k n^4(V_i(t)-E_k) + -g_L(V_i(t)-E_L) + I^i_{tot}(t), \qquad (4.1)$$

where $C = 0.25$ nF (0.50 nF) is the membrane capacitance for inhibitory (excitatory) neurons, the constants $g_{Na} = 12.5$ $\mu$S, $g_K = 4.74$ $\mu$S, and $g_L = 0.025$ $\mu$S are the maximal conductances of the sodium, potassium, and leakage channels, respectively, and $E_{Na} = 40$ mV, $E_K = -80$ mV, and $E_L = -65$ mV stand for the corresponding reversal potentials. The equations describing the voltage-gated ion channels have been introduced in Section 2.1.3. In

Equation (4.1), $I_{i,tot}$ is the total synaptic input current and is given by the sum of all the synaptic inputs entering the i-th neuron:

$$I_{i,tot}(t) = \sum_{N_{i,AMPArec}} I_{i,AMPArec}(t) + \sum_{N_{i,GABA}} I_{i,GABA}(t) + I^{i}_{AMPAext}(t), \tag{4.2}$$

the value of $N_{i,AMPArec}$ (respectively $N_{i,GABA}$) being the set of excitatory (respectively inhibitory) neurons projecting into the i-th neuron, and $I_{i,AMPArec}(t)$, $I_{i,GABA}(t)$, $I_{i,AMPAext}(t)$ the different synaptic inputs entering the i-th neuron from: recurrent AMPA, GABA, and external AMPA synapses respectively. These synaptic input currents $I_{syn}$ depend also on the membrane potential and are defined as (see Section 2.2):

$$I_{syn}(t) = g_{syn} s_{syn}(t)(V(t) - E_{syn}), \tag{4.3}$$

where $g_{syn}$ and $V_{syn}$ are the conductance and the reversal potential of the synapse, respectively. For positive values of $E_{syn}$ the synapse is depolarizing or excitatory ($E_{syn} = 0$ mV for glutamate receptors), otherwise it is hyperpolarizing or inhibitory ($E_{syn} = -70$ mV for GABA receptors). The reference values of reversal potentials and synaptic conductances are displayed in Table 4.2. The values of the parameters $g_{syn}$ in Equation (4.3) are tuned in order to obtain a balance between excitation and inhibition and to maintain the postsynaptic potential (PSP) amplitudes within physiological ranges. All parameters values can be found as well in Gutfreund et al. (1995).

The function $s_{syn}(t)$ describes the time course of the synaptic currents; it depends both on the synapse type and on the kind of neuron receiving the input. Every time a presynaptic spike occurred at time $t^*$, $s_{syn}(t)$ of the postsynaptic neuron is incremented by an amount described by a delayed difference of exponentials (Brunel and Wang, 2003) (see Section 2.2):

$$\Delta s_{syn}(t) = \frac{\tau_m}{\tau_{decay} - \tau_{rise}} \left[ exp\left( -\frac{t - \tau_{axo} - t^*}{\tau_{decay}} \right) - exp\left( -\frac{t - \tau_{axo} - t^*}{\tau_{rise}} \right) \right], \tag{4.4}$$

where $\tau_{decay}$ and $\tau_{rise}$ are the decay and rise synaptic time, respectively, and $\tau_{axo}$ is the latency, drawn from a Gamma distribution and defined above. Their values are shown in Table 4.1.

| Synaptic time constants ( ms) | $\tau_{rise}$ | $\tau_{decay}$ |
|---|---|---|
| AMPA | 0.5 ms | 2 ms |
| GABA | 2 ms | 5 ms |

Table 4.1 Synaptic time constants.

In the Equation (4.2), $I_{AMPAext}$ represents an heterogeneous Poisson train of excitatory presynaptic potentials with a mean event rate that varies following an Ornstein-Uhlenbeck

| Synaptic conductances $g_{syn}$( nS) | |
|---|---|
| GABA on inhibitory | 325 nS |
| GABA on excitatory | 360 nS |
| $AMPA_{recurrent}$ on inhibitory | 4.2 nS |
| $AMPA_{recurrent}$ on excitatory | 4.2 nS |
| $AMPA_{external}$ on inhibitory | 4.2 nS |
| $AMPA_{external}$ on excitatory | 5.5 nS |
| Synaptic reversal potential $E_{syn}$( mV) | |
| $E_{GABA}$ | $-70$ mV |
| $E_{AMPA}$ | 0 mV |

Table 4.2 Synaptic conductances and synaptic reversal potentials.

process (defined as well in Section 3.2). This incoming external current mimics the direct input from any other area external to the network considered here. The instantaneous rate, $\lambda(t)$, of the external excitatory train of spikes is generated according to an Ornstein-Uhlenbeck process, as considered in Mazzoni et al. (2008):

$$\frac{d\lambda}{dt} = -\lambda(t) + \sigma(t)\sqrt{\frac{2}{\tau}}\eta(t) \tag{4.5}$$

where $\sigma(t)$ is the standard deviation of the noisy process and is set to 0.6 spikes/s. $\tau$ is set to 16 ms, leading to a power spectrum for the $\lambda$ time series that is flat up to a cut-off frequency $f = \frac{1}{2\pi\tau} = 9.9$ Hz. $\eta(t)$ is a Gaussian white noise. The model has been integrated using the Heun algorithm (Toral and Colet, 2014), with a time step of 0.05 ms. All simulations represent 2 seconds of activity. The connectivity, initial conditions and noise realization were varied from trial to trial. Further details can be found in Barardi et al. (2014b).

## 4.3 Dynamics of populations of HH neurons

With the model described in the previous Section we represent mathematically two reciprocally connected identical neuronal populations, and study how the heterogeneous axonal delays between the populations affect their synchronization. We characterize the collective dynamics of these populations by means of averaging measures such as the local field potential (LFP) and the multi-unit activity (MUA) (see Appendix A.1). In this Section we focus on the dynamical properties of only one neuronal population.

We consider an isolated population of 2000 neurons, of which 80% are excitatory and 20% are inhibitory. Each neuron forms on average 200 random connections within the network, and all pairs of coupled neurons exhibit a certain time delay, taken from a gamma distribution whose scale and shape parameters are both equal to unity. All neurons receive an

external Poisson-distributed spike train whose instantaneous firing rate follows an Ornstein-Uhlenbeck process with a mean value set to 7300 spikes/s. Excitatory and inhibitory synaptic currents are balanced by compensating the higher number of excitatory neurons (80% of the whole network) with fast spiking by the inhibitory neurons and with strong inhibitory synaptic conductances.

As a consequence, the neurons remain excitable but spent most of their time with a membrane voltage that fluctuates under the firing threshold, occasionally crossing it (Markram et al., 2004). Despite the fact that the neurons fire sparsely and irregularly (see Figure 4.1A), a rhythmicity emerges when considering the dynamics of multiple action potentials elicited by thousands of neurons (Brunel and Wang, 2003). Therefore this network of HH neurons exhibits well-known features of cortical dynamics, namely the coexistence of irregular firing at the single-neuron level with collective rhythmicity at the population level, arising from the synaptic recurrent connections between the excitatory and inhibitory neurons (Brunel and Wang, 2003). These oscillations represent the transient synchronized activity of neuronal assemblies, and can be revealed by population measures such as the LFP (Figure 4.1B) and the MUA (Figure 4.1C). Lower frequency bands contain a strong component arising from the noisy Poissonian distribution of interspike intervals (ISI), which affect the synaptic activation and do not reflect the intrinsic dynamics of the network. On the contrary, higher frequency bands of small amplitude reflect the fast dynamics of the action potentials, also affecting the synapse activation time course. The collective oscillatory dynamics exhibits a prominent gamma rhythm (Figure 4.1D), whose period is mainly determined by the decay time constant of inhibition (Brunel and Wang, 2003; Geisler et al., 2005; Sancristóbal et al., 2013). The gamma rhythm emerges from the periodic changes of the balanced synaptic current, which leads to periodic modulation of the distance to threshold.

Another way of understanding the emergent gamma oscillations is by looking at the coupling between the MUA and the LFP. Since the LFP mainly captures the synaptic currents impinging on the pyramidal neurons (see Appendix A), it is a measure of the excitability of the network. Hence, at those intervals in which inhibition is low (i.e. the inhibitory synaptic current fades away), the probability of firing is high. Due to the recurrent connections between the excitatory and inhibitory neurons, both the initiation and termination of the population bursts occur with a certain periodicity. Here this oscillatory pattern is around $\sim$45 Hz due to the inhibitory decay time constants (Galarreta and Hestrin, 2002). The LFP and MUA are mutually locked to this frequency (Figure 4.2A), and the spikes occur with higher probability close to the troughs of the LFP (i.e. the minimum of inhibition, Figure 4.2B) (Barardi et al., 2014b).

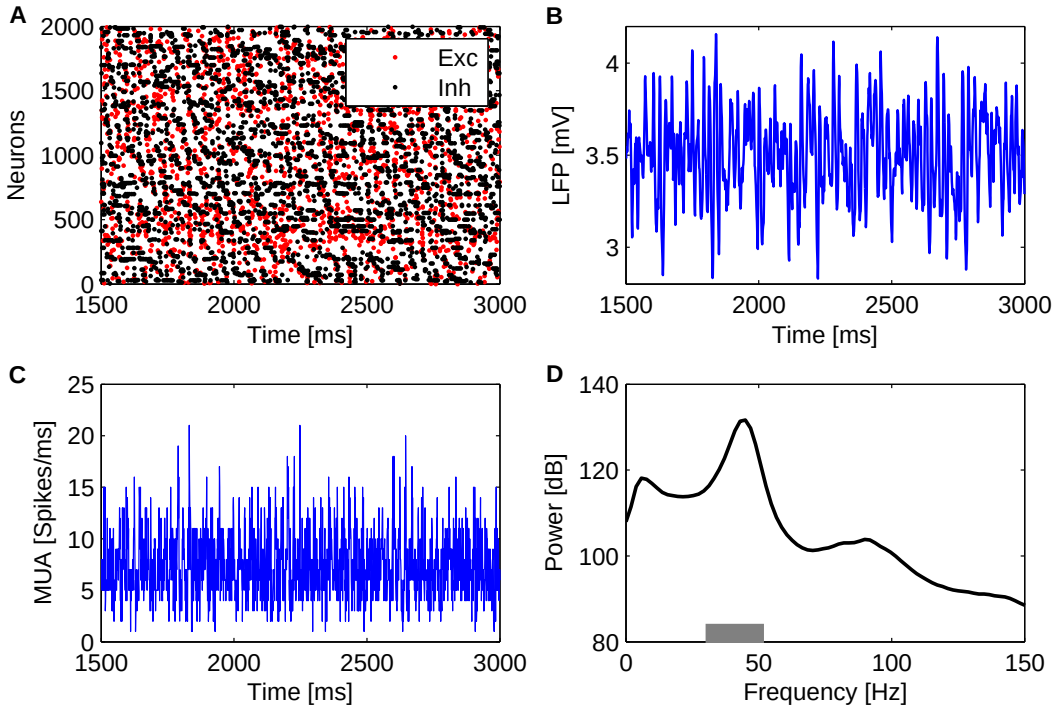


Fig. 4.1 **Collective oscillations of a population of 2000 neurons.** (A) Raster plot of 2000 neurons (in red the excitatory and in black the inhibitory neurons) for a 1500-ms interval. (B) LFP time trace in a 1500-ms interval for an external mean rate of 7300 spikes/s. (C) MUA signal calculated counting the number of spikes of the neural population per unit time. (D) LFP power spectrum calculated using the Welch method averaged over 200 trials. The gray horizontal bar delimits the gamma peak band (30 Hz−52 Hz). From Barardi et al. (2014b).

## 4.4 In-phase synchronization of collective oscillations under instantaneous coupling

We next consider two bidirectionally coupled neuronal networks of the type described above. Connections between the two areas are excitatory: 60% of the excitatory neurons of each network project randomly to 10% of the neurons belonging to the other pool. Although these parameter values cannot be generalized to any two separate brain areas, for which the specific connectivity might determine their interaction, it is known that the probability of connection decays with distance (Boucsein et al., 2011; Kaiser et al., 2009; van Pelt and van Ooyen, 2013). Here we assume that the connectivity within a network is 2-fold the connectivity across networks, neglecting heterogeneity across neurons. Moreover, in order to obtain a certain amount of phase coherence between the two networks, we consider that the majority of excitatory neurons project onto the other network. A stronger (weaker) coupling will lead to unrealistically

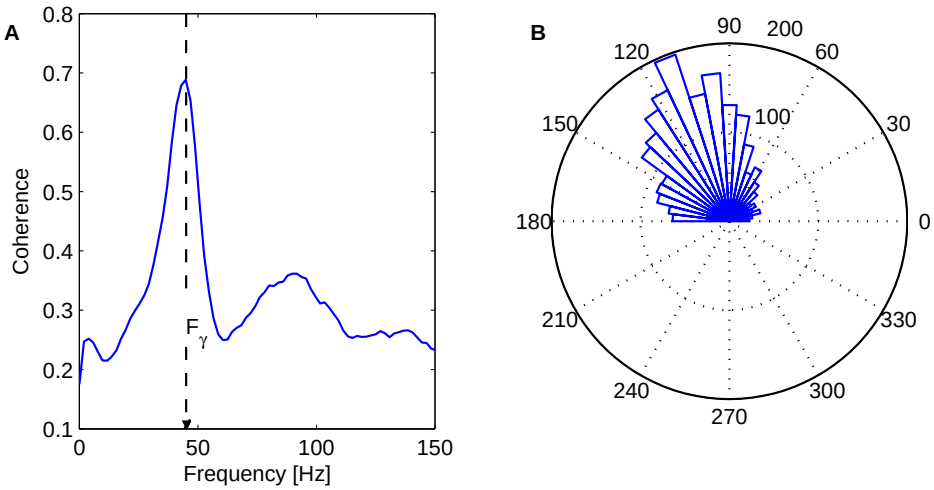


Fig. 4.2 **Phase locking between LFP and MUA of a network.** (A) LFP-MUA phase coherence for a single population. (B) Angle histogram of the phase difference between the LFP and MUA. The measures are averaged over 200 trials. From Barardi et al. (2014b).

higher (lower) phase coherence values (Womelsdorf et al., 2007). We introduce time delays in the coupling between networks, assuming that the inter-areal delays are larger than the intra-areal delays due to long-range connections. We also consider that the inter-areal delays are distributed heterogeneously across the system (Aboitiz et al., 1992), following a gamma distribution whose mean and variance increase systematically with the mean delay (Vicente et al., 2008). This accounts for the variability of transmission delays through axons with heterogeneous properties (see Section 4.2 for the definition of the gamma distribution parameters). The mean inter-areal delay shown in the figures, hereafter termed $\tau_{axo}$, accounts for the latency between the generation of a spike in a presynaptic neuron from one network and the elicitation of a postsynaptic potential in the other network.

When coupled, the LFP power spectra of the two networks show the same gamma profile as in the absence of coupling (Figure 4.3), while the corresponding time series exhibit a substantial degree of correlation (Figure 4.4A inset). We next ask whether the broad spectrum of these neuronal oscillations allows for partial phase coherence to arise in specific frequency regions. Our phase coherence measure, described in the Appendix A.3, quantifies between 0 and 1 the reliability of the phase difference $\Delta\phi$ between pairs of oscillations, at a given frequency. Figure 4.4B shows the phase coherence between the LFPs of the two populations for instantaneous coupling ($\tau_{axo} = 0$ ms). According to the regions of statistical significance observed experimentally (Womelsdorf et al., 2007), we considered phase coherence values above 0.08, which mainly occurs within the gamma band around the peak of the LFP power spectrum (horizontal gray bar in Figure 4.4B). This threshold corresponds to around four times

the average phase coherence of the uncoupled case (see Appendix A.3 and black dashed line in Figure 4.3B).

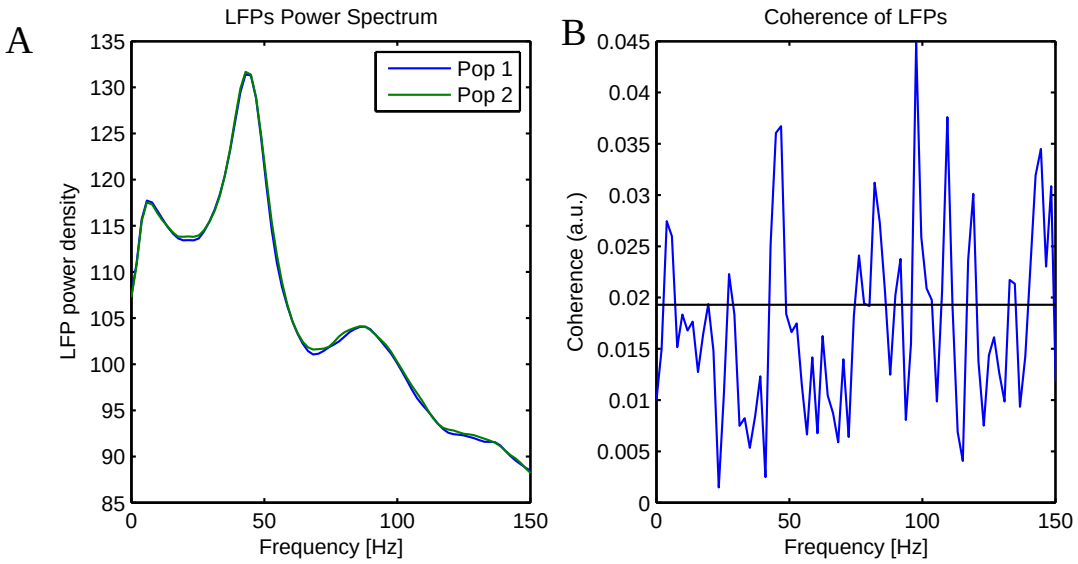


Fig. 4.3 **Phase coherence of the uncoupled neuronal populations.** (A) Power spectral density of the two isolated neuronal populations of HH neurons. (B) Phase coherence between LFPs of the two neuronal populations. The measures are averaged over 200 trials. In order to consider the frequency bias in the phase coherence we computed this measure in the absence of coupling. Due to the finite number of trials considered, the phase coherence is not perfectly zero. Panel B shows random fluctuations with no specific bias for any given frequency. The threshold of phase coherence chosen (namely 0.08) corresponds to around four times the average phase coherence of the uncoupled case.

We also compute the time lag $\tau_{lag}$ between the two signals (i.e. the time shift separating two equal phases of the coupled LFPs arising from each population) for all frequencies (Figure 4.4C), still in the case $\tau_{axo} = 0$ ms. This time lag is only meaningful for significant phase coherence values that lead to a consistent $\Delta\phi$ across trials (red crosses in Figure 4.4B). The figure shows that for frequencies at which the phase coherence is significant, the LFP gamma rhythms of the two populations oscillate in phase ($\tau_{lag} \approx 0$), i.e. the two LFPs are synchronized at zero lag. The error bars in Figure 4.4B,C represent the standard deviation across trials of phase coherence and $\tau_{lag}$ respectively, and are only shown for the region of significant phase coherence, since outside that region the phase distribution is very broad due to the variability across trials. Even within the significant region the standard deviation of $\tau_{lag}$ can be seen to decrease with increasing values of phase coherence, which confirms the inverse relation between phase coherence and the broadness of the phase distribution (Barardi et al., 2014b).

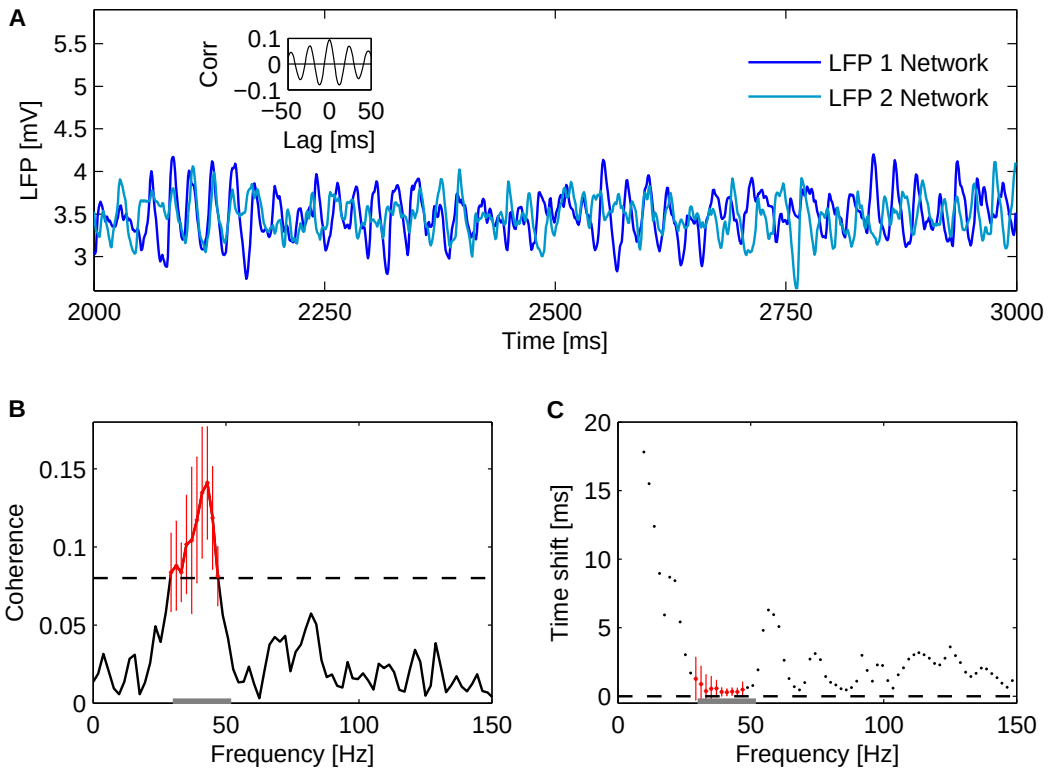


Fig. 4.4 **Collective oscillations of two coupled bidirectionally neural populations.** The inter-areal axonal delay $\tau_{axo}$ between the two neuronal pools is zero. (A) LFP time trace of the two populations in a 1000-ms interval, for an external mean rate of 7300 spikes/s. The inset shows the averaged time correlation of 200 LFP pairs. (B) Phase coherence between the LFPs of the two networks for varying frequency. The measure is averaged over 200 trials. The black dashed line represents the threshold (0.08) above which the phase coherence is considered significant (in red). (C) Time shift between the LFP oscillations of the networks for varying frequency. Red crosses show the time shifts corresponding to the frequencies at which the phase coherence is above threshold. The time shift is calculated as $\tau_{lag} = \Delta\phi/2\pi f_{max}$, where $\Delta\phi$ is the phase difference at the frequency $f_{max}$ of maximum phase coherence. The gray bar delimits the gamma peak band (30 Hz−52 Hz). The measure is averaged over 200 trials. From Barardi et al. (2014b).

## 4.5 Phase-coherence transitions for increasing coupling delay

The fact that the two populations synchronize at zero lag when the coupling delay is zero is to be expected, and we now ask what happens in the presence of time delays. Figure 4.5 shows the phase coherence spectrum between the LFP oscillations for three different values

of $\tau_{axo}$. While the phase coherence is again significant only around the gamma band (Figures 4.5A,C,E), the time traces look very different for small and large delays, with mostly in-phase dynamics for small delays (Figure 4.5B), whereas the populations are mostly in anti-phase for large delays (Figure 4.5F). For intermediate delays, interestingly, two coherence peaks appear (Figure 4.5C), and the corresponding time series exhibit both in-phase and anti-phase episodes (Figure 4.5D). These results indicate that in-phase dynamics seems to persist for non-zero coupling delays, eventually transitioning to an anti-phase regime with smaller, although still significant, phase coherence. Both types of dynamics seem to coexist for intermediate delays. In order to verify these conclusions, we extend the analysis to a range of

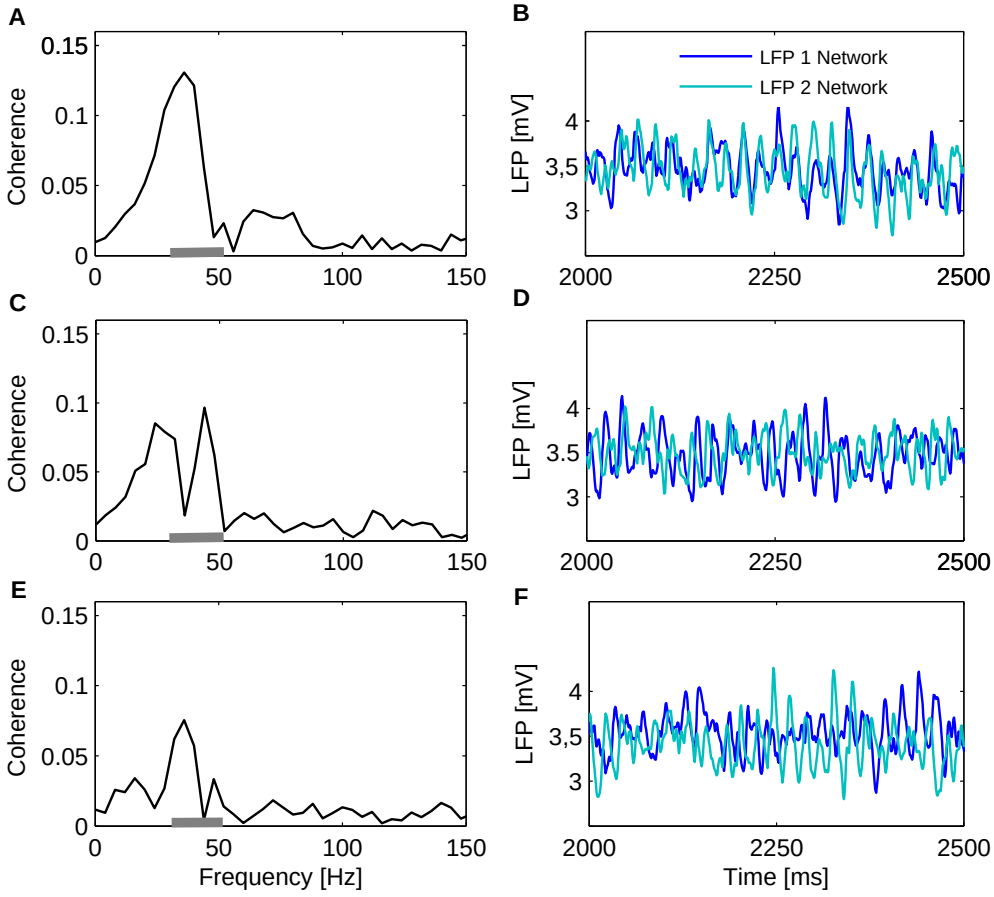


Fig. 4.5 **Phase coherence of two coupled bidirectionally neural populations for three different values of the inter-areal axonal delays $\tau_{axo}$.** Phase coherence spectrum and corresponding representative time series for $\tau_{axo} = 3$ ms (A,B), 9 ms (C,D), and 17 ms (E,F). The inter-areal delays follow a gamma distribution with a mean equal to corresponding inter-areal axonal delay $\tau_{axo}$. The gray bars on the x-axes of plots A, C, and E delimit the gamma peak band (30 Hz−52 Hz). The phase coherence measure is averaged over 200 trials. From Barardi et al. (2014b).

axonal delays, from 0 ms to 30 ms, calculating the phase shift for the frequencies corresponding to both the peak of the power and the phase coherence spectra, termed $f_{max}$. Figure 4.6A shows the value of the frequency at which the power spectrum is maximum, $F_\gamma$, as a function of the coupling delay $\tau_{axo}$. Note that varying $\tau_{axo}$ does not change the frequency peak of the LFP power spectrum, which remains around 45 Hz for all coupling delays. We add a gray bar delimiting the maximum power spectrum range within the gamma band corresponding to the extent of this local peak, highlighting the fact that the LFP gamma rhythm expands over a range of frequencies between approximately $30-52$ Hz.

On the other hand, $\tau_{axo}$ clearly affects the frequency $f_{max}$ at which phase coherence is maximal, as shown by Figure 4.6B. In particular, $f_{max}$ exhibits a discontinuous jump around a coupling delay $\sim 9$ ms, where two peaks of phase coherence coexist (consistent with the result shown in Figure 4.5C). The phase coherence values themselves are shown in color code in Figure 4.6C for different frequencies (vertical axis) and for varying $\tau_{axo}$ (horizontal axis). We superimpose in that plot the line shown in panel A, which marks the maximum of the LFP power spectrum (black dashed line) within the gamma range, $F_\gamma$, as well as the whole extent of the peak (vertical gray bar). The local peaks of phase coherence $f_{max}$ (black lines) corresponding to panel B are also superimposed to Figure 4.6C. For $\tau_{axo} = 0$ ms (as in Figure 4.4) the peak of phase coherence almost coincides with the peak of power spectrum. For increasing $\tau_{axo}$, below 9 ms, only the coherence peak at the lower frequency is significant, whereas between 10 ms and 22 ms only the coherence peak at the faster frequency is above threshold. The transition between these two regimes involves a coexistence of the local coherence peaks. We also observe that in both branches the frequency at which phase coherence is maximum $f_{max}$ decreases with the axonal delay, becoming clearly smaller than the gamma frequency peak $F_\gamma$ (dashed black line in Figure 4.6C). Making $\tau_{axo}$ greater than 22 ms, which approximately matches the period of the power spectrum peak $T_\gamma$ ($1/F_\gamma \approx 22$ ms), a new branch of phase coherence appears, thus leading again to coexistence of the two regimes. This emerging pattern is shown in Figure 4.6C for large inter-areal axonal delays and it is not marked in Figure 4.6B because the phase coherence is under the threshold. Hence, as $\tau_{axo}$ exceeds $T_\gamma$, the scenario of relative phases is repeated but now with cycle skipping.

According to Figure 4.6C, maximum values of phase coherence $f_{max}$ appear at different frequencies for each $\tau_{axo}$. Significant values of phase coherence at a certain frequency can occur provided that there is a certain amount of spikes being simultaneously and reliably sent between the two networks. Since, by construction, the two neuronal pools are identical, the information flow can only be symmetrically transmitted for an in-phase, $\Delta\phi = 0$, and/or an anti-phase, $\Delta\phi = \pi$, relationship between the two LFPs. Therefore, for any $\tau_{axo}$ we can obtain the corresponding $f_{max}$ that satisfies $2\pi\tau_{axo}f_{max} = 0$ or $\pi$. From this expression we can thus

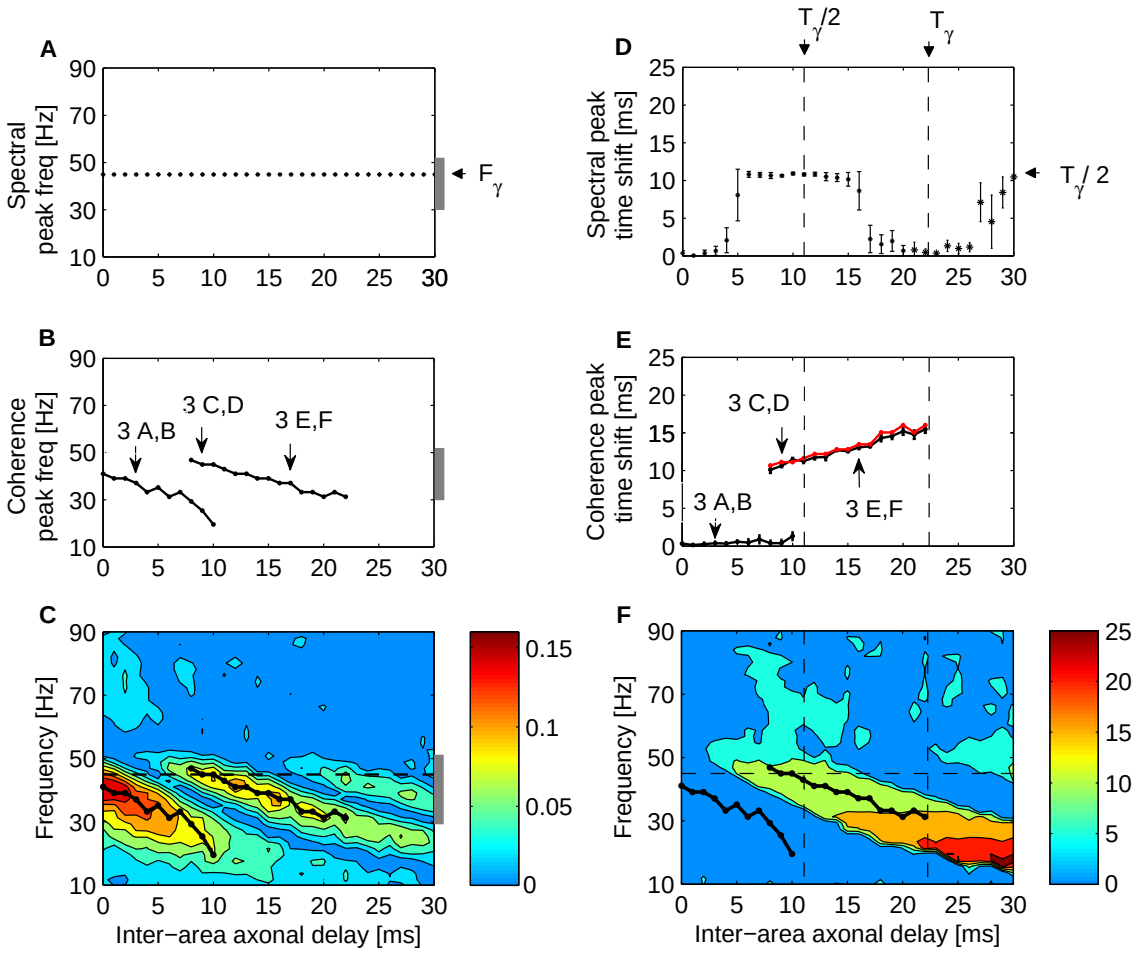


Fig. 4.6 **Phase coherence and time shift behavior in the case of bidirectional symmetric coupling for increasing inter-areal axonal delays $\tau_{axo}$.** (A) Frequency $F_\gamma$(black arrow) at which the power spectrum is maximum and extent of the gamma peak (gray bar) (results for only one population are shown, since they are the same for both populations). (B) Frequencies at which the phase coherence exhibits local maxima, $f_{max}$. (C) Phase coherence, in color code, as a function of frequency (y-axis) and of the inter-areal axonal delay $\tau_{axo}$ (x-axis). (D) Time shift $\tau_{lag}$ at the peak frequency $F_\gamma$ of the power spectrum. (E) Time shift $\tau_{lag}$ at $f_{max}$, the frequencies labeled in (B). The red line corresponds to $1/(2f_{max})$. The labels in panels B and E correspond to panels of Figure 4.5. (F) Time shift $\tau_{lag}$, in color code, as a function of frequency (y-axis) and of the inter-areal axonal delay $\tau_{axo}$ (x-axis). The solid black lines in panels C and F show $f_{max}$ (as in panel B) and the dashed black line represents the power spectrum maximum within the gamma range shown in panel A. In plots A, B, and C the total extent of the gamma peak is displayed as a vertical gray bar. In plot D, the arrows point at the gamma period and half of it, $T_\gamma$ being $1/F_\gamma$. The measures are averaged over 1000 trials for each $\tau_{axo}$. From Barardi et al. (2014b).

expect that a larger $\tau_{axo}$ leads to a smaller $f_{max}$, and that the anti-phase configuration is given by $\tau_{axo}$ equal to half the period corresponding to $f_{max}$ (not to be mistaken with $T_\gamma/2$, half the gamma period and equal to 11 ms).

To verify the aforementioned remarks we next calculate the time shift $\tau_{lag}$ between the two coupled LFPs as $\frac{\Delta\phi}{2\pi f}$. Figure 4.6D shows that, at the peak of the LFP power spectrum (here $f = F_\gamma$), $\tau_{lag}$ is zero for low (0 ms $\leq \tau_{axo} \leq$ 5 ms) and large delays (17 ms $\leq \tau_{axo} \leq$ 26 ms). On the other hand, for intermediate (6 ms $\leq \tau_{axo} \leq$ 16 ms) and large delays ($\tau_{axo} \geq$ 27 ms) $\tau_{lag}$ corresponds to half the period of the gamma rhythm ($T_\gamma/2 = 1/(2F_\gamma) \approx 11$ ms). As mentioned before (see Figure 4.2), at frequency $F_\gamma$ the MUA and the LFP in each population are frequency locked. Therefore, for any axonal delay, the presynaptic spikes arrive within the troughs of the postsynaptic LFP. We can interpret these sharp transitions from in-phase to anti-phase oscillations, appearing with a periodicity given by $T_\gamma$, as the way by which the system keeps the symmetry for any $\tau_{axo}$.

Since the maximum of phase coherence $f_{max}$ does not coincide with $F_\gamma$, we also obtain $\tau_{lag}$ along the peaks of phase coherence. Figure 4.6E confirms that only two patterns arise: in-phase and anti-phase, which can simultaneously occur in the region between 9 ms and 10 ms. The lowest frequency branch corresponds to $\tau_{lag} \approx 0$ ms, and thus to zero-lag synchronization. On the other hand, the highest frequency branch corresponds to a $\tau_{lag}$ value that matches half the period of the corresponding frequency, i.e. $1/(2f_{max})$ (labeled by a red line in the plot), and thus corresponds to anti-phase synchronization.

The full values of the time shift for all frequencies are shown in color code in Figure 4.6F. The region of zero-lag synchronization disappears as the delay increases, giving way to a region of anti-phase synchronization. Due to the oscillatory dynamics, for $\tau_{axo}$ greater than $T_\gamma$, frequencies close to the gamma peak are again compatible with an in-phase pattern. However, it is important to note that phase coherence is strongly decreased as the cycle is repeated again ($\tau_{axo} \geq T_\gamma$), probably due to loss of temporal self-coherence of the oscillations themselves. Thus, provided that the LFP-LFP phase coherence is significant, an effective coupling exists at which the two populations oscillate with a constant phase difference, which depends on the frequency and on the axonal delay. In particular, only two possible phase shifts are allowed, namely zero-lag ($\tau_{lag} \approx 0$ ms) and an anti-phase ($\tau_{lag} \approx 1/(2f)$) synchronization.

Figure 4.6C shows that the frequency at which maximum phase coherence occurs, $f_{max}$, might not correspond to the predominant gamma rhythm at $F_\gamma \sim$45 Hz, although it is close to it and within the extent of the gamma peak (gray vertical bar). Thus, the phase coherence is bounded by the region in which spikes are still phase locked to the LFP (Figure 4.2). The separation between $f_{max}$ and $F_\gamma$ is clear when $\tau_{axo}$ varies between 0 and $T_\gamma/2$. Phase coherence is achieved at slower rhythms that still reliably carry the action potentials. Hence, the

spikes elicited by each population systematically reach the other one at its excitability windows. Moreover, a lower $f_{max}$ implies larger excitability windows and allows the networks to be synchronized in phase. For larger $\tau_{axo}$, corresponding slower frequencies lying outside the gamma peak do not efficiently transmit spikes, due to the bounded region in which MUA is locked to the LFP. Therefore, at large $\tau_{axo}$ the system moves towards an anti-phase configuration, where the time lag matches and compensates for the inter-areal axonal delay.

Note that the phase coherence patterns shown in Figure 4.6C are affected by the inter-areal delay variability. If $\tau_{axo}$ is fixed to a constant value (instead of being drawn from gamma distribution), the region of coexistence between the in-phase and anti-phase coherence patterns increases, and for delays approaching the oscillation period $T_\gamma$ the new peak emerging at $F_\gamma$ (detectable in Figure 4.6C and corresponding to in-phase dynamics in Figure 4.6E) becomes significant. This is shown in Figure 4.7, which displays the phase coherence for constant $\tau_{axo} = 20$ ms (green line), in comparison with the case $\tau_{axo} = 0$ ms (blue line) and the one with $\tau_{axo}$ drawn from a gamma distribution with mean 20 ms (red line) (Barardi et al., 2014b).

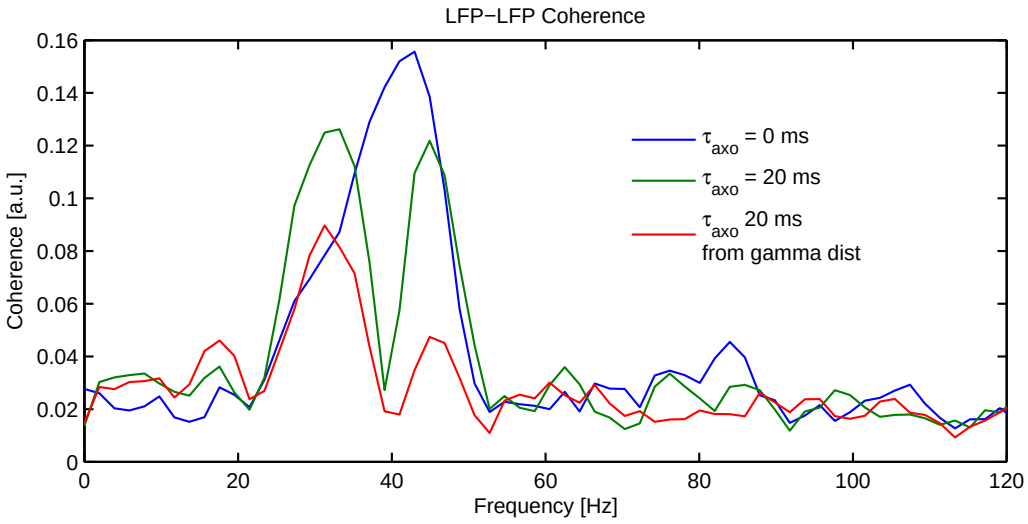


Fig. 4.7 **Phase coherence for constant inter-areal delay.** Phase coherence between the two LFP oscillations in the bidirectional coupling configuration when $\tau_{axo} = 0$ ms (blue line), $\tau_{axo} = 20$ ms (green line) and $\tau_{axo}$ is taken from a gamma distribution of mean 20 ms (red line). From Barardi et al. (2014b).

## 4.6 From phase coherence to communication

### 4.6.1 In-phase and anti-phase coherence transitions under external stimulation

The LFP oscillations studied so far are complex rhythms that convey a wide range of frequencies with a predominant component in the gamma range. We have seen before that the axonal delay $\tau_{axo}$ determines the relative dynamics of the coupled neuronal pools, which fall in either an in-phase or an anti-phase pattern. The phase relationship set by the two LFP signals is proposed to regulate the effectiveness of communication (Fries, 2005). In other words, a stable phase difference $\Delta\phi$ determines the response of a neuronal population to inputs perturbing directly another area. Therefore, depending on the phase difference $\Delta\phi$ between two coherent LFPs, the response of the unperturbed population will replicate to a certain extent the response of the other population to the perturbation. We next study how, in the two different synchronization scenarios described above, inter-areal axonal delays affect information transmission during temporal windows, in which the phase difference and the frequency cannot be independent of each other. Note here the difference between phase coherence and effective communication. Rigorously speaking, communication occurs whenever spikes from one population arrive to the other one, and this is guaranteed provided that there is some coupling across networks. In contrast, effective communication refers to a more specific situation in which information about the stimulus is being carried by the coupled populations.

We can obtain a good proxy for communication by quantifying the response of a neuronal population (the receiver) to a perturbation that affects indirectly its dynamics via a second population coupled to it (the emitter), and which receives directly the perturbation. The success in communication can be observed in the transient amplification of the neuronal oscillations of the receiver (Sancristóbal et al., 2014). The perturbation simulates different stimulus features, and consists of increases in the mean firing rate of the background synaptic activity impinging on a subpopulation of the emitter. We then examine, at different inter-areal axonal delays $\tau_{axo}$, how well the LFP and MUA power spectra of the receiver convey information about the external stimulus being applied to the emitter.

Since the connectivity within and between the two neuronal networks exhibits a certain degree of clustering (Appendix A.5), exciting a subpopulation of adjacent excitatory neurons from an area in the emitter population triggers a response in a well-defined subpopulation of neighboring neurons in the receiving population. We choose a set of different input intensities, $S = 8300, 8800, 9300, 9800, 10300, 10800, 11300$ spikes/s, affecting 400 long-range excitatory neurons from the emitter population during a 2-second time window. As a consequence of

this perturbation, the amplitude of the LFP power spectrum increases with the strength of the perturbation (Figures 4.8A,B with $\tau_{axo} \approx 9$ ms), without altering the position of the gamma frequency peak (Figure 4.9A), consistent with the results were reported in Mazzoni et al. (2008).

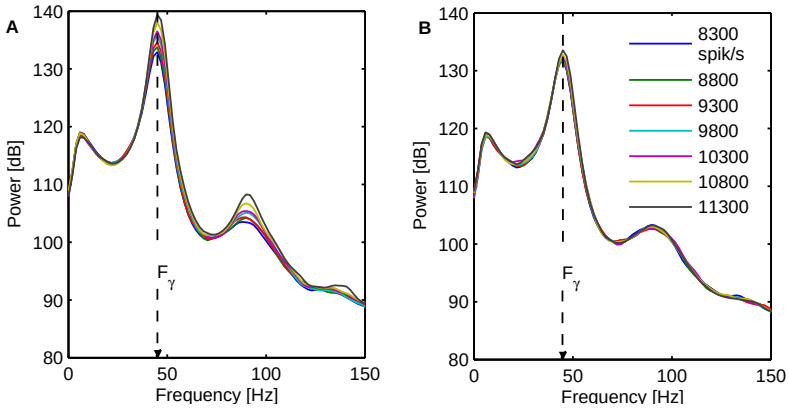


Fig. 4.8 **Effect of external stimulation for increasing coupling delay.** (A) LFP power spectrum of the directly stimulated population for different external rates $(8300, 8800, 9300, 9800, 10300, 10800, 11300$ spikes/s). (B) LFP power spectrum of the second population. The mean inter-delay between the pools is $\approx 3$ ms. The measures are averaged over 200 trials. From Barardi et al. (2014b).

Perturbing one of the populations breaks the symmetry of the system, since now the firing activity of the emitter is enhanced with respect to the receiver. As shown by the maps of phase coherence plotted in Figure 4.10, an increase of the external firing rate boosts phase coherence between the two LFPs. Moreover, the two frequency bands where phase coherence is significant merge into a single region at larger values of $S$ concentrating closer to the gamma frequency peak $F_\gamma \sim 45$ Hz. The corresponding $\tau_{lag}$ values are shown in Figure 4.11 (note the different ranges of the axes, which now concentrate on the significant values of phase coherence to better observe the transition to the out-of-phase regime).

At the gamma frequency peak $F_\gamma$ the system undergoes a transition from in-phase to anti-phase dynamics as $\tau_{axo}$ increases. Small $\tau_{axo}$ lead to time shifts $\tau_{lag} \sim 0$ of the emitter's LFP relative to the receiver's LFP (Figure 4.11A,B) and thus, the two signals oscillate approximately in phase. However, the route to the anti-phase configuration changes as $S$ is strengthened. In particular higher $S$ levels trigger smoother transitions and a narrower anti-phase regime. Figure 4.9B shows $\tau_{lag}$ values tracked at the gamma frequency peak $F_\gamma = 45$ Hz. Here, larger $S$ values lead to a leader-laggard configuration in which the emitter LFP precedes the receiver LFP by a time lag that equals the axonal delay (see dashed black lines). Figures 4.14A,B, 4.14C,D and 4.14E,F show the phase coherence and time shift for $\tau_{axo} = 3$, 9,

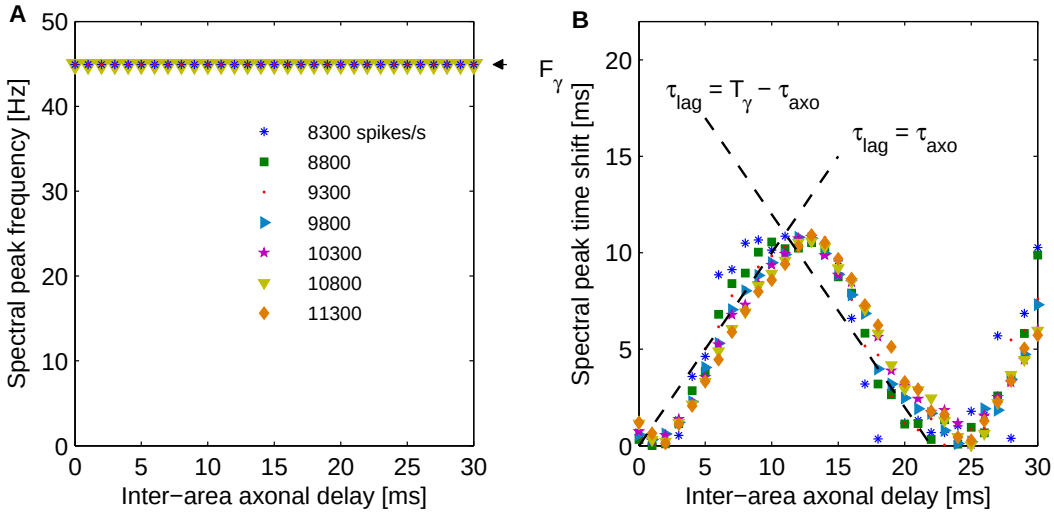


Fig. 4.9 **Time shift behavior at the peak of power spectrum for increasing inter-areal axonal delays for different extra inputs.** Effect of the external input perturbation on the coupled neuronal populations for increasing stimulus strengths $S = 8300, 8800, 9300, 9800, 10300, 10800, 11300$ spikes/s. (A) Frequency of the power spectrum peak. (B) Time shift corresponding to spectral peak frequency. The dashed lines show the ideal cases for which $\tau_{lag} = \tau_{axo}$ and its anti-phase equivalent. From Barardi et al. (2014b).

and 17 ms, respectively (the same delays as Figure 4.5), for the whole range of frequencies. The dependence of the phase coherence on $\tau_{axo}$ for different $S$ values is shown in Figure 4.10A-D, corresponding to a shift from a symmetric to an effectively asymmetric coupling. As the extra perturbation is applied only to one of the populations, the effective coupling approaches an unidirectional connectivity, although the structural links are not changed. This can be further explained by carrying on the same analysis in a structurally unidirectional scenario, in which only one population projects onto neurons from the other network. Figure 4.13A shows that increasing the delay $\tau_{axo}$ of the unidirectional transmission, the networks keep the phase difference constant at approximately the same frequency close to the power spectrum peak frequency. This represents a leader-laggard configuration and is similar to what happens in Figure 4.10D, where an over-excited subpopulation is driving the coupling between the two networks, still bidirectional but strongly asymmetric. The decrease of phase coherence with axonal delay is due to the variability in delay times: fixing $\tau_{axo}$ to a constant value of 20 ms leads to maximal phase coherence values comparable to the case of no delay (Figure 4.14A). Figure 4.13B shows that for increasing inter-areal axonal delays $\tau_{axo}$, the time shift between the two synchronized networks (at frequencies corresponding to the significant phase coherence of Figure 4.13A) increases as long as $\tau_{axo}$ is smaller than half the period of LFP oscil-

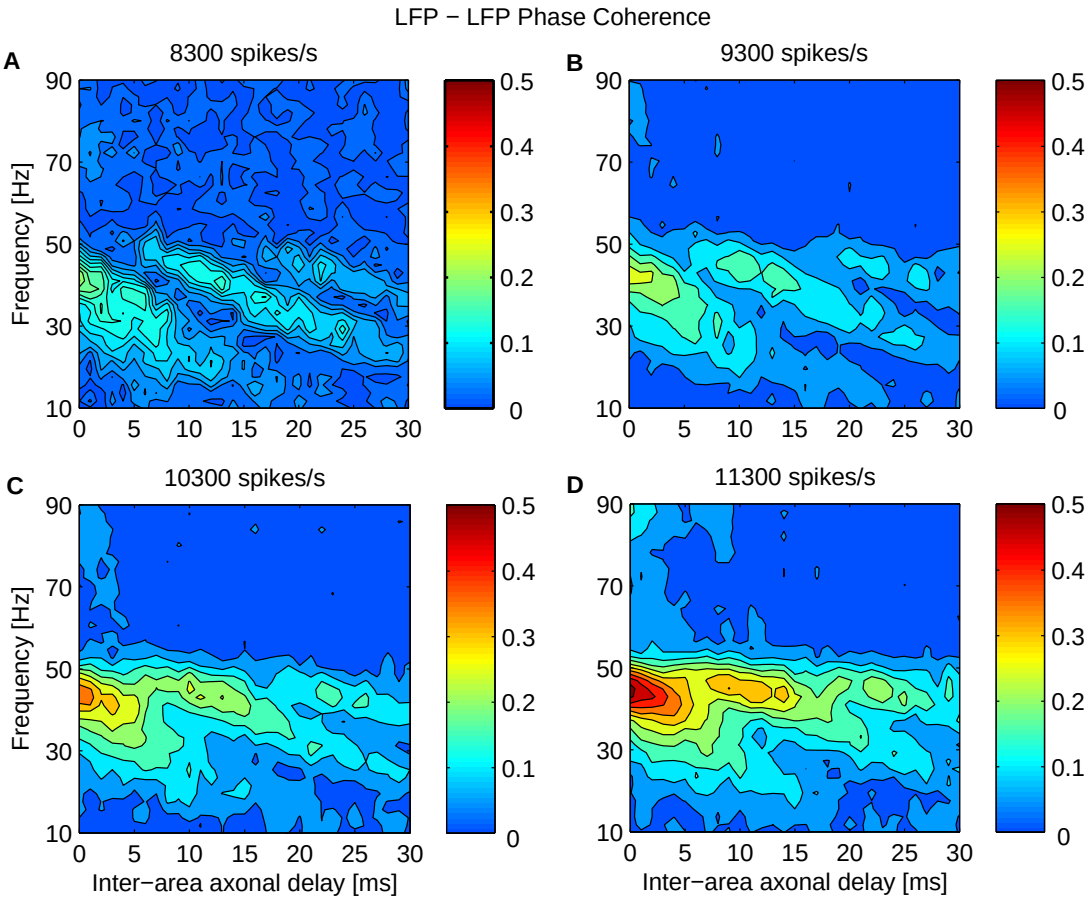


Fig. 4.10 **Phase coherence in the case of bidirectional asymmetric coupling for increasing extra inputs.** Phase coherence between LFPs of the two networks, in color code, as a function of frequency (y-axis) and of the inter-areal axonal delay $\tau_{axo}$ (x-axis) for different stimuli: (A) 8300, (B) 9300, (C) 10300, (D) 11300 spikes/s. The measures are averaged over 200 trials for each $\tau_{axo}$ and stimulus. From Barardi et al. (2014b).

lation ($1/f_{max}$) and then approaches zero, thus leading again to a transition from in-phase to anti-phase synchronization at frequencies close to that of the power spectrum peak $F_\gamma$.

### 4.6.2 Information transmission between coherent delay-coupled neuronal populations

Phase coherence can influence the transmission of information between neuronal populations. As mentioned in the Introduction, the CTC hypothesis (Fries, 2005) suggests that phase relations between coupled areas modulate the response of a receiver area to presynaptic input coming from an emitter area. In order to maximize this response, the axonal delay $\tau_{axo}$, the fre-

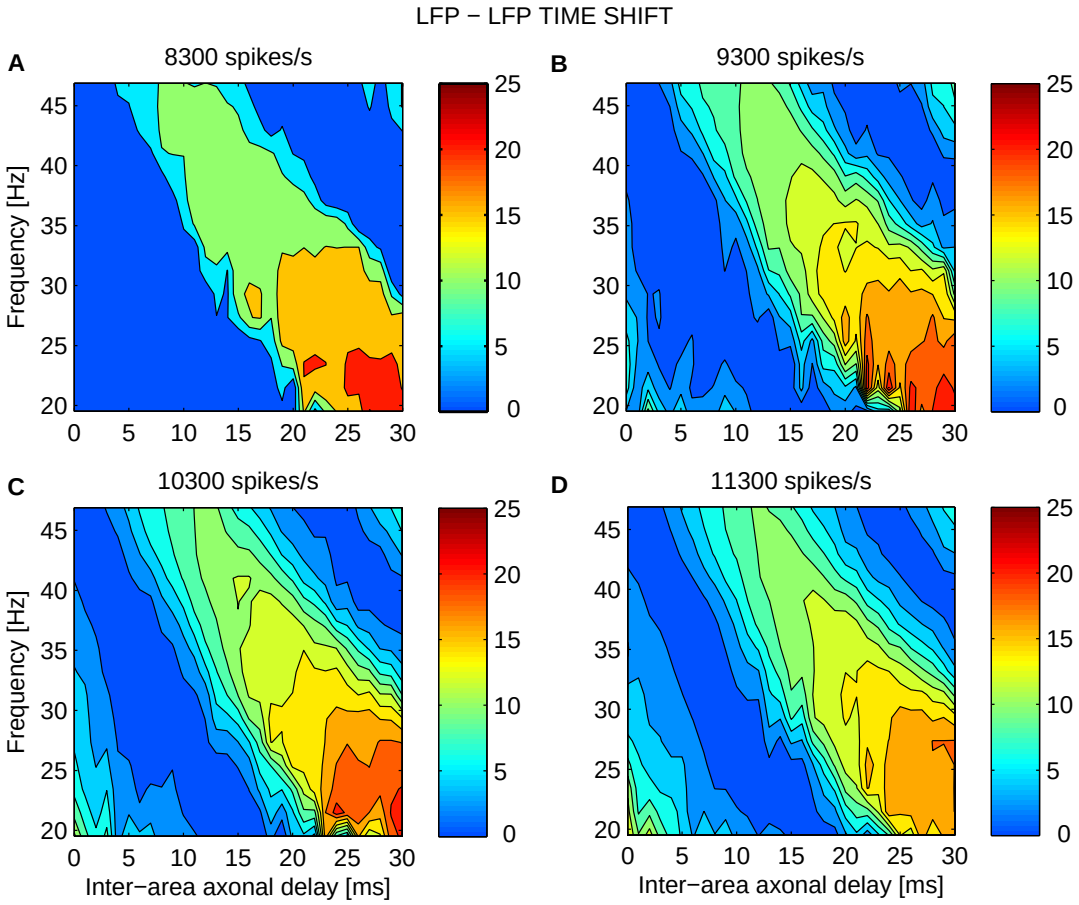


Fig. 4.11 **Time shift in the case of bidirectional asymmetric coupling for increasing extra inputs.** Effective time shift in milliseconds between LFPs of the two networks, in color code, as a function of frequency (y-axis) and of the inter-areal axonal delay $\tau_{axo}$ (x-axis) for different stimuli: (A) 8300, (B) 9300, (C) 10300, (D) 11300 spikes/s. The measures are averaged over 200 trials for each $\tau_{axo}$ and stimulus. From Barardi et al. (2014b).

quency $f$ of the oscillations and the phase difference $\Delta\phi$ should verify $\Delta\phi = 2\pi\tau_{axo}f$. When this relationship holds, spikes fired in the emitting population at a specific phase of the signal (for instance at the troughs of the LFP, which correspond to the maxima of excitability) arrive at the receiving area at the same phase (and thus at the same excitability maximum), triggering a maximal response in the receiving area. On the contrary, if $\Delta\phi$ does not fulfill the relationship given above (or if it randomly varies), effective communication will not be achieved (Sancristóbal et al., 2014). This condition is relevant at the frequencies at which the MUA and the LFP are phase locked (Figure 4.2). Otherwise, the troughs of the LFP do not correspond to intervals of maximum firing within the same population, and the peaks of MUA do not occur reliably with the same periodicity as the LFP.

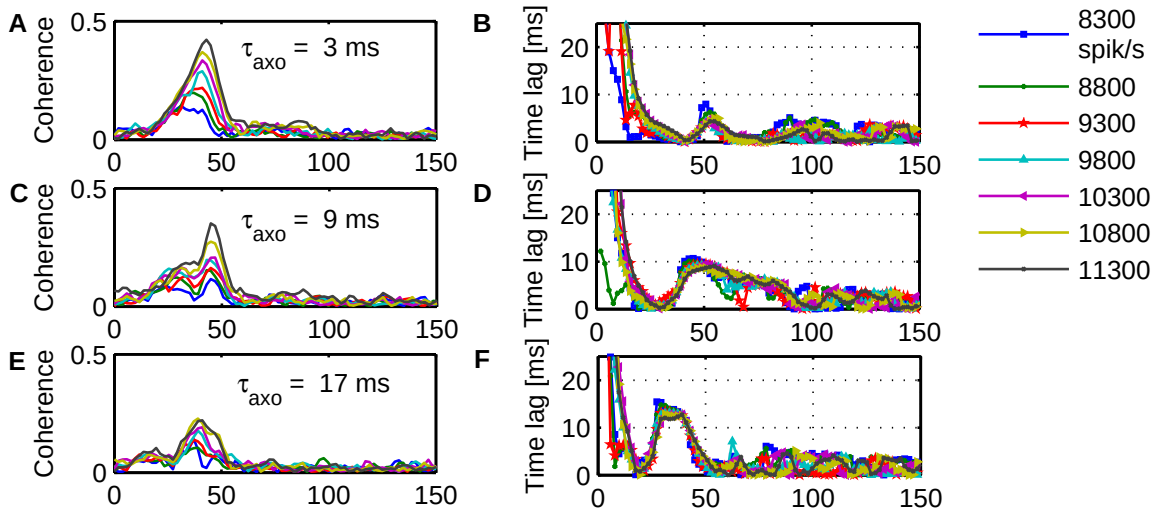


Fig. 4.12 **Effect of external stimulation for increasing coupling delay.** Phase coherence between the two LFPs for different external rates and effective time delay between the two pairs of LFP oscillations at frequencies where the phase coherence is significant for different external rates ($8300, 8800, 9300, 9800, 10300, 10800, 11300$ spikes/s) with the mean inter-delay between the pools $\approx 3$ ms (A,B), $\approx 9$ ms (C,D) and $\approx 17$ ms (E,F). The measures are averaged over 200 trials.

In order to quantify the efficiency of communication, we compute the mutual information $I(\mathbf{R}_f, S)$ between the set of stimuli $S$ and the response $\mathbf{R}_f$ as follows (defined in the Appendix A.4). The broadband LFP signal reproduces the variations in neural population activity over a wide range of time scales (Buzsáki et al., 2012). Thus LFPs signals are useful to qualitatively characterize mechanisms of information processing, because it is possible through them to verify if there are privileged time scales for information processing. We can think that information is spread over all frequencies, or that each frequency contributes separately to the information representation. Given that we were interested in how the collective dynamics of the population carries information, we quantify the neural response $\mathbf{R}_f$ as the power of either the LFP or the MUA at frequency $f$, and we have considered as stimuli different external firing rates impinging on one of the two populations. This measure allows us to evaluate how well the power $\mathbf{R}_f$ of either the LFP or MUA encodes the stimulus at a certain frequency $f$. This definition of information does not require any assumption about the stimulus features being encoded by the neural signals (Belitski et al., 2008; de Ruyter van Steveninck et al., 1997). $I(\mathbf{R}_f, S)$ quantifies the reduction of the uncertainty in predicting the applied stimulus given a single observation of the triggered response, and is measured in units of bits (1 bit means a reduction of uncertainty of a factor of two). Several experiments have been done with this tool to characterize information transmission in the primary visual cortex of macaques in response to

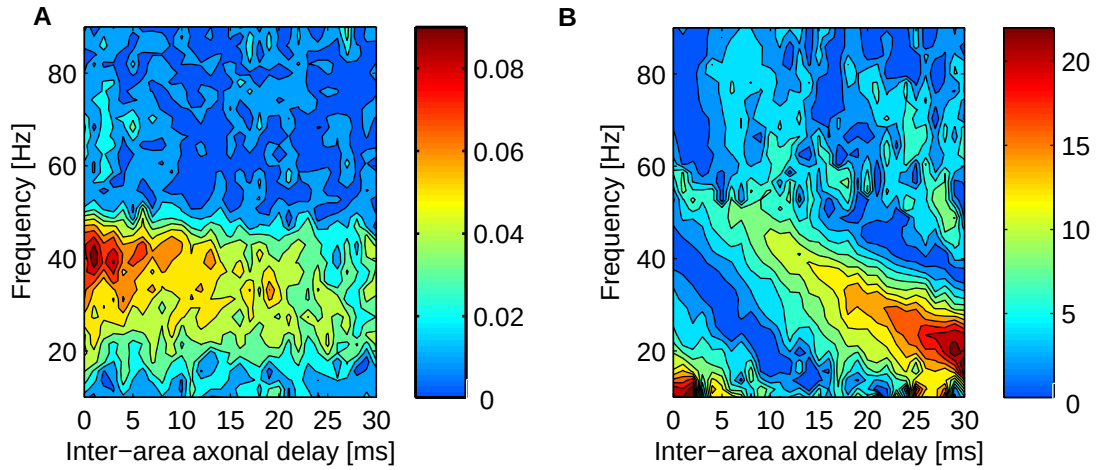


Fig. 4.13 **Phase coherence and time shift in the case of unidirectional coupling.** (a) Phase coherence, in color code, as a function of frequency (y-axis) and of the inter-areal axonal delay $\tau_{axo}$ (x-axis) in the case of unidirectional coupling from the emitter to the receiver. (b) Time shift $\tau_{lag}$, in color code, as a function of frequency (y-axis) and of the inter-areal axonal delay $\tau_{axo}$ (x-axis) in the case of unidirectional coupling from the emitter to the receiver. The measures are averaged over 1000 trials consistently with the symmetric coupling. From Barardi et al. (2014b).

a naturalistic stimulus (Belitski et al., 2008). Several other studies have been performed using the LFP power spectrum as a measure of mutual information, showing the usefulness of this approach both experimentally and computationally (Mazzoni et al., 2008). The advantages of this approach are described in detail in Quian Quiroga and Panzeri (2009) and Ince et al. (2010). To facilitate the sampling of response probabilities, the space of power values at each frequency was binned into 6 equipopulated bins (Belitski et al., 2008). We have used seven different firing rates of the external Poisson-distributed input, for a time $T = 2$ s. To compute $I(\mathbf{R}_f, S)$, we run extensive simulations to properly estimate the conditional probabilities used in mutual information measures. The techniques adopted in order to reduce the bias error of the estimation of conditional probability due to the finite number of samples are explained in the Appendix A.5.

Figure 4.15 shows that the mutual information is non-negligible only within the gamma range ($p < 0.05$; bootstrap test), in a narrow region around the peak of the power spectrum $F_\gamma$. This is consistent with the fact that the emitter encodes the different stimulus strengths in the gamma band, i.e. other regions of the LFP power spectrum are not affected (Figure 4.14-4.8A,C,E). Therefore, information transmission occurs within the gamma peak. Moreover,

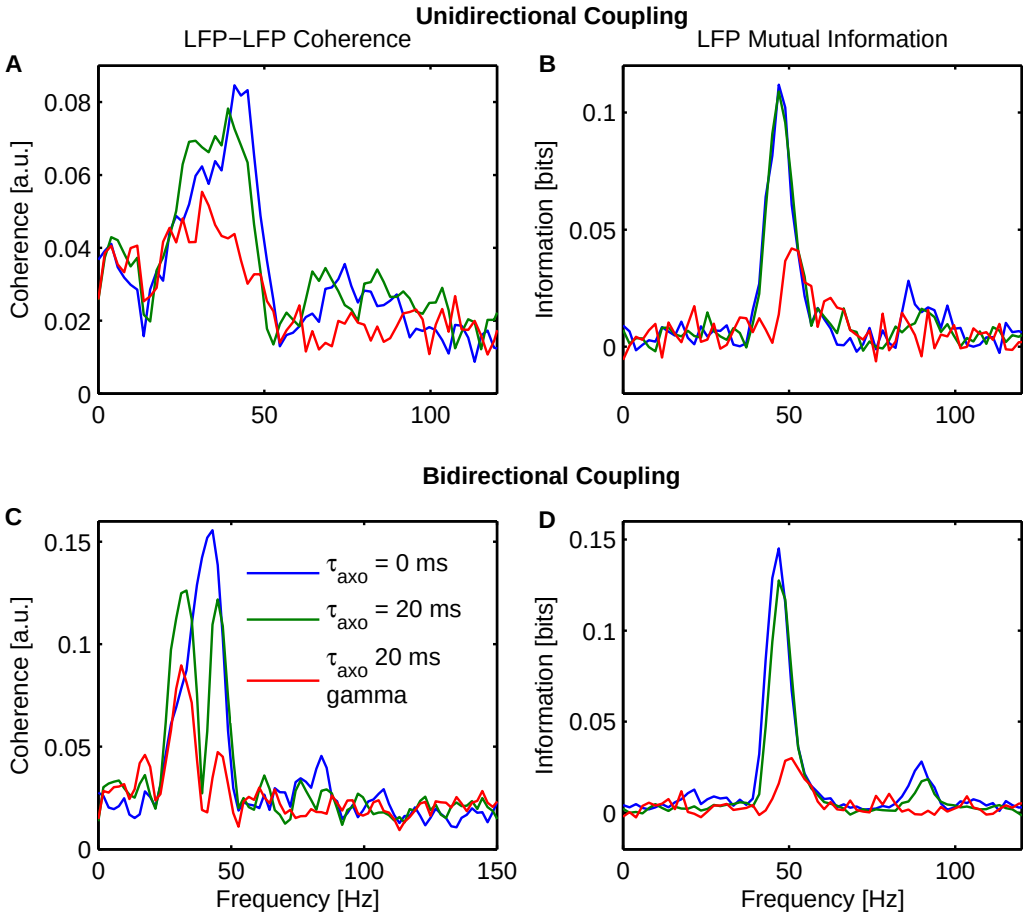


Fig. 4.14 **Phase coherence for constant inter-areal delay.** (A) Phase coherence between the two LFP oscillations in the unidirectional coupling configuration when $\tau_{axo} = 0$ ms (black line), $\tau_{axo} = 20$ ms (blue line) and $\tau_{axo}$ is taken from a gamma distribution of mean 20 ms (red line). (B) Mutual information between the set of stimuli $S = 8300, 8800, 9300, 9800, 10300, 10800, 11300$ spikes/s and the neural response given by the LFP in the same unidirectional coupling configuration. (C) Phase coherence and (D) mutual information in the bidirectional coupling configuration. Phase coherence measures are averaged over 1000 trials. Mutual information measures are averaged over 5 sets of 200 trials for each stimulus. From Barardi et al. (2014b).

functional interactions between coupled neuronal populations can be maximized if their phase difference is close to zero, i.e. for short axonal delays.

While $I(\mathbf{R}_f, S)$ is lower when computed for the LFP power spectrum (Figure 4.15A) than for the MUA power spectrum (Figure 4.15B), it decreases monotonically in both cases for increasing axonal delays. This behavior contrasts with the one shown in Figure 4.6C, in which the maximum phase coherence in the absence of stimulus occurs at varying frequencies $f_{max}$

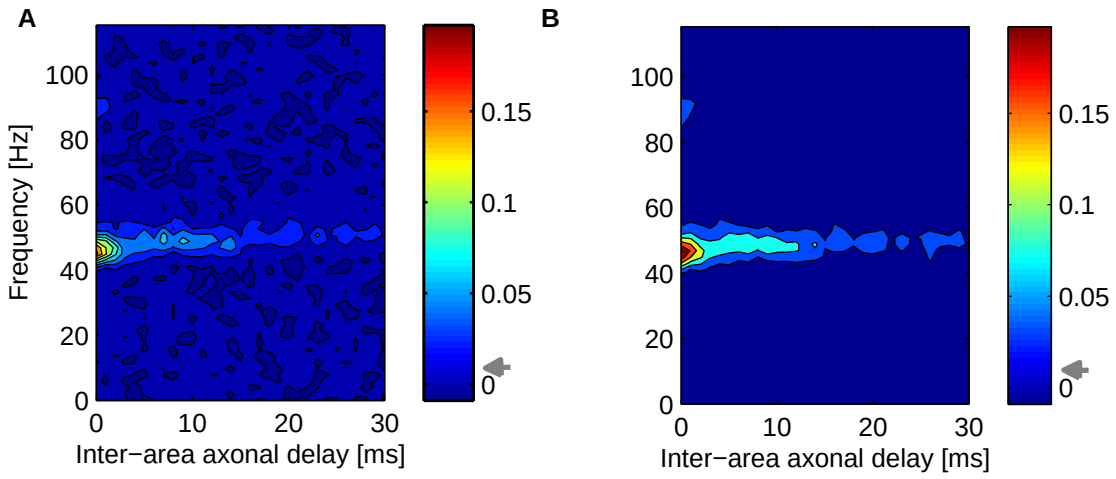


Fig. 4.15 **Mutual information carried by LFP and MUA power spectrum of the receiver.** Mutual information between the set of stimuli $S = 8300, 8800, 9300, 9800, 10300, 10800, 11300$ spikes/s and the neural response given by the LFP (A) and MUA (B) power spectra for increasing coupling delays $\tau_{axo}$. The gray arrow in the color scale refers to significance threshold ($p < 0.05$, bootstrap test). The measures are averaged over 200 trials for each $\tau_{axo}$ and stimulus. From Barardi et al. (2014b).

for different $\tau_{axo}$. Moreover, $f_{max}$ lies outside the significant mutual information spectrum. However, at large enough $S$ the phase coherence pattern (Figure 4.10D) closely resembles the mutual information dependency with $\tau_{axo}$ (Figure 4.15), since here $f_{max} = F_\gamma$.

Mutual information encoded in the power spectrum is bounded to the frequencies at which spikes are maximally frequency locked (Figure 4.2). Although this measure does not take into account the phase difference between the two LFP signals, their dynamics clearly rely on their relative time lag. Therefore, significant phase coherence is needed in order to reliably connect in time the excitability time windows of both networks, but it is not sufficient to achieve a maximal response of the receiver. In order to meet this second requirement, the frequency at which phase coherence is obtained needs to carry a precise timing of the action potentials, otherwise the presynaptic current will not elicit a postsynaptic response. Even the emitter population can only encode the stimulus strength as variations in the amplitude of the gamma frequency peak, since it is at $F_\gamma$ that changes in the LFP represent synchronized alterations in the MUA.

A symmetric coupling scenario allows for two emerging stable regimes, in-phase $\Delta\phi_{lag} = 0$ and anti-phase $\Delta\phi = \pi$, while in an asymmetric regime the most excitable network leads the dynamics ($\tau_{lag} = \tau_{axo}$). Therefore, in the presence of axonal delays, the latter case is

not compatible with the in-phase/anti-phase condition. The symmetry breaking allows for $\tau_{lag}$ to follow $\tau_{axo}$, increasing phase coherence at the gamma rhythm and thus the receiver's response. In summary, efficient communication needs a sufficient locking between the spikes being transmitted and the LFP, the carrier of this information. This is maximized at the gamma frequency peak $F_\gamma$, here $\sim$ 45 Hz, at which changes in the power spectrum due to external stimuli become particularly evident. The coupling axonal delay $\tau_{axo}$ modulates the level of phase coherence within all the gamma range, and strong driving of one of the populations precisely favors the $\sim$45 Hz frequency channel. As observed above, the variability of axonal delay affects the regions where the phase coherence maximum is significant.

Figures 4.16A,B show the LFP and MUA mutual information in the unidirectional case. As in the case of bidirectional coupling, the flow of information occurs at $F_\gamma$, where the MUA and LFP are frequency locked and the emitter encodes the stimulus strength. Specially, mutual information is higher at small $\tau_{axo}$, when the networks are synchronized in phase. In the unidirectional configuration the mutual information shows a strong dependence on $\tau_{axo}$, as in the case of phase coherence discussed above. This is due again to the variability of axonal delays. For a fixed time delay, the mutual information in the unidirectional coupling case does not show a substantial decrease for increasing $\tau_{axo}$ (Figure 4.14B). The bidirectional configuration also exhibits a less significant decrease of the mutual information maximum for constant increasing $\tau_{axo}$ (Figure 4.14D). This is consistent with the phase coherence peak corresponding to in-phase dynamics that persists for increasing constant delay (Figure 4.14C).

Our results show that phase coherence cannot be taken as a precursor of information transmission. Phase coherence can be achieved in a broad range of frequencies around the gamma peak $F_\gamma$ (Figure 4.10). Therefore, the spikes impinging on each network are able to bound the two populations in a constant phase relationship, constrained by the symmetry of the effective coupling. However, in order to communicate, presynaptic spikes must trigger a postsynaptic response. This requires that the presynaptic action potentials are synchronized in time to facilitate the integration of the synaptic currents. Hence, changes in the LFP and MUA amplitude occur precisely at $F_\gamma$ and mutual information does the same (Figure 4.15). Stimulus that are able to modify the response of a population within a wider frequency range (i.e. not frequency specific) could possibly alter the situation here described (Barardi et al., 2014b).

## 4.7 Conclusion

Here we have examined how heterogeneous inter-areal synaptic delay influences the coupling between the collective dynamics of two neuronal populations. To that end, we first use pop-

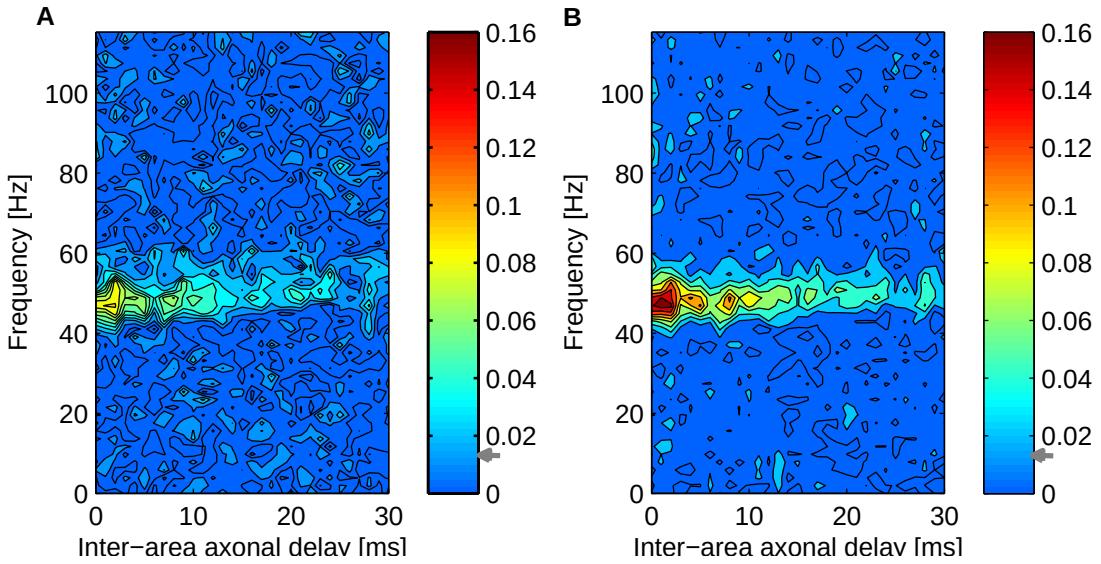


Fig. 4.16 **Mutual information in the case of unidirectional coupling.** Mutual information between the set of stimuli $S$ and the LFP (A) and MUA (B) power spectra for increasing coupling delays $\tau_{axo}$ when the coupling is unidirectional from the emitter to the receiver. Note the different colorbar scales in the two cases. The gray arrow in the color scale refers to significance threshold ($p < 0.05$, bootstrap test). The measures are averaged over 200 trials for each $\tau_{axo}$ and stimulus. From Barardi et al. (2014b).

ulation measures such as the local field potential and the multi-unit activity, by analogy with experimental studies, to capture the collective oscillatory dynamics of individual neuronal populations. In the presence of excitatory coupling, the LFP and MUA activities of two identical delayed neuronal networks oscillate in the gamma range, with a significant broad peak between 30 and 52 Hz, which does not depend on the axonal delay $\tau_{axo}$. The emergence of this gamma peak in the isolated populations is due to the recurrence between excitatory and inhibitory synaptic activity, as revealed by the phase locking between the LFP and MUA signals (Figure 4.2). In contrast with the power spectrum, phase coherence is strongly affected by the axonal delays between the populations (Figure 4.6). We see that in-phase and anti-phase patterns occur at various frequencies for different ranges of $\tau_{axo}$ in a purely symmetrical connectivity (in contrast with the unidirectional case of Figure 4.13), with high values of phase coherence occurring at frequencies below the gamma frequency peak $F_\gamma$ (Figure 4.6). We use spectral analysis and information theory to quantify the information exchanged between the two networks (Figure 4.15) in relation with in-phase and anti-phase coherence patterns. In particular, for different transmission delays between the two coupled populations, we analyze how the local field potential and multi-unit activity calculated from one population convey information in response to a set of external inputs applied to the other population.

Our results reveal the following features:

- the two populations exhibit consistent phase coherence for a wide range of coupling delays, undergoing a transition from in-phase (zero-lag) to anti-phase collective oscillations as the delay increases;
- in the transition region, the in-phase and anti-phase dynamics coexist:
- when one of the populations is synaptically stimulated, the stimulus is transmitted to the second population in both in-phase and anti-phase regimes, depending on the coupling delay. This ensures an effective communication for an unusually large range of delays.

The phase coherence pattern shown in Figure 4.6C corresponds to a pure symmetrical connectivity, in which both the structural and functional coupling are equal in both directions (in contrast with the unidirectional case of Figure 4.13). The reciprocity between the feedback and feedforward pathways across cortical areas is not an unrealistic assumption (Siegel et al., 2000), although the specificity of such synapses might differ in each direction in order to account for the different effects of the top-down and bottom-up projections. Here we show that increasing axonal delays $\tau_{axo}$ lead to either an in-phase or anti-phase synchronization with a vanishing maximal phase coherence at frequencies $f_{max}$ below $F_\gamma$ although lying within the gamma peak. Hence, in *basal conditions*, there is always a certain reliable phase relationship, provided $\tau_{axo}$ is small, relative to the period $T_\gamma$.

The interesting point raised by the communication through coherence hypothesis (Fries, 2005), is whether phase coherence can forecast efficient communication between two populations in the presence of a stimulus. According to the modulatory role of the top-down pathway, attention can determine which visual cues we are aware of (Bosman et al., 2012; Desimone and Duncan, 1995). In principle two situations can arise: either a stimulus catches our attention (such as an unexpected noise or object) or we are being attentive to an expected stimulus (such as waiting the traffic light to turn green). In the first situation the communication outline between a primary cortical area and the associative areas is driven by the stimulus, while in the second case it is due to the internal cognitive state. The firing activity in visual areas has been shown to significantly increase even in the attentive state prior to the stimulus presentation (Kastner et al., 1999). Hence our results, in which we progressively increase the firing rate impinging on one population, could be viewed as arising from the alteration of the underlying attentional state.

The experimental study of Bosman et al. (2012) shows that a neuronal cell assembly in V4 is phase coherent with an area in V1 that responds to a selected stimulus, while it is not with a V1 area that is not driven by the input. Here we do not model a competitive scenario

between two networks. Instead we focus on the mechanisms by which two neural pools can modulate their communication when they are simultaneously oscillating in the gamma band. We quantify the efficiency of communication between the two neuronal networks as the ability of a population to encode information of an input which perturbs directly another coupled population. Mutual information measures between either the LFP or MUA power spectrum and the set of applied stimuli $S$ show that significant values concentrate around the gamma frequency peak ($\approx$ 45 Hz). Mutual information decreases for long inter-areal axonal delays, and is slightly lower when the neural response is characterized by the LFP power spectrum than by the MUA power spectrum.

Despite the fact that the LFP reflects the afferent and local synaptic currents within a given neuronal network, and that the MUA only captures the action potentials within this network, these two signals are closely related. As mentioned above, the gamma LFP rhythm reflects the dynamics of the excitatory balance. Increases in inhibition silence the spiking activity and therefore the MUA signal, although the GABAergic current is enhanced. Decreases in inhibition boost the spiking activity and therefore the MUA signal, although the GABAergic current is reduced. The peak at 45 Hz in the LFP-MUA phase coherence (Figure 4.2) reveals this phase locking between the two signals.

The arrival of each set of presynaptic spikes perturbs the postsynaptic LFP and might or might not elicit a postsynaptic suprathreshold response (captured by the postsynaptic MUA) depending on the mean distance to the excitatory threshold of the populations. Bursts of activity occur at each pool with a periodicity that fluctuates within the gamma band and are locked to the troughs of the LFP at this frequency. According to the CTC hypothesis, maximum communication requires that spikes from each population reach the peaks of excitability of the target area simultaneously in both coupling directions. Thus, efficient communication is restricted to the gamma peak, as revealed by the mutual information (Figure 4.15) and preferentially at relatively small $\tau_{axo}$. This condition is only met for in-phase or anti-phase synchronization of the gamma rhythm: small axonal delays $\tau_{axo}$ are able to tie two LFP troughs only at zero-lag synchronization, while larger $\tau_{axo}$ require anti-phase synchronization. In principle, as $\tau_{axo}$ increases zero-lag synchronization could again mediate communication by skipping one cycle. However, due to loss of phase consistence, mutual information decays with increasing $\tau_{axo}$.

Here we have shown that phase coherence emerges spontaneously due to the excitatory coupling between areas without the need of further constrains (Figure 4.6C). Higher stimulation of a particular population (the emitter), which enhances the LFP power spectrum amplitude of the gamma peak, increases the range of phase coherence to larger axonal delays (Figure 4.10D). The delay determines the phase shift between the two signals, with the emit-

ter leading the oscillations. According to Bosman et al. (2012), phase coherence is revealing communication in the sense of spike propagation, which in our case extends to frequencies within the gamma peak. However, *efficient communication* in the sense of the information encoding in the postsynaptic response, is restricted to a narrower band (Figure 4.15) that maximizes spike synchronization. Adopting a spectrum of delays with increasing variability for increasing values of $\tau_{axo}$, instead of an (unrealistic) constant delay, affects quantitatively the results of phase coherence and mutual information but does not produce any strong qualitative change in the findings of the paper. However the effect of variability cannot be ignored, given the dispersion of axonal delays observed in experimental studies (Aboitiz et al., 1992). Figure 4.17 shows a schematic diagram of the two oscillatory LFPs filtered around the gamma frequency peak ($1/F_\gamma = T_\gamma = 22$ ms) with the bursts of spikes locked at their troughs in agreement with Figure 4.2. For a delayed coupling, zero-lag synchronization does not lead to a symmetric configuration demanding that the two oscillations are reciprocally influenced at the same phase. Therefore the system rapidly shifts toward an anti-phase synchronization at which $\tau_{axo}$ roughly equals half of the period of the LFP (Figure 4.17B). Importantly, when the symmetry of the system is broken (for instance by perturbing just one of the populations), the possible stable solutions are no longer the in-phase or the anti-phase regime. In this case, phase coherence can be achieved through a leader-laggard configuration in which the time lag equals the inter-axonal delay. Without the symmetry constraint, this situation is achieved at the gamma frequency peak, for which the spikes of each population are preferentially locked to the LFP and changes in their power spectrum are maximized.

In conclusion, our results show that effective communication can be reached even in the presence of relatively large delays between the populations, which self-organize in either in-phase or anti-phase synchronized states. In those states the transmission delays, phase difference, and oscillation frequency match to allow for communication at a wide range of coupling between brain areas (Barardi et al., 2014b). Furthermore our study has shown the dichotomy between phase coherence and communication. Whereas phase coherence arises due to LFP phase perturbations through the propagated spikes, communication is caused here by an increase in the firing response. The first occurs at different frequencies for every $\tau_{axo}$ in order to conserve the functional connectivity. The second requires the spikes to be tightly locked to the LFP and at a faster frequency $F_{gamma}$ to enable spike integration, and hence a signal response that can be synaptically propagated.

In this Chapter we have used a microscopic model to describe the synchronization between two distant neuronal populations. Modeling the synchronization dynamics of multiple brain regions from a purely microscopic scale is computationally unfeasible. Currently, as in this Chapter, this is accomplished by modeling the two neuronal populations (or more) while repre-

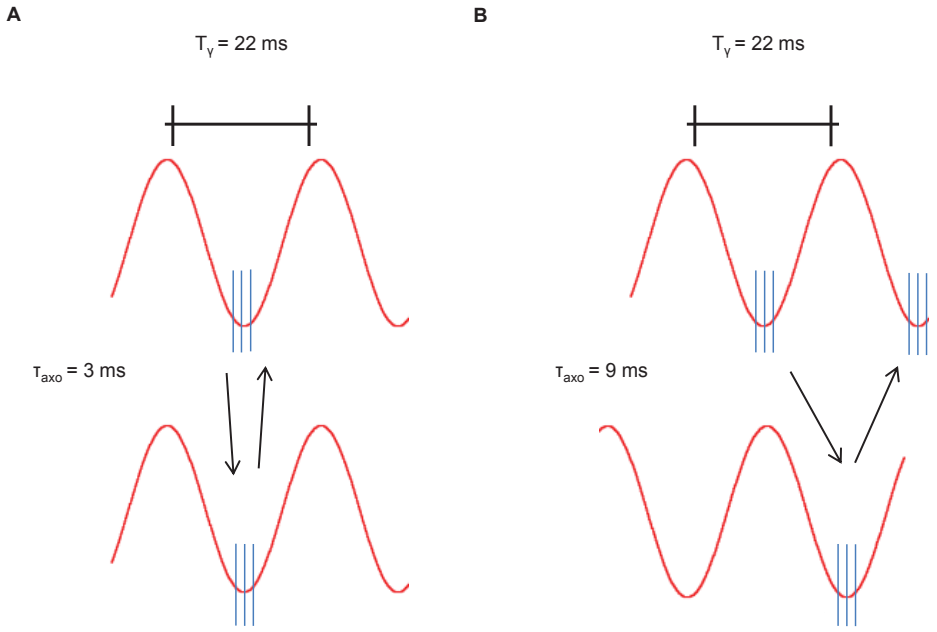


Fig. 4.17 **Carriers of information and signals.** Diagram of two oscillatory LFPs filtered around the power spectrum peak (≈45 Hz), with a short spike train locked at their troughs for different $\tau_{axo}$: (A) $\tau_{axo} = 3$ ms, representing zero-lag synchronization and (B) $\tau_{axo} = 9$ ms, representing anti-phase synchronization. From Barardi et al. (2014b).

senting the activity of the rest of the brain by a background noisy activity, but this approach is not useful when the neuronal population of interest feeds back into those other brain regions, thereby modifying the background activity that acts upon the population itself. Thus, a hybrid description of the brain that encompasses multiple scales is an appealing concept. In that scenario, it would only be necessary to represent microscopically those neuronal populations involved in a particular task, and which are monitored with single-cell resolution. The rest of the brain, while modulating the activity of the population of interest, would not necessarily need to be represented with microscopic detail. In the next Chapter we will consider one way of facing this situation, based on coupling bidirectionally microscopic and mesoscopic descriptions of neuronal populations and then we use synchronization in order to probe the interaction between the two scales.

# Chapter 5

# Probing scale interaction in brain dynamics through synchronization

Brain dynamics is usually described by theoretical models that involve one of three separate scales: either the microscopic scale of neuronal networks, the mesoscopic scale of cortical columns, or the macroscopic level of coupled neural-mass models. In the previous Chapter, we have focused on possible synchronization mechanisms between distant populations described at the level of neuronal networks, focusing in particular on gamma-band synchronization. However, brain activity is based on the coordination across temporal and spatial scales, and synchronization, as a mechanism of large-scale integration, could be a measure of the interaction of multiple scales.

In this Chapter we intend to bridge these scales by building a model that contains different levels of description, and exploring the effect of one of the scales on the other. In particular, we incorporate a neuronal population within a system of coupled cortical columns, and study the joint influence between the different dynamical regimes exhibited by the cortical columns and the cortical oscillatory regime displayed by the neuronal network. Specifically, we consider the coupled behavior of two mesoscopic neural masses that communicate with each other through a microscopic neuronal network. We use synchronization as a tool to probe the interaction between the two scales of description and we also examine which characteristics of the neuronal network connectivity allow the efficient cross-talk between dynamical scales, i.e. to determine which are the microscopic features that modulate the mesocopic activity. The Chapter is organized as follows. In Section 5.1 we introduce our study and the large-scale integration problem, and in Section 5.2 we describe the dynamical model with the coupling between the neural masses and the neural network used in this study. Evidence of scales interaction through synchronization as a function of topological properties of neural network is presented in Section 5.3 and discussed in Section 5.4. These results are reported in Barardi et al. (2014a).

## 5.1 Towards a multi-scale approach

The mammalian brain is composed of a myriad of coupled neurons that interact dynamically. It possesses a rich topological structure and exhibits complex dynamics, operating as a noisy, nonlinear, and highly dimensional system. Neuronal activity evolves at temporal scales ranging from a few milliseconds to tens of seconds, and emerges from neuronal assemblies that extend from micrometers to several centimeters. Consequently, the study of the brain is usually partitioned into different research fields devoted to distinct brain structures, cortical functional areas or particular microscopic circuits, from the level of cortical columns down to single-neuron responses. Moreover, studies of the global activity of the brain usually focus for convenience on specific cognitive or motor tasks, in order to compare them with a control state such as the resting one (see Section 1.4.3).

The various aforementioned approaches deal with different scales of description, from the macroscopic to the microscopic level. Accordingly, different computational models have been developed to account for the activity at each scale (see Chapter 2). We have seen that single neurons, for instance, can be characterized by detailed biophysical models that consider ion-channel dynamics, as initially proposed by Hodgkin and Huxley (HH) (Dayan and Abbott, 2005; Koch and Segev, 1988), or by more abstract models of neural excitation such as the integrate-and-fire (IF) model (Brunel and Van Rossum, 2007; Gerstner and Kistler, 2002). The set of equations associated to these models (introduced in the Section 2.1) representing each neuron's membrane potential can be coupled in a way that mimics the synaptic junction (see Section 2.2). Thus, given a connectivity matrix, one can ideally build any neuronal network *in silico* from its individual constituents, and thereby move towards the mesoscopic level of neuronal assemblies. This allows the brain to be traditionally investigated in a reductionist way, using different simplified levels of description. We have adopted these microscopic approaches to explain spindle patterns in the LGN of the thalamus in Chapter 3 and to characterize the dynamical properties of the gamma synchronization between coupled neuronal populations in Chapter 4.

Another set of models, named neural mass (NM) models (David and Friston, 2003; Grimbert and Faugeras, 2006b; Jansen and Rit, 1995; Spiegler et al., 2011), avoid the single-neuron perspective and consider instead the averaged behavior of the neuronal population (see Section 2.3.1). This mesoscopic description is more phenomenological than the single-neuron models, in the sense that it represents directly the collective behavior of the network, without singling out individual cells. Moreover, single neurons operate at time scales faster than neural mass models. The former exhibit action potentials that last about 1 ms, while the coordinated activity of neuronal tissue, which emerges from the synchronization of multiple spikes, oper-

ates on time scales up to tens of seconds. Within a neuronal population all temporal scales work simultaneously, and the relative relevance of the different scales might change depending on the biological process. For instance, spike-timing precision is key to synaptic plasticity, and therefore to the formation of functional cell assemblies (Ahissar et al., 1992; Singer and Gray, 1995). On the other hand, as seen in Section 1.4.3, the frequency of collective oscillations is relevant for the synchronization of distant areas, and thus for their effective interaction within specific information-processing tasks (Fries, 2005; Sancristóbal et al., 2014).

Recently, large-scale models of the brain have received special attention. So far, global brain activity has been modeled by dividing the brain into discrete volume elements, or voxels, and coupling them according to statistical correlations and structural information (Alivisatos et al., 2012; Deco et al., 2013; Pons et al., 2010; Sotero et al., 2007). While new theoretical studies have attempted to connect the microscopic (neuronal network) and mesoscopic (neural mass) descriptions of brain tissue, by directly applying mean-field approaches to derive the latter from the former (Faugeras et al., 2008; Rodrigues et al., 2010), these strategies are fraught with limitations and hard-to-justify assumptions. Here we propose an alternative approach to explore scale interaction, by considering a system formed by two neural masses that are coupled exclusively via an intermediate population described by a spiking neuronal network model (Barardi et al., 2014a).

## 5.2 Dynamical model

As mentioned above, our model combines two different levels of description (Figure 5.1). The neural mass description evolves at a slow scale and represents the average dynamical evolution of a set of three different neural populations (pyramidal, excitatory interneurons and inhibitory interneurons) (Jansen and Rit, 1995) (see Section 2.3). The fast scale, on the other hand, is represented by a conductance-based neural network formed by excitatory and inhibitory neurons. In this case, the time course of every neuron's transmembrane potential is given by the dynamics of voltage-dependent ion channels (see Section 2.1.3). We merge these two levels of description in a simple dynamical structure, shown in Figure 5.1, in which two neural mass models (NMs) are coupled with a subpopulation of neurons belonging to the neuronal network (NN).

The two NMs are set to oscillate in two different well-defined frequencies, corresponding to two slightly different brain rhythms. The NN also displays a collective oscillatory dynamics with a different frequency. Here we investigate how both the inter-scale coupling strength and the features of the NN contribute to the cross-talk between the three systems. The NN is composed of 4000 HH neurons (80% excitatory and 20% inhibitory). Each neuron forms

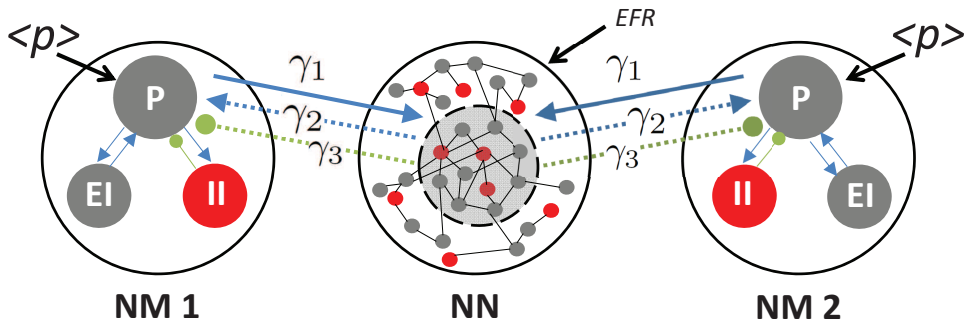


Fig. 5.1 **Diagram representing the coupling between different scale-based models.** Two groups of neuronal populations, described by neural mass models (NMs), are coupled with a neuronal network (NN). The NMs represent the average dynamics of three coupled neural populations: pyramidal (P), excitatory interneurons (EI), and inhibitory interneurons (II). The NN consists of a set of 4000 excitatory and inhibitory interconnected neurons. Only a subset of neurons of the NN is coupled with the NMs. The coupling strength between the NMs and the NN is given by the three parameters, $\gamma_1$, $\gamma_2$ and $\gamma_3$. $\gamma_1$ quantifies the coupling from the pyramidal population of the NMs to the NN subpopulation. $\gamma_2$ and $\gamma_3$ represent the intensity of the excitatory and inhibitory couplings, respectively, from the NN subpopulation to the NMs' pyramidal population. From Barardi et al. (2014a).

400 chemical synaptic connections on average with other neurons of the network. The dynamics of the transmembrane potential of the soma of each neuron is described by the set of conductance-based differential equations introduced in Section 2.1.3 (Equations (2.9)-(2.11)) and the voltage dynamics is described by:

$$C\frac{dV_i}{dt} = -g_{Na}m^3h(V_i(t)-E_{Na}) - g_k n^4(V_i(t)-E_k) + -g_L(V_i(t)-E_L) + I_{i,tot}(t) \tag{5.1}$$

where the variables and the parameters have been defined in Section 4.2, but here all neurons receive an additional train of excitatory presynaptic potentials explicitly modeled by the NMs to whom the NN is connected, which contributes to the external current term $I_{i,AMPAext}$ of $I_{i,tot}$:

$$I_{i,tot}(t) = \sum_{N_{i,AMPArec}} I_{i,AMPArec}(t) + \sum_{N_{i,GABA}} I_{i,GABA}(t) + I_{i,AMPAext}(t). \tag{5.2}$$

Those spikes follow an heterogeneous Poisson process with a mean event rate, which varies following an Ornstein-Uhlenbeck process (see Section 4.2, Equation (4.5)). This NN model is able to reproduce the well-known synchronous irregular regime (Brunel, 2000), in which recurrent activity leads collective oscillations at the population level while single neurons fire irregularly. The emergent rhythmicity is achieved by a balance between the excitatory and

inhibitory synaptic currents and can be explained by periodic changes of the excitability in the network, i.e. periodic modulation of the distance to threshold. Despite the fact that excitatory neurons are dominant in the network, the stronger synaptic inhibitory conductances and the higher firing rate of the inhibitory neurons allows the system to reach a balance between excitation and inhibition. In order to obtain collective oscillations in the alpha (gamma) band, we set the decay synaptic time to be $\tau_{decay} = 15\ ms$ (5 $ms$) (see Section 4.1).

The description of the mesoscopic neuronal ensemble is based on a model proposed by Jansen and coauthors (Jansen and Rit, 1995) and presented in Section 2.3.1. This model characterizes the dynamics of a cortical column by using a mean field approximation. After some mathematical derivations (described in Section 2.3.1), the set of equations is:

$$\begin{aligned}
\dot{y}_0(t) &= y_3(t) \\
\dot{y}_1(t) &= y_4(t) \\
\dot{y}_2(t) &= y_5(t) \\
\dot{y}_3(t) &= Aa_{NM}S[y_1(t) - y_2(t)] - 2a_{NM}y_3(t) - a_{NM}^2 y_0(t) \\
\dot{y}_4(t) &= Aa_{NM}(p_e(t) + C_2 S[C_1 y_0(t)]) - 2a_{NM}y_4(t) - a_{NM}^2 y_1(t) \\
\dot{y}_5(t) &= Bb_{NM}(p_i(t) + C_4 S[C_3 y_0(t)]) - 2b_{NM}y_5(t) - b_{NM}^2 y_2(t),
\end{aligned} \tag{5.3}$$

where $y_0(t)$ is the EPSP produced by the pyramidal population on the interneurons population, and $y_1(t)$ is the EPSP acting upon the pyramidal population and arriving from (i) the excitatory interneurons, (ii) other areas of the brain and, differently from Section 2.3.1, (iii) the neural network (see Equation (5.6) below). Finally, $y_2(t)$, is the IPSP acting upon the pyramidal population and arriving from the inhibitory interneurons and, again, the neural network (see Equation (5.7) below). The intra-columnar connectivity constants values are defined in terms of $C_i$, with $i = 1, \ldots, 4$. We use the values given in Jansen and Rit (1995).

### 5.2.1 Inter-scale coupling terms

The effect of the mass models upon the neural network also contributes to the $I_{i,AMPAext}$ term of the NN (see Equation (5.2)), together with the external excitatory Poissonian train of spikes. Hence, each neuron of the NN receives a train of excitatory spikes whose mean firing rate, $FR$, is given by:

$$FR(t) = EFR(t) + k\gamma_1 S(y_1(t) - y_2(t)), \tag{5.4}$$

where $S(y_1(t) - y_2(t))$ translates the postsynaptic potential of the pyramidal population of the NM that affects that particular neuron (or both NMs if that is the case) into a spiking rate. $\gamma_1$ and $k$ control the strength of this coupling. Here $\gamma_1 = 200$, while $k$ will be a varying parameter.

$EFR(t)$ corresponds to aforementioned Poissonian train of spikes:

$$EFR(t) = \langle EFR \rangle + \lambda_{OU}(t), \tag{5.5}$$

with $\langle EFR \rangle$ being the mean external firing rate and $\lambda_{OU}(t)$ an Ornstein-Uhlenbeck process (see Equation (4.5)) representing the fluctuations around the mean. We set $\langle EFR \rangle = 8.5$ KHz. The neuronal network acts upon the NM models through $p_e(t)$ and $p_i(t)$ (see Equations (5.3)):

$$p_e(t) = \langle p \rangle + k\gamma_2 \overline{MUA}(t) \tag{5.6}$$

$$p_i(t) = k\gamma_3 \overline{MUA}(t), \tag{5.7}$$

where $\overline{MUA}(t)$ is the multiunit activity coming from the neural network, i.e. the sum of spikes over the subset of neurons coupled to the NMs, calculated within a sliding window of length 1 ms (see Appendix A.1). $\langle p \rangle$ is a constant input coming from other areas of the brain distinct from those considered explicitly in our model ($\langle p \rangle = 0.160$ KHz for both NMs). $\gamma_2$, $\gamma_3$ and $k$ are scaling factors that take into account the synaptic efficiency. Here, $\gamma_2 = 25$ and $\gamma_3 = 3$. Note that we assume that NN neurons affect only the pyramidal population in the NM. This is in accordance with the Jansen-Rit's model of two coupled NMs (Jansen and Rit, 1995), which considers that only pyramidal cells receive excitatory input from the other column (Barardi et al., 2014a).

## 5.3 Probing scales interaction

The effective interaction between neuronal ensembles described at different scales can be studied by coupling mesoscopic and microscopic models. As mentioned in the first section, mesoscopic models are best exemplified by NM descriptions, which are derived phenomenologically from experimental studies, and characterize the average population activity by means of a mean field approximation. In particular, NMs describe the neuronal activity happening at slow time scales, such as synaptic potentials arising from the synchronized firing of thousands of neurons. On the other hand, models of single neurons reproduce the time course of the electric currents crossing the neuronal membrane, and thus account for the individual action potentials and the postsynaptic response of each cell composing the network. In order to preserve the precision of the spiking times, these models involve fast time scales. Certainly, networks built from spiking-neuron models can also provide measures of the population activity by averaging across neurons. Thus, patterns of collective activity can be observed in the synaptic current, evoked by the summation of multiple spikes on the target neurons.

To analyze the evolution of the model introduced in the previous Section we consider two different dynamical variables corresponding to each of the two scales. The NM model activity is given by $y(t) = y_1(t) - y_2(t)$, where $y_1(t)$ is the EPSP and $y_2(t)$ the IPSP acting upon the pyramidal population (see Equation (5.3) above). The NN activity is quantified in terms of the LFP as defined in Appendix A.1. Both types of models operate in an oscillatory regime. The NM model is an intrinsic oscillator whose frequency can be varied by changing the parameters B and $b_{NM}$ (see blue and green lines in Figures 5.2A,B). On the other hand, the oscillations of the neuronal network are an emergent property of the system, reflecting the variability of the individual postsynaptic potentials (i.e. the microscopic events). Hence, its frequency is less well-defined (see red line in Figures 5.2A,B and power spectra in Figures 5.3C,D below).

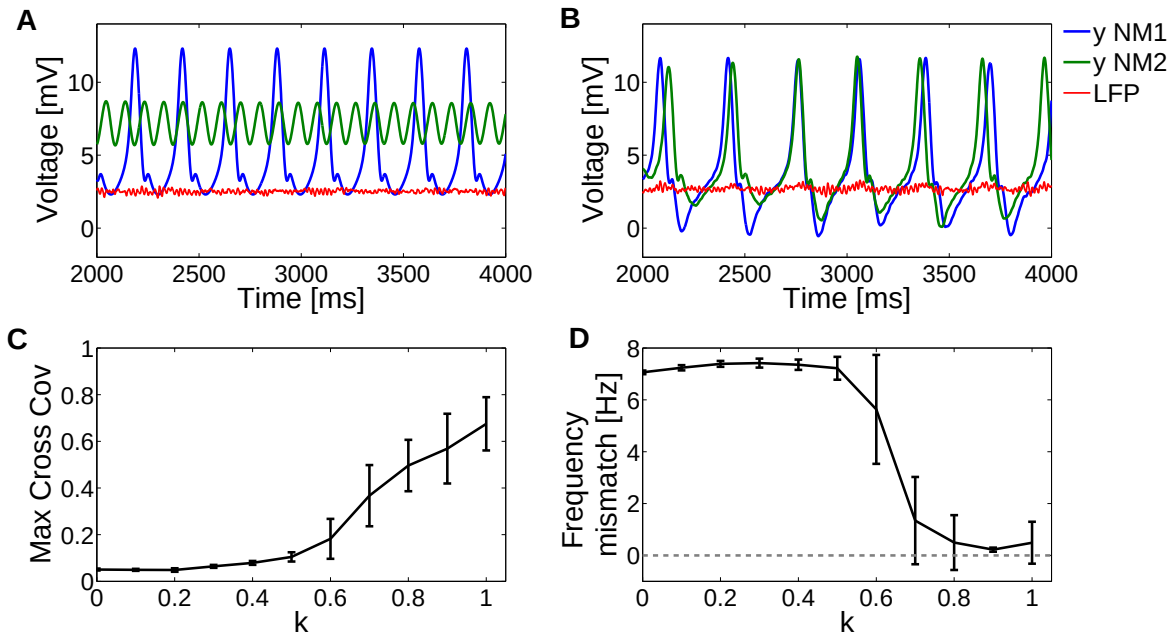


Fig. 5.2 **Collective dynamics of the coupled system.** (A) Time traces of the net postsynaptic potential $y(t) = y_1(t) - y_2(t)$ of both NMs working at different frequencies: at 4.5 Hz within the theta band (blue), and at 11 Hz within the alpha band (green). The local field potential, LFP, of the NN (red) oscillates in the gamma range around 45 Hz. The three neural ensembles are uncoupled. (B) Time traces of the postsynaptic potentials of both NM models and local field potential of the NN when the system is coupled ($k = 1$). Averaged maximum cross covariance (C) and frequency mismatch (D) between the postsynaptic potential time traces of the NMs for increasing inter-scale coupling strength $k$. From Barardi et al. (2014a).

Our aim here is to find fingerprints of an effective interaction of scales. To do so we study how the two NM models, one oscillating in the theta band and the other in the alpha band, synchronize their dynamics when the coupling is mediated by the neuronal network (Figure 5.1).

The interaction mechanism is bidirectional. This architecture was used by Vicente et al. (2008) and Gollo et al. (2010) to demonstrate the emergence of zero-lag synchronization mediated by dynamical relaying between neuronal network populations. In our case, the output of each NM is converted into a firing rate (see Equation (5.4) above) impinging on a subpopulation of 2000 neurons within the neuronal network. In turn, the firing rate of these selected neurons contributes to both the excitatory and inhibitory postsynaptic potential densities that act upon the pyramidal populations of the NMs. We also examine the effect of varying several properties of the subpopulation of neurons of the NN, including its number, involved in the coupling, in order to explore the effect of the structural properties of that network on the scale interaction efficiency.

The effect of the coupling intensity $k$ on the dynamics of the interacting populations is shown in Figure 5.2. When the NMs are uncoupled, they oscillate in different dynamical regimes that evolve at different frequencies, around 4.5 Hz and 11 Hz respectively. One NM oscillates in a spike-like fashion, while the other one oscillates more harmonically (Figure 5.2A, compare the blue and green lines). The neuronal network, in turn, exhibits collective oscillations within the gamma range, around 45 Hz. The dynamical evolution for the coupled case, at $k = 1$, is shown in Figure 5.2B. In this case, the dynamical regimes of the NMs are similar, and they become frequency locked. We scan $k$ in order to track the transition to the frequency locked regime as coupling increases. Figure 5.2C shows the increase in the maximum cross covariance between the net postsynaptic potentials of the two NMs models, averaged over 20 trials, when increasing $k$. When the NMs operate at different regimes they hardly synchronize but, for sufficiently high $k$, they increase their synchronization with increasing $k$. The averaged frequency mismatch decreases sharply at $k \approx 0.6$ (see Figure 5.2D). According to these results, frequency locking for the two NMs is achieved through a neuronal network that oscillates naturally at a much faster scale.

We further characterize the effect of the interaction through the power spectrum of the time traces. As can be expected, the power spectrum of the mass models in isolation (Figure 5.3A) shows a clear peak at their natural frequencies (4.5 Hz and 11 Hz), while the LFP shows a strong peak around 45 Hz (Figure 5.3C) that exceeds the non-zero contribution of the slower frequencies $\sim$4 Hz. We see that increasing coupling leads to a frequency locking regime between the NMs, which is reflected in their spectral behavior. For instance, at $k = 1$ the power spectra of the two NMs overlap, with a dominant peak around 4 Hz (Figure 5.3B). The local gamma peak of the neuronal network is preserved (Figure 5.3D), although the major change in amplitude occurs at smaller rhythms, around the frequency of the NMs. This increase in the NN power at the alpha band is due to the emergence of phase locking between this population and the outer NMs, as shown in Figure 5.3E. This phase locking results in a sizable

cross-correlation between the activities of the microscopic and mesoscopic populations for intermediate values of the size $N$ of the NN subpopulation coupling the two NMs, as depicted in Figure 5.3F (the difference between cross-correlations with NM1 and NM2 for small $N$ is due to the different intrinsic dynamics of the two mesoscopic populations). The effect of $N$ is studied in more detail below. The slower time scale of the NMs cannot follow the faster dynamics of the NN and average out the gamma rhythm, resulting in a frequency shift towards the slower rhythm, which is also enhanced in the neuronal network.

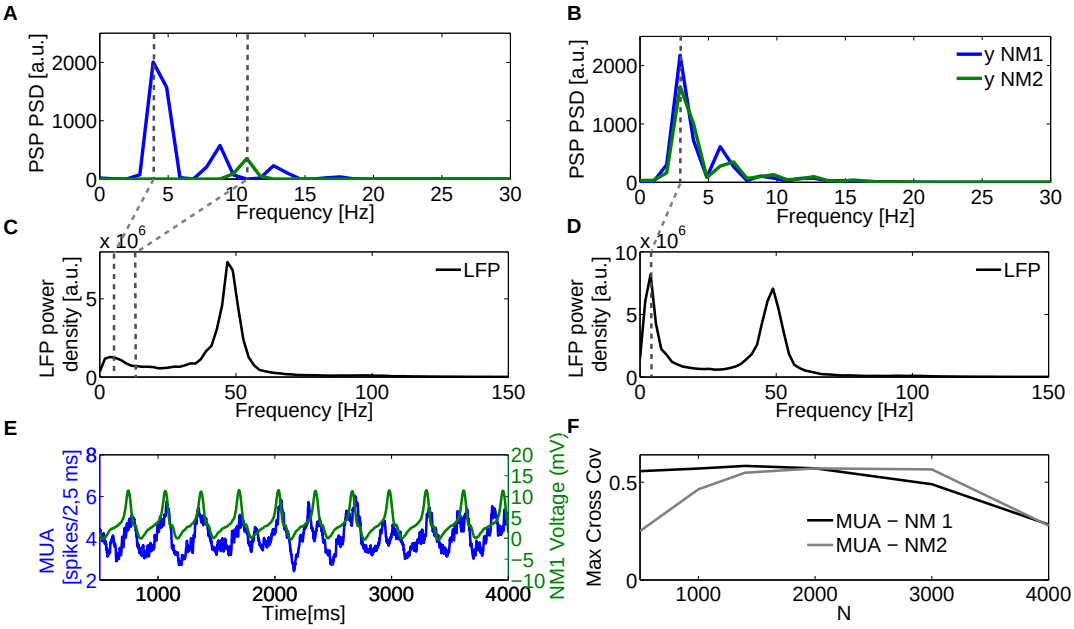


Fig. 5.3 **Effect of coupling on the power spectra of the three neuronal populations.** (A) Power spectra of the net postsynaptic potential $y(t)$ of the NMs in isolation. Primary peaks are tagged with vertical dashed lines at ∼4.5 Hz and ∼11 Hz. (B) Power spectra of the net postsynaptic potential $y(t)$ of the NMs when coupled ($k = 1$) through a subpopulation of 2000 neurons within the NN. The common primary peak is tagged with a vertical dashed line at ∼ 4 Hz. (C) Power spectrum of the LFP of the neuronal network in isolation. (D) Power spectrum of the LFP when the subpopulation of the neuronal network is coupled ($k = 1$) to the NM models. Spectral densities are averaged over 20 trials. (E) Time traces of the MUA signal of the neuronal network (blue, left axis) and the voltage of neural mass 1 (green, right axis). The MUA is calculated using a sliding window of length 50 ms. (F) Correlation between the MUA and voltage signals shown in panel E as a function of the number of neurons from the central NN involved in the communication between the two NMs. From Barardi et al. (2014a).

Since the output of the neuronal network arises from the spiking activity of thousands of neurons, the interaction across models is mainly driven by the average dynamics of the population. Although the modeled LFP evolves in a faster time scale, NM models filter out

rapid fluctuations. Therefore, the NMs mainly respond to changes of the mean input coming from the neuronal network modulated by $k$.

The input contribution into the NMs coming from the NN dynamics increases the average excitatory and inhibitory input signal into the pyramidal population (denoted by $p_e$ and $p_i$, respectively, in Equations (5.6)-(5.7) above). Since increasing the constant input to a NM can lead to changes in the dynamical regime (and thus the frequency) of the oscillator (Grimbert and Faugeras, 2006b), one could argue that the role of the neuronal network dynamics is unnecessary to mediate the synchronization transition observed. However, simulations in which the terms given in Equations (5.6)-(5.7) are replaced by the temporal average of the coupling contributions indicate that the NMs are unable to synchronize their phases in these conditions (Figures 5.4A,B). This result shows that the NN dynamics is a key ingredient to achieve not only frequency locking but also phase locking between the two NMs.

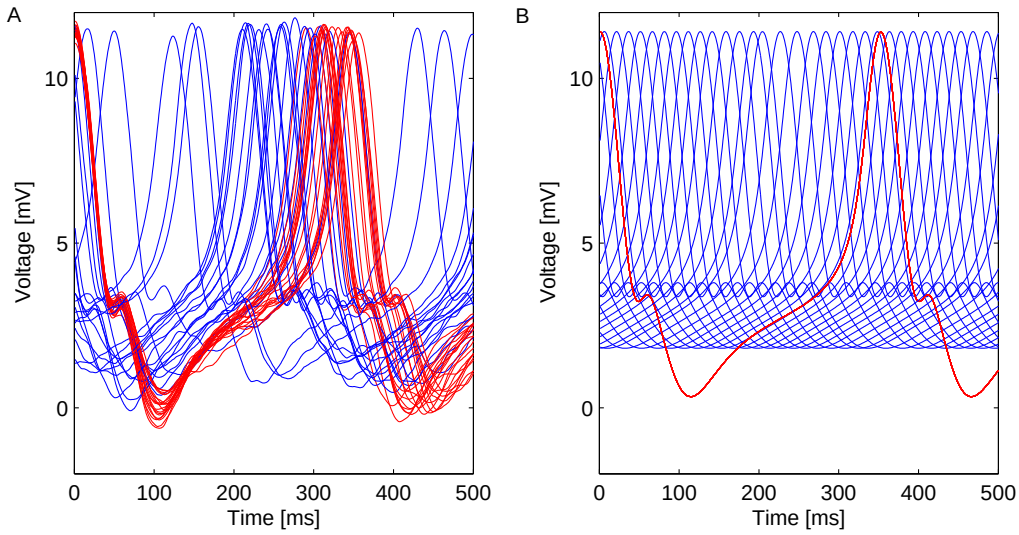


Fig. 5.4 **Coupling of NMs through dynamically evolving NN vs constant input.** Phase consistence of different trials of PSPs of the NMs (the two colors correspond to the two NMs) when the coupling is mediated by a variable MUA (coming from the NN) (A) and when MUA is replaced by its temporal average (B). In the latter case NMs are unable to synchronize their phases.

In order to take advantage of the microscopic description of the NN we also vary two main features of its architecture: its clustering (see definition in Appendix A.5) (Figures 5.5A,B) and the size of the area involved in the coupling, determined by the number of neurons projecting onto the NMs (Figure 5.6). Figure 5.5A,B outlines the dependence of the maximum cross covariance and the frequency mismatch between the two NMs on the coupling strength

$k$ for different $r_p$ values. Note that the case $r_p = 1$ corresponds to the results shown in Figures 5.2C,D. Networks with higher clustering ($r_p = 0.2$) are less efficient in synchronizing the oscillatory output of the NMs. In this case, larger coupling strengths $k$ are needed, with respect to a random network ($r_p = 1$), to reach the frequency locking regime. Thus, the topology of the NN affects the synchronization between the neural ensembles. Random networks have small path lengths at the expense of low clustering, and thus the average transmission time of the action potentials across the population is decreased. In this situation, synchronization arises for smaller coupling strengths. The result for a regular network, $r_p = 0$ (which is not a realistic situation in the brain because the NN dynamics is lost), is also included.

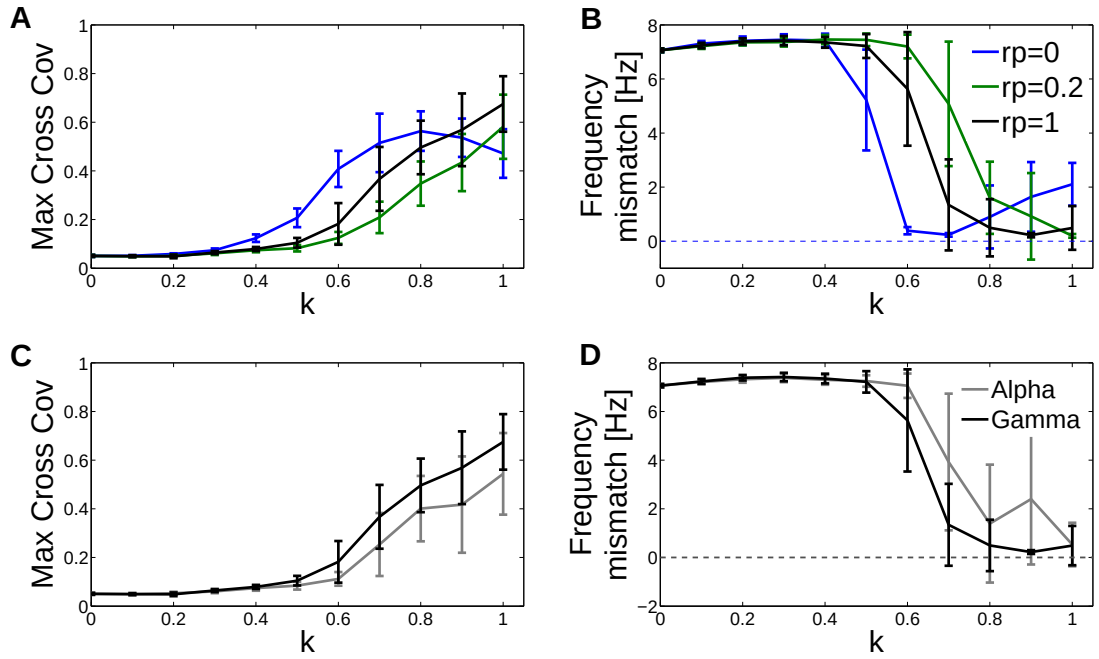


Fig. 5.5 **Influence of the topological and dynamical properties of the neuronal network on the interaction between the NMs.** Maximum cross covariance (A) and frequency mismatch (B) between the NM average postsynaptic potentials for increasing rewiring probabilities $r_p$ of the neuronal network. Maximum cross covariance (C) and frequency mismatch (D) between the NM average postsynaptic potentials when the neuronal network works in the alpha regime, compared with the gamma case ($r_p = 1$). From Barardi et al. (2014a).

Besides topology, the intrinsic dynamics of the neuronal network also has an impact on the synchronization of NMs. In our NN model we can slow down the frequency peak of the LFP by increasing the decay time constant $\tau_{decay}$ of the inhibitory synapses, without altering the firing rate of the population. If the peak of the NN power spectrum is shifted towards the

alpha band, closer to where the NMs oscillate, the maximum cross covariance is reduced and the frequency mismatch is increased for a given $k$ value (Figures 5.5C and 5.5D, respectively). Thus, even though the NN is operating closer in frequency to the NMs, and its individual neurons fire at the same rate as when the network operates in the gamma band (resulting in a similar MUA activity, result not shown), the NMs are more difficult to synchronize. In the NN, the action potentials are transiently synchronized and paced according to the time course of inhibition, leading to a recurrent behavior that causes the global oscillatory dynamics. Faster rhythms, like gamma, correspond to a better precise timing of the firing, i.e. the action potentials of multiple neurons are tightly bounded in time, which seems to be key for the synchronization of the NMs.

Finally, and as mentioned above, we also study how the synchronization of the NMs is affected by the size $N$ of the subpopulation of neurons that mediate the coupling between them. In the results presented so far, this subpopulation was formed by $N = 2000$ neurons, randomly chosen from the whole population of 4000 neurons of the NN. We scan $N$ between 1 and 4000 neurons, the latter case corresponding to all neurons in the NN contributing to the firing rate impinging on the NMs and receiving their input. Figures 5.6A,B show the maximum cross covariance and the frequency mismatch for increasing coupling $k$ at varying subpopulation sizes. The interaction between the NMs decreases as $N$ decreases, and synchronization is only significant for $N > 1000$. $N$ directly affects the strength of the coupling between the NN and the NMs, since this parameter determines the average MUA, i.e. the number of spikes elicited within the subpopulation. Hence, given a coupling strength $k$ that enables an efficient interaction of the models, larger values of $N$ lead to a lower frequency mismatch (Figures 5.6C,D).

It is important to note that, although the size of the NN is kept constant, increasing $N$ boosts the coupling term, spreading the input from the NM across a larger population of neurons within the NN. Figure 5.6E shows the LFP power spectrum for increasing values of $N$ for $k = 0.9$. Similarly to the transition from Figure 5.3C (network in isolation) to Figure 5.3D ($k = 1$ for $N = 2000$), the major changes produced by the coupling occur at small frequencies, where the synchronization scale is centered, while the gamma rhythm interacts directly with the slower dynamics of the NMs. Decreasing $N$ dramatically affects the dynamics of the coupling, which only takes into account the activity of this subpopulation. For sizes below $N \sim 1000$ the interaction is carried out by the low firing and highly noisy activity of small numbers of neurons, which are unable to synchronize large ensembles (Barardi et al., 2014a).

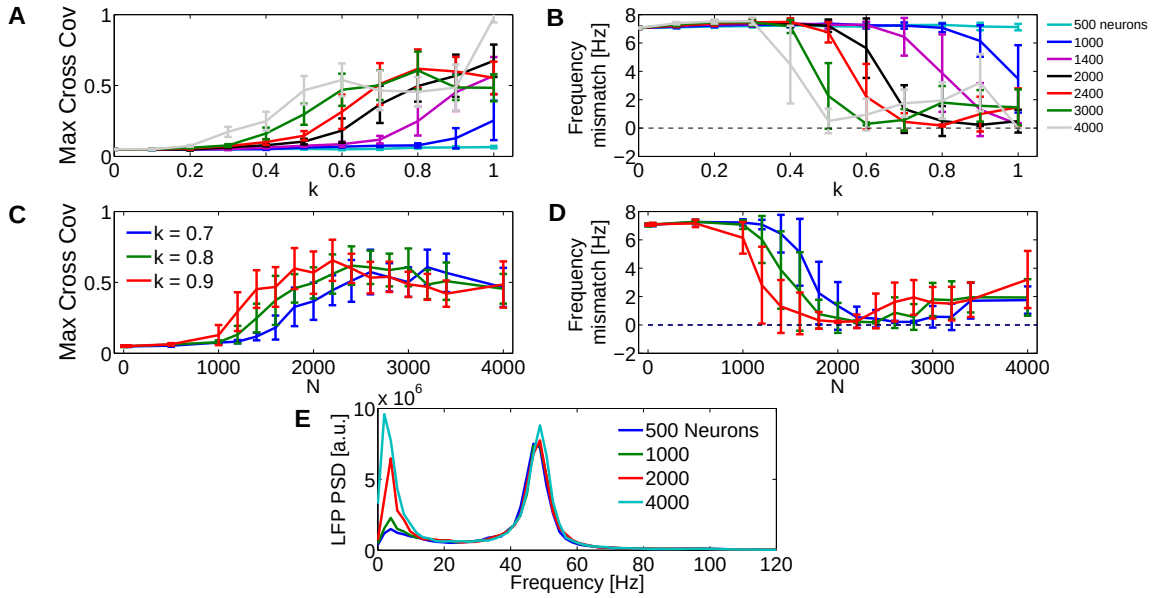


Fig. 5.6 **Dynamics of coupled NMs.** Maximum cross covariance (A) and frequency mismatch (B) between the NM average postsynaptic potentials as a function of coupling strength $k$, for various values of the size $N$ of the subpopulation of the neuronal network that mediates the coupling. (C,D) Same quantities as a function of $N$ for various values of the inter-scale coupling strength $k$. (E) Spectral power density of the LFP of the whole NN, when the NMs are connected with NN subpopulations of various sizes ($k = 0.9$). All results are averaged over 20 trials. From Barardi et al. (2014a).

## 5.4 Conclusion

In this Chapter we have focused on how the microscopic and macroscopic scales coexist in a system-wide description of the brain. Due to the computational unfeasibility of modeling the dynamics of the full brain from a purely microscopic scale, we envision the need of including both scales in a hybrid description of the brain. In this scenario, one would need to represent at the level of neuronal networks only those neuronal populations involved in a particular task (for instance a certain region of the visual cortex in the case of situations involving visual stimulation), and which are monitored with single-cell resolution. The rest of the brain, while modulating the activity of the population of interest, would not require being represented with microscopic detail (and it would be impractical to do so). Currently this is accomplished by substituting the activity of the rest of the brain by a background *noisy* activity, but this approach is not useful when the neuronal population of interest feeds back into the external brain regions, thereby modifying the background activity acting upon the population itself.

One way of facing this situation is by coupling bidirectionally microscopic and mesoscopic descriptions of neuronal populations, as is considered in this work. Both types of descriptions have been carefully studied in the past (in particular both the fine-grained activity of neuronal networks and the simplifications inherent in neural mass models have been well characterized), and here we intend to make these two well-known descriptions interact. In particular, we use synchronization in order to probe the interaction between the two scales. Our reason for employing specifically a scheme in which two mesoscopic populations are coupled through a third microscopic network is that the behavior that can be expected from two coupled neural mass models is well known, and can be used as a reference for the coordinated behavior emerging from our hybrid scenario.

Furthermore our results do not imply that two NM oscillators can only synchronize through the mediation of a neuronal network. In fact if all three neuronal populations were described by NNs (or by NMs, for that matter) synchronization will also arise (see for instance Vicente et al. (2008) and Gollo et al. (2010) for the case of three coupled NNs leading to zero-lag synchronization). Neither do we claim that two brain oscillators can only synchronize through the mediation of a third one (see for instance David and Friston (2003) for an example of synchronization between two coupled NMs). The results show that two mesoscopic brain oscillators can synchronize even when they are coupled only through a mediating population that is described by a microscopic model. In that sense, we use synchronization as a tool to probe the interaction between different spatial scales of neuronal populations. Previous efforts have been devoted to analyzing this interaction by performing a direct comparison of the behaviors of the microscopic and mesoscopic models. Faugeras et al. (2008), for instance, derived the equations of evolution of NMs from the dynamics of a network of neurons described by a voltage-based model, by performing an involved mean field analysis of the network, an approach that would be very challenging to apply to spiking neuron models. In order to perform such a multi-scale mapping, Rodrigues et al. (2010) had to apply strong assumptions that included high correlation between the neurons in the microscopic populations and low-amplitude input currents. Here we have attempted to circumvent the complexity of those approaches by using a more phenomenological strategy, whose goal is to test whether microscopic and mesoscopic descriptions of neuronal populations communicate with one another by using synchronization as a proxy of effective communication.

Even when the neuronal network operates in a fast dynamical collective regime in the gamma range, a sufficiently large subpopulation of neurons within that network is able to mediate the communication and subsequent synchronization between two NMs that are described mesoscopically and operate at much lower frequencies (Figure 5.3). Frequency and phase locking arise even when the two NMs operate at very different frequencies (in the theta

and alpha bands) and with very different dynamical features (spike-like dynamics in one case and quasi-harmonic dynamics in the other). Structural clustering within the neuronal network diminishes the ability of the microscopic neuronal population to induce synchronization (Figure 5.5). The size of the subpopulation of neurons that directly coupled the two NMs must also be large enough to allow the intrinsically irregular neurons to reach a sufficiently strong collective regime through which the two neural masses can communicate (Figure 5.6).

Two main features indicate the nontrivial contribution of the microscopic neuronal network in mediating the synchronization between the mesoscopic models. First, the two mesoscopic populations lock not only in frequency, but also in phase, when they interact with a dynamically evolving neuronal network. If the role of the network is played by an increased constant input to the neural masses equal to the average activity of the neuronal network, phase locking disappears (Figure 5.4). Second, if the neuronal network is made to operate in a slower collective regime (e.g. in the alpha band) the synchronization between the NMs is decreased (while being still significant), even though the three oscillators are now closer in frequency.

The synchronization between the NMs is mediated by the locking between the NMs and the NN, which leads to an increase in the alpha-band activity of the NN, as reflected in Figure 5.3. The fact that synchronization is maintained even when the NN is operating in the alpha band (Figures 5.5C,D) indicates that the intrinsic NN dynamics does not interfere noticeably in the communication between the NM populations. Furthermore, the fact that synchronization improves slightly when the NN is operating in gamma (as shown also in Figures 5.5C,D) shows that fast and slow scales interact to a certain extent in order to drive the synchronization. We interpret this to be due to an increase in the precise timing of the firing that is associated with a faster neuronal rhythm. The results reported here point towards an alternative way to probe the interaction of scales in the activity of the brain, by using synchronization between neuronal populations as a way of testing the structural and functional conditions under which scale interaction occurs (Barardi et al., 2014a).

So far, we have broadly studied spatiotemporal patterns of activity arising from the coordinated activity of many neurons. Neuronal oscillations, omnipresent in the brain, reveal a certain synchrony if measured at multiple sites with intracranial electrodes or with EEG (Buzsáki and Draguhn, 2004). The temporal progression of activity behind this neuronal synchrony exhibits approximately identical phase across different recordings sites (Zanos et al., 2015). However, out-of-phase activity exists and could give rise to complex spatiotemporal patterns such as traveling waves. In the next Chapter, we mathematically investigate the emergence of traveling waves across different neuronal systems.

# CHAPTER 6

# WAVE PROPAGATION IN INHIBITION-DOMINATED NEURONAL CHAINS

The correct operation of the brain relies on a careful spatiotemporal coordination of selective neural populations which self-organize in different collective patterns at various scales. In the previous chapters we have described the synchronization of neuronal oscillations within and between populations located at distant brain areas using different modeling approaches. Neuronal collective oscillations are a ubiquitous property of neural activity and reveal a certain consistence in space (in the form of the same phase across recording sites). However, out-of-phase synchronous oscillations also exist, in the form of complex spatiotemporal patterns such as propagating waves. These waves, from macroscopic scales spanning multiple cortical areas to microscopic scales involving single neurons, constitute another important signature of neuronal collective dynamics likely to subserve network-level computations among brain areas. Localized neural activity either remains spatially confined in time or propagates as a wave among neural assemblies that are spatially separated but engaged in the same computation or behavioral state. In what follows we study the propagation of traveling waves in a one-dimensional network of inhibitory neurons with asymmetric synaptic coupling. We first show the phenomenon of wave propagation arising from a network of Hodgkin-Huxley neurons in a chain of inhibitory neurons with asymmetric connections. This has opened interesting questions that need to be addressed from a mathematical point of view. Therefore, we provide a continuum model with topology similar to the HH model to explain several counterintuitive properties of these traveling waves. Then we investigate how general this wave-propagation is by considering various parameters that characterize neuronal interactions such as the balance of external excitation and recurrent inhibition, the axonal delays, the synaptic temporal time constants and the structural connectivity. To do so, we move to the analysis of a continuum approximation of the IF model that allows the calculation of the dispersion curve relating the velocity and wavelength of these waves, and study how the dispersion relation, and thus the

wave dynamics, depend on different parameters. In this way we aim at providing analytically important insights on the necessary and sufficient conditions that support the wave-like behavior in such a system.

The structure of this Chapter is as follows. In Section 6.1 we discuss the phenomenon of traveling waves in the brain, following Section 1.5. We first present, using a Hodgkin-Huxley model, how inhibitory neurons, asymmetrically connected along a chain, organize themselves in propagating waves under specific conditions (Section 6.2). After this phenomenological analysis, we proceed with an analytical explanation of the observed pattern. We begin in Section 6.3 by introducing a continuum model with topology similar to the HH model based on a one-dimensional chain of inhibitory neurons with asymmetric coupling and then turn to a integrate-and-fire continuum model (Section 6.4) that provides an understanding of numerical results and of the necessary conditions under which a system can exhibit waves propagation. Conclusions about our work are presented in Section 6.5. This work is developed in collaboration with prof. Evgueniy V. Lubenov, who led the project and prof. Athanassios G. Siapas (Caltech).

## 6.1 Wave propagation

A number of experimental studies have revealed the propagation of traveling bursts of activity in slices of excitable neural tissue spanning from the retina to the neocortex (Destexhe et al., 1996a; Golomb and Amitai, 1997; Golomb et al., 1996; Kim et al., 1995; Traub et al., 1993). Traveling waves constitute a highly coordinated activity of neurons which fire rhythmically, with the oscillation phase varying as a function of time and space (Ermentrout and Kleinfeld, 2001). Such wave propagation phenomena are enabled by spatial confinement of connections between neurons. In fact within a certain brain area, the probability of a synaptic connection to exist between a pair of neurons decreases with their physical distance separation (Gilbert, 1993; Sik et al., 1995; Stepanyants et al., 2008). In that situation, spiking activity spreads from a group of neurons to its neighbors and onto the rest of the network as a propagating wave (Wang, 2010b). Neuronal wave propagation has been observed on multiple spatial scales. In fact as we have discussed in Section 1.5.2, traveling waves have been found in a diversity of studies (reviewed in Ermentrout and Kleinfeld, 2001 and Wu et al., 2008), including MEG gamma oscillations (Llinas and Ribary, 1993; Ribary et al., 1991), EEG slow sleep oscillations (Massimini et al., 2007), evoked responses in the cortex (Arieli et al., 1995; Freeman and Barrie, 2000; Prechtl et al., 1997), waves in developing cerebellar cortex (Watt et al., 2009) and hippocampal theta oscillations in rats (Lubenov and Siapas, 2009) and humans (Zhang and Jacobs, 2015). In a recent study, Lubenov and Siapas (2009) observed

traveling waves during theta oscillations propagating along the septotemporal axis of the CA1 region of the hippocampus, with phase velocity $v \approx 80$–$100$ mm/s and spatial wavelength $\lambda \approx 10$–$15$ mm. Given that the length of the septotemporal axis of CA1 is L $\approx$10 mm, the total phase difference is L/$\lambda$, between $1.3\pi$ and $2\pi$ radians, i.e., two-thirds to a full theta cycle. Interestingly, in all existing studies, the total phase shift is often $\approx \pi/2$, always less than $2\pi$ radians (i.e., the spatial extent of the wave is less than one wavelength). Thus, the observed pattern of variation in peak amplitude is less than the full oscillation cycle, regardless of oscillation frequency (e.g., theta or gamma), the physical size of the neural system, or the species examined (see Table 1 in Ermentrout and Kleinfeld, 2001).

Neural field models have been successfully applied to model a diversity of brain spatiotemporal wave patterns, and one of the main issues when modeling neural fields is the connectivity among neurons (Bressloff et al., 2003; Coombes and Laing, 2011). Many theoretical and modeling works based on neural field theory have focused on the study of traveling waves under variations in neural connectivity, concentrating mainly on symmetric connectivity among neurons (Coombes, 2005; Coombes et al., 2003; Ermentrout, 1998b). In contrast, less attention has been given to the emergence of propagating waves when the neural connectivity is asymmetric (Bressloff and Wilkerson, 2015; Horikawa, 2014; Woodman and Jirsa, 2013). A typical mechanism for generating traveling pulses in an excitatory network is to include for instance spike frequency adaptation (SFA) (Coombes and Owen, 2005; Pinto and Ermentrout, 2001) or synaptic depression (Kilpatrick and Bressloff, 2010a,b), which suppress the trailing edge of the wave. One of the motivations for considering excitatory neural fields is that traveling pulses are observed in *in vitro* cortical slices that have been disinhibited. By way of example, Bressloff and Wilkerson (2015) used a one-dimensional scalar neural field with an asymmetric weight distribution to analyze the effects of extrinsic noise on traveling pulses in a neural field model of direction selectivity. Instead of SFA or synaptic depression, they considered a mechanism based on asymmetric excitatory synaptic connections and showed that such a network architecture supports freely propagating pulses.

Computational models of synaptically generated waves have also been developed, in which neural tissue is treated as a one-dimensional continuum (Destexhe et al., 1996b; Golomb et al., 1996; Traub et al., 1993). From these studies, it follows that wave propagation in cortical and hippocampal slices only occurs if the synaptic strength of neuronal interactions exceeds some threshold, and provided above threshold the velocity is approximately linear in the coupling (Golomb and Amitai, 1997). How wave properties depend on the synaptic and intrinsic cellular properties of the neurons and on the topology of the network is an interesting question. This is difficult to extract from detailed computational models. In this Chapter we perform a qualitative analysis of the phenomenon using a conductance-based model, and we provide a

continuum approximation of the analytically tractable IF model to derive some conclusions on the conditions leading to wave propagation.

In this study, we focus on exploring the emergence of traveling waves in a chain of only inhibitory neurons with asymmetric couplings. To do so we use first a spiking neural network model, specifically the conductance-based model (see Section 2.1.3), to show how a chain of inhibitory neurons supports traveling waves. Our results demonstrate that these networks behave as excitable media that exhibit anomalous dispersion, and therefore have counterintuitive wave-propagation properties. In particular, when neurons at the head of the chain are periodically forced, traveling waves emerge with wavefronts moving from the tail to the head of the chain, in a direction opposite to that of synaptic connectivity. We develop a continuum model with topology similar to the HH model that can be solved analytically (based on Kistler and van Hemmen, 1998) to demonstrate the existence of backward waves. This study provides an analytic explanation of some properties of wave propagation exhibited by the system in specific conditions, and speculate on why long wavelengths are not allowed under the conditions adopted in this configuration. We ask if wave patterns arise in a different system, e.g. with a varying degree of asymmetry in the direction of connectivity, in presence of synaptic axonal delays and different synaptic conditions, thus if our results can be extended to different configurations. However, it is very challenging to systematically proceed with a sensitivity analysis starting from a detailed physiological model.

Ermentrout (1998a) showed that a simple integrate-and-fire (IF) model (Section 2.1.1) of a neuron captures much of the process underlying an excitation wave in cortical slices. In fact, he demonstrated that the velocity of a wave in the case of strong synaptic coupling is essentially independent of the ionic details of cell membranes, depending mainly on the integration rise time from the resting potential to threshold. Thus, inspired by Bressloff (2000), we propose an integrate-and-fire continuum approximation to study systematically the properties of these waves in a framework commonly used in this kind of studies. We derive a self-consistency condition for the existence of traveling waves, from which we calculate a dispersion relation as a function of the phase velocity and spatial wavelength, and use it to investigate how wave-propagation depends on various parameters that characterize the neuronal system. Specifically, we explore how the shape of the dispersion relation varies by introducing axonal delays in the signals transmission between neurons, by varying the GABA temporal decay time constant, by modulating the level of excitation and inhibition in the networks by means of synaptic strengths, and finally by altering the degree of asymmetry in the network.

## 6.2 Phenomenological analysis

As mentioned above, we focus on the dynamical propagation of neuronal waves across one-dimensional chain of inhibitory HH neurons with asymmetric connections. By periodically forcing a small subset of neurons at the head of the chain, we demonstrate that this system can support the propagation of wave patterns, provided that some conditions are met. We then characterize this behavior by calculating the dispersion relation that relates the entrained angular frequency to the wavenumber of the propagating waves. After this phenomenological analysis, we provide mathematical insights on how this phenomenon, which arises here under strong assumptions, can be extended to different dynamical systems with different properties.

### 6.2.1 Computational model

We model a chain of inhibitory Hodgkin-Huxley (HH) neurons using a conductance-based formalism. Neurons are arranged along a one-dimensional chain of $N = 1000$ inhibitory cells. Initially we assume that all neurons project asymmetrically to one-side of the 1-d chain in a regular way, namely each neuron $i$ makes synaptic connections with neighboring neurons $j$ ranging from $j = i+1$ to $j = i+\gamma$ along the chain, where $\gamma$ is the window connectivity, initially set to $\gamma = 50$ neurons (see scheme in Figure 6.1). In this first study only chemical synapses are considered and synaptic delays are not taken in consideration. In Section 6.3 we will consider a network with a different level of asymmetry in the connectivity and introduce increasing synaptic delays. One mechanism that allows this system to generate and sustain wave-like behavior consists on driving some neurons at the bottom of the chain with an external source, while keeping constant in time the external current over all the remaining neurons of the chain. In particular, a certain number of neurons at the bottom of the chain are periodically driven with a constant external current during a period $T_f = T_{ON} + T_{OFF}$. This current takes the voltage of the neuron above the firing threshold, thus enabling the generation of the action potential, provided that its refractory window has expired. $T_{ON}$ and $T_{OFF}$ represent the interval where the neuron is forced to spike and where it is shut down, respectively. This perturbation starts at the bottom of the chain and propagates in time across the size of the network, provided different parameters are properly tuned: e.g. the forcing period, the number of perturbed neurons at the bottom, the synaptic strengths and the temporal constants of postsynaptic potentials. Note that these parameters are functions of each other, e.g. the number of perturbed neurons at the bottom is tuned accordingly to the synaptic strengths and the forcing period. Therefore under certain conditions, the network presented here exhibits wave-like patterns that will be described in the next Sections.

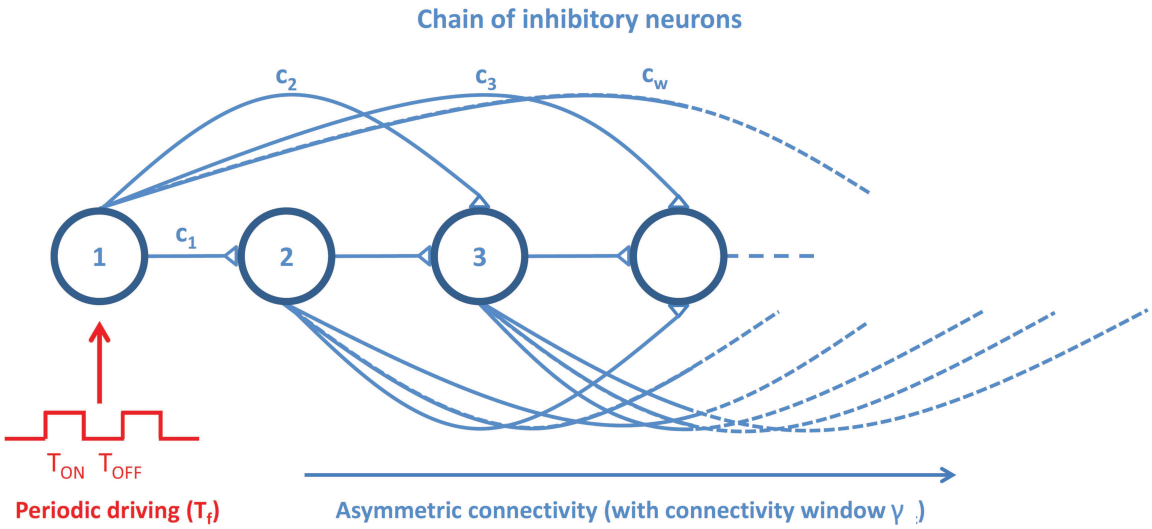


Fig. 6.1 **Illustrative plot of chain of inhibitory neurons asymmetrically connected.** Scheme of the network with asymmetric connectivity. Each neuron project to its $\gamma = 50$ neighbors along the chain of $N = 1000$ neurons. A subset of 45 neurons at the bottom of the chain is periodically driven with a forcing period $T_f = T_{ON} + T_{OFF}$.

All neurons are modeled according to the Hodgkin and Huxley (HH) model described in Chapter 4, where the evolution of the membrane voltage and voltage-gated ion channels is described by Equations (2.9)-(2.11) introduced in Chapter 2. In this analysis, the membrane capacitance of inhibitory neurons is set to $C = 0.125$ nF, the maximal conductances of the sodium, potassium and leakage channels are respectively $g_{Na} = 12.5\ \mu$S, $g_K = 4.74\ \mu$S, and $g_L = 0.025\ \mu$S and the reversal potentials $E_{Na} = 40$ mV, $E_K = -80$ mV, and $E_L = -65$ mV respectively. The time course of the synaptic currents between neurons is given by the alpha function introduced in Equation (4.4) in Chapter 3, which depends on the GABA rise $\tau_{rise}$ and decay $\tau_{decay}$ temporal constants and on the synaptic strengths defined in Tables 6.1 and 6.2, respectively. Different $\tau_{decay}$ values will be explored in Section 6.3. The model is integrated using the Heun algorithm (Toral and Colet, 2014), with a time step of 0.05 ms.

| Synaptic time constants ( ms) | $\tau_{rise}$ | $\tau_{decay}$ |
|---|---|---|
| AMPA | 0.5 ms | 2 ms |
| GABA | 2 ms | 15 ms |

Table 6.1 Synaptic time constants.

| Synaptic conductances $g_{syn}$( nS) | |
|---|---|
| GABA on inhibitory ($q_c$) | 240 nS |
| $AMPA_{external}$ on inhibitory ($Q_c$) | 3.2 nS |
| **Synaptic reversal potential $E_{syn}$( mV)** | |
| $E_{GABA}$ | $-70$ mV |
| $E_{AMPA}$ | 0 mV |

Table 6.2 Synaptic conductances and synaptic reversal potentials.

### 6.2.2 Backward wave propagation

Our results reveal that one-dimensional chains of inhibitory neurons with asymmetric connections exhibit wave-like behavior. If a subset of neurons at the bottom of the chain is periodically driven with a given driving period $T_f$, traveling waves emerge with wavefronts moving from the tail to the head of the chain, in a direction *opposite* to that of synaptic connectivity (see Figure 6.3). The characteristics of these traveling waves depend on the connectivity window $\gamma$ and the *forcing period* $T_f$ that determines the duration of the active band (Figure 6.3A). If the chain is not properly driven at the bottom, namely $T_{ON}$ is not large enough to allow perturbations to propagate, and $T_{OFF}$ is not large enough to allow neurons to recover from inhibition, the system settles into an horizontal attractor, with horizontal stripes spaced every $\gamma$ neurons (Figure 6.2).

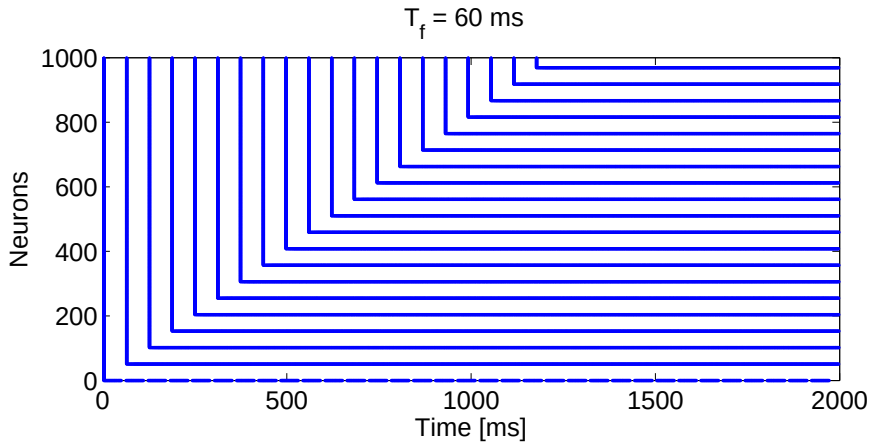


Fig. 6.2 **Firing dynamical patterns of the chain at its horizontal attractor.** The chain is composed of 1000 inhibitory neurons and each cell is connected with the neighboring $\gamma = 50$ neurons. The network is driven with a driving period $T_f$ = 60 ms. $T_{ON}$ is not properly set thus the network settles into its natural horizontal attractor, taking the form of constant stripes of active neurons spaced at the connectivity window $\gamma$. $T_{OFF}$ is not large enough to make the postsynaptic partner recover from inhibition and fire during that time interval. So, if not properly driven at the bottom, the system can not exhibit traveling wave patterns.

In order to obtain this wave-like behavior, the synaptic strengths need to be tuned to have an appropriate balance between external excitation and recurrent inhibition, so the network can foster wave propagation. In Section 6.3 we will study how the excitation over inhibition ratio affects wave dynamics. To this aim, we define two additional parameters $Q$ and $q$, that represent the magnitude of the persistent excitatory conductance and inhibitory synaptic conductance respectively, as $Q = Q_c * 10$ and $q = q_c/8$, where $Q_c$ and $q_c$ are the basal values of the model defined in the Table 6.2. In Figure 6.4, wave patterns with decreasing spatial wavelength for increasing values of $T_{OFF}$ are presented. These results are robust across different models such as current-based and conductance-based integrate-and-fire models under the same conditions (results not shown).

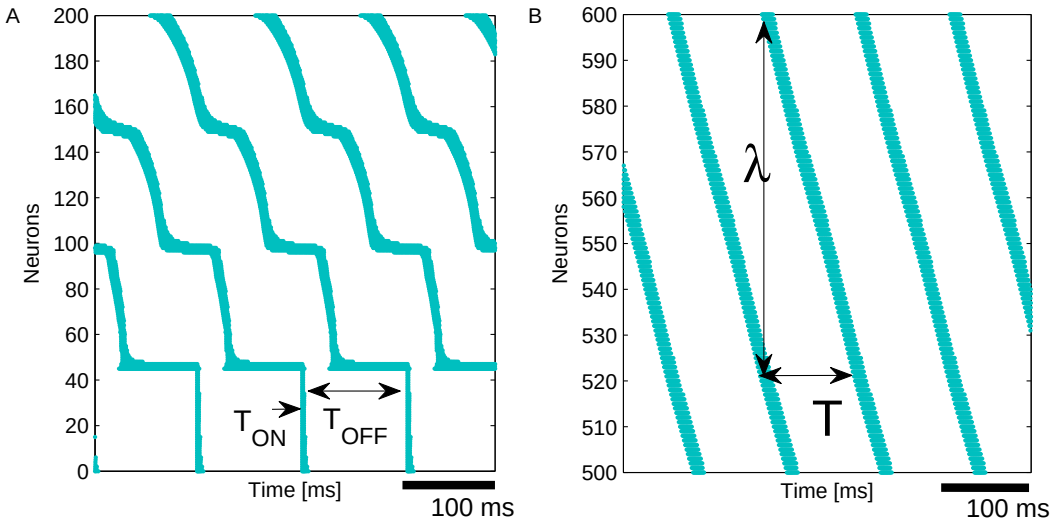


Fig. 6.3 **Zoom of propagation of backward waves in inhibition-dominated chains.** Propagation of backward -with respect to the direction of connectivity- waves with inhibition-dominated chains using a Hodgkin-Huxley neuron model. Here it is shown the zoom of backward waves in case of $T_{ON} = 2$ *ms* and $T_{OFF} = 90$ *ms* for neurons in the range (A) $0-200$, where $T_{ON}$ and $T_{OFF}$ are depicted and in the range (B) $500-600$, the spatial wavelength $\lambda$ and the wave period $T$ are drawn.

The spatial wavelength $\lambda$ and the period $T$ of the wave cycle, depicted in Figure 6.3B, determine the phase velocity of the wave, is defined as $v = \lambda/T$, which represents the speed at which the phase of the wave at any frequency propagates in space. It is equivalently defined as $v = \omega/k$, where $\omega$ is the angular frequency of the wave and $k$ is the wavenumber. In contrast, the group velocity is equal to $v_g = d\omega/dk$, and represents the velocity of propagation of the wave envelope. The dependence of the angular frequency $\omega$ on the wavenumber $k$ is known as the dispersion relation $\omega = \Omega(k)$. Figure 6.5A shows the dispersion relation as $f = \theta(m)$, where $f$ is the frequency and $m$ is the ratio between the size of the chain $N$ and the

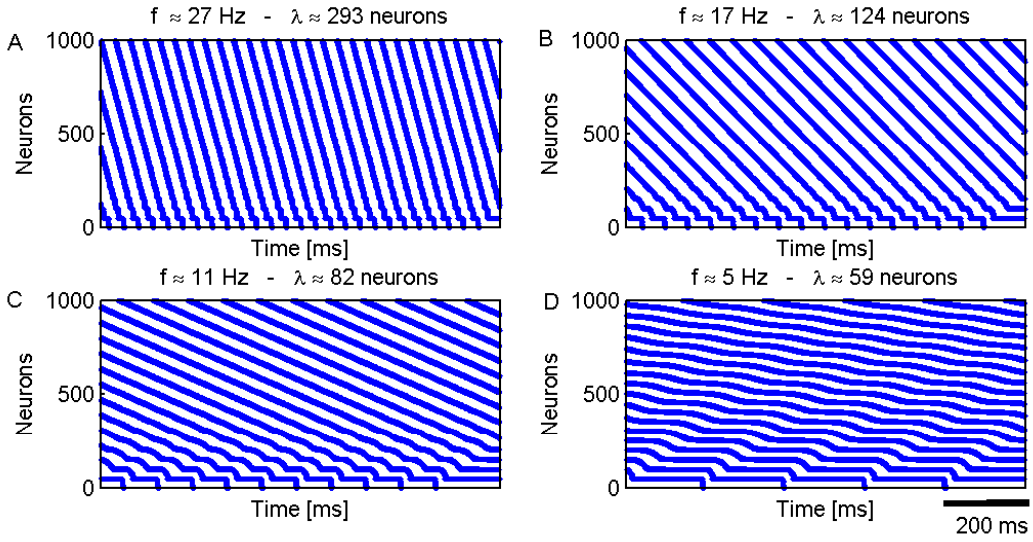


Fig. 6.4 **Propagation of backward waves in inhibition-dominated chains.** Propagation of backward waves -with respect to the direction of connectivity- with inhibition-dominated chains using a Hodgkin-Huxley neuron model. Each neuron projects to its $\gamma = 50$ neighbors along a chain of $N = 1000$ neurons. A subset of neurons at the bottom of the chain is periodically driven with a forcing period $T_f = T_{ON} + T_{OFF}$. In this plot $T_{ON}$ is equal to 2 ms, while $T_{OFF}$ is equal to (A) 35 ms, (B) 55 ms, (C) 85 ms and (D) 200 ms. For each panel the wave frequency $f$ and the spatial wavelength $\lambda$ are calculated, from which the dispersion relation is derived (Figure 6.5).

spatial wavelength $\lambda$ ($m = N/\lambda$). Therefore $m$ indicates the spatial wavelength as a factor of the network size. The dispersion relation of Figure 6.5 is derived from the computation of the wave frequency $f$ and $\lambda$ indicated in the corresponding wave patterns of Figure 6.4.

Novel experimental methods based on high-density multielectrode arrays have revealed the existence, in certain situations, of traveling waves of neuronal activity characterized by a long spatial wavelength of the order of the size of the network. In a recent paper, Lubenov and Siapas (2009) reported on this type of neuronal wave propagation through the hippocampus of mammals. Figure 6.5A suggests that under specific conditions this system can exhibit waves with long spatial wavelengths of the order of the size of the network (small $m$ values correspond to long spatial wavelengths in Figure 6.5A). Figure 6.5B shows the raster plot corresponding to a $T_f$ defined by $T_{ON} =$ ms and $T_{OFF} = 22$ ms, for which $f \simeq 41.6$ Hz and $m =$0.8 (red point in Figure 6.5A). However, the conditions accounting for long spatial wavelengths need to be further explored. To that end, instead of using high values of the external current (enough to bring the neurons above threshold, named from now on *noiseless* regime), we introduce an heterogeneous Poisson train of excitatory presynaptic potentials with a mean event rate that varies following an Ornstein-Uhlenbeck process (defined in Section 3.2) im-

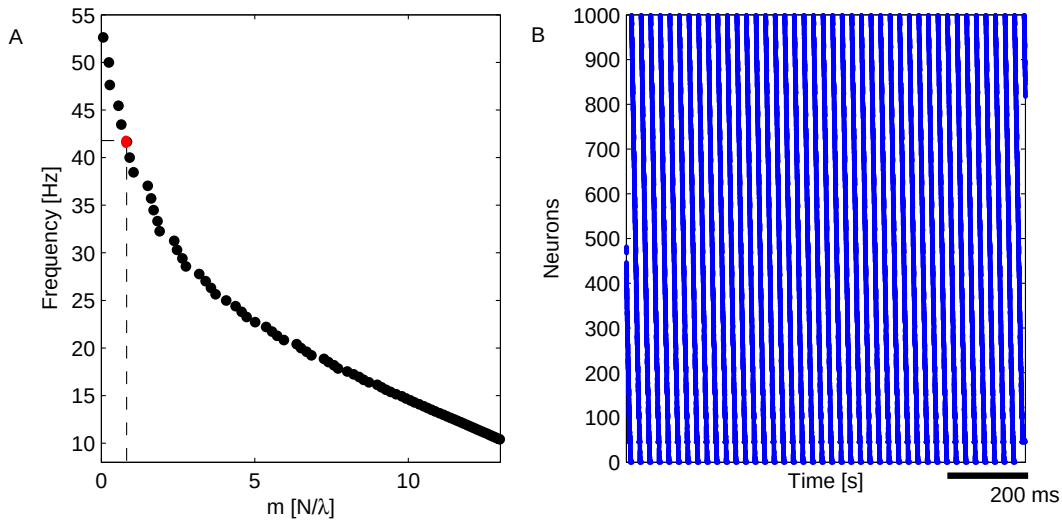


Fig. 6.5 **Dispersion relation of waves arising from a chain of inhibitory HH neurons receiving an excitatory input.** (A) Dispersion relation of inhibition-dominated chain of HH neurons. 45 neurons at the bottom are periodically driven with constant $T_{ON}$ =2 ms and varying $T_{OFF}$. (B) Raster plot of traveling waves corresponding to a specific $T_f$, defined by $T_{ON}$ =2 ms and $T_{OFF}$ =22 ms.

pinging on all the neurons (except the ones at the bottom, which are periodically driven with a constant current). Under this condition, the system (green plot in Figure 6.6A) cannot sustain propagation at frequencies higher than $f \approx 24$ Hz, and the smallest spatial wavelength corresponds to a fraction 7.7 of the size $N$ of the network, meaning that $\lambda$ is approximately 130 neurons. Figure 6.6A shows the dispersion relation of the noiseless (blue, the same as in Figure 6.5A) and noisy (green) cases. Furthermore, for increasing values of the GABA decay time constant $\tau_{decay}$, the frequency of wave propagation decreases. Figure 6.6B shows that for large values of $\tau_{decay}$ the system cannot sustain the propagation of waves with long spatial wavelengths (the smallest $m$ values are obtained with the smallest GABA $\tau_{decay}$). For GABA $\tau_{decay}$ =25 ms, $m = 3.9$ corresponds to $f \approx 15$ Hz (Figure 6.6B). Notice that the frequency of the collective synchronous oscillation decreases with increasing $\tau_{decay}$, and this will be matter of study in Section 6.3. In summary, Figure 6.6 shows that inhibition slow-down hinders long wavelengths. Systems where neurons have a limited memory capacity to integrate incoming inputs can still exhibit waves with long spatial wavelength, because in that way the effect of the noise or the slower GABA $\tau_{decay}$ is greatly reduced (results not shown). However this analysis needs a further exploration that necessarily has to include all the parameters involved in the generation of these patterns.

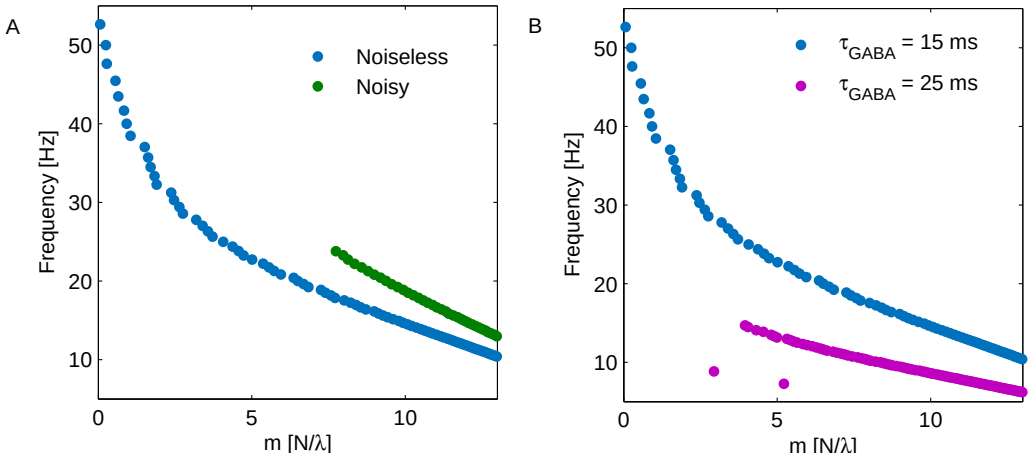


Fig. 6.6 **Numerical results of a chain of inhibitory HH neurons receiving an excitatory input under different conditions** (A) Dispersion relation of inhibitory-dominated chain of HH neurons without noise (blue) and in presence of noise (green). GABA $\tau_{decay}$ is equal to 15ms. (B) Dispersion relation of inhibitory-dominated chain of HH neurons for different GABA $\tau_{decay}$. GABA $\tau_{decay}$ is equal to 15ms (blue) and 25ms (purple). In both plots, 45 neurons at the bottom are periodically driven with constant $T_{ON} = 2$ms and $T_{OFF}$ varying.

We next ask to what extent these backward wave dynamics can be generalized, and which are the necessary and sufficient conditions for the phenomenon to occur. To this aim, we first develop a continuum approximation of the HH model presented above.We derive a self-consistency condition for the existence of traveling waves, from which the dispersion relation between velocity and wavelength can be calculated.

## 6.3 Continuum model approximation starting from Hodgkin-Huxley model

We base our investigation on the continuum approximation developed by Kistler and van Hemmen (1998), and aim at applying their approach to our network topology: one-dimensional chain with regular asymmetric connections. This approximation follows the HH model introduced in the previous Section, and allows us to explore the backward propagation phenomenon from an analytical point of view. In their work, Kistler and van Hemmen (1998) considered a two-dimensional lattice of spiking neurons with local interactions, focusing not on the mean firing rate of the neurons, but on the single firing events when an action potential is released. They were interested in studying patterns including all active neurons, namely all neurons that are currently firing an action potential. With that model, they found a diversity of patterns of

collective excitation in the form of traveling pulses and waves, and calculated the dispersion relation.

Starting from Equation (7) of Kistler and van Hemmen (1998), in our continuum approximation we define the local field $V(x,t)$ as the membrane potential at location $x$ and time $t$, and assume that a spike $S(x,t)$ is triggered if the local field crosses the spiking threshold $\vartheta$ from below. The expression for the local field in a one-dimensional asymmetric network is:

$$V(x,t) = Q_{ext} + \int_{-\infty}^{\infty} \mathrm{dx}' J(x-x') \int_{0}^{\infty} \mathrm{dt}' \, \varepsilon(t') \, S(x', t-t') \tag{6.1}$$

where $Q_{ext}$ represents the magnitude of the external excitation, since all internal connections in our network are inhibitory. The chain topology with postsynaptic connections going only in the positive $x$-direction is captured by the synaptic strength function

$$J(x) = -q \, \Theta(x) \, \Theta(\gamma - x), \tag{6.2}$$

where $q$ is the magnitude of inhibitory connections, $\Theta(x)$ the Heaviside function (0 for $x < 0$ and 1 for $x \geq 0$) and $\gamma$ the window connectivity. For the response kernel $\varepsilon(t)$ we use the postsynaptic alpha function from the full spiking model

$$\varepsilon(t) = \frac{1}{\tau_{decay} - \tau_{rise}} \left( e^{-\frac{t}{\tau_{decay}}} - e^{-\frac{t}{\tau_{rise}}} \right) \Theta(t) \tag{6.3}$$

with $\tau_{decay}$ and $\tau_{rise}$ being respectively the GABA decay and rise temporal constants defined in Table 6.1. The analysis of a collective phenomenon employs a corresponding ansatz $S(x,t)$ for the spike activity. For equidistant waves traveling in the positive $x$-direction (direction of connectivity) we assume

$$S(x,t) = \sum_{n=-\infty}^{\infty} \delta \left( \frac{x}{v} - t - n\frac{\lambda}{v} \right), \tag{6.4}$$

where $v > 0$ is the wave phase velocity and $\lambda > 0$ is the spatial wavelength. Our first objective is to integrate the local field equation for the forward propagating waves with the kernel response, and after some mathematical steps (detailed in Appendix B), we obtain:

$$\begin{aligned} V^{\mathrm{fw}}(x,t) \;=\; & Q_{ext} - q \sum_{n=n_0}^{\infty} \left( \frac{\tau_{decay}}{\tau_{decay} - \tau_{rise}} e^{-\frac{vt+n\lambda}{v\tau_{decay}}} \left( e^{-\frac{\bar{x}}{v\tau_{decay}}} - e^{-\frac{x-\gamma}{v\tau_{decay}}} \right) - \right. \\ & \left. - \frac{\tau_{rise}}{\tau_{decay} - \tau_{rise}} e^{-\frac{vt+n\lambda}{v\tau_{rise}}} \left( e^{-\frac{\bar{x}}{v\tau_{rise}}} - e^{-\frac{x-\gamma}{v\tau_{rise}}} \right) \right), \end{aligned} \tag{6.5}$$

where $n_0$ and $\bar{x}$ are given by

$$\begin{aligned} n_0 &= \left\lceil \frac{x-vt-\gamma}{\lambda} \right\rceil, \\ \bar{x} &= \min(x, vt+n\lambda). \end{aligned}$$

In order to evaluate the sum, we split it into two parts: for $n_0 \le n \le n_1$ and for $n > n_1$ and thus $\bar{x} = vt+n\lambda$ and $\bar{x} = x$ respectively in the two sums. After some calculations, we obtain the local field equation

$$\begin{aligned} V^{\mathrm{fw}}(x,t) &= Q_{ext} - q\Bigg\{ \bar{n} - \frac{\tau_{decay}}{\tau_{decay}-\tau_{rise}} \left( \frac{1-e^{-\frac{\bar{n}\lambda}{v\tau_{decay}}}}{1-e^{-\frac{\lambda}{v\tau_{decay}}}} \right) e^{-\frac{vt+n_0\lambda-x+\gamma}{v\tau_{decay}}} \\ &\quad + \frac{\tau_{rise}}{\tau_{decay}-\tau_{rise}} \left( \frac{1-e^{-\frac{\bar{n}\lambda}{v\tau_{rise}}}}{1-e^{-\frac{\lambda}{v\tau_{rise}}}} \right) e^{-\frac{vt+n_0\lambda-x+\gamma}{v\tau_{rise}}} \\ &\quad + \frac{\tau_{decay}}{\tau_{decay}-\tau_{rise}} \left( \frac{1-e^{-\frac{\gamma}{v\tau_{decay}}}}{1-e^{-\frac{\lambda}{v\tau_{decay}}}} \right) e^{-\frac{vt+(n_1+1)\lambda-x}{v\tau_{decay}}} \\ &\quad - \frac{\tau_{rise}}{\tau_{decay}-\tau_{rise}} \left( \frac{1-e^{-\frac{\gamma}{v\tau_{rise}}}}{1-e^{-\frac{\lambda}{v\tau_{rise}}}} \right) e^{-\frac{vt+(n_1+1)\lambda-x}{v\tau_{rise}}} \Bigg\} \end{aligned} \tag{6.6}$$

where

$$\begin{aligned} n_0 &= \left\lceil \frac{x-vt-\gamma}{\lambda} \right\rceil, \\ n_1 &= \min\left\{ \left\lfloor \frac{x-vt}{\lambda} \right\rfloor, \left\lceil \frac{x-vt}{\lambda} \right\rceil - 1 \right\}, \\ \bar{n} &= n_1 - n_0 + 1. \end{aligned}$$

To evaluate the solutions we also need to calculate the time derivative of the local field $V^{\mathrm{fw}}(x,t)$

$$\begin{aligned} \frac{\partial V^{\mathrm{fw}}(x,t)}{\partial t} &= \frac{q}{\tau_{decay}-\tau_{rise}} \Bigg\{ - \left( \frac{1-e^{-\frac{\bar{n}\lambda}{v\tau_{decay}}}}{1-e^{-\frac{\lambda}{v\tau_{decay}}}} \right) e^{-\frac{vt+n_0\lambda-x+\gamma}{v\tau_{decay}}} \\ &\quad + \left( \frac{1-e^{-\frac{\bar{n}\lambda}{v\tau_{rise}}}}{1-e^{-\frac{\lambda}{v\tau_{rise}}}} \right) e^{-\frac{vt+n_0\lambda-x+\gamma}{v\tau_{rise}}} \\ &\quad + \left( \frac{1-e^{-\frac{\gamma}{v\tau_{decay}}}}{1-e^{-\frac{\lambda}{v\tau_{decay}}}} \right) e^{-\frac{vt+(n_1+1)\lambda-x}{v\tau_{decay}}} \\ &\quad - \left( \frac{1-e^{-\frac{\gamma}{v\tau_{rise}}}}{1-e^{-\frac{\lambda}{v\tau_{rise}}}} \right) e^{-\frac{vt+(n_1+1)\lambda-x}{v\tau_{rise}}} \Bigg\}. \end{aligned} \tag{6.7}$$

The proposed ansatz is a valid solution only if there are values of $\lambda$ and $v$ that satisfy the self-consistency conditions

$$V^{\mathrm{fw}}(vt+n\lambda,t)=\vartheta \quad \text{and} \quad \left.\frac{\partial V^{\mathrm{fw}}}{\partial t}\right|_{x=vt+n\lambda} > 0, \qquad \forall n\in\mathbb{Z}. \tag{6.8}$$

If we set a fixed threshold $\vartheta$, synaptic inhibition $q$, and external excitation $Q_{ext}$, the above self-consistency condition yields a dispersion relation. We first consider the case when $\lambda$ is larger than $\gamma$, i.e. $\gamma/\lambda<1$. Setting $x=vt+n\lambda$ and substituting we obtain

$$\begin{aligned} n_0 &= \left\lceil \frac{vt+n\lambda-vt-\gamma}{\lambda} \right\rceil = \left\lceil n-\frac{\gamma}{\lambda} \right\rceil = n, \\ n_1 &= \min\left\{ \left\lfloor \frac{vt+n\lambda-vt}{\lambda} \right\rfloor, \left\lceil \frac{vt+n\lambda-vt}{\lambda} \right\rceil - 1 \right\} = n-1, \\ \bar{n} &= n_1-n_0+1 = n-1-n+1 = 0. \end{aligned}$$

Because $\bar{n}=0$, the first three terms in the local field Equation (6.6) drop out and we obtain the following self-consistency relation between $\lambda$ and $v$

$$\frac{Q_{ext}-\vartheta}{q} = \frac{\tau_{decay}}{\tau_{decay}-\tau_{rise}}\left(\frac{1-e^{-\frac{\gamma}{v\tau_{decay}}}}{1-e^{-\frac{\lambda}{v\tau_{decay}}}}\right) - \frac{\tau_{rise}}{\tau_{decay}-\tau_{rise}}\left(\frac{1-e^{-\frac{\gamma}{v\tau_{rise}}}}{1-e^{-\frac{\lambda}{v\tau_{rise}}}}\right). \tag{6.9}$$

By replacing $\lambda=2\pi/k$ and $v=\omega/k$, we find the dispersion relation for the forward traveling waves which is shown in Figure 6.7. Actually we prefer to express the dispersion relation shown in that plot in terms of the normalized wavenumber $M'=\gamma/\lambda$ and the temporal frequency $F=v/\lambda$:

$$\frac{Q_{ext}-\vartheta}{q} = \frac{\tau_{decay}}{\tau_{decay}-\tau_{rise}}\left(\frac{1-e^{-\frac{M'}{F\tau_{decay}}}}{1-e^{-\frac{1}{F\tau_{decay}}}}\right) - \frac{\tau_{rise}}{\tau_{decay}-\tau_{rise}}\left(\frac{1-e^{-\frac{M'}{F\tau_{rise}}}}{1-e^{-\frac{1}{F\tau_{rise}}}}\right). \tag{6.10}$$

However, we need to evaluate the condition that the local field $V^{\mathrm{fw}}$ reaches the threshold from below, meaning that the temporal derivative of the local field $\frac{\partial V^{\mathrm{fw}}(x,t)}{\partial t}$ is positive. Evaluating Equation (6.7) with the above values for $n_0$ and $n_1$ we obtain

$$\left.\frac{\partial V^{\mathrm{fw}}}{\partial t}\right|_{x=vt+n\lambda} = \frac{q}{\tau_{decay}-\tau_{rise}}\left\{\left(\frac{1-e^{-\frac{\gamma}{v\tau_{decay}}}}{1-e^{-\frac{\lambda}{v\tau_{decay}}}}\right) - \left(\frac{1-e^{-\frac{\gamma}{v\tau_{rise}}}}{1-e^{-\frac{\lambda}{v\tau_{rise}}}}\right)\right\}. \tag{6.11}$$

It turns out that the above derivative is non-positive for all values of $\lambda$ and $v$ (Figure 6.8). Hence the chain cannot sustain forward traveling waves.

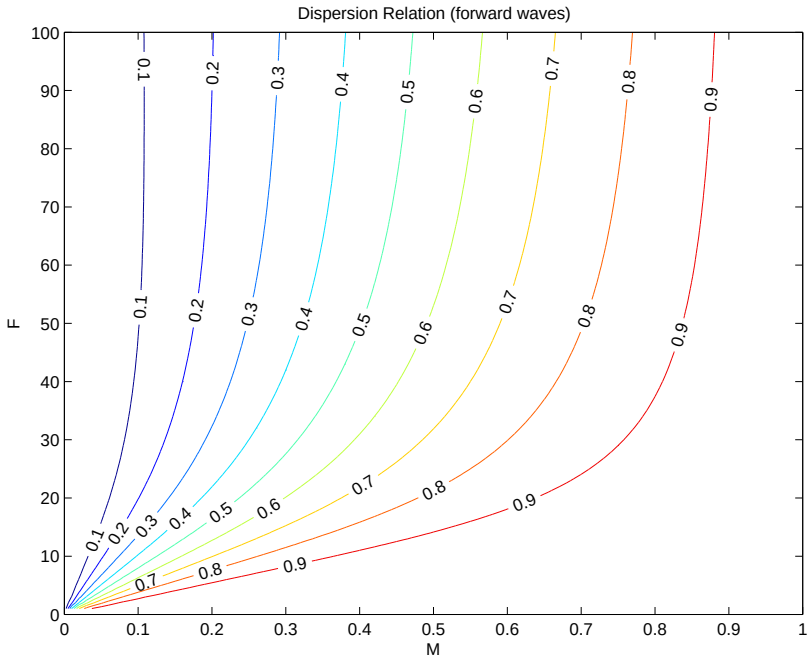


Fig. 6.7 **Dispersion relation for forward waves.** Dispersion relation derived from the self-consistency condition (6.8) for forward propagating waves as a function of the normalized wavenumber $M' = \gamma/\lambda$ and the temporal frequency $F = \nu/\lambda$ for different ratio of $\frac{Q_{ext}-\vartheta}{q}$.

Now we turn to study the backward propagation. To this aim, we cannot simply substitute a negative value for $\nu$ in the expressions for the forward traveling case, because the derivation explicitly relies on the sign of $\nu$ when evaluating the integration and summation limits. Therefore, we propose a similar derivation with a spiking pattern for equidistant waves traveling in the negative $x$-direction (opposite to the direction of connectivity):

$$S(x,t) = \sum_{n=-\infty}^{\infty} \delta\left(\frac{x}{\nu} + t - n\frac{\lambda}{\nu}\right), \tag{6.12}$$

where again $\nu > 0$ is the wave phase velocity (in this case in the negative $x$-direction), and $\lambda > 0$ is the spatial wavelength. The local field equation $V^{\mathrm{bw}}(x,t)$ for the backward propagating waves after integrating the kernel response is:

$$\begin{aligned} V^{\mathrm{bw}}(x,t) \;=\; & Q_{ext} - q \sum_{n=-\infty}^{n_{max}} \left( \frac{\tau_{decay}}{\tau_{decay}-\tau_{rise}} e^{-\frac{\nu t - n\lambda}{\nu\tau_{decay}}} \left( e^{-\frac{x}{\nu\tau_{decay}}} - e^{-\frac{x}{\nu\tau_{decay}}} \right) - \right. \\ & \left. - \frac{\tau_{rise}}{\tau_{decay}-\tau_{rise}} e^{-\frac{\nu t - n\lambda}{\nu\tau_{rise}}} \left( e^{-\frac{x}{\nu\tau_{rise}}} - e^{-\frac{x}{\nu\tau_{rise}}} \right) \right), \end{aligned} \tag{6.13}$$

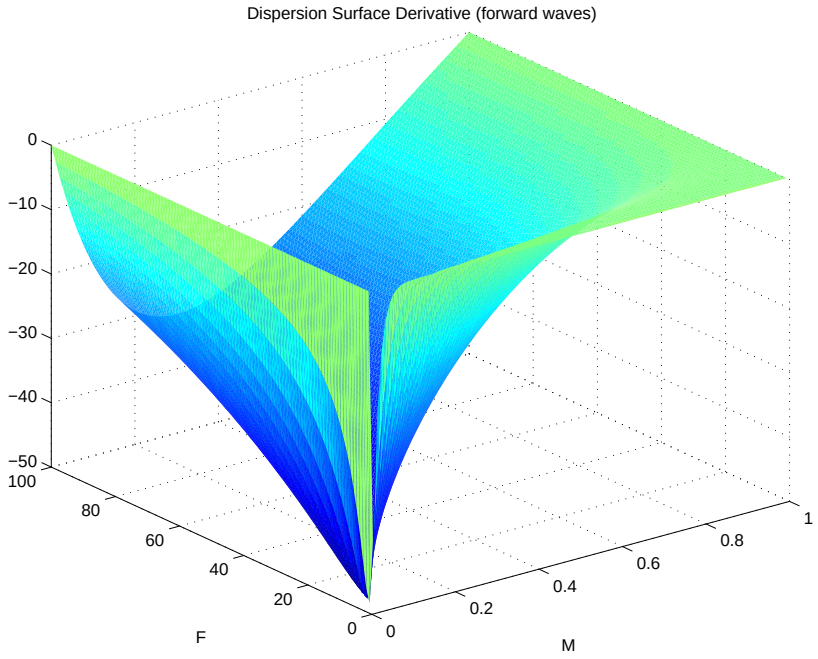


Fig. 6.8 **Local field temporal derivative for forward waves.** Plot of local field temporal derivative as a function of the temporal frequency and the normalized wavenumber for forward propagating waves is non-positive for all values of $\lambda$ and $v$, meaning that the local field $V^{\mathrm{fw}}$ does not reach the threshold from below as it should be, thus demonstrating that the chain cannot sustain forward traveling waves.

where $n_{max}$ and $\underline{x}$ are given by

$$\begin{aligned} n_{max} &= \min\left\{\left\lfloor\frac{x+vt}{\lambda}\right\rfloor, \left\lceil\frac{x+vt}{\lambda}\right\rceil - 1\right\}, \\ \underline{x} &= \max(x-\gamma, n\lambda - vt). \end{aligned}$$

At the same way, in order to evaluate the sum we break it into two parts: for $n < n_2$ and for $n_2 \le n \le n_{max}$, thus $\underline{x} = x - \gamma$ and $\underline{x} = n\lambda - vt$, respectively. We obtain the local field equation

$$\begin{aligned} V^{\mathrm{bw}}(x,t) &= Q_{ext} - q\Bigg\{\bar{n} - \frac{\tau_{decay}}{\tau_{decay}-\tau_{rise}}\left(\frac{1-e^{-\frac{\bar{n}\lambda}{v\tau_{decay}}}}{1-e^{-\frac{\lambda}{v\tau_{decay}}}}\right)e^{-\frac{vt-n_{max}\lambda+x}{v\tau_{decay}}} \\ &+ \frac{\tau_{rise}}{\tau_{decay}-\tau_{rise}}\left(\frac{1-e^{-\frac{\bar{n}\lambda}{v\tau_{rise}}}}{1-e^{-\frac{\lambda}{v\tau_{rise}}}}\right)e^{-\frac{vt-n_{max}\lambda+x}{v\tau_{rise}}} \\ &+ \frac{\tau_{decay}}{\tau_{decay}-\tau_{rise}}\left(\frac{1-e^{-\frac{\gamma}{v\tau_{decay}}}}{1-e^{-\frac{\lambda}{v\tau_{decay}}}}\right)e^{-\frac{vt-(n_2-1)\lambda+x-\gamma}{v\tau_{decay}}} \\ &- \frac{\tau_{rise}}{\tau_{decay}-\tau_{rise}}\left(\frac{1-e^{-\frac{\gamma}{v\tau_{rise}}}}{1-e^{-\frac{\lambda}{v\tau_{rise}}}}\right)e^{-\frac{vt-(n_2-1)\lambda+x-\gamma}{v\tau_{rise}}}\Bigg\}, \end{aligned} \tag{6.14}$$

where

$$\begin{aligned} n_2 &= \max\left\{\left\lceil\frac{x+vt-\gamma}{\lambda}\right\rceil, \left\lfloor\frac{x+vt-\gamma}{\lambda}\right\rfloor+1\right\}, \\ n_{max} &= \min\left\{\left\lfloor\frac{x+vt}{\lambda}\right\rfloor, \left\lceil\frac{x+vt}{\lambda}\right\rceil-1\right\}, \\ \bar{n} &= n_{max}-n_2+1. \end{aligned}$$

The time derivative of the local field $\frac{\partial V^{\mathrm{bw}}(x,t)}{\partial t}$ is

$$\begin{aligned} \frac{\partial V^{\mathrm{bw}}(x,t)}{\partial t} &= \frac{q}{\tau_{decay}-\tau_{rise}}\Bigg\{-\left(\frac{1-e^{-\frac{\bar{n}\lambda}{v\tau_{decay}}}}{1-e^{-\frac{\lambda}{v\tau_{decay}}}}\right)e^{-\frac{vt-n_{max}\lambda+x}{v\tau_{decay}}} + \left(\frac{1-e^{-\frac{\bar{n}\lambda}{v\tau_{rise}}}}{1-e^{-\frac{\lambda}{v\tau_{rise}}}}\right)e^{-\frac{vt-n_{max}\lambda+x}{v\tau_{rise}}} \\ &+ \left(\frac{1-e^{-\frac{\gamma}{v\tau_{decay}}}}{1-e^{-\frac{\lambda}{v\tau_{decay}}}}\right)e^{-\frac{vt-(n_2-1)\lambda+x-\gamma}{v\tau_{decay}}} \\ &- \left(\frac{1-e^{-\frac{\gamma}{v\tau_{rise}}}}{1-e^{-\frac{\lambda}{v\tau_{rise}}}}\right)e^{-\frac{vt-(n_2-1)\lambda+x-\gamma}{v\tau_{rise}}}\Bigg\}. \end{aligned} \tag{6.15}$$

Now we turn to the self-consistency conditions for backward traveling waves, and we first consider the case when the spatial wavelength is larger than the connectivity window, i.e.

$\gamma/\lambda < 1$. Setting $x = -\nu t + n\lambda$ and substituting we obtain

$$\begin{aligned} n_2 &= \max\left\{\left\lceil\frac{-\nu t + n\lambda + \nu t - \gamma}{\lambda}\right\rceil, \left\lfloor\frac{-\nu t + n\lambda + \nu t - \gamma}{\lambda}\right\rfloor + 1\right\} \\ &= \max\left\{\left\lceil n - \frac{\gamma}{\lambda}\right\rceil, \left\lfloor n - \frac{\gamma}{\lambda}\right\rfloor + 1\right\} = n, \\ n_{max} &= \min\left\{\left\lfloor\frac{-\nu t + n\lambda + \nu t}{\lambda}\right\rfloor, \left\lceil\frac{-\nu t + n\lambda + \nu t}{\lambda}\right\rceil - 1\right\} \\ &= \min\left\{\left\lfloor n\right\rfloor, \left\lceil n\right\rceil - 1\right\} = n - 1, \\ \bar{n} &= n_{max} - n_2 + 1 = n - 1 - n + 1 = 0. \end{aligned}$$

Because $\bar{n} = 0$ the first three terms in the local field Equation (6.14) drop out, and we obtain the following self-consistency relation between $\lambda$ and $\nu$:

$$\frac{Q_{ext} - \vartheta}{q} = \frac{\tau_{decay}}{\tau_{decay} - \tau_{rise}}\left(\frac{1 - e^{-\frac{\gamma}{\nu\tau_{decay}}}}{1 - e^{-\frac{\lambda}{\nu\tau_{decay}}}}\right)e^{-\frac{\lambda-\gamma}{\nu\tau_{decay}}} - \frac{\tau_{rise}}{\tau_{decay} - \tau_{rise}}\left(\frac{1 - e^{-\frac{\gamma}{\nu\tau_{rise}}}}{1 - e^{-\frac{\lambda}{\nu\tau_{rise}}}}\right)e^{-\frac{\lambda-\gamma}{\nu\tau_{rise}}}. \tag{6.16}$$

Next, we check that the local field gets close to the threshold from below, i.e. that the temporal derivative of the local field is positive.

$$\left.\frac{\partial V^{\mathrm{bw}}}{\partial t}\right|_{x=-\nu t+n\lambda} = \frac{q}{\tau_{decay} - \tau_{rise}}\left\{\left(\frac{1 - e^{-\frac{\gamma}{\nu\tau_{decay}}}}{1 - e^{-\frac{\lambda}{\nu\tau_{decay}}}}\right)e^{-\frac{\lambda-\gamma}{\nu\tau_{decay}}} - \left(\frac{1 - e^{-\frac{\gamma}{\nu\tau_{rise}}}}{1 - e^{-\frac{\lambda}{\nu\tau_{rise}}}}\right)e^{-\frac{\lambda-\gamma}{\nu\tau_{rise}}}\right\}. \tag{6.17}$$

The above derivative is non-negative everywhere and strictly positive for most values of $\lambda$ and $\nu$ (Figure 6.9). Hence, unlike forward waves, the chain can sustain backward traveling waves. This result confirms the phenomenological findings we have presented in Section 6.2. The dispersion relation for backward traveling waves in terms of the normalized wavenumber $M' = \gamma/\lambda$ and the temporal frequency $F = \nu/\lambda$ is:

$$\frac{Q_{ext} - \vartheta}{q} = \frac{\tau_{decay}}{\tau_{decay} - \tau_{rise}}\left(\frac{1 - e^{-\frac{M'}{F\tau_{decay}}}}{1 - e^{-\frac{1}{F\tau_{decay}}}}\right)e^{-\frac{1-M'}{F\tau_{decay}}} - \frac{\tau_{rise}}{\tau_{decay} - \tau_{rise}}\left(\frac{1 - e^{-\frac{M'}{F\tau_{rise}}}}{1 - e^{-\frac{1}{F\tau_{rise}}}}\right)e^{-\frac{1-M'}{F\tau_{rise}}}. \tag{6.18}$$

This dispersion relation is plotted in Figure 6.10 and has a number of noteworthy properties. First, as $F \to 0$, $M' \to 1$ and hence $\lambda \to \gamma$ for all parameter values. This corresponds to the equilibrium state of the non-driven chain where the spatial wavelength is equal to the connectivity window. Second, as $F \to \infty$, $M'$ approaches a non-zero value that is parameter dependent. This means that there is a limit to the longest wavelength that a particular network can exhibit. Specifically, the closer $(Q_{ext} - \vartheta)/q$ is to 0, the longer the maximal wavelength

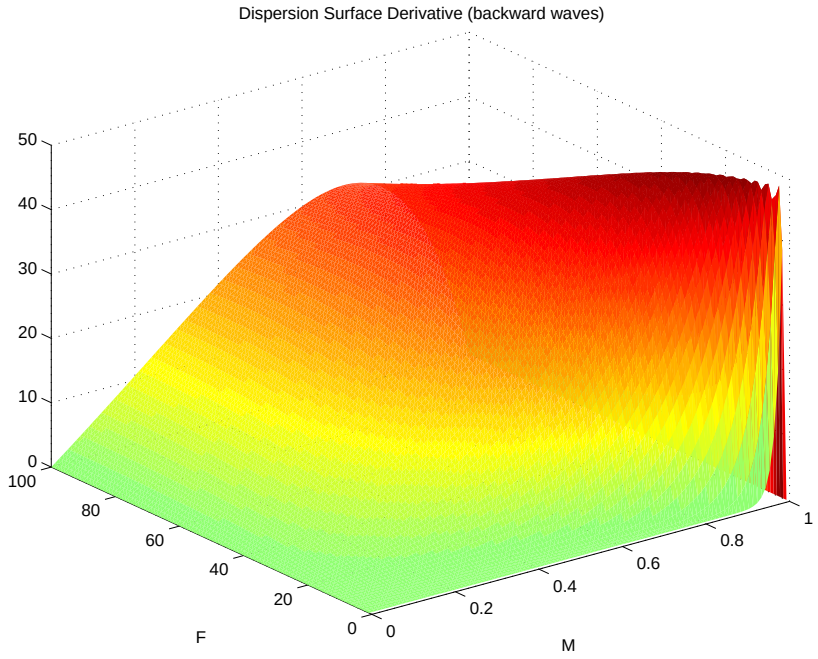


Fig. 6.9 **Local field temporal derivative for backward waves.** Plot of local field temporal derivative as a function of the temporal frequency and the normalized wavenumber for backward propagating waves is non-negative everywhere and strictly positive for most values of $\lambda$ and $\nu$, meaning that the local field $V^{\text{fw}}$ can reach the threshold from below, thus demonstrating that the chain can sustain backward traveling waves.

that the chain can sustain. This captures the observation that there seems to be a parameter-specific limit to the longest wavelength possible for a given set of excitation and inhibition values.

The study of the propagation of traveling waves in the long-wavelength limit requires further development. In what follows, we propose an analytically tractable continuum integrate-and-fire approximation to investigate how wave-propagation depends on various parameters that characterize neuronal interactions such as synaptic and axonal delays, the time course of postsynaptic potentials, and the degree of asymmetry in the topology.

## 6.4 Integrate-and-fire model continuum approximation

In this Section we refer to the analysis carried out by Bressloff (2000), where he introduced a continuum model of cortical tissue based on a one-dimensional network of IF neurons with symmetric excitatory connections, with individual neurons operating in the excitable regime. An IF neuron fires a spike whenever its membrane potential reaches the threshold $\vartheta$, and imme-

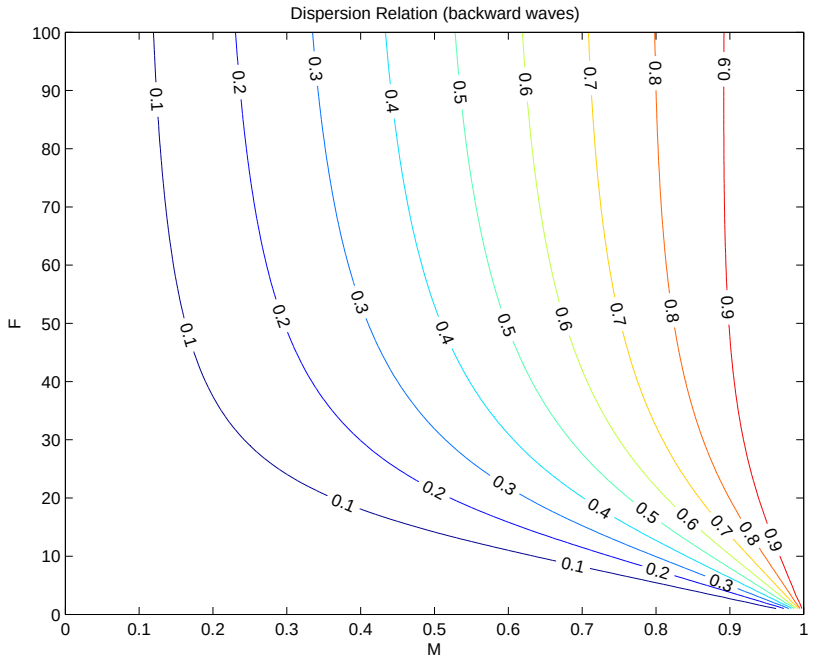


Fig. 6.10 **Dispersion relation for backward waves.** Dispersion relation derived from the self-consistency condition (6.16) for backward propagating waves as a function of the normalized wavenumber $M' = \gamma/\lambda$ and the temporal frequency $F = \nu/\lambda$ for different ratio of $\frac{Q_{ext}-\vartheta}{q}$.

diately after firing the membrane potential is reset to some resting level (Keener et al., 1981). Each neuron is assumed to receive a constant external bias $I_0$ such that, if synaptically isolated, the neuron oscillates (periodically fires and resets) when $I_0 > \vartheta$ (oscillatory regime) and is quiescent (in the absence of additional stimulation) when $I_0 < \vartheta$ (excitable regime) (Bressloff, 2000). Our objective is to apply that approach to one-dimensional networks with asymmetric inhibitory connections, with individual neurons operating in the oscillatory regime ($I_0 > \vartheta$). It is also worth stressing that IF models that neglect refractoriness will lead to poor predictions of wave speed (for periodic waves) at small periods and this is explored in James et al. (2003), where authors model an absolute refractory time-scale by clamping the system at reset.

As in the continuum approximation of the previous Section, $V(x,t)$ is the membrane potential of neuron at location $x \in \mathbb{R}$ at time $t$. Whenever $V(x,t)$ reaches the firing threshold $\vartheta$ a spike is generated $T_m = t$, and the membrane potential is reset to $V(x,t^+) = \zeta$. The evolution equation for the membrane potential is

$$\frac{\partial V(x,t)}{\partial t} = I_0 - \frac{V(x,t)}{\tau_m} + I(x,t), \tag{6.19}$$

where $I(x,t)$ is the total synaptic input at position $x$ and time $t$, and $\tau_m$ represents the membrane time constant. Following Bressloff (2000), we set $\tau_m = 1$ and $\vartheta = 1$ for convenience, so one unit of time represents approximately one membrane time constant, i.e. 10 ms. The synaptic current is given by

$$I(x,t) = g \int_{-\infty}^{\infty} \int_{0}^{\infty} W(x-x') J(t') E(x', t-t') \mathrm{d}t' \mathrm{d}x', \tag{6.20}$$

with $g$ and $W(x-x')$ being the (scalar) synaptic coupling parameter and the absolute weight of synaptic connection from $x'$ to $x$, respectively. As in the HH continuum approximation, we express a chain topology with postsynaptic connections going only in the positive $x$-direction over a window of length $\gamma$ by means of the synaptic weight function

$$W(x) = \gamma^{-1} \Theta(x)\, \Theta(\gamma - x), \tag{6.21}$$

where $\Theta$ is the Heaviside function. Notice that $W(x)$ is normalized to integrate to 1, so that the sign and strength of synaptic coupling are determined by the parameter $g$. For the response kernel we can use the postsynaptic alpha function from the full spiking model

$$J(t) = \frac{1}{\tau_{decay} - \tau_{rise}} \left( e^{-\frac{t}{\tau_{decay}}} - e^{-\frac{t}{\tau_{rise}}} \right) \Theta(t), \tag{6.22}$$

with $\tau_{decay}$ and $\tau_{rise}$ being the GABA temporal time decay and rise, respectively. The output spike train of neuron at position $x$ is expressed as a sum of delta functions centered at the spike times $T_m(x)$:

$$E(x,t) = \sum_{m=-\infty}^{\infty} \delta(t - T_m(x)). \tag{6.23}$$

The spike train ansatz corresponding to equidistant waves traveling in the positive $x$-direction (direction of connectivity) is

$$E(x,t) = \sum_{m=-\infty}^{\infty} \delta(t - (kx+m)T) = \sum_{m \in \mathbb{Z}} \delta(t - c^{-1}x - mT), \tag{6.24}$$

where $T$ is the wave period, $f = T^{-1}$ is the wave frequency, $k$ is the wavenumber, $\lambda = k^{-1}$ is the spatial wavelength, $\nu = (kT)^{-1} = \lambda f$ is the wave phase velocity, and $T_m(x) = mT + kxT = mT + \theta(x)T$ are the spike times. In the last expression $\theta(x) = kx$ is the firing phase of the neuron at $x$. We focus on the interval $(0,t)$ and assume that the neuron at $x$ has not fired in this

interval. We can integrate Equation (6.19) over this interval to obtain

$$V(x,t) = V(x,0)e^{-t} + (1-e^{-t})I_0 + \int_0^t e^{-(t-t')} I(x,t')\mathrm{d}t'. \tag{6.25}$$

Then we consider the above expression under the traveling wave ansatz, and assume that the neuron at $x = 0$ has just fired at time 0, i.e. $V(x,0) = \zeta$. Since all neurons are firing with period $T$, it then follows that $V(x,T) = \vartheta = 1$. Letting $t = T$ in Equation (6.25) above and substituting we obtain

$$1 = \zeta e^{-T} + (1-e^{-T})I_0 + e^{-T}\int_0^T e^{t'} I(x,t')\mathrm{d}t'. \tag{6.26}$$

To evaluate the integral above we first look at the synaptic current $I(x,t)$ in the presence of traveling waves. Substituting the spike train expression (Equation (6.24)) into the synaptic current definition (Equation (6.20))

$$\begin{aligned} I(x,t) &= g\int_{-\infty}^{\infty}\int_0^{\infty} W(x-x')\,J(t')\sum_{m\in\mathbb{Z}}\delta(t-t'-(kx'+m)T)\mathrm{d}t'\mathrm{d}x' \\ &= g\int_{-\infty}^{\infty} W(x-x')\sum_{m\in\mathbb{Z}}\int_0^{\infty} J(t')\,\delta(t-t'-(kx'+m)T)\mathrm{d}t'\mathrm{d}x' \\ &= g\int_{-\infty}^{\infty} W(x-x')\sum_{m\in\mathbb{Z}} J(t-(kx'+m)T)\,\mathrm{d}x'. \end{aligned} \tag{6.27}$$

Notice that the last expression above relies on the fact that $J(t) = 0$ for $t < 0$, so that the lower limit of the integral over $t'$ can be set to $-\infty$. There is no loss of generality in considering $x = 0$, so the integral in Equation (6.26) becomes

$$\begin{aligned} e^{-T}\int_0^T e^t I(0,t)\mathrm{d}t &= e^{-T}\int_0^T e^t g\int_{-\infty}^{\infty} W(-x')\sum_{m\in\mathbb{Z}} J(t-(kx'+m)T)\,\mathrm{d}x'\mathrm{d}t \\ &= g\int_{-\infty}^{\infty} W(-x')e^{-T}\int_0^T e^t\sum_{m\in\mathbb{Z}} J(t-(kx'+m)T)\,\mathrm{d}t\mathrm{d}x' \\ &= g\int_{-\infty}^{\infty} W(x)e^{-T}\int_0^T e^t\sum_{m\in\mathbb{Z}} J(t-(m-kx)T)\,\mathrm{d}t\mathrm{d}x \\ &= g\int_{-\infty}^{\infty} W(x)K_T(kx)\mathrm{d}x, \end{aligned} \tag{6.28}$$

where the function $K_T(\theta)$ is defined as

$$K_T(\theta) = e^{-T}\int_0^T e^t\sum_{m\in\mathbb{Z}} J(t-(m-\theta)T)\,\mathrm{d}t. \tag{6.29}$$

$K_T(\theta)$ expresses the contribution of an infinite periodic spike train with period $T$ and phase offset $\theta T$ to the membrane potential at time $T$ following leaky integration. These contributions are spatially integrated after scaling by the synaptic weight function $W(x)$ and the coupling parameter $g$. Equation (6.29) corresponds to Equation (2.6) in Bressloff (2000), where the integrand is $J(t+(m-\theta)T)$ instead of $J(t-(m-\theta)T)$ as above. The expression in Bressloff (2000) relies on the assumption of a symmetric synaptic weight function $W(x) = W(-x)$, and does not hold under the asymmetric case. After substituting Equation (6.28) into Equation (6.26) and re-arranging we obtain Equation (2.5) in Bressloff (2000):

$$1 - e^{-T}\zeta = (1-e^{-T})I_0 + g\int_{-\infty}^{\infty} W(x)K_T(kx)\mathrm{dx}. \tag{6.30}$$

The above expression generates a dispersion relation between $f = T^{-1}$ and $k$, but the integral still needs to be evaluated. To do so, we first notice that $K_T(\theta)$ is a real-valued periodic function of the phase $\theta$ with period 1, and hence can be expanded as a Fourier series

$$K_T(\theta) = \sum_{n=-\infty}^{\infty} c_n e^{j2\pi n\theta}, \tag{6.31}$$

where the Fourier coefficients $c_n$ are defined as

$$c_n = \int_0^1 K_T(\theta)e^{-j2\pi n\theta}\mathrm{d}\theta. \tag{6.32}$$

Substituting Equation (6.29) above we get

$$\begin{aligned}
c_n &= \int_0^1 e^{-T}\int_0^T e^t \sum_{m\in\mathbb{Z}} J(t-(m-\theta)T)e^{-j2\pi n\theta}\,\mathrm{dtd}\theta \\
&= e^{-T}\int_0^T e^t \int_0^1 \sum_{m\in\mathbb{Z}} J(\theta T + t - mT)e^{-j2\pi n\theta}\,\mathrm{d}\theta\mathrm{dt} \\
&= \frac{e^{-T}}{T}\int_0^T e^t \sum_{m\in\mathbb{Z}} \int_0^T J(\theta' + t - mT)e^{-j\frac{2\pi n}{T}\theta'}\,\mathrm{d}\theta'\mathrm{dt} \\
&= \frac{e^{-T}}{T}\int_0^T e^t \int_{-\infty}^{\infty} J(\theta' + t)e^{-j\frac{2\pi n}{T}\theta'}\,\mathrm{d}\theta'\mathrm{dt} \\
&= \frac{e^{-T}}{T}\int_0^T e^t\, e^{j\omega t}\tilde{J}(j\omega)\,\mathrm{dt} = \frac{e^{-T}}{T}\tilde{J}(j\omega)\int_0^T e^{(1+j\omega)t}\,\mathrm{dt} \\
&= \frac{e^{-T}}{T}\frac{\tilde{J}(j\omega)}{1+j\omega}(e^{(1+j\omega)T}-1) = \frac{e^{j\omega T}-e^{-T}}{T}\frac{\tilde{J}(j\omega)}{1+j\omega} \\
&= \frac{1-e^{-T}}{T}\frac{\tilde{J}(j\omega)}{1+j\omega}\bigg|_{\omega=\frac{2\pi n}{T}},
\end{aligned} \tag{6.33}$$

where $\tilde{J}(j\omega)$ is the Fourier transform of $J(t)$

$$\tilde{J}(j\omega) = \int_{-\infty}^{\infty} J(t)e^{-j\omega t}\,\mathrm{dt}, \tag{6.34}$$

$$J(t) = \frac{1}{2\pi}\int_{-\infty}^{\infty} \tilde{J}(j\omega)e^{j\omega t}\,\mathrm{d}\omega. \tag{6.35}$$

Now we can evaluate the total contribution of synaptic inputs to the membrane potential $V_s(k,T)$, which corresponds to the integral in Equations (6.28)-(6.30)

$$\begin{aligned}
V_s(k,T) &= e^{-T}\int_0^T e^t I(0,t)\mathrm{dt} \\
&= g\int_{-\infty}^{\infty} W(x)K_T(kx)\mathrm{dx} \\
&= g\int_{-\infty}^{\infty} W(x)\sum_{n=-\infty}^{\infty} c_n e^{j2\pi nkx}\mathrm{dx} \\
&= g\sum_{n=-\infty}^{\infty} c_n \int_{-\infty}^{\infty} W(x)e^{j2\pi nkx}\mathrm{dx} \\
&= g\sum_{n=-\infty}^{\infty} c_n \tilde{W}(-j\omega')\Big|_{\omega'=2\pi nk} \\
&= g\frac{1-e^{-T}}{T}\sum_{n=-\infty}^{\infty}\frac{\tilde{J}(j\omega)}{1+j\omega}\tilde{W}(-j\omega kT)\Big|_{\omega=\frac{2\pi n}{T}}.
\end{aligned} \tag{6.36}$$

Several things are worth noting here. First, $V_s(k,T)$ is a real-valued function and its sign is determined by the sign of $g$. This follows from the fact that both $W(x)$ and $K_T(\theta)$ are real non-negative functions. Second, $V_s(k,T)$ is expressed as an infinite sum of complex quantities as both $\tilde{J}(j\omega)$ and $\tilde{W}(j\omega)$ are complex. The sum yields a real value because of the conjugate symmetries $\tilde{J}(j\omega) = \tilde{J}^*(-j\omega)$ and $\tilde{W}(j\omega) = \tilde{W}^*(-j\omega)$, which hold because both functions are defined as Fourier transforms of real-valued functions $J(t)$ and $W(x)$. This in fact allows for an alternative expression for Equation (6.36) emphasizing that $V_s(k,T) = \mathfrak{Re}\{V_s(k,T)\}$ is real:

$$V_s(k,T) = g\frac{1-e^{-T}}{T}\left(\tilde{J}(0)\tilde{W}(0) + 2\sum_{n=1}^{\infty}\mathfrak{Re}\left\{\frac{\tilde{J}(j\omega)\tilde{W}(-j\omega kT)}{1+j\omega}\right\}\Big|_{\omega=\frac{2\pi n}{T}}\right). \tag{6.37}$$

If $J(t)$ and $W(x)$ are both defined to integrate to 1, then $\tilde{J}(0) = \tilde{W}(0) = 1$. Furthermore, if the synaptic weight function is symmetric, $W(x) = W(-x)$, as in Bressloff (2000), then its Fourier transform is real and even, $\tilde{W}(j\omega) = \tilde{W}(-j\omega) = \mathfrak{Re}\{\tilde{W}(-j\omega)\}$. So Equation (6.37) can be

rewritten as

$$V_s(k,T) = g\frac{1-e^{-T}}{T}\left(1+2\sum_{n=1}^{\infty}\mathfrak{Re}\left\{\frac{\tilde{J}(j\omega)}{1+j\omega}\right\}\tilde{W}(j\omega kT)\Big|_{\omega=\frac{2\pi n}{T}}\right), \tag{6.38}$$

corresponding to the conditions considered in Equation (2.11) of Bressloff (2000). Finally, to evaluate the infinite sum in practice, we truncated to $n_{max}$ terms according to the spectral content of $\tilde{J}(j\omega)$ and $\tilde{W}(j\omega)$. After the derivation of an expression for $V_s(k,T)$, it is useful to collect the remaining terms in Equation (6.30) and define

$$V_r(T) = 1-e^{-T}\zeta-(1-e^{-T})I_0. \tag{6.39}$$

With this definition the dispersion relation can be thought of as the solution to $V_s(k,T) = V_r(T)$ or as the 0 level set of $F(k,T) = V_s(k,T) - V_r(T)$. Notice however that the above condition only guarantees that $V(0,t)$ reaches threshold at $t = T$, consistent with the traveling wave ansatz. It does not guarantee that $V(0,t)$ does not also reach threshold at an earlier point $t < T$, which would be inconsistent with the traveling wave ansatz. This condition is termed *re-excitation*, and is considered in Section 2.3 by Bressloff (2000). There is another pathological condition, which is inconsistent with the traveling wave solution, namely the possibility that $V(0,t)$ reaches threshold at $T$, but from above, instead of from below, i.e. $V(0,T^-) > 1$. We therefore require that solutions $(k,T)$ meet both self-consistency conditions below to be part of the dispersion relation, as we have imposed in the previous Section:

$$F(k,T) = V_s(k,T) - V_r(T) = 0 \quad \text{and} \quad \frac{\partial V(0,t)}{\partial t}\Big|_{t=nT} > 0, \qquad \forall n \in \mathbb{Z}. \tag{6.40}$$

In order to compute the derivative we start with the membrane potential (Equation (6.25)) under the traveling wave ansatz and assume the neuron at $x = 0$ has fired at time $t = 0$

$$\begin{aligned} V(0,t) &= \zeta e^{-t} + (1-e^{-t})I_0 + e^{-t}\int_0^t e^{t'} I(x,t')\mathrm{d}t' \\ &= \zeta e^{-t} + (1-e^{-t})I_0 + V_s(k,T,t) \\ &= 1 - V_r(t) + V_s(k,T,t), \end{aligned} \tag{6.41}$$

where $V_s(k,T,t)$ is the total contribution of synaptic inputs to the membrane potential at time $t$ after firing, given traveling waves with wavenumber $k$ and period $T$

$$\begin{aligned} V_s(k,T,t) &= e^{-t}\int_0^t e^{t'} I(x,t')\mathrm{d}t' \\ &= \frac{g}{T}\sum_{n=-\infty}^{\infty}(e^{j\omega t}-e^{-t})\frac{\tilde{J}(j\omega)}{1+j\omega}\tilde{W}(-j\omega kT)\Big|_{\omega=\frac{2\pi n}{T}}. \end{aligned} \tag{6.42}$$

The above expression generalizes the earlier definition in Equation (6.36), so that $V_s(k,T) = V_s(k,T,T)$, and the derivation is very similar. The derivative is then

$$\begin{aligned} \frac{\partial V(0,t)}{\partial t} &= (I_0-\zeta)e^{-t}+\frac{\partial V_s(k,T,t)}{\partial t} \\ &= (I_0-\zeta)e^{-t}+\frac{g}{T}\sum_{n=-\infty}^{\infty}(j\omega e^{j\omega t}+e^{-t})\frac{\tilde{J}(j\omega)}{1+j\omega}\tilde{W}(-j\omega kT)\Big|_{\omega=\frac{2\pi n}{T}}. \end{aligned} \tag{6.43}$$

Evaluating the derivative at $t=T$ gives

$$\begin{aligned} \frac{\partial V(0,t)}{\partial t}\Big|_{t=T} &= (I_0-\zeta)e^{-T}+\frac{g}{T}\sum_{n=-\infty}^{\infty}(j\omega+e^{-T})\frac{\tilde{J}(j\omega)}{1+j\omega}\tilde{W}(-j\omega kT)\Big|_{\omega=\frac{2\pi n}{T}} \\ &= (I_0-\zeta)e^{-T}+\frac{g}{T}\sum_{n=-\infty}^{\infty}\tilde{J}(j\omega)\tilde{W}(-j\omega kT)\Big|_{\omega=\frac{2\pi n}{T}} \\ &\quad -\frac{g}{T}(1-e^{-T})\sum_{n=-\infty}^{\infty}\frac{\tilde{J}(j\omega)}{1+j\omega}\tilde{W}(-j\omega kT)\Big|_{\omega=\frac{2\pi n}{T}} \\ &= (I_0-\zeta)e^{-T}+I(0,T)-V_s(k,T). \end{aligned} \tag{6.44}$$

In the above we have used $I(0,T)$ simply as a symbol to denote

$$I(0,T)=\frac{g}{T}\sum_{n=-\infty}^{\infty}\tilde{J}(j\omega)\tilde{W}(-j\omega kT)\Big|_{\omega=\frac{2\pi n}{T}} \tag{6.45}$$

but the above expression correctly represents the synaptic input received by neuron $x=0$ at time $T$. Now, if the first self-consistency condition is met, then $V_s(k,T)=V_r(T)$ and substituting in Equation (6.44) and rearranging we obtain

$$\frac{\partial V(0,t)}{\partial t}\Big|_{t=T} = I(0,T)-1+I_0. \tag{6.46}$$

Given that the first self-consistency condition requires $V(0,T)=1$, we could have written the above expression directly from the evolution Equation (6.19), but this would not have yielded an expression for $I(0,T)$. However, a general expression for $I(x,t)$ can in fact be derived independently of the above. In particular, recognizing that under the traveling wave ansatz, $I(x,t)$ is periodic with period $T$ and following a derivation similar to that in Equation (6.36), we can show that

$$I(x,T)=\frac{g}{T}\sum_{n=-\infty}^{\infty}e^{j\omega(t-kTx)}\tilde{J}(j\omega)\tilde{W}(-j\omega kT)\Big|_{\omega=\frac{2\pi n}{T}}, \tag{6.47}$$

which of course reduces to the expression in Equation (6.45) for $I(0,T)$. Independently of the approach, the final result is the same. The second self-consistency condition on the derivative of $V(0,T)$ reduces to

$$I(0,T)>1-I_0. \tag{6.48}$$

We now consider several choices for the response kernel, $J(t)$, and the synaptic weight function $W(x)$. The single time constant response kernel and its associated Fourier transform are given by

$$J_1(t) = \frac{1}{\tau_{decay}^2}(t-\xi)e^{-\frac{t-\xi}{\tau_{decay}}}\Theta(t-\xi), \tag{6.49}$$

$$\tilde{J}_1(j\omega) = \frac{e^{-j\omega\xi}}{(1+\tau_{decay}j\omega)^2}, \tag{6.50}$$

where $\xi$ represents the axonal conduction delays. The corresponding equations for a response kernel with different rise and decay time constants are

$$J_2(t) = \frac{1}{\tau_{decay}-\tau_{rise}}\left(e^{-\frac{t-\xi}{\tau_{decay}}}-e^{-\frac{t-\xi}{\tau_{rise}}}\right)\Theta(t-\xi), \tag{6.51}$$

$$\tilde{J}_2(j\omega) = \frac{e^{-j\omega\xi}}{(1+\tau_{decay}j\omega)(1+\tau_{rise}j\omega)}. \tag{6.52}$$

The finite support equal weight synaptic function is given by

$$W_1(x) = \gamma^{-1}\Theta(\frac{\gamma}{2}+x-\chi)\,\Theta(\frac{\gamma}{2}-x+\chi), \tag{6.53}$$

$$\tilde{W}_1(j\omega) = e^{-j\omega\chi}\frac{\sin(\frac{\omega\gamma}{2})}{\frac{\omega\gamma}{2}}=e^{-j\omega\chi}\mathrm{sinc}(\frac{\omega\gamma}{2}), \tag{6.54}$$

where the parameter $\chi$ controls the degree and direction of the asymmetry in the synaptic connections. For example, $\chi=\gamma/2$ corresponds to the chain topology in Equation (6.21). For

a synaptic weight function with infinite support and exponential decay we consider

$$W_2(x) = \frac{1}{2\sigma_x} e^{-\frac{|x-\chi|}{\sigma_x}}, \tag{6.55}$$

$$\tilde{W}_2(j\omega) = \frac{e^{-j\omega\chi}}{1+(\sigma_x\omega)^2}. \tag{6.56}$$

For the purposes of concreteness, we consider the chain topology with asymmetric inhibitory connections and response kernel $J(t) = J_2(t)$ with both rise and decay time constants. The chain topology requires that $W(x) = W_1(x)$, $\chi = \gamma/2$, and we set $\gamma = 50$. Figure 6.11 shows the dispersion relation obtained as the zero level curve of $F(k,T) = V_s(k,T) - V_r(T)$. Notice that the level curves exist for both positive and negative values of $k$, implying that both forward and backward propagation satisfy the first self-consistency condition. However, only the solid black portion, corresponding to backward propagation, satisfies the second self-consistency condition. Hence, only backward waves are allowed under this choice of topology and parameters.

We now focus on the analysis of networks with purely inhibitory coupling and consequently set $g < 0$. Since all synaptic interactions are inhibitory, how much external excitation $I_0$ must neurons receive in order to exhibit collective behavior, and how does the balance between the inhibitory coupling $g$ and external excitation $I_0$ affect this behavior? Notice that $g$ controls the sign and magnitude of both $V_s(k,T)$ and $I(0,T)$, so it is useful to express them as $V_s(k,T) = g\bar{V}_s(k,T)$ and $I(0,T) = g\bar{I}(0,T)$, where the bar denotes non-negative quantities. Using this notation the self-consistency conditions become

$$\bar{V}_s(k,T) = \frac{V_r(T)}{g} \quad \text{and} \quad \bar{I}(0,T) > \frac{1-I_0}{g} = \alpha \tag{6.57}$$

and the left hand sides of both equations are positive. Since $g < 0$ it then follows that $V_r(T)$ must also be negative for a solution to exist. Since the after spike reset potential must be lower than the firing threshold, $\zeta < 1$ and so $V_r(T) \geq (1-e^{-T})(1-I_0) \geq (1-I_0)$. In the excitable regime $I_0 < 1$ and then clearly $V_r(T) \geq 0$, so no solutions to the first self-consistency condition exist. Therefore, only the oscillatory regime, $I_0 > 1$, is consistent with traveling waves under inhibitory coupling, $g < 0$. Since $\bar{I}(0,T)$ does not depend on either $g$ or $I_0$, the second self-consistency condition in Equation (6.57) is purely determined by the ratio of excitation above threshold to inhibition $\alpha = (1-I_0)/g = |I_0-1|/|g|$. Similarly, $\bar{V}_s(k,T)$ does not depend on either $g$ or $I_0$ and the first self-consistency condition can be expressed as

$$\bar{V}_s(k,T) = \frac{1-I_0}{g} + \frac{I_0-\zeta}{g} e^{-T} = \alpha - \frac{I_0-\zeta}{|g|} e^{-T}. \tag{6.58}$$

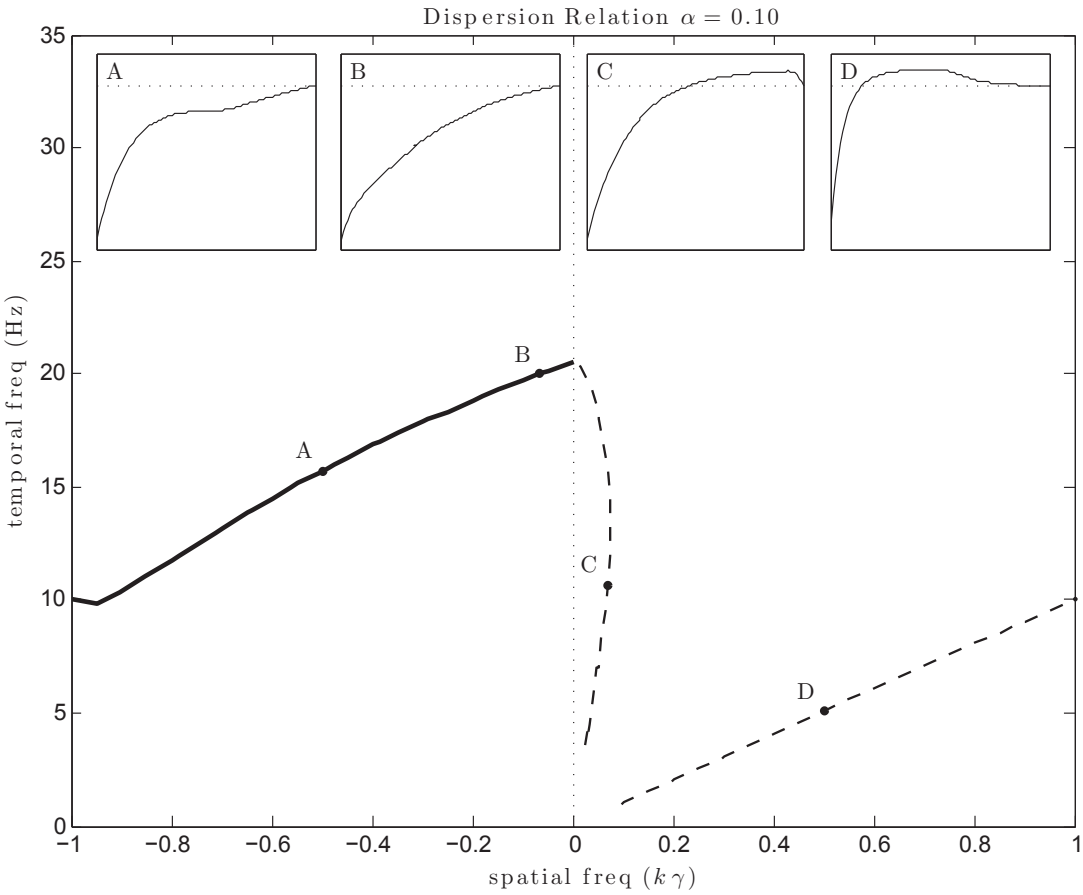


Fig. 6.11 **Dispersion relation derived from IF continuum approximation.** Curves show solution branches that meet the first self-consistency condition. Only the solid black portion meets the second self-consistency condition as well. Insets show $V(0,t)$ over the interval $[0,T]$ for the choices of spatial and temporal frequencies indicated by the labeled points on the dispersion curve. In all examples $V(0,0) = \zeta$ and $V(0,T) = 1$, however in C and D, $V(0,t)$ crosses threshold (dotted line) at an earlier point as well. Hence $V$ is decreasing at $T$ and does not meet the second self-consistency condition. Notice also that $k < 0$ for the solid curve, so that only backward waves are allowed. The parameters are as follow: $W(x) = W_1(x), J(t) = J_2(t), g = -1, I_0 = 1.1, \zeta = 0, \tau_m = 10, \tau_{rise} = 1, \tau_{decay} = 20, \gamma = 50, \chi = 25, \xi = 0$.

For large $T$, the above can be approximated as $\bar{V}_s(k,T) = \alpha$, so the dispersion relation is also approximately determined by $\alpha$. This is illustrated in Figure 6.12. Consider the value of the dispersion relation at $|k|\gamma = 1$. It is easy to see that under this choice of $k$, $\tilde{W}(j\omega) = 0 \quad \forall \omega \neq 0$ and is 1 otherwise. Consequently, $\bar{V}_s(k,T) = (1-e^{-T})/T \approx 1/T \approx \alpha$. The analysis above shows that the shape of the dispersion relation is primarily governed by the ratio of excitation to inhibition $\alpha$ and is less sensitive to the absolute magnitude of $g$ or $I_0$.

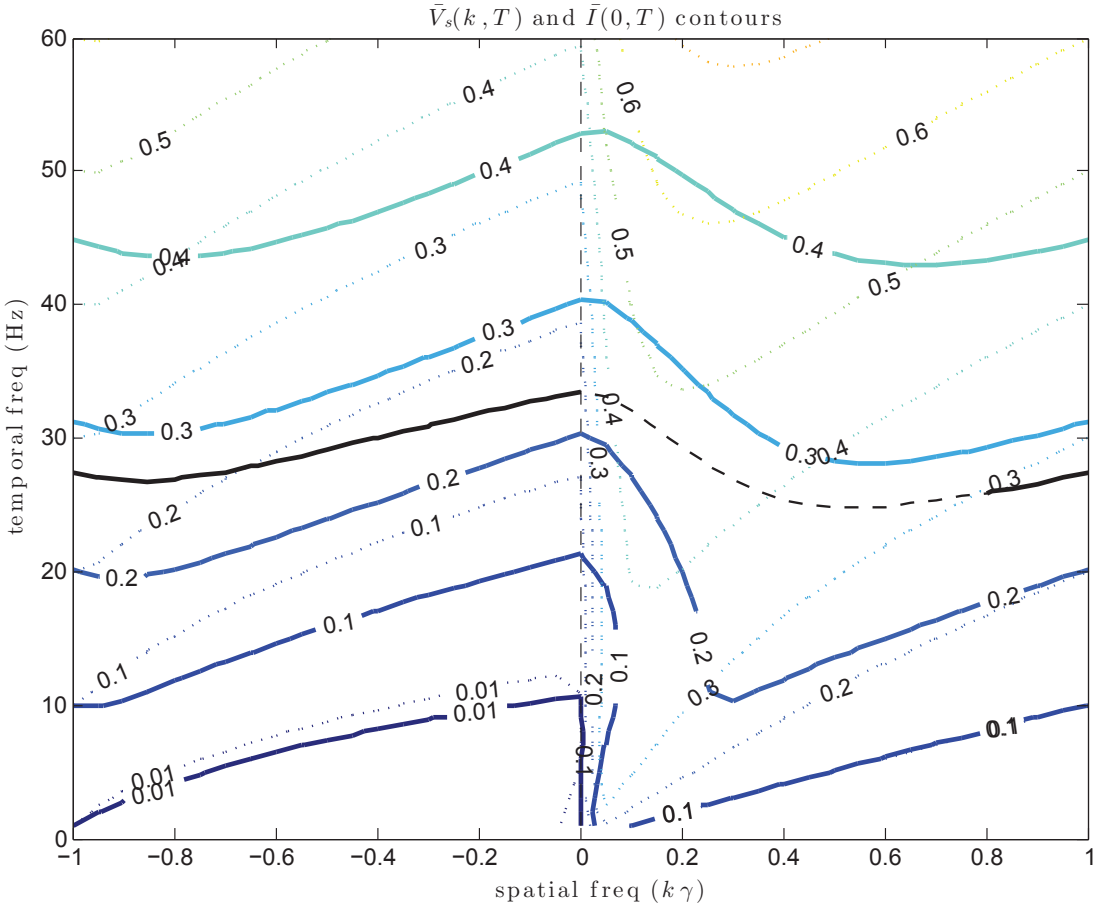


Fig. 6.12 **Dispersion relations under different ratios of excitation to inhibition.** Solid lines correspond to $\bar{V}_s(k,T) = \alpha$ and dotted lines to $\bar{I}(0,T) = \alpha$. The values of $\alpha$ are indicated on the contour lines. Solid lines are approximations to the dispersion relations and hold best for small temporal frequencies. Only the portions of the dispersion relations that lie below the corresponding dotted contour lines meet the second self-consistency condition. This is the case for most curves in the left half-plane ($k < 0$) and not true for most curves in the right half-plane ($k > 0$). However, the true dispersion relation for any $\alpha$ lies below the corresponding $\bar{V}_s(k,T) = \alpha$ contour, as indicated by the black line for $\alpha = 0.3$. Here a portion of the dispersion relation for positive $k > 0.8$ also meets the second self-consistency condition.

Next we turn our attention to how the level of asymmetry in the synaptic connections affects the shape of the dispersion relation. To do so, we fix $\alpha = 0.1$ and systematically vary the offset $\chi$ in the synaptic weight function $W_1(x)$. The results are illustrated in Figure 6.13 and show that significant directionality in the connectivity is required for the network to exhibit backward traveling waves. In particular, $\chi > 0.4\gamma$ before we recover the dispersion relation corresponding to the forward chain topology, $\chi = 0.5\gamma$.

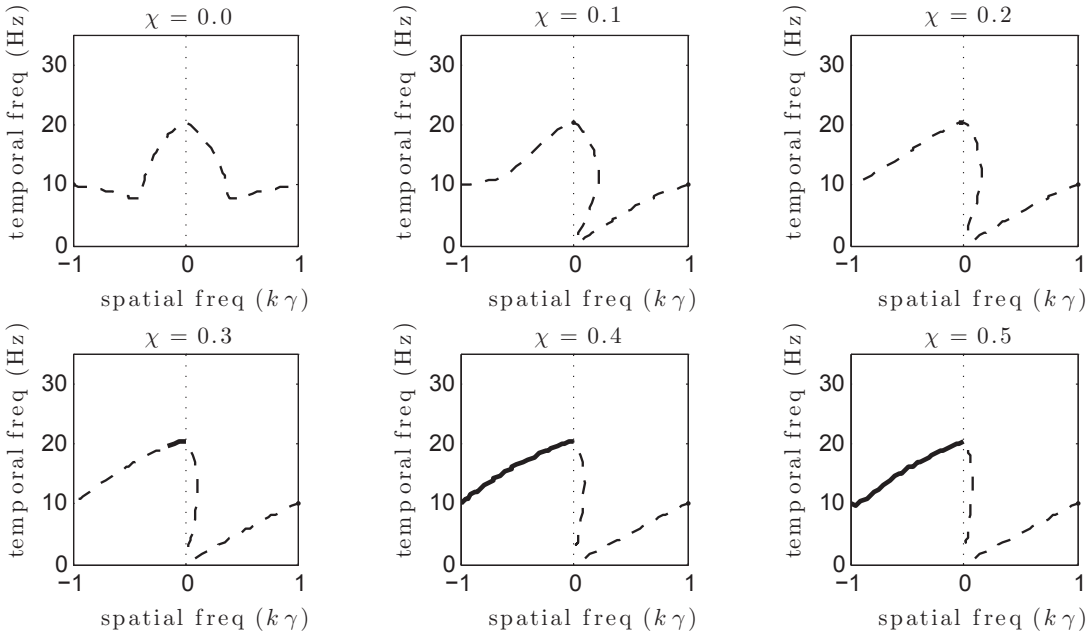


Fig. 6.13 **Dispersion relations under different levels of connection asymmetry.** Same parameters as in Figure 6.11, but the asymmetry ratio $\chi/\gamma$ is varied from 0 to 0.5 as indicated above the panels. Here 0 corresponds to symmetric connections and 0.5 to forward connections only. Notice that significant directionality in the connectivity is required for the network to exhibit backward traveling waves.

We can also systematically vary the axonal conduction delay, $\xi$, in the spike response kernel $J_2(t)$. The results are illustrated in Figure 6.14 and show that with progressively increasing delays, long wavelength solutions for forward-propagating waves become possible. Finally, we vary the decay time constant, $\tau_{decay}$, of the spike response kernel $J_2(t)$. The results are illustrated in Figure 6.15 and show that the frequency of the collective synchronous oscillation decreases with increasing synaptic decay time constant.

## 6.5 Conclusion

Starting from experimental findings (Lubenov and Siapas, 2009), our purpose has been to model traveling wave patterns using a biophysically plausible model, and to investigate the mechanisms generating this wave-like behavior. We have first explored phenomenologically the wave dynamics arising from a inhibitory chain of HH neurons with asymmetric connections. Our results show that if a set of neurons at the head of the chain is periodically forced, traveling waves propagate in a direction opposite to that of synaptic connectivity. In order

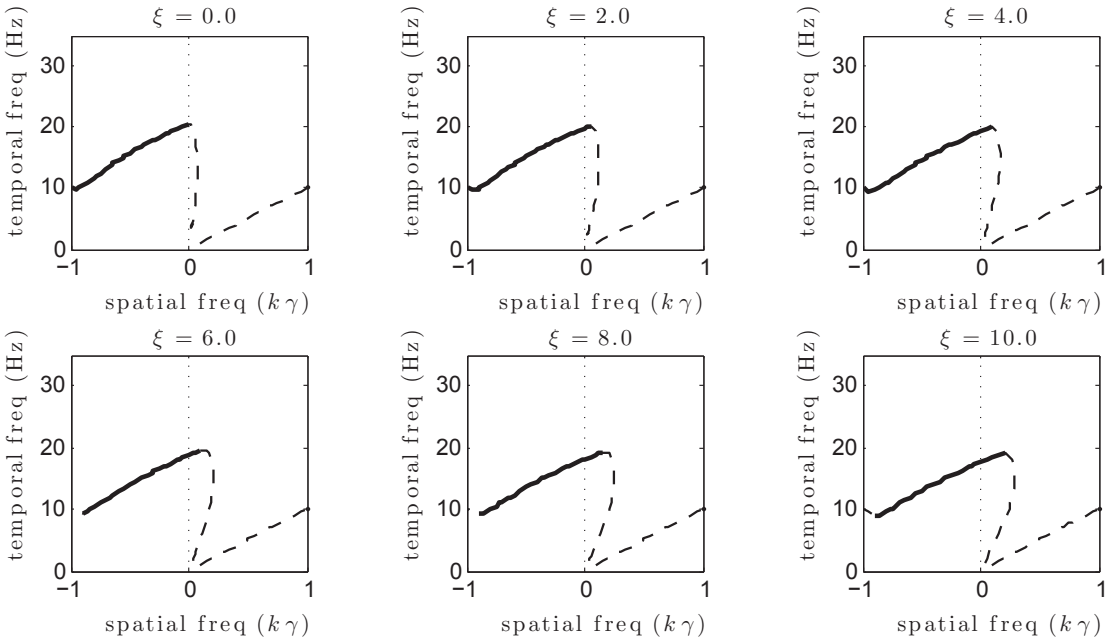


Fig. 6.14 **Dispersion relations under different axonal delays.** Same parameters as in Figure 6.11, but the axonal delay $\xi$ is varied from 0 to 10 ms as indicated above the panels. Notice that with increasing delays long wavelength solutions for positive $k$ become possible.

to shed light on the mechanisms and properties underlying these wave patterns, we have provided a continuum approximation with a topology similar to HH model to verify the existence of backward waves under our assumptions. In fact our analysis demonstrates that such a specific chain-like system, with purely inhibitory asymmetric connections and periodic driving at the bottom, can exhibit only backward waves and forward waves are not admitted. Furthermore the analysis of the wave dispersion relation predicts that there is a limit to the longest wavelength that the network can display. This analytical study reinforces the numerical results obtained with the spiking HH model:

- in the limit of zero driving frequency (the non-driven state) the spatial wavelength converges to the connectivity window. This is exactly what we see in the spiking model with the equilibrium state taking the form of constant stripes of active neurons spaced at the connectivity window (Figure 6.2);
- for each set of parameter values there is a limit to the longest wavelength that the chain can sustain, even if this requires a further investigation. In fact, the dispersion relation does not guarantee that the system will exhibit the corresponding patterns, therefore the next step should be the calculation of regions of stability in the space of solutions.

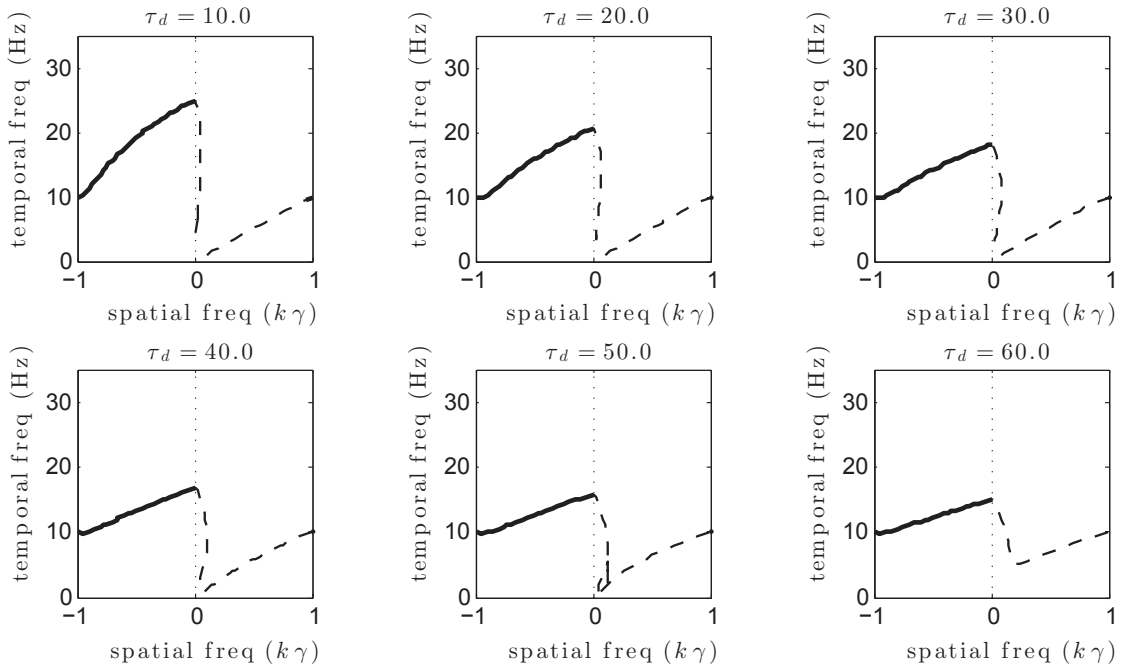


Fig. 6.15 **Dispersion relations under different synaptic decay.** Same parameters as in Figure 6.11, but the synaptic decay time constant $\tau_m$ is varied from 10 to 60 ms as indicated above the panels. Notice that the frequency of the synchronous oscillation at $k = 0$ decreases with increasing decay time constant.

Next we have investigated the robustness of these patterns by varying the previous assumptions. This parameter analysis is carried out with a simpler model. Specifically we have developed an IF continuum approximation for our chain of asymmetrically connected inhibitory neurons, which is analytically tractable and at the same time it is able to capture the most relevant properties of the waves. We have derived with this model the dispersion relation as a function of various parameters of the system, thus exploring the sufficient and necessary conditions yielding traveling waves. Our results show that (i) the dispersion relation is primarily affected by the ratio of excitation over inhibition, rather than the magnitude of external excitation or recurrent inhibition separately (Figure 6.12), (ii) forward waves with long spatial wavelength can arise in presence of increasing delays (Figure 6.14), (iii) the wave frequency is a function of the GABA decay temporal constant (Figure 6.15) and finally that (iv) backward traveling waves can be generated in networks with a significant degree of asymmetry in the neuronal connectivity (Figure 6.13). This analytical methodology captures the results that we obtained with the spike response model, and provides further insights on the relevance of a variety of network properties that underlies the wave propagation.

# Part III

# Conclusions

# Chapter 7

# Conclusions

The brain is a complex multi-scale dynamical system that displays population oscillations, whose properties vary in time and space according to the behavioral state. Instances of this highly coordinated oscillatory dynamics, such as periodic synchronization of neuronal spiking at different scales or spatial propagation of neuronal oscillations, may have a computational role in high-level processes and subserve many cognitive functions. In this Thesis we have explored a variety of spatiotemporal phenomena arising from the collective cooperation of neurons in different brain areas, by means of computational models at microscopic and mesoscopic scales. We have studied rhythmic coordination between thalamic cells in different brain states and its potential role in thalamocortical communication process. We have also examined gamma-band synchronization across different areas and how neuronal assemblies engaged in this oscillatory activity can efficiently communicate by means of microscopic models. Furthermore we have proposed a large-scale model to study how processes taking place at different scales interact in the multi-scale brain by means of synchronization measures. Finally we have mathematically explored emerging patterns of propagation of neuronal oscillations based on experimental observations in the hippocampus of rats. All these different complex phenomena are characterized by a collective cooperation between single cells and brain regions that lead to highly spatiotemporal patterns at different scales. In what follows we will summarize the main results of Part II and provide future perspectives.

## 7.1 Transition between functional regimes in an integrate-and-fire network model of the thalamus

In Chapter 3 we have explored two clearly distinct dynamical regimes with different functionalities that characterize thalamic activity. During slow-wave sleep the thalamus is dominated by internal activity and is hardly sensitive to external stimuli (bursting mode). This activity is characterized by spindle oscillations, namely rhythmic oscillations at $7-14$ Hz. In contrast, in the awake state the thalamus modulates its activity according to the stimuli coming from the periphery (firing mode). Our network model includes glutamatergic thalamocortical (TC) relay neurons and GABAergic reticular (RE) neurons described by adaptive exponential integrate-and-fire models (aEIF), in which spikes are induced by either depolarization or hyperpolarization rebound. Our results have shown that TC-RE loops generate spindle-like oscillations. The generation of this rhythm during slow-wave sleep is due to the rebound bursting properties of TC cells, which are mutually connected with RE neurons thus giving rise to highly temporal coordinated patterns. Our results have demonstrated that clustering in the RE-RE connections allows the model to exhibit coexistence of the two regimes introduced above: one dominated by oscillations and insensitive to external stimuli (like sleep) and one insensitive to them (like wake). We have observed that the transition between the two regimes occurs when the external excitatory input on TC neurons (mimicking sensory stimulation) is large enough to cause a significant fraction of these neurons to switch from hyperpolarization-rebound-driven firing to depolarization-driven firing. In fact if the external stimulus is below a given threshold, the network is in a purely rebound-bursting state insensitive to external stimuli, while when this threshold is crossed there is a non-zero contribution of the spikes due to depolarization, and this makes the TC neurons (and not the RE neurons) sensitive to the stimulus intensity, in agreement with experimental observations (Halassa et al., 2014). Our aEIF network model provides a computationally efficient description of the dynamical features of the thalamus while preserving the properties of the individual neurons.

Choosing a simple model for the single neurons allowed us to focus on capturing the network effects. This choice also opens a number of interesting perspectives: due to their relative simplicity, IF models can be tackled analytically (Barbieri et al., 2014; Brunel, 2000), and facilitate the search for basic canonical computations (Schwartz, 2015). Finally, most primary sensory cortex network models are built on IF neurons (Battaglia and Hansel, 2011; Potjans and Diesmann, 2014), and hence aEIF neurons seem a more coherent choice to build models of corticothalamic interactions (Muller and Destexhe, 2012). In our model, the switch from inhibitory-rebound-driven activity to depolarization-driven firing is proposed to represent a switch from sleep to awake state (Dang-Vu et al., 2008). The information analysis depicted in

Figures 3.9-3.10 has shown the separation between a stimulus-independent state (sleep) and a stimulus-sensitive state (wakefulness). We have not directly dealt with the role of thalamus, and in particular of RE neuronal activity, in attention, to which a wealth of works have been devoted (McAlonan et al., 2008; Wimmer et al., 2015) after the seminal intuition of Crick (1984). To compare our model results with these experimental observations we should (1) contrast different states inside the awake regime, and (2) take into account the temporal structure of the TC spike trains rather than their rate alone. This will be certainly feasible on the ground of the results presented in Chapter 3. We have emphasized that our model is based on single-neuron models that are much simpler than those used previously. Although this has a number of advantages, as discussed above, some features of thalamic behavior that are captured by more detailed models are not reproduced by our model. For instance, our spindle oscillations constitute a stable state, both in small and large TC-RE networks, and do not reproduce the wax-and-wane dynamics that has been observed experimentally (Bal and McCormick, 1996), and which has been reproduced by more detailed models that take explicitly into account the dynamics of hyperpolarization-activated cation currents (Bazhenov et al., 1999). On the other hand, our results pave the way for the development of efficient models of the transmission of sensory information from periphery to cortex.

The work presented in Chapter 3 has taken into account only stable external inputs from the periphery to TC neurons or from the cortex to RE neurons. Preliminary analysis suggested that an accurate description of thalamocortical inputs and corticothalamic feedbacks required a separate study. In the future this network will be integrated in a full corticothalamic model in order to investigate the role of the thalamus in the thalamocortical information system, because it still remains unclear. The thalamus cannot be exclusively classified as machine-like relay, because in that case sensory information from the periphery would be faithfully transmitted to the neocortex. Instead it has been shown that the thalamus can dynamically process information in a way that it reflects different behavioral states such as attention, consciousness and drowsiness. Furthermore recent morphological evidences demonstrated that the major source of excitatory synapses impinging on the thalamus is represented by feedback cortical projections (Destexhe, 2000; Erişir et al., 1997; Liu and Jones, 1999), thus there is a good reason to think that thalamus plays a role in gating and modulating the flow of information towards the cortex (Sherman and Guillery, 2002). Many experiments in the intact brain have revealed that thalamic oscillations are entrained by the cortex, appointing to the cortico-thalamic feedback an important role in coordinating widespread, coherent and synchronized oscillations (Destexhe, 2000). Reinhold et al. (2015) found that the sensory-evoked activity in the visual cortex upon the appearance of a stimulus does not simply reflect a self-sustaining activity due to intracortical recurrent circuits, but it is entrained and amplified by the direct thalamocortical

communication pathway. Future studies will be devoted to understand the effect of corticothalamic feedback on thalamic circuits as well as investigating whether the role of the thalamus is simply to relay information to the cortex and/or to process and modulate it according to different attentional states.

Another interesting continuation of this work would be to contribute to the open challenge of modeling the LFP of the thalamus (Einevoll et al., 2013). Mazzoni et al. (2015) recently showed that an integrate-and-fire model like the one presented in Chapter 3 can be combined with morphological data and transmembrane current simulation (Lindén et al., 2013) to capture the LFP dynamics in a patch of cortex. Since morphological data are available for the thalamus, a similar procedure can be applied to our network, and would hopefully shed light on the way extracellular signals and neural activity are linked in this area, thus enhancing the possibility of experimental validations of the thalamic models. The potential applications of this work include the study of the consequences of deep brain stimulation (DBS) [1]. Thalamic DBS has been shown to contribute to the symptom mitigation of a variety of neural diseases including Parkinson (Tasker, 1998) and Tourette's syndrome (Servello et al., 2008). However, the precise mechanisms of this mitigation are not completely clear, nor is the procedure to design specific trains of stimulations suited for different patients/conditions. Neural models are already exploited to test DBS patterns (McIntyre et al., 2004). We think that a simple yet efficient model like the one presented in Chapter 3 can valuably contribute to this field.

[1] **Deep brain stimulation**. DBS stands for the implantation of electrodes within certain areas of your brain to produce electrical impulses that regulate abnormal impulses. The amount of stimulation in DBS is controlled by a pacemaker-like device placed under the skin in the upper chest, and a wire that travels under the skin connects this device to the electrodes in the brain. DBS is nowadays used to treat a number of neurological conditions, such as tremor, Parkinson's disease, epilepsy, Tourette's syndrome, chronic pain and obsessive compulsive disorder. It is also experimentally used for the treatment of depression, stroke recovery, addiction and dementia.

## 7.2 Phase-coherence transitions and communication in the gamma band between delay-coupled neuronal populations

Synchronization of collective neuronal oscillations has been suggested to mediate communication between brain areas, with the global oscillations acting as *information carriers*, on which signals encoding specific stimuli or brain states are superimposed. But neuronal signals travel at finite speeds across the brain, thus leading to a wide range of delays in the coupling between neuronal populations. In Chapter 4 we have approached this question in the case of two delay-coupled neuronal populations exhibiting collective oscillations in the gamma range by means of conductance-based HH neurons. We have characterized the global activity of the neuronal populations by means of averaging measures such as LFP and MUA (see Appendix A.1). In the presence of excitatory coupling, the LFP and MUA activities of two identical delayed neuronal networks oscillate in the gamma range due to the recurrence between excitatory and inhibitory synaptic activity. We have used these measures to quantify phase coherence between the oscillatory activity of the two delay-coupled populations at varying mean axonal delays. The two populations exhibit consistent phase coherence for a wide range of coupling delays, undergoing a transition from in-phase (zero-lag) to anti-phase collective oscillations as the delay increases. In the transition region, the in-phase and anti-phase dynamics coexist (see Figure 4.6). We next used information theory to quantify the response of one population (the receiver) to a varying external input impinging originally on the other population (the emitter). For different transmission delays between the two coupled populations, we have analyzed how the LFP and MUA calculated from one population convey information in response to a set of external inputs applied to the other population. Our results have shown that effective communication can be reached even in the presence of relatively large delays between the populations, which self-organize in either in-phase or anti-phase synchronized states.

Our results reinforce the perspective that inter-region coherence of oscillatory networks activity can modulate functional connectivity among anatomically connected regions (Fries, 2005; Salinas and Sejnowski, 2001; Varela et al., 2001), thus subserving an important role in cognition by allowing the function of brain networks to be dynamically reconfigured in response to different task demands (Akam and Kullmann, 2012). Within this context, the CTC hypothesis (Fries, 2005) proposed that selective communication can be achieved by coherence between firing rate modulation in a sending region and gain modulation in a receiving region; hence a sending group of neurons will have the highest impact on a receiving group, if its inputs consistently arrive when gain is high. In that case, information could be efficiently gated

by modulating the coherence between populations. Fries (2005) proposed that unidirectional communication is due to rhythmic entrainment with an inter-areal delay and, in this case, the conduction delay is directly translated for a given frequency into a relative nonzero phase (delayed coherence). Our results have confirmed that unidirectional couplings, either structural or functional, lead to a leader-laggard configuration with an out-of-phase synchronization determined by the axonal delay (Figure 4.13). Differently from the unidirectional case, CTC stated that bidirectional inter-areal communication neurons participating in a communication link were synchronized at zero phase both within and between areas (see Figure 3 of Fries, 2005).

What happens in the presence of interaxonal delays? In its original form, the CTC hypothesis assumed that inter-areal conduction delays were small relative to the respective cycle lengths. Thereby two communicating areas, oscillating at zero phase, send output at the same time in the oscillation cycle, and their mutual inputs arrive shortly afterward, still within the excitatory phase of the same cycle. A given cycle length, i.e. oscillation frequency, can in this scheme only subserve communication up to a certain conduction delay. This led to the prediction that longer delays, observed between more distant brain areas, result in communication through coherence at lower frequencies (Bastos et al., 2015b). While this has sometimes been assumed to be the case (Von Stein and Sarnthein, 2000), it has recently been shown that neuronal groups in widely separated areas, even over very large cortico-cortical distances, can be coherent in the gamma band, i.e., at a relatively high frequency (Bastos et al., 2015a; Bosman et al., 2012; Fries, 2015; Gregoriou et al., 2009; Grothe et al., 2012)

In Section 1.3.2 we have revised some modeling studies on how neuronal groups engage in zero-phase synchrony in presence of variable conduction delays. Vicente et al. (2008) showed that two neuronal groups, if they were both bidirectionally connected to a third population, could display oscillatory coherence at zero phase (Vicente et al., 2008). This could be plausible because this motif is often observed in anatomical networks involving cortical (Markov et al., 2012) or sub-cortical sources (Shipp, 2003a). In Chapter 4 we have studied two neuronal populations coupled synaptically with non-negligible delays. Our modeling results have shown that the populations organize their joint collective dynamics in patterns of in-phase or anti-phase synchronization, depending on the delay. As one can expect, the two populations oscillating in the gamma range synchronize at zero lag when the coupling delay is zero or very small (Figure 6.6). For increasing delays instead, the networks try to synchronize at lower frequencies (as suggested by Fries, 2005), and eventually transition to an anti-phase regime with smaller, although still significant, phase coherence (for delays up to tens of milliseconds). Both types of dynamics seem to coexist for intermediate delays. This allows communication to be reached effectively even in the presence of relatively large delays between the popula-

tions. In those cases the transmission delay, phase difference, and oscillation frequency match to allow for communication at a wide range of coupling delays between brain areas (Barardi et al., 2014b). Our modeling results thus demonstrate the biophysical plausibility of zero-phase synchronization despite relatively long conduction delays provided that the coupling is symmetric, i.e. the two synchronized local circuits should be similar e.g. in their local organization and activity level, their conduction delays to the respective other circuit, and the strength of their feed-forward inhibition (Bastos et al., 2015b).

In accordance with our results in Chapter 4, and contrarily to the original CTC hypothesis, recent studies found that interareal gamma-band synchronization can entail a non-zero phase lag (Bastos et al., 2015b). Due to these new experimental observations, it became clear that even though the areas are bidirectionally coupled, this gamma-band coherence does not occur at zero phase, but with a systematic delay, i.e., with a directedness (Bastos et al., 2015b; Bosman et al., 2012; Zandvakili and Kohn, 2015). Fries (2015) formulated a new version of CTC proposing that bidirectional cortical communication is realized separately for the two directions by unidirectional CTC mechanisms entailing delays in both directions (Bastos et al., 2015b; Fries, 2015). In that context he suggested that entrainment with delay is the general mechanism that sets up phase relations subserving CTC, both for unidirectional communication and for bidirectional communication.

Akam and Kullmann (2012) have also proposed a mathematical implementation of CTC, assuming a sinusoidal oscillation and a linear relation between phase and excitability. Their analysis showed that presynaptic groups, which are incoherent to the postsynaptic group, might still have a substantial impact. In other words, CTC mechanisms are possible, but only if some constraints on the structure of oscillatory activity are imposed (Akam and Kullmann, 2012). In fact, the accuracy of information transmission in presence of distractors depends on the structure and strength of oscillatory activity across a set of inputs. Akam and Kullmann (2012) demonstrated that to achieve a high signal to noise ratio the oscillatory modulation of the target signal must be strong, and distracting inputs must be distinguished from the target by frequency, phase or amplitude of oscillation. If these requirements are not fulfilled, the accuracy of information transmission is reduced (Akam and Kullmann, 2012). Given that such oscillatory activity spans several orders of magnitude in frequency (Section 1.1.2), and that in several brain regions the phase of firing is actively modulated relative to a single coherent oscillation (O'Keefe and Recce, 1993), the brain can indeed exploit phase and frequency separation to minimize interference between oscillatory signals (multiplexing mechanism proposed by Akam and Kullmann, 2010). The new formulation of the CTC hypothesis (Fries, 2015) requires that excitability be modulated by rhythmic synchronization in a way that is nei-

ther sinusoidal nor linear, in agreement with mathematical models entailing spiking excitatory and inhibitory neurons (Börgers and Kopell, 2008; Cannon et al., 2014; Gielen et al., 2010).

While there is substantial experimental support of the CTC hypothesis (Cardin et al., 2009; Schoffelen et al., 2011; Siegle et al., 2014; van Elswijk et al., 2010), some studies posed challenges to the original CTC formulation that motivated the new view (Fries, 2015), and which need to be further explored. Now there is increasing experimental evidence that different visual areas are gamma-band synchronized with a non-zero phase lag. Therefore non-zero phase synchronization likely has a key role in the establishment of communication links, and this needs to be further explored. In conclusion, how the brain reaches the required level of coordination in presence of large delays is unclear yet. Here we have proposed a solution that is consistent with the original CTC formulation and with new experimental results. It will be important to experimentally test if two distant neuronal populations engage in gamma synchronized patterns in presence of large delays, eventually transitioning from in-phase to anti-phase dynamics to subserve efficient and selective information transmission. It would be interesting to study if it is possible to experimentally manipulate neuronal synchronization, while leaving other aspects of neuronal activity unchanged, and thereby show effects on neuronal communication.

## 7.3 Probing scale interaction in brain dynamics through synchronization

The preceding Thesis chapters were devoted to develop different microscopic models of cortical neuronal networks to explore a diverse range of collective dynamical phenomena: temporally organized patterns arising from the coordination of TC and RE neurons in the thalamus, and different information processing functionalities through thalamocortical pathways and gamma-band synchronization between neuronal networks that could subserve as a mechanism for selectively routing the flow of information. Using different simplified levels of description has been, and still is, very fruitful in unveiling the mechanisms that lay at the basis of the observed neural tissue behavior (Fourcaud-Trocmé et al., 2003; Goldbach et al., 2008; Kopell et al., 2000a; Sancristóbal et al., 2013). However the brain is a multi-scale dynamical system. In fact the mammalian brain operates in multiple spatial scales simultaneously, from the microscale to cortical regions. These levels of description are associated with distinct temporal scales, ranging from milliseconds in the case of neurons to tens of seconds in the case of brain areas.

In Chapter 5 we have examined theoretically how spatial and temporal scales interact in the functioning brain, by considering the coupled behavior of two mesoscopic neural mass models (NMs) that communicate with each other through a microscopic neuronal network (NN) (Figure 5.1). We have used the synchronization between the two NM models in order to probe the interaction between the mesoscopic scales of those neural populations and the microscopic scale of the mediating NN. The two NM oscillators were taken to operate in a low-frequency regime with different peak frequencies (in the theta and alpha bands) and with very different dynamical features (spike-like dynamics in one case and quasi-harmonic dynamics in the other). The microscopic neuronal population, in turn, was described by a network of several thousand excitatory and inhibitory spiking neurons operating in a synchronous irregular regime, in which the individual neurons fire very sparsely but collectively give rise to a well-defined rhythm in the gamma range (as in the neuronal network studied in Chapter 4). Our results have shown that this NN, which operates at a fast temporal scale, is indeed sufficient to mediate coupling between the two mesoscopic oscillators, which evolve dynamically at a slower scale. Therefore frequency and phase locking arise even when the two NMs operate at very different frequencies and with very different dynamical features (Figure 5.3). We have also established how this synchronization depends on the topological properties of the microscopic NN, on its size and on its oscillation frequency. In particular, structural clustering within the neuronal network reduces the ability of the microscopic neuronal population to induce synchronization (Figure 5.5), and the size of the subpopulation of neurons that directly

coupled the two NMs must also be large enough to allow the intrinsically irregular neurons to reach a sufficiently strong collective regime through which the two neural masses can communicate (Figure 5.6).

In general, analyzing this scale interaction by comparing the behaviors of the microscopic and mesoscopic models is a very complicated task. In 2009, for instance, Faugeras et al. (2008) derived the equations of evolution of NMs from the dynamics of a NN described by a voltage-based model, through a Herculean mean field analysis of the network, an approach that as the authors themselves mention in the concluding paragraph of their paper, would be very ambitious to apply to spiking neuronal models. One year later, Rodrigues et al. (2010) performed such a multi-scale mapping under strong assumptions (in some cases hard to justify biologically) that included high correlation between the neurons in the microscopic populations and low-amplitude input currents. In our work, we have attempted to circumvent the complexity of those approaches by using a more phenomenological strategy, whose goal is to test whether microscopic and mesoscopic descriptions of neuronal populations communicate with one another by using synchronization as a proxy of effective communication. On this regard, Figure 5.3E,F shows that the MUA exhibited by the NN is phase-locked to the voltage of the NM model when synchronization between the two NMs arises. This indicates that the neuronal network is actively involved in the communication of information between the two mesoscopic models. We have also quantified the efficiency of this effect as the number of NN neurons involved in the communication between the NMs changes.

Modeling the dynamics of the full brain from a purely microscopic scale is computational unfeasible. Thus a hybrid description of the brain that encompasses multiple scales is an appealing concept. In that scenario, it would only be necessary to represent microscopically those neuronal populations involved in a particular task, and which are monitored with single-cell resolution. The rest of the brain, while modulating the activity of the population of interest, would not necessarily require being represented with microscopic detail. Currently this is accomplished by representing the activity of the rest of the brain by a background noisy activity, but this approach is not useful when the neuronal population of interest feeds back into those other brain regions, thereby modifying the background activity that acts upon the population itself. In Chapter 5 we have considered one way of facing this situation, based on coupling bidirectionally microscopic and mesoscopic descriptions of neuronal populations and using synchronization to probe the interaction between the two scales. We have employed that scheme in which two mesoscopic populations are coupled through a third microscopic network, since the behavior that can be expected from two coupled NM models is well known (David and Friston, 2003; Jansen and Rit, 1995), and can be used as a reference to interpret the coordinated behavior emerging from our hybrid scenario.

However, if one is interested in a level of detail that can only be reflected by NNs and not by NMMs, then the appropriate level of description throughout has to be adopted. In other words, it would be also interesting to test whether microscopic and mesoscopic descriptions of neuronal populations communicate, by means of a model where both levels of representation coexist. So far, global brain activity has been modeled by dividing the brain into discrete volume elements, or voxels, and coupling them according to statistical correlations and structural information (Alivisatos et al., 2012; Deco et al., 2013; Pons et al., 2010; Sotero et al., 2007). Recently, large-scale models of the brain have received special attention. Both the Human Brain Project and the Brain Activity Map project propose integrated views to bridge the gap between the behavior of single neurons and the functions of the full brain (Alivisatos et al., 2012), but this quest is still in its infancy.

## 7.4 Wave propagation in inhibition-dominated neuronal chains

In Chapter 6 we have analyzed the behavior of one-dimensional chains of inhibitory neurons with asymmetric connections. We have shown that such chain-like networks exhibit backward propagating waves with respect to the direction of synaptic connectivity if neurons at the bottom are periodically forced. These numerical results show that in the absence of noise and for small GABA decay times, wave patterns with long spatial wavelength can arise within the network. Importantly, however, the long wavelength regime, which is a hallmark of many neuronal tissues, cannot be readily achieved and is very sensitive to network parameters and noise. To explore and understand our numerical results we have first developed a continuum model approximation with a topology similar to the HH model, deriving a self-consistence condition for the existence of these backward traveling waves and calculating the dispersion relation that fully characterizes the main properties of the wave patterns. This mathematical analysis predicts that there is a limit to the longest wavelength that the network can display depending on different conditions. Moreover the shape of the dispersion relation qualitatively agrees with the numerical results.

The results discussed above strongly depend on the assumptions made at the beginning of the analysis regarding the topology of the network and other synaptic properties. In order to study systematically which are the necessary and sufficient conditions for the generation of these patterns, or in other words to investigate the robustness of these results across different systems, we propose an integrate-and-fire continuum approximation based on a network with asymmetric inhibitory connections, with individual neurons operating in the oscillatory regime. We have tested self-consistency conditions to verify the existence of backward and forward waves and derived the dispersion relation. Specifically, we have constructed families of dispersion relations as parameters are varied, including level of asymmetry, delay, strength of coupling and GABA decay time constant. Our results have shown that the wave pattern generation is primarily affected by coupling strengths, in terms of the magnitude of the external excitation in relation with that of recurrent inhibition, as well as from the degree of asymmetry in the structural connectivity. Furthermore. the presence of large axonal delays could underlie the generation of forward waves with long spatial wavelength. Finally, as our numerical results have predicted, an increase of the GABA decay time constant corresponds to a decrease of the wave frequency that the system can support. Our results are informative regarding the mechanisms underlying the generation and propagation of wave patterns.

## 7.5 Perspectives

In this Thesis we have studied different spatiotemporal patterns arising from the coordinated activity of populations of neurons. This high level of organization is an ubiquitous property of brain activity, and involves different spatial and temporal scales simultaneously. Our results provide the basis for further research work.

We have learned that the coordinated response of TC and RE neurons to an external input on top of a well-defined anatomical structure (the thalamus) accounts for the different information transmission modes that underlie distinct dynamical regimes, corresponding to the sleep and awake states( (Barardi et al., 2016), under revision). Future studies will be devoted to understand the effect of corticothalamic feedback on thalamic circuits, as well as investigating whether the role of the thalamus is simply to relay information to the cortex and/or to process and modulate it according to different attentional states. To do so the thalamic network model in Chapter 3 will be integrated in a full corticothalamic model comprising a primary visual cortex network. The next step will be to take into account (i) the layered structure of the cortex and (ii) areas of the thalamus and the cortex associated to different sensory receptive fields and their interactions.

We have also shown that the synchronization of neuronal oscillations between several regions could subserve different brain functions such as long-range communication. Our studies have revealed a possible role of the delay in the collective behavior of neuronal systems (Barardi et al., 2014b). Since the impact of a neuronal network to downstream neurons increases when spikes are synchronous, networks with delayed connections can serve as gatekeeper layers mediating the firing transfer to other regions. This mechanism can provide flexible functional channels of communication by regulating the opening and closing of pathways between cortical layers on demand (Esfahani et al., 2016). It would be necessary to test experimentally our theoretical predictions in that respect. In particular, together with the lab of Dr. Mavi Sanchez-Vives we are planning to analyze the LFP activity recorded simultaneously in different layers of the primary visual cortex (V1M) and the lateral geniculate nucleus (LGN) of the thalamus in a ketamine-medetomidine anesthetized rat.

We have also asked which are the mechanisms behind out-of-phase synchronized neuronal oscillations that propagate across different brain areas. For instance, the hippocampal theta oscillation is a key brain signal that underlies various aspects of cognition and behavior, including memory and spatial navigation. Recent studies reveal that theta oscillations are actually waves traveling continuously along the septal-temporal axis. Therefore, the existence of phase variations across the hippocampus indicates that neurons at different positions simultaneously represent information about events at different times (Lubenov and Siapas, 2009).

In collaboration with the authors who first revealed the wave-like organization of theta oscillations (Lubenov and Siapas) we have developed mathematical models to study how this phenomenon depends on the topological structure of the network and synaptic delays in the connections between neurons. In such models, these spatial synchronization patterns are governed by the strength and topology of the coupling as well as by the presence of axonal delays. We will continue our work on traveling waves in different directions. On the one hand, we will study the dispersion relation of a inhibitory-dominated ring-topology with periodic boundary conditions and check that mathematical results hold in integrate-and-fire simulations. We expect that the dispersion relation is quantized by the network size $N$. On the other hand, we will study how the chain of inhibitory neurons behaves in presence of excitatory neurons. We expect that the backward waves described in this Thesis can act as a dynamic backbone that modulates the activity of the excitatory neurons of the network. With our theoretical analysis, our goal has been to address the design of future experiments to test the direction of connectivity in the hippocampus, the type of connections, and the role of inhibitory neurons versus excitatory ones.

A complete appreciation of the rich dynamics that engage local and distributed neural groups requires a transition from the focus on either isolated cells or isolated areas to a focus on the coordination between local populations, and on the integration of distributed functional networks. In this Thesis we propose a first step towards this direction, by developing a hybrid description of the brain that encompasses multiple scales through different descriptions (Barardi et al., 2014a). The need to bridge spatial scales is due to the intricate structure of neural activity patterns at multiple levels of spatial resolution. Therefore efforts need to be done to bridge the different spatial scales used in isolation in order to explore how interactions at different scales are coordinated by cognitive demands and determine behavior and sensory processing (Lewis et al., 2015a). This goal will require the increase of computational efficiency and the development of high-density multichannel amplifiers and new recording technologies that could shed light on how local functional populations integrate extrinsic and intrinsic signals, giving rise to distributed patterns of coherent activity (Varela et al., 2001).

# Part IV

# Appendices

# APPENDIX A

# METHODS

## A.1 Local field potential and multi-unit activity

We quantify the activity of the network in two different ways. We calculate the multi-unit activity (MUA) as the total number of spikes per unit time in the population, and the local field potential (LFP) as the sum of the absolute values of the excitatory and inhibitory synaptic currents acting upon the excitatory neurons, averaged over this population (Mazzoni et al., 2008):

$$LFP = R_e \langle |I_{AMPA}| + |I_{GABA}| \rangle , \tag{A.1}$$

where $\langle ... \rangle$ denotes the average over all excitatory neurons. The term $I_{AMPA}$ accounts for both the external excitatory heterogeneous Poisson spike train and the recurrent excitatory synaptic current due to the network, while $I_{GABA}$ corresponds to the recurrent inhibitory synaptic current. $R_e$ represents the resistance of a typical electrode used for extracellular measurements, here chosen to be $1M\Omega$.

## A.2 Spectral analysis

We compute the power spectral density of the LFP using the Welch method: the signal is split up into $N_{seg}$ point segments (Table A.1) with 50% overlap. The overlapping segments are windowed with a Hamming window. The modified periodogram is calculated by computing the discrete Fourier Transform, and then computing the square magnitude of the result. The periodograms are then averaged to obtain the PSD estimate, which reduces the variance of the individual power measurements. The code has been implemented in MATLAB. Spectral quantities are averaged over $n_{sp}$ trials (Table A.1).

In Chapter 5 we computed the power spectral density (PSD) of the LFPs and of the post-synaptic potentials (PSPs) of the pyramidal population of the NMs. The frequency mismatch

between the PSP of the two neural mass models was calculated as the inverse of the difference between the periods of the mass models, averaging over trials. The periods correspond to the temporal distance between two maxima of the auto-correlation function. Each trial corresponds to a different set of random initial conditions, NN architecture and realization of the Ornstein-Uhlenbeck process.

## A.3 Phase coherence

Phase coherence is calculated in the way introduced by Womelsdorf et al. (2007):

$$C_{xy}(f) = \left| \frac{1}{N} \sum_{n=1}^{N} \frac{S_{xy}(f,n)}{|S_{xy}(f,n)|} \right|, \tag{A.2}$$

where $x$ and $y$ denote the two signals, and $S_{xy}(f,n)$ is the cross-spectrum between them. Since in each trial the cross spectral density is normalized by its amplitude, each term of the sum is a unit-length vector representation of the phase relation $\Delta\phi(f,n)$. In other words, $\Delta\phi(f,n) = \phi_y - \phi_x$ is the phase lag between the two signals at frequency $f$ in the data segment $n$. Hence $C_{xy}(f)$ quantifies how broad is the distribution of $\Delta\phi(f,n)$ within the $2\pi$-cycle. Averaging $\Delta\phi(f,n)$ across all $N$ data segments provides a mean angle $\Delta\phi(f)$. In Chapter 4 $\Delta\phi(f)$ is converted into a time shift, termed $\tau_{lag}$, dividing by the corresponding frequency $\tau(f) = \frac{\Delta\phi(f)}{2\pi f}$. This quantity measures the time separation between an LFP maximum in one population and the following maximum belonging to the other population. Phase coherence is considered significant for values above 0.08. Phase coherence is averaged over $n_{pc}$ trials (Table A.1).

| | $N_{seg}$ | $n_{sp}$ | $n_{pc}$ |
|---|---|---|---|
| Chapter 3 | 32768 | 50 | 50 |
| Chapter 4 | 256 | 200 | 1000 |
| Chapter 5 | 500 | 20 | - |

Table A.1 $N_{seg}$ is the number of discrete Fourier transform points. $n_{sp}$ and $n_{pc}$ are the number of trials used to calculate averaged spectral quantities and phase coherence, respectively.

## A.4 Mutual information

An important mathematical tool to quantify information transmission in noisy systems is provided by information theory. We consider a case study in which the system is presented with $N_s$ stimuli $s_1, s_2, \ldots s_N$, and the corresponding neural response $\mathbf{s}$ is recorded and quantified in a

given post-stimulus time-window. The way in which the neural response is estimated depends on the experimental questions being addressed (Magri et al., 2009).

We compute the information between the stimulus $S$ and the general response $\mathbf{r}$ as follows:

$$I(\mathbf{R},S) = \sum_{s=1}^{N_s} P(s) \sum_{r} P(\mathbf{r}|s) \log_2 \frac{P(\mathbf{r}|s)}{P(r)}, \tag{A.3}$$

where $P(s)$ is the probability of presenting the stimulus $s$ (equal to the inverse of the total number of different stimuli), $P(\mathbf{r})$ is the probability of observing the response power $\mathbf{r}$ across all trials in response to any stimulus, and $P(\mathbf{r}|s)$ is the probability of observing the response $\mathbf{r}$ in response to a single stimulus $s$. In general $I(\mathbf{R},S)$ quantifies the reduction of uncertainty about the stimulus that can be gained from observing a single-trial neural response, and we measured it in units of bits (1 bit means a reduction of uncertainty of a factor of two) (Ince et al., 2010).

An important issue to be solved regarding the calculation of the theoretical mutual information is that it requires knowledge of the full stimulus-response probability distributions, and obviously these probabilities are calculated from a finite number of stimulus-response trials. This leads to the so-called limited sampling bias, which corresponds to a systematic error in the estimate of information. We used the method described by Panzeri and Treves (1996) to estimate the bias of the information quantity and then we checked for the residual bias by applying a *bootstrap procedure* in which mutual information is calculated when the stimuli and responses are paired at random. If the information quantity is not zero (it should be in the case of non-finite samples), this is an indication of bias, and the bootstrap estimate of this error should be removed from the mutual information. After applying these procedures, the information quantity estimation could be defined as significant. Several toolboxes provide different bias-correction techniques, which allow accurate estimates of information theoretic quantities from realistically collectable amounts of data (Magri et al., 2009; Victor, 2006). In order to accomplish those tasks, we used the Information Breakdown Toolbox (ibTB), a MATLAB toolbox implementing several information estimates and bias corrections. It does this via a novel algorithm to minimize the number of operations required during the direct entropy estimation, which results in extremely high speed of computation. It contains a number of algorithms which have been thoroughly tested and exemplified not only on spike train data but also on data from analogue brain signals such as LFPs and EEGs (Magri et al., 2009).

## A.5 Clustering coefficient

In graph theory, networks composed of nodes and edges can be characterized by their clustering coefficient, which quantifies the *connectedness* or local connectivity of the network (i.e. the probability that two nodes that are connected to a given node, are also connected between them). According to the Watts and Strogatz algorithm (Watts and Strogatz, 1998), a pure regular network can be turned into a small-world network, in which few edges separate any two nodes, by rewiring the connections. A rewiring probability parameter, $r_p$, determines the probability of replacing an existing edge by another one chosen randomly. Therefore, a rewiring probability equal to 0 implies a regular network whereas a rewiring probability equal to 1 implies a completely random network.

# APPENDIX B

# CONTINUUM MODEL APPROXIMATION STARTING FROM HODGKIN-HUXLEY MODEL

In Section 6.3 we propose a continuum approximation model with a topology similar to HH model. Starting from the definition of the local field $V(x,t)$ (Equation (6.1)), we derive the equations for forward propagating and backward propagating waves by integrating the local field with the corresponding kernel (Equation (6.3)).

## B.1 Local field $V^{\mathrm{fw}}(x,t)$ for forward waves

The integration of the local field Equation (6.1) for the forward propagating waves is:

$$\begin{aligned}
V^{\mathrm{fw}}(x,t) &= Q_{ext} - q\int_{x-\gamma}^{x} \mathrm{dx}' \int_{0}^{\infty} \mathrm{dt}'\, \varepsilon(t') \sum_{n=-\infty}^{\infty} \delta(x' - v(t-t') - n\lambda) \\
&= Q_{ext} - q\int_{x-\gamma}^{x} \mathrm{dx}' \sum_{n=-\infty}^{\infty} \int_{0}^{\infty} \mathrm{dt}'\, \varepsilon(t')\, \delta\big(vt' - (vt + n\lambda - x')\big) \\
&= Q_{ext} - \frac{q}{v}\int_{x-\gamma}^{x} \mathrm{dx}' \sum_{n=-\infty}^{\infty} \int_{0}^{\infty} \mathrm{dt}''\, \varepsilon(\frac{t''}{v})\, \delta\big(t'' - (vt + n\lambda - x')\big) \\
&= Q_{ext} - \frac{q}{v}\sum_{n=-\infty}^{\infty} \int_{x-\gamma}^{x} \mathrm{dx}'\, \varepsilon(\frac{vt + n\lambda - x'}{v})\, \Theta(vt + n\lambda - x') \\
&= Q_{ext} - \frac{q}{v}\sum_{n=n_0}^{\infty} \int_{x-\gamma}^{\bar{x}} \mathrm{dx}'\, \varepsilon(\frac{vt + n\lambda - x'}{v}) \qquad \text{(B.1)}
\end{aligned}$$

where the sum and integration limit adjustments are given by

$$\begin{aligned}
n_0 &= \left\lceil \frac{x - vt - \gamma}{\lambda} \right\rceil \\
\bar{x} &= \min(x, vt + n\lambda).
\end{aligned}$$

After integrating the response kernel we obtain

$$\begin{aligned} V^{\mathrm{fw}}(x,t) &= Q_{ext} - q\sum_{n=n_0}^{\infty}\left(\frac{\tau_{decay}}{\tau_{decay}-\tau_{rise}}e^{-\frac{vt+n\lambda}{v\tau_{decay}}}\left(e^{-\frac{\bar{x}}{v\tau_{decay}}}-e^{-\frac{x-\gamma}{v\tau_{decay}}}\right)-\right. \\ &\left.-\frac{\tau_{rise}}{\tau_{decay}-\tau_{rise}}e^{-\frac{vt+n\lambda}{v\tau_{rise}}}\left(e^{-\frac{\bar{x}}{v\tau_{rise}}}-e^{-\frac{x-\gamma}{v\tau_{rise}}}\right)\right), \end{aligned} \tag{B.2}$$

where $n_0$ and $\bar{x}$ are given by

$$\begin{aligned} n_0 &= \left\lceil\frac{x-vt-\gamma}{\lambda}\right\rceil, \\ \bar{x} &= \min(x, vt+n\lambda). \end{aligned}$$

## B.2 Local field $V^{\mathbf{fw}}(x,t)$ for backward waves

The integration of the local field Equation (6.1) for the backward propagating waves is:

$$\begin{aligned}
V^{\mathrm{bw}}(x,t) &= Q_{ext} - q\int_{x-\gamma}^{x} \mathrm{dx}' \int_{0}^{\infty} \mathrm{dt}'\, \varepsilon(t') \sum_{n=-\infty}^{\infty} \delta(x' + v(t-t') - n\lambda) \\
&= Q_{ext} - q\int_{x-\gamma}^{x} \mathrm{dx}' \sum_{n=-\infty}^{\infty} \int_{0}^{-\infty} -\frac{\mathrm{dt}''}{v}\, \varepsilon(-\frac{t''}{v})\, \delta\left(t'' - (-vt + n\lambda - x')\right) \\
&= Q_{ext} - \frac{q}{v}\int_{x-\gamma}^{x} \mathrm{dx}' \sum_{n=-\infty}^{\infty} \int_{-\infty}^{0} \mathrm{dt}''\, \varepsilon(-\frac{t''}{v})\, \delta\left(t'' - (-vt + n\lambda - x')\right) \\
&= Q_{ext} - \frac{q}{v}\sum_{n=-\infty}^{\infty} \int_{x-\gamma}^{x} \mathrm{dx}'\, \varepsilon(\frac{vt - n\lambda + x'}{v})\, \Theta(vt - n\lambda + x') \\
&= Q_{ext} - \frac{q}{v}\sum_{n=-\infty}^{n_{max}} \int_{\underline{x}}^{x} \mathrm{dx}'\, \varepsilon(\frac{vt - n\lambda + x'}{v}),
\end{aligned} \tag{B.3}$$

where the sum and integration limit adjustments are given by

$$\begin{aligned}
n_{max} &= \min\left\{ \left\lfloor \frac{x+vt}{\lambda} \right\rfloor, \left\lceil \frac{x+vt}{\lambda} \right\rceil - 1 \right\} \\
\underline{x} &= \max(x-\gamma, n\lambda - vt)
\end{aligned}$$

Notice that if $(x+vt)/\lambda$ is an integer the value of $n_{max}$ is decremented by one. This is because in this case $\underline{x} = x$ and so the corresponding integral is zero (the lower and upper limits of integration coincide). After integrating the response kernel we obtain

$$\begin{aligned}
V^{\mathrm{bw}}(x,t) &= Q_{ext} - q\sum_{n=-\infty}^{n_{max}} \left( \frac{\tau_{decay}}{\tau_{decay} - \tau_{rise}} e^{-\frac{vt - n\lambda}{v\tau_{decay}}} \left( e^{-\frac{\underline{x}}{v\tau_{decay}}} - e^{-\frac{x}{v\tau_{decay}}} \right) - \right. \\
&\quad \left. - \frac{\tau_{rise}}{\tau_{decay} - \tau_{rise}} e^{-\frac{vt - n\lambda}{v\tau_{rise}}} \left( e^{-\frac{\underline{x}}{v\tau_{rise}}} - e^{-\frac{x}{v\tau_{rise}}} \right) \right),
\end{aligned} \tag{B.4}$$

where $n_{max}$ and $\underline{x}$ are given by

$$\begin{aligned}
n_{max} &= \min\left\{ \left\lfloor \frac{x+vt}{\lambda} \right\rfloor, \left\lceil \frac{x+vt}{\lambda} \right\rceil - 1 \right\}, \\
\underline{x} &= \max(x-\gamma, n\lambda - vt).
\end{aligned}$$

# List of publications and research activities

## List of publications

- Barardi A, Sancristóbal B, Garcia-Ojalvo J (2014) Phase-Coherence Transitions and Communication in the Gamma Range between Delay-Coupled Neuronal Populations. PLoS Comput Biol 10(7): e1003723. http://journals.plos.org/ploscompbiol/article?id=10.1371/journal.pcbi.1003723
- Barardi A, Malagarriga D, Sancristobal B, Garcia-Ojalvo J, Pons AJ (2014) Probing scale interaction in brain dynamics through synchronization. Phil. Trans. R. Soc. B 369: 20130533. http://rstb.royalsocietypublishing.org/content/369/1653/20130533.short
- Barardi A, Mazzoni A, Garcia-Ojalvo J. (2015) Modeling thalamic dynamics with a network of integrate and fire neurons. BMC Neuroscience. 2015;16(Suppl 1):P76. http://bmcneurosci.biomedcentral.com/articles/10.1186/1471-2202-16-S1-P76
- Barardi A, Mazzoni A, Garcia-Ojalvo J (2016) Transition between functional regimes in an integrate-and-fire network model of the thalamus PLoS ONE, under revision
- Barardi A, Garcia-Ojalvo J, Siapas AG, Lubenov E (2016) Wave propagation in inhibition-dominated neuronal chains Paper in preparation

## Research stays

- California University of Technology (Caltech), Pasadena, California, USA
  February-March, 2014
  July-September, 2014
  June-July, 2015
  Research collaboration focused on the development of analytical models to study the propagation of traveling waves. The visit was supervised by prof. Thanos Siapas and Dr Eugene Lubenov of Department of Biology and Biological Engineering at Caltech.

- Imperial College, London, UK, from September 28 to October 1, 2014
  Research collaboration focused on the study of thalamocortical models.
  The visit was in collaboration with Stefania Garasto and supervised by prof. Simon Schultz of Department of Bioengineering at Imperial College.

- The BioRobotics Institute, Scuola Superiore Sant'Anna, Pisa, Italy
  September, 2014 - May 2015
  Research collaboration focused on the development of thalamic models. Project done with prof. Alberto Mazzoni.

## Scientific events organization

- Co-organizer of *Neural Engineering Transformative Technologies – Second Induction Meeting* Parc de Recerca Biomédica de Barcelona – Barcelona, Spain, from Nov 27 to 29, 2013
  http://www.neural-engineering.eu/barcelona2013/index.html
  Talk: "Phase-coherence transitions and communication in the gamma range between delay-coupled neuronal populations"

- Chief local organizer and coordinator of: *NETT International Conference on System Level Approaches to Neural Engineering*
  Parc de Recerca Biomédica de Barcelona – Barcelona, Spain, from Sep 21 to 23, 2015
  http://www.neural-engineering.eu/BarcelonaConference2015/index.html
  Link to the booklet of the conference:
  http://www.neural-engineering.eu/resources/The-booklet.pdf

## Invited talks

- Mathematics Department, Politecnico di Torino, Turin, Italy, May 22, 2014
  Seminar: Modeling and simulation of the brain
  Talk: *Collective dynamics of neuronal populations*

- The BioRobotics Institute, Scuola Superiore Sant'Anna, Pisa, Italy, September 16, 2014
  Talk: *Collective dynamics and synchronization of neuronal populations*

## Seminars and conferences

- Institute Henri Poincarè, Paris, France, from Jun 3 to 4, 2013
  Interdisciplinary Symposium on Signals and Systems for medical applications - Workshop on feedback and synchronization in neuroscience
  http://isssma2013.sciencesconf.org/
  Poster presentation: *Phase-coherence transitions in the gamma range between delay-coupled neuronal populations*

- Instituto de Fisica Interdisciplinar y Sistemas Complejos (IFISC), Palma de Mallorca Spain, from September 2 to 13, 2013
  III Summer School on Statistical Physics of Complex and Small Systems
  http://www.gefenol.es/school2013
  Talk: *Phase-coherence transitions in the gamma range between delay-coupled neuronal populations and inter-areal communication*

- Parc de Recerca Biomèdica de Barcelona – Barcelona, Spain, from Nov 27 to 29, 2013
  Neural Engineering Transformative Technologies – NETT Fellows' Second Induction Meeting
  http://www.neural-engineering.eu/barcelona2013/index.html
  Talk: *Phase-coherence transitions and communication in the gamma range between delay-coupled neuronal populations*

- El Escorial, Madrid, Spain, from Dec 11 to 13, 2013
  Net-Works 2013 International Conference – Complex and Multiplex Networks: Structure, Applications and Related Topics
  http://www.gsc.upm.es/networks2013/call.htm
  Talk: *Multi-scale integration in a brain network model*

- Consiglio Nazionale delle Ricerche (CNR), Sesto Fiorentino, Florence, Italy, from March 17 to 20, 2014
  Dynamics of Neural Circuits
  http://neuro.fi.isc.cnr.it/index.php?page=NETT2014
  Poster presentation: *Multiscale brain integration*

- Universidade de Vigo, Ourense, Spain, from April 2 to 4, 2014
  XIX Congreso de Fisica Estadistica
  https://www.gefenol.es/FisEs/14/
  Talk: *Gamma band synchronization and communication between delay-coupled neuronal populations*

- De Poort Conference, Nijmagen, the Netherlands, from Jun 9 to 11, 2014
  Mid Term Review Meeting
  http://www.neural-engineering.eu/styled/index.html
  Talk: *Collective oscillations in the brain*

- Institut d'Estudis Catalans, Barcelona, Spain, from June 16 to 17, 2014
  Barcelona Computational and systems neuroscience meeting (2nd Annual Conference - BARCSYN 2014)
  Talk: *Phase-coherence transitions and communication in the gamma range between delay-coupled neuronal populations*

- Barcelona Biomedical Research Park, Barcelona, Spain, November 26, 2014
  New insights in Genetics and Neuroscience – Third Symposium
  Poster presentation: *Communication in the gamma range between neuronal populations*

- Barcelona Biomedical Research Park, Barcelona, Spain, December 17, 2014
  Systems Neuroscience Christmas Mini Symposium
  Selected Poster: *Communication in the gamma range between neuronal populations*

- University of Economics, Prague, Czech Republic, from July 18th to 23rd, 2015
  Computational Neuroscience Meeting (CNS 2015)
  http://www.cnsorg.org/cns-2015
  Selected Poster: *Modeling thalamic dynamics with a network of integrate and fire neurons*

- Barcelona Biomedical Research Park, Barcelona, Spain, from September 21sth to 23rd, 2015

NETT International Conference on System Level Approaches to Neural Engineering
http://www.neural-engineering.eu/BarcelonaConference2015/index.html
Selected poster: *Phase-coherence transitions and communication in the gamma range between delay-coupled neuronal populations*

## Summer schools

- De Poort Conference, Nijmagen, the Netherlands, from August 25 to 30, 2013
  Brain Networks and Neuronal Communication - Donders Institute for Brain, Cognition and Behavior
  One week of intensive study for 30 selected students on brain networks spanning communication between single neurons to large scale network interactions.

## Advisorship

- Co-advisor of Master's Thesis of student Andrea Valenti from Politecnico di Torino
  Thesis Topic: Synaptic Plasticity in conductance-based models

# GLOSSARY

**Parameters**

| | |
|---|---|
| $\gamma$ | Window of connectivity |
| $\lambda$ | Traveling wave spatial wavelength [mm] |
| $v$ | Traveling wave phase velocity [mm/s] |
| $\tau_m$ | Membrane time constant [ms] |
| $\vartheta$ | Spike threshold [mV] |
| $\zeta$ | Reset value of membrane potential after firing [mV] |
| $I_0$ | Constant external input [nA] |
| $\alpha$ | Rate of receptor opening $[1/(mM \cdot s)]$ |
| $\beta$ | Rate of receptor closing [1/s] |
| $\Delta$ | Steepness of the exponential approach to threshold [mV] |
| $v_0$ | Net PSP for which a 50% firing rate is achieved in the neural mass model [mV] |
| $T_\omega$ | Angular frequency [rads/s] |
| $\sigma$ | Number of open receptors relative to the total number of receptors |
| $\tau_w$ | Time constant of adaptation [ms] |
| $\tau_{axo}$ | Latency between the generation of a spike in a presynaptic neuron from one network and the elicitation of a postsynaptic potential in the other network [ms] |
| $\tau_{decay}$ | Decay synaptic time [ms] |
| $\tau_{lag}$ | Time shift corresponding to a given phase difference [ms] |

| | |
|---|---|
| $\tau_{ref}$ | Absolute refractory period [ms] |
| $\tau_{rise}$ | Rise synaptic time [ms] |
| $\varepsilon(t)$ | Response kernel (postsynaptic potential) [mV] |
| $A$ | Maximum height of excitatory postsynaptic potential [mV] |
| $a$ | Conductance that mediates subthreshold adaptation [$\mu$S] |
| $a_{NM}$ | Inverse of the membrane time constant in the neural mass model [Hz] |
| $B$ | Maximum height of inhibitory postsynaptic potential [mV] |
| $b$ | Spike-triggering adaptation strength [nA] |
| $b_{NM}$ | Dendritic delay [ms] |
| $C_m$ | Membrane capacitive current [nF] |
| $C_i$ | Intra-columnar connectivity constant |
| $E_K$ | Nerst equilibrium potential of the potassium current [mV] |
| $E_L$ | Nerst equilibrium potential of the leakage current [mV] |
| $E_{Na}$ | Nerst equilibrium potential of the sodium current [mV] |
| $e_0$ | Maximum firing rate of the neural population |
| $E_{syn}$ | Nerst equilibrium potential of the synapse [mV] |
| $E_{thresh}$ | Voltage threshold value [mV] |
| $T$ | Traveling wave temporal frequency [Hz] |
| $F_\gamma$ | Frequency of maximum power spectrum [Hz] |
| $f_{max}$ | Frequency of maximum phase coherence [Hz] |
| $g$ | Scalar synaptic coupling parameter |
| $g_K$ | Maximal conductance of potassium [$\mu$S] |
| $g_L$ | Leak membrane conductance [$\mu$S] |
| $g_{Na}$ | Maximal conductance of sodium [$\mu$S] |

$g_{max}$ Conductance peak [$\mu$S]

$g_{syn}$ Synaptic conductance [$\mu$S]

$I$ Current [nA]

$I_{ionic}$ Ionic currents [nA]

$I_K$ Potassium current [nA]

$I_L$ Leak current [nA]

$I_{Na}$ Sodium current [nA]

$I_{syn}$ Synaptic current [nA]

$k$ Wavenumber, traveling wave spatial frequency [1/mm]

$m$ Net PSP input into a population [mV]

$N$ Number of neurons in the network

$p_m$ Average density of action potentials produced by the presynaptic population acting upon the postsynaptic population [mV]

$q$ Magnitude of inhibitory connections

$Q_{ext}$ Magnitude of external excitation

$r$ Steepness of the sigmoidal transformation

$r_p$ Rewiring probability for network architecture

$T$ Wave period [ms]

$T(t)$ Time-varying neurotransmitter concentration

$T_\gamma$ Period of maximum power spectrum [ms]

$t_{peak}$ Duration of the response [ms]

$V_r$ Voltage reset value [mV]

**Variables**

$I(x,t)$ Total synaptic input into neuron at position $x$ and time $t$

$J(t)$ Shape of postsynaptic potential (response kernel)

$J(x)$ Strength of postsynaptic connection at distance $x$

$S(x,t)$ Spiking (at given time and location)

$T_m(x)$ $m^{\text{th}}$ spike time of neuron at $x$

$V(x,t)$ Local field (membrane potential at given time and location) [mV]

$W(x-x')$ Absolute weight of synaptic connection from $x'$ to $x$

$h$ Inactivation variable of sodium channels

$m$ Activation variable of sodium channels

$n$ Activation variable of potassium channels

$t$ Time [ms]

$V$ Voltage [mV]

$w$ Adaptation [nA]

$y_i$ Average postsynaptic excitatory or inhibitory membrane potential [mV]

**Acronyms / Abbreviations**

$aEIF$ Adaptive exponential integrate-and-fire

CTC Communication through coherence

$CV$ Coefficient of variation

$DBS$ Deep brain stimulation

$ECoG$ Electrocorticography

$EEG$ Electroencephalography

EPSP Excitatory postsynaptic potential

$ERP$ Event-related potential

$fMRI$ Functional magnetic resonance imaging

$FR$ Mean firing rate

| | |
|---|---|
| *HH* | Hodgkin-Huxley |
| *IF* | integrate-and-fire |
| IPSCs | Inhibitory postsynaptic currents |
| IPSP | Inhibitory postsynaptic potential |
| *ISI* | Inter-spike interval |
| *LFP* | Local Field Potential |
| *LGN* | Lateral geniculate nucleus |
| *LIF* | Leaky integrate-and-fire |
| *MEAs* | Multielectrode arrays |
| *MEG* | Magnetoencephalography |
| *MRI* | Magnetic resonance imaging |
| *MUA* | Multi-unit activity |
| *NM* | Neural Mass |
| *NN* | Neural network of HH neurons |
| PSP | Postsynaptic potential |
| *RE* | Reticular thalamic cells |
| ROC | Receiver operating characteristic |
| *SFA* | Spike-frequency adaptation |
| *TC* | Thalamocortical relay cells |
| *VPN* | Ventral posterior nucleus |
| *VSD* | Voltage-sensitive dye |
| *VSDI* | Voltage-sensitive dye imaging |

# REFERENCES


Aboitiz, F., Scheibel, A. B., Fisher, R. S., and Zaidel, E. (1992). Fiber composition of the human corpus callosum. *Brain research*, 598(1-2):143–53.

Adrian, E. D. (1941). Afferent discharges to the cerebral cortex from peripheral sense organs. *The Journal of physiology*, 100(2):159–191.

Ahissar, E., Vaadia, E., Ahissar, M., Bergman, H., Arieli, A., and Abeles, M. (1992). Dependence of cortical plasticity on correlated activity of single neurons and on behavioral context. *Science*, 257(5075):1412–1415.

Ahmed, B., Hanazawa, A., Undeman, C., Eriksson, D., Valentiniene, S., and Roland, P. E. (2008). Cortical dynamics subserving visual apparent motion. *Cerebral Cortex*, 18(12):2796–2810.

Akam, T. and Kullmann, D. M. (2010). Oscillations and filtering networks support flexible routing of information. *Neuron*, 67(2):308–320.

Akam, T. E. and Kullmann, D. M. (2012). Efficient "communication through coherence" requires oscillations structured to minimize interference between signals. *PLoS Comput Biol*, 8(11):e1002760.

Alivisatos, A. P., Chun, M., Church, G. M., Greenspan, R. J., Roukes, M. L., and Yuste, R. (2012). The brain activity map project and the challenge of functional connectomics. *Neuron*, 74(6):970–974.

Alonso, J. and Swadlow, H. (2015). Thalamus controls recurrent cortical dynamics. *Nature neuroscience*, 18(12):1703–1704.

Andersen, P. and Eccles, J. (1962). Inhibitory Phasing of Neuronal Discharge. *Nature*, 196(4855):645–647.

Arieli, A., Shoham, D., Hildesheim, R., and Grinvald, A. (1995). Coherent spatiotemporal patterns of ongoing activity revealed by real-time optical imaging coupled with single-unit recording in the cat visual cortex. *Journal of neurophysiology*, 73(5):2072–2093.

Arnolds, D., Da Silva, F. L., Aitink, J., Kamp, A., and Boeijinga, P. (1980). The spectral properties of hippocampal eeg related to behaviour in man. *Electroencephalography and clinical neurophysiology*, 50(3):324–328.

Ayzenshtat, I., Meirovithz, E., Edelman, H., Werner-Reiss, U., Bienenstock, E., Abeles, M., and Slovin, H. (2010). Precise spatiotemporal patterns among visual cortical areas and their relation to visual stimulus processing. *The Journal of Neuroscience*, 30(33):11232–11245.

Bal, T. and McCormick, D. A. (1996). What stops synchronized thalamocortical oscillations? *Neuron*, 17(2):297–308.

Barardi, A., Garcia-Ojalvo, J., and Mazzoni, A. (2016). Transition between functional regimes in an integrate-and-fire network model of the thalamus. *Under revision to PLoS One*.

Barardi, A., Malagarriga, D., Sancristobal, B., Garcia-Ojalvo, J., and Pons, A. J. (2014a). Probing scale interaction in brain dynamics through synchronization. *Phil. Trans. R. Soc. B*, 369(1653):20130533.

Barardi, A., Sancristóbal, B., and Garcia-Ojalvo, J. (2014b). Phase-coherence transitions and communication in the gamma range between delay-coupled neuronal populations. *PLoS Comput Biol*, 10(7):e1003723.

Barbieri, F., Mazzoni, A., Logothetis, N. K., Panzeri, S., and Brunel, N. (2014). Stimulus dependence of local field potential spectra: experiment versus theory. *The Journal of Neuroscience*, 34(44):14589–14605.

Bastos, A. M., Vezoli, J., Bosman, C. A., Schoffelen, J.-M., Oostenveld, R., Dowdall, J. R., De Weerd, P., Kennedy, H., and Fries, P. (2015a). Visual areas exert feedforward and feedback influences through distinct frequency channels. *Neuron*, 85(2):390–401.

Bastos, A. M., Vezoli, J., and Fries, P. (2015b). Communication through coherence with inter-areal delays. *Current opinion in neurobiology*, 31:173–180.

Battaglia, D. and Hansel, D. (2011). Synchronous chaos and broad band gamma rhythm in a minimal multi-layer model of primary visual cortex. *PLoS computational biology*, 7(10):e1002176+.

Baudry, C. T., Bertrand, O., and Fischer, C. (2001). Oscillatory synchrony between human extrastriate areas during visual short-term memory maintenance. *Journal of Neuroscience*, 21(20):177RC+.

Bauer, M., Oostenveld, R., Peeters, M., and Fries, P. (2006). Tactile spatial attention enhances gamma-band activity in somatosensory cortex and reduces low-frequency activity in parieto-occipital areas. *The Journal of Neuroscience*, 26(2):490–501.

Bazhenov, M., Timofeev, I., Steriade, M., and Sejnowski, T. (1999). Self-sustained rhythmic activity in the thalamic reticular nucleus mediated by depolarizing gabaa receptor potentials. *Nature neuroscience*, 2(2):168–174.

Belitski, A., Gretton, A., Magri, C., Murayama, Y., Montemurro, M. a., Logothetis, N. K., and Panzeri, S. (2008). Low-frequency local field potentials and spikes in primary visual cortex convey independent visual information. *J Neurosci*, 28(22):5696–709.

Benson, D. L. and Cohen, P. A. (1996). Activity-independent segregation of excitatory and inhibitory synaptic terminals in cultured hippocampal neurons. *The Journal of neuroscience*, 16(20):6424–6432.

Berger, H. (1929). Über das elektrenkephalogramm des menschen. *European Archives of Psychiatry and Clinical Neuroscience*, 87(1):527–570.

Bibbig, A., Middleton, S., Racca, C., Gillies, M. J., Garner, H., Lebeau, F. E., Davies, C. H., and Whittington, M. A. (2007). Beta Rhythms (15-20 Hz) Generated by Nonreciprocal Communication in Hippocampus. *J Neurophysiol*, 97(4):2812–2823.

Bibbig, A., Traub, R. D., and Whittington, M. a. (2002). Long-range synchronization of gamma and beta oscillations and the plasticity of excitatory and inhibitory synapses: a network model. *J Neurophysiol*, 88(4):1634–54.

Bishop, G. (1936). The interpretation of cortical potentials. *Cold Spring Harbor Symp Quant Biol*, (4):305–319.

Bojak, I., Oostendorp, T. F., Reid, A. T., and Kötter, R. (2010). Connecting mean field models of neural activity to eeg and fmri data. *Brain topography*, 23(2):139–149.

Börgers, C. and Kopell, N. J. (2008). Gamma oscillations and stimulus selection. *Neural computation*, 20(2):383–414.

Bosman, C. a., Schoffelen, J.-M., Brunet, N., Oostenveld, R., Bastos, A. M., Womelsdorf, T., Rubehn, B., Stieglitz, T., De Weerd, P., and Fries, P. (2012). Attentional stimulus selection through selective synchronization between monkey visual areas. *Neuron*, 75(5):875–88.

Boucsein, C., Nawrot, M. P., Schnepel, P., and Aertsen, A. (2011). Beyond the cortical column: abundance and physiology of horizontal connections imply a strong role for inputs from the surround. *Front Neurosci*, 5(32):doi: 10.3389/fnins.2011.00032.

Bragin, A., Jandó, G., Nádasdy, Z., Hetke, J., Wise, K., and Buzsáki, G. (1995). Gamma (40-100 hz) oscillation in the hippocampus of the behaving rat. *The Journal of Neuroscience*, 15(1):47–60.

Braitenberg, V. and Schüz, A. (1998). *Cortex statistics and geometry of neuronal connectivity*. Springer.

Breakspear, M., Roberts, J., Terry, J. R., Rodrigues, S., Mahant, N., and Robinson, P. (2006). A unifying explanation of primary generalized seizures through nonlinear brain modeling and bifurcation analysis. *Cerebral Cortex*, 16(9):1296–1313.

Bremer, F. (1938). Effets de la déafférentation complète d'une région de l'écorce cérébrale sur son activité électrique spontanée. *CR Soc. Biol.(Paris)*, 127:355–359.

Bressler, S. L., Coppola, R., and Nakamura, R. (1993). Episodic multiregional cortical coherence at multiple frequencies during visual task performance. *Nature*, 366(6451):153–156.

Bressler, S. L. and Kelso, J. A. S. (2001). Cortical coordination dynamics and cognition. *TRENDS in Cognitive Sciences*, pages 26–36.

Bressloff, P. and Coombes, S. (1998). Traveling waves in a chain of pulse-coupled oscillators. *Physical review letters*, 80(21):4815.

Bressloff, P. C. (2000). Traveling waves and pulses in a one-dimensional network of excitable integrate-and-fire neurons. *Journal of Mathematical Biology*, 40(2):169–198.

Bressloff, P. C. (2001). Traveling fronts and wave propagation failure in an inhomogeneous neural network. *Physica D: Nonlinear Phenomena*, 155(1):83–100.

Bressloff, P. C., Folias, S. E., Prat, A., and Li, Y.-X. (2003). Oscillatory waves in inhomogeneous neural media. *Physical review letters*, 91(17):178101.

Bressloff, P. C. and Wilkerson, J. (2015). Traveling pulses in a stochastic neural field model of direction selectivity. *Neural Masses and Fields: Modelling the Dynamics of Brain Activity*, page 8.

Brette, R. and Gerstner, W. (2005). Adaptive exponential integrate-and-fire model as an effective description of neuronal activity. *Journal of Neurophysiology*, 94(5):3637–3642.

Brosch, M., Budinger, E., and Scheich, H. (2002). Stimulus-related gamma oscillations in primate auditory cortex. *Journal of neurophysiology*, 87(6):2715–2725.

Brown, P., Salenius, S., Rothwell, J. C., and Hari, R. (1998). Cortical correlate of the piper rhythm in humans. *Journal of Neurophysiology*, 80(6):2911–2917.

Brunel, N. (2000). Dynamics of sparsely connected networks of excitatory and inhibitory spiking neurons. *Journal of computational neuroscience*, 8(3):183–208.

Brunel, N. and Hakim, V. (2008). Sparsely synchronized neuronal oscillations. *Chaos (Woodbury, N.Y.)*, 18(1).

Brunel, N. and Van Rossum, M. C. (2007). Lapicque's 1907 paper: from frogs to integrate-and-fire. *Biological cybernetics*, 97(5-6):337–339.

Brunel, N. and Wang, X.-J. (2003). What determines the frequency of fast network oscillations with irregular neural discharges? I. Synaptic dynamics and excitation-inhibition balance. *J Neurophysiol*, 90(1):415–30.

Buehlmann, A. and Deco, G. (2010). Optimal information transfer in the cortex through synchronization. *PLoS Comput Biol*, 6(9)(9):e1000934. doi:10.1371/journal.pcbi.1000934.

Buia, C. and Tiesinga, P. (2006). Attentional modulation of firing rate and synchrony in a model cortical network. *Journal of computational neuroscience*, 20(3):247–264.

Bullmore, E. and Sporns, O. (2009). Complex brain networks: graph theoretical analysis of structural and functional systems. *Nature Reviews Neuroscience*, 10(3):186–198.

Buonomano, D. V. (2003). Timing of neural responses in cortical organotypic slices. *Proceedings of the National Academy of Sciences*, 100(8):4897–4902.

Butts, D. A., Weng, C., Jin, J., Yeh, C.-I., Lesica, N. A., Alonso, J.-M., and Stanley, G. B. (2007). Temporal precision in the neural code and the timescales of natural vision. *Nature*, 449(7158):92–95.

Buzsáki, G. (2002). Theta oscillations in the hippocampus. *Neuron*, 33(3):325–340.

Buzsáki, G., Anastassiou, C. a., and Koch, C. (2012). The origin of extracellular fields and currents–EEG, ECoG, LFP and spikes. *Nat. Rev. Neurosci.*, 13(6):407–20.

Buzsáki, G. and Draguhn, A. (2004). Neuronal Oscillations in Cortical Networks. *Science*, 304(5679):1926–1929.

Buzsáki, G., Geisler, C., Henze, D. A., and Wang, X. J. (2004). Interneuron Diversity series: Circuit complexity and axon wiring economy of cortical interneurons. *Trends in Neurosciences*, 27(4):186–193.

Buzsáki, G. and Wang, X.-J. (2012). Mechanisms of gamma oscillations. *Annu. Rev. Neurosci.*, 35:203–25.

Cannon, J., McCarthy, M. M., Lee, S., Lee, J., Börgers, C., Whittington, M. A., and Kopell, N. (2014). Neurosystems: brain rhythms and cognitive processing. *European Journal of Neuroscience*, 39(5):705–719.

Cardin, J. A., Carlén, M., Meletis, K., Knoblich, U., Zhang, F., Deisseroth, K., Tsai, L.-H., and Moore, C. I. (2009). Driving fast-spiking cells induces gamma rhythm and controls sensory responses. *Nature*, 459(7247):663–667.

Castelo-Branco, M., Neuenschwander, S., and Singer, W. (1998). Synchronization of visual responses between the cortex, lateral geniculate nucleus, and retina in the anesthetized cat. *J Neurosci*, 18(16):6395–410.

Castro-Alamancos, M. A. and Oldford, E. (2002). Cortical sensory suppression during arousal is due to the activity-dependent depression of thalamocortical synapses. *The Journal of physiology*, 541(1):319–331.

Cohen, M. X. (2011). It's about time. *Frontiers in human neuroscience*, 5.

Constantinople, C. M. and Bruno, R. M. (2011). Effects and mechanisms of wakefulness on local cortical networks. *Neuron*, 69(6):1061–1068.

Contreras, D., Curro-Dossi, R., and Steriade, M. (1993). Electrophysiological properties of cat reticular thalamic neurones in vivo. *Journal of Physiology (Lond)*, 470:273–94.

Coombes, S. (2003). Dynamics of synaptically coupled integrate-and-fire-or-burst neurons. *Physical Review E*, 67(4):041910.

Coombes, S. (2005). Waves, bumps, and patterns in neural field theories. *Biological cybernetics*, 93(2):91–108.

Coombes, S. (2010). Large-scale neural dynamics: simple and complex. *Neuroimage*, 52(3):731–739.

Coombes, S. and Laing, C. (2011). Pulsating fronts in periodically modulated neural field models. *Physical Review E*, 83(1):011912.

Coombes, S., Lord, G. J., and Owen, M. R. (2003). Waves and bumps in neuronal networks with axo-dendritic synaptic interactions. *Physica D: Nonlinear Phenomena*, 178(3):219–241.

Coombes, S. and Owen, M. (2005). Bumps, breathers, and waves in a neural network with spike frequency adaptation. *Physical Review Letters*, 94(14):148102.

Crick, F. (1984). Function of the thalamic reticular complex: the searchlight hypothesis. *Proceedings of the National Academy of Sciences of the United States of America*, 81(14):4586–4590.

Csicsvari, J., Jamieson, B., Wise, K. D., and Buzsáki, G. (2003). Mechanisms of gamma oscillations in the hippocampus of the behaving rat. *Neuron*, 37(2):311–322.

Curio, G. (2000). Linking 600-hz "spikelike" eeg/meg wavelets ("ς-bursts") to cellular substrates: Concepts and caveats. *Journal of Clinical Neurophysiology*, 17(4):377–396.

Da Silva, F. L., Hoeks, A., Smits, H., and Zetterberg, L. (1974). Model of brain rhythmic activity. *Kybernetik*, 15(1):27–37.

Damasio, A. R. (1990). Synchronous activation in multiple cortical regions: A mechanism for recall. *Seminars in the Neurosciences*, 2:287–96.

Dang-Vu, T. T. T., Schabus, M., Desseilles, M., Albouy, G., Boly, M., Darsaud, A., Gais, S., Rauchs, G., Sterpenich, V., Vandewalle, G., Carrier, J., Moonen, G., Balteau, E., Degueldre, C., Luxen, A., Phillips, C., and Maquet, P. (2008). Spontaneous neural activity during human slow wave sleep. *Proceedings of the National Academy of Sciences of the United States of America*, 105(39):15160–15165.

David, O. and Friston, K. J. (2003). A neural mass model for meg/eeg:: coupling and neuronal dynamics. *NeuroImage*, 20(3):1743–1755.

Dayan, P. and Abbott, L. F. (2005). *Theoretical neuroscience: computational and mathematical modeling of neural systems*. MIT Press.

de Ruyter van Steveninck, R. R., Lewen, G. D., Strong, S. P., Koberle, R., and Bialek, W. (1997). Reproducibility and variability in neural spike trains. *Science*, 275(5307):1805–8.

Deco, G., Jirsa, V. K., and McIntosh, A. R. (2013). Resting brains never rest: computational insights into potential cognitive architectures. *Trends in neurosciences*, 36(5):268–274.

Desimone, R. and Duncan, J. (1995). Neural mechanisms of selective visual attention. *Annu Rev Neurosci*, 18:193–222.

Destexhe, A. (2000). Modelling corticothalamic feedback and the gating of the thalamus by the cerebral cortex. *Journal of Physiology Paris*, 94:391–410.

Destexhe, A. (2009). Self-sustained asynchronous irregular states and Up-Down states in thalamic, cortical and thalamocortical networks of nonlinear integrate-and-fire neurons. *Journal of computational neuroscience*, 27(3):493–506.

Destexhe, A. (2014). Spindle oscillations: Models. In Jaeger, D. and Jung, R., editors, *Encyclopedia of Computational Neuroscience*, pages 1–8. Springer New York.

Destexhe, A., Bal, T., McCormick, D. A., and Sejnowski, T. J. (1996a). Ionic mechanisms underlying synchronized oscillations and propagating waves in a model of ferret thalamic slices. *Journal of neurophysiology*, 76(3):2049–70.

Destexhe, A., Bal, T., McCormick, D. A., and Sejnowski, T. J. (1996b). Ionic mechanisms underlying synchronized oscillations and propagating waves in a model of ferret thalamic slices. *Journal of Neurophysiology*, 76(3):2049–2070.

Destexhe, A., Contreras, D., Sejnowski, T. J., and Steriade, M. (1994a). A model of spindle rhythmicity in the isolated thalamic reticular nucleus. *Journal of neurophysiology*, 72(2):803–818.

Destexhe, A., Mainen, Z. F., and Sejnowski, T. J. (1994b). An efficient method for computing synaptic conductances based on a kinetic model of receptor binding. *Neural computation*, 6(1):14–18.

Destexhe, A., McCormick, D. A., and Sejnowski, T. J. (1993). A model for 8-10 Hz spindling in interconnected thalamic relay and reticularis neurons. *Biophysical journal*, 65(6):2473–7.

Destexhe, A. and Rudolph, M. (2004). Extracting information from the power spectrum of synaptic noise. *Journal of computational neuroscience*, 17(3):327–345.

Destexhe, a. and Sejnowski, T. J. (2003). Interactions between membrane conductances underlying thalamocortical slow-wave oscillations. *Physiological reviews*, 83(4):1401–53.

Domich, L., Oakson, G., and Steriade, M. (1986). Thalamic burst patterns in the naturally sleeping cat: a comparison between cortically projecting and reticularis neurones. *J Neurophysiol*, 379:429–449.

Eckhorn, R., Bauer, R., Jordan, W., Brosch, M., Kruse, W., Munk, M., and Reitboeck, H. J. (1988). Coherent oscillations: a mechanism of feature linking in the visual cortex? Multiple electrode and correlation analyses in the cat. *Biological cybernetics*, 60(2):121–130.

Edwards, E., Soltani, M., Deouell, L. Y., Berger, M. S., and Knight, R. T. (2005). High gamma activity in response to deviant auditory stimuli recorded directly from human cortex. *Journal of neurophysiology*, 94(6):4269–4280.

Einevoll, G. T., Kayser, C., Logothetis, N. K., and Panzeri, S. (2013). Modelling and analysis of local field potentials for studying the function of cortical circuits. *Nature Reviews Neuroscience*, 14(11):770–785.

Elijah, D. H., Samengo, I., and Montemurro, M. A. (2015). Thalamic neuron models encode stimulus information by burst-size modulation. *Frontiers in computational neuroscience*, 9.

Engel, A. K., Fries, P., and Singer, W. (2001). Dynamic Predictions: Oscillations and Synchrony in Top-down Processing. *Nature Reviews. Neuroscience*, 2(10):704–716.

Engel, A. K., König, P., Kreiter, A. K., and Singer, W. (1991). Interhemispheric synchronization of oscillatory neuronal responses in cat visual cortex. *Science*, 252(5009):1177–1179.

Erişir, A., Van Horn, S. C., and Sherman, S. M. (1997). Relative numbers of cortical and brainstem inputs to the lateral geniculate nucleus. *Proceedings of the National Academy of Sciences of the United States of America*, 94(4):1517–20.

Ermentrout, B. (1996). Type i membranes, phase resetting curves, and synchrony. *Neural computation*, 8(5):979–1001.

Ermentrout, B. (1998a). The analysis of synaptically generated traveling waves. *Journal of Computational Neuroscience*, 5(2):191–208.

Ermentrout, B. (1998b). Neural networks as spatio-temporal pattern-forming systems. *Reports on progress in physics*, 61(4):353.

Ermentrout, G. B. and Kleinfeld, D. (2001). Traveling electrical waves in cortex: insights from phase dynamics and speculation on a computational role. *Neuron*, 29(1):33–44.

Ermentrout, G. B. and Kopell, N. (1998). Fine structure of neural spiking and synchronization in the presence of conduction delays. *Proceedings of the National Academy of Sciences*, 95(3):1259–1264.

Esfahani, Z. G., Gollo, L. L., and Valizadeh, A. (2016). Stimulus-dependent synchronization in delayed-coupled neuronal networks. *Scientific Reports*, 6:23471.

Faugeras, O., Touboul, J., and Cessac, B. (2008). A constructive mean-field analysis of multi-population neural networks with random synaptic weights and stochastic inputs. *Frontiers in computational neuroscience*, 3:1–1.

Feldman, D. E. (2000). Timing-based LTP and LTD at vertical inputs to layer ii/iii pyramidal cells in rat barrel cortex. *Neuron*, 27(1):45–56.

Fell, J., Klaver, P., Lehnertz, K., Grunwald, T., Schaller, C., Elger, C., and Fernandez, G. (2001). Human memory formation is accompanied by rhinal-hippocampal coupling and decoupling. *Nature Neuroscience*, 4(5):1259–64.

Feller, M. B. (1999). Spontaneous correlated activity in developing neural circuits. *Neuron*, 22(4):653–656.

Ferezou, I., Bolea, S., and Petersen, C. C. (2006). Visualizing the cortical representation of whisker touch: voltage-sensitive dye imaging in freely moving mice. *Neuron*, 50(4):617–629.

Fischer, I., Vicente, R., Buldú, J. M., Peil, M., Mirasso, C. R., Torrent, M. C., and Ojalvo, J. G. (2006). Zero-Lag Long-Range Synchronization via Dynamical Relaying. *Physical Review Letters*, 97(12):123902+.

FitzGibbon, T., Tevah, L., and Jervie-Sefton, A. (1995). Connections between the reticular nucleus of the thalamus and pulvinar-lateralis posterior complex: A WGA-HRP study. *Journal of Comparative Neurology*, 363:489–504.

Fourcaud-Trocmé, N., Hansel, D., Van Vreeswijk, C., and Brunel, N. (2003). How spike generation mechanisms determine the neuronal response to fluctuating inputs. *The Journal of neuroscience*, 23(37):11628–11640.

Freeman, W. J. and Barrie, J. M. (2000). Analysis of spatial patterns of phase in neocortical gamma eegs in rabbit. *Journal of neurophysiology*, 84(3):1266–1278.

Frien, A., Eckhorn, R., Bauer, R., Woelbern, T., and Kehr, H. (1994). Stimulus-specific fast oscillations at zero phase between visual areas V1 and V2 of awake monkey. *Neuroreport*, 5(17):2273–22.

Fries, P. (2005). A mechanism for cognitive dynamics: neuronal communication through neuronal coherence. *Trends Neurosci*, 9(10):474–480.

Fries, P. (2009). Neuronal gamma-band synchronization as a fundamental process in cortical computation. *Annual review of neuroscience*, 32:209–224.

Fries, P. (2015). Rhythms for cognition: communication through coherence. *Neuron*, 88(1):220–235.

Fries, P., Nikolić, D., and Singer, W. (2007). The gamma cycle. *Trends in neurosciences*, 30(7):309–316.

Fries, P., Schröder, J.-H., Roelfsema, P. R., Singer, W., and Engel, A. K. (2002a). Oscillatory neuronal synchronization in primary visual cortex as a correlate of stimulus selection. *J Neurosci*, 22(9):3739–54.

Fries, P., Schröder, J.-H. H., Roelfsema, P. R., Singer, W., and Engel, A. K. (2002b). Oscillatory neuronal synchronization in primary visual cortex as a correlate of stimulus selection. *The Journal of neuroscience : the official journal of the Society for Neuroscience*, 22(9):3739–3754.

Fries, P., Womelsdorf, T., Oostenveld, R., and Desimone, R. (2008). The effects of visual stimulation and selective visual attention on rhythmic neuronal synchronization in macaque area V4. *J Neurosci*, 28(18):4823–35.

Friston, K. J. (1999). Schizophrenia and the disconnection hypothesis. *Acta Psychiatrica Scandinavica*, 99(s395):68–79.

Friston, K. J. (2000). The labile brain. I. Neuronal transients and nonlinear coupling. *Philosophical transactions of the Royal Society of London. Series B, Biological sciences*, 355(1394):215–236.

Frostig, R. D., Ferezou, I., Matyas, F., and Petersen, C. C. (2009). Imaging the brain in action: Real-time voltage-sensitive dye imaging of sensorimotor cortex of awake behaving mice.

Fukuda, M., Hata, Y., Ohshima, M., and Tsumoto, T. (1998). Role of nmda receptors in the propagation of excitation in rat visual cortex as studied by optical imaging. *Neuroscience research*, 31(1):9–21.

Gabriel, A. and Eckhorn, R. (2003). A multi-channel correlation method detects traveling $\gamma$-waves in monkey visual cortex. *Journal of neuroscience methods*, 131(1):171–184.

Galarreta, M. and Hestrin, S. (2002). Electrical and chemical synapses among parvalbumin fast-spiking gabaergic interneurons in adult mouse neocortex. *Proc Natl Acad Sci U S A*, 99(19):12438–43.

Gao, X., Xu, W., Wang, Z., Takagaki, K., Li, B., and Wu, J.-Y. (2012). Interactions between two propagating waves in rat visual cortex. *Neuroscience*, 216:57–69.

Geisler, C., Brunel, N., Wang, X.-j., Rene, P., Brunel, N., and Contribu, X.-j. W. (2005). Contributions of Intrinsic Membrane Dynamics to Fast Network Oscillations With Irregular Neuronal Discharges. *J Neurophysiol*, 94:4344–4361.

Gerstner, W. and Kistler, W. M. (2002). *Spiking neuron models: Single neurons, populations, plasticity*. Cambridge university press.

Gibson, J. R., Beierlein, M., and Connors, B. W. (1999). Two networks of electrically coupled inhibitory neurons in neocortex. *Nature*, 402(6757):75–79.

Gielen, S., Krupa, M., and Zeitler, M. (2010). Gamma oscillations as a mechanism for selective information transmission. *Biological cybernetics*, 103(2):151–165.

Gil, Z., Connors, B. W., and Amitai, Y. (1997). Differential regulation of neocortical synapses by neuromodulators and activity. *Neuron*, 19(3):679–686.

Gilbert, C. D. (1993). Circuitry, architecture, and functional dynamics of visual cortex. *Cerebral cortex*, 3(5):373–386.

Gilbert, C. D. and Wiesel, T. N. (1992). Receptive field dynamics in adult primary visual cortex. *Nature*, 356(6365):150–152.

Giocomo, L. M., Zilli, E. A., Fransén, E., and Hasselmo, M. E. (2007). Temporal frequency of subthreshold oscillations scales with entorhinal grid cell field spacing. *Science*, 315(5819):1719–1722.

Girard, P., Hupe, J., and Bullier, J. (2001). Feedforward and feedback connections between areas v1 and v2 of the monkey have similar rapid conduction velocities. *Journal of neurophysiology*, 85(3):1328–1331.

Goldbach, M., Loh, M., Deco, G., and Garcia-Ojalvo, J. (2008). Neurodynamical amplification of perceptual signals via system-size resonance. *Physica D: Nonlinear Phenomena*, 237(3):316–323.

Gollo, L. L., Mirasso, C., and Villa, A. E. P. (2010). Dynamic control for synchronization of separated cortical areas through thalamic relay. *NeuroImage*, 52(3):947–55.

Golomb, D. and Amitai, Y. (1997). Propagating neuronal discharges in neocortical slices: computational and experimental study. *Journal of neurophysiology*, 78(3):1199–1211.

Golomb, D., Wang, X.-J., and Rinzel, J. (1996). Propagation of spindle waves in a thalamic slice model. *Journal of Neurophysiology*, 75(2):750–769.

Granger, C. W. (1969). Investigating causal relations by econometric models and cross-spectral methods. *Econometrica: Journal of the Econometric Society*, pages 424–438.

Gray, C. M., Konig, P., Engel, A. K., and Singer, W. (1989). Oscillatory responses in cat visual cortex exhibit inter-columnar synchronization which reflects global stimulus properties. *Nature*, 338:334–337.

Gray, C. M. and McCormick, D. A. (1996). Chattering cells: superficial pyramidal neurons contributing to the generation of synchronous oscillations in the visual cortex. *Science (New York, N.Y.)*, 274(5284):109–113.

Green, J. D. and Arduini, A. A. (1954). Hippocampal electrical activity in arousal. *Journal of neurophysiology*.

Gregoriou, G. G., Gotts, S. J., Zhou, H., and Desimone, R. (2009). High-frequency, long-range coupling between prefrontal and visual cortex during attention. *science*, 324(5931):1207–1210.

Grimbert, F. and Faugeras, O. (2006a). Analysis of Jansen's model of a single cortical column. *[Research Report]*, pages RR–5597, INRIA. 2006, pp.34.

Grimbert, F. and Faugeras, O. (2006b). Bifurcation analysis of Jansen's neural mass model. *Neural Computation*, 18(12):3052–3068.

Grinvald, A., Lieke, E. E., Frostig, R. D., and Hildesheim, R. (1994). Cortical point-spread function and long-range lateral interactions revealed by real-time optical imaging of macaque monkey primary visual cortex. *The Journal of neuroscience*, 14(5):2545–2568.

Gross, J., Schmitz, F., Schnitzler, I., Kessler, K., Shapiro, K., Hommel, B., and Schnitzler, A. (2004). Modulation of long-range neural synchrony reflects temporal limitations of visual attention in humans. *Proc Natl Acad Sci U S A*, 101(35):13050–5.

Grothe, B. (2003). New roles for synaptic inhibition in sound localization. *Nature Reviews Neuroscience*, 4(7):540–550.

Grothe, I., Neitzel, S. D., Mandon, S., and Kreiter, A. K. (2012). Switching neuronal inputs by differential modulations of gamma-band phase-coherence. *The Journal of Neuroscience*, 32(46):16172–16180.

Guillery, R. W., Feig, S. L., and Lozsadi, D. A. (1998). Paying attention to the thalamic reticular nucleus. *Trends in Neurosciences*, 21:28–32.

Gutfreund, Y., Yarom, Y., and Segev, I. (1995). Subthreshold oscillations and resonant frequency in guinea-pig cortical neurons: physiology and modelling. *J. Physiol.*, 483 ( Pt 3):621–40.

Halassa, M. M., Chen, Z., Wimmer, R. D., Brunetti, P. M., Zhao, S., Zikopoulos, B., Wang, F., Brown, E. N., and Wilson, M. A. (2014). State-dependent architecture of thalamic reticular subnetworks. *Cell*, 158(4):808–821.

Han, F., Caporale, N., and Dan, Y. (2008). Reverberation of recent visual experience in spontaneous cortical waves. *Neuron*, 60(2):321–327.

Hanslmayr, S., Staresina, B. P., and Bowman, H. (2016). Oscillations and episodic memory: Addressing the synchronization/desynchronization conundrum. *Trends in neurosciences*, 39(1):16–25.

Harris, K. D., Csicsvari, J., Hirase, H., Dragoi, G., and Buzsáki, G. (2003). Organization of cell assemblies in the hippocampus. *Nature*, 424(6948):552–556.

Hasenstaub, A., Shu, Y., Haider, B., Kraushaar, U., Duque, A., and McCormick, D. A. (2005). Inhibitory postsynaptic potentials carry synchronized frequency information in active cortical networks. *Neuron*, 47(3):423–435.

Hodgkin, A. L. and Huxley, A. F. (1952). A quantitative description of membrane current and its application to conduction and excitation in nerve. *The Journal of physiology*, 117(4):500–544.

Horikawa, Y. (2014). Effects of asymmetric coupling and self-coupling on metastable dynamical transient rotating waves in a ring of sigmoidal neurons. *Neural Networks*, 53:26–39.

Huang, X., Troy, W. C., Yang, Q., Ma, H., Laing, C. R., Schiff, S. J., and Wu, J.-Y. (2004). Spiral waves in disinhibited mammalian neocortex. *The Journal of Neuroscience*, 24(44):9897–9902.

Huertas, M. A., Groff, J. R., and Smith, G. D. (2005). Feedback inhibition and throughput properties of an integrate-and-fire-or-burst network model of retinogeniculate transmission. *Journal of computational neuroscience*, 19(2):147–180.

Hussman, J. P. (2001). Letters to the editor: suppressed gabaergic inhibition as a common factor in suspected etiologies of autism. *Journal of autism and developmental disorders*, 31(2):247–248.

Ince, R., Mazzoni, A., Petersen, R. S., and Panzeri, S. (2010). Open source tools for the information theoretic analysis of neural data. *Front Neurosci*, 4(1):62–70.

Izhikevich, E. (2004). Which model to use for cortical spiking neurons? *Neural Networks, IEEE Transactions on*, 15(5):1063–1070.

Izhikevich, E. M. (2006). *Dynamical Systems in Neuroscience: The Geometry of Excitability and Bursting (Computational Neuroscience)*. The MIT Press, 1 edition.

Izhikevich, E. M. and Edelman, G. M. (2008). Large-scale model of mammalian thalamocortical systems. *Proceedings of the National Academy of Sciences*, 105(9):3593–3598.

Izhikevich, E. M. et al. (2003). Simple model of spiking neurons. *IEEE Transactions on neural networks*, 14(6):1569–1572.

Jahnsen, H. and Llinás, R. (1984). Electrophysiological properties of guinea-pig thalamic neurones: an in vitro study. *The Journal of physiology*, 349:205–26.

James, M., Coombes, S., and Bressloff, P. (2003). Effects of quasiactive membrane on multiply periodic traveling waves in integrate-and-fire systems. *Physical Review E*, 67(5):051905.

Jancke, D., Chavane, F., Naaman, S., and Grinvald, A. (2004). Imaging cortical correlates of illusion in early visual cortex. *Nature*, 428(6981):423–426.

Jansen, B. H. and Rit, V. G. (1995). Electroencephalogram and visual evoked potential generation in a mathematical model of coupled cortical columns. *Biological cybernetics*, 73(4):357–366.

Jansen, B. H., Zouridakis, G., and Brandt, M. E. (1993). A neurophysiologically-based mathematical model of flash visual evoked potentials. *Biological cybernetics*, 68(3):275–283.

Jedynak, M., Pons, A. J., and Garcia-Ojalvo, J. (2015). Cross-frequency transfer in a stochastically driven mesoscopic neuronal model. *Frontiers in computational neuroscience*, 9.

Jensen, O. and Colgin, L. L. (2007). Cross-frequency coupling between neuronal oscillations. *Trends in cognitive sciences*, 11(7):267–269.

Jirsa, V. (2004). Connectivity and dynamics of neural information processing. *Neuroinformatics*, 2(2):183–204.

Jones, E. G. (2002). Thalamic circuitry and thalamocortical synchrony. *Philosophical transactions of the Royal Society of London. Series B, Biological sciences*, 357(1428):1659–1673.

Kaiser, M., Hilgetag, C. C., and van Ooyen, A. (2009). A simple rule for axon outgrowth and synaptic competition generates realistic connection lengths and filling fractions. *Cereb Cortex*, 19(12):3001–10.

Kandel, E. R., Schwartz, J. H., and Jessell, T. M. (2000). *Principles of Neural Science*. McGraw-Hill Medical, 4th edition.

Kastner, S., Pinsk, M. A., De Weerd, P., Desimone, R., and Ungerleider, L. G. (1999). Increased activity in human visual cortex during directed attention in the absence of visual stimulation. *Neuron*, 22(4):751–61.

Katz, L. C. and Shatz, C. J. (1996). Synaptic activity and the construction of cortical circuits. *Science*, 274(5290):1133–1138.

Keener, J. P., Hoppensteadt, F., and Rinzel, J. (1981). Integrate-and-fire models of nerve membrane response to oscillatory input. *SIAM Journal on Applied Mathematics*, 41(3):503–517.

Kilpatrick, Z. P. and Bressloff, P. C. (2010a). Effects of synaptic depression and adaptation on spatiotemporal dynamics of an excitatory neuronal network. *Physica D: Nonlinear Phenomena*, 239(9):547–560.

Kilpatrick, Z. P. and Bressloff, P. C. (2010b). Spatially structured oscillations in a two-dimensional excitatory neuronal network with synaptic depression. *Journal of computational neuroscience*, 28(2):193–209.

Kim, U., Bal, T., and McCormick, D. A. (1995). Spindle waves are propagating synchronized oscillations in the ferret lgnd in vitro. *Journal of Neurophysiology*, 74(3):1301–1323.

Kim, U., Sanchez-Vives, M., and McCormick, D. (1997). Functional dynamics of gabaergic inhibition in the thalamus. *Science (New York, N.Y.)*, 278(5335):130—134.

Kistler, W. M. and van Hemmen, J. L. (1998). An analytically solvable model of collective excitation patterns in cortical tissue. In *A Perspective Look at Nonlinear Media*, pages 244–270. Springer.

Klug, A. and Albrecht, O. (2015). Neural circuits: Introducing different scales of temporal processing. *Current Biology*, 25(13):R557–R559.

Koch, C. and Segev, I. (1988). *Methods in neuronal modeling: from synapses to networks*. MIT press.

Kopell, N., Ermentrout, G., Whittington, M., and Traub, R. (2000a). Gamma rhythms and beta rhythms have different synchronization properties. *Proceedings of the National Academy of Sciences*, 97(4):1867–1872.

Kopell, N., Ermentrout, G. B., Whittington, M. A., and Traub, R. D. (2000b). Gamma rhythms and beta rhythms have different synchronization properties. *Proceedings of the National Academy of Sciences*, 97(4):1867–1872.

Ladenbauer, J., Augustin, M., Shiau, L., and Obermayer, K. (2012). Impact of adaptation currents on synchronization of coupled exponential integrate-and-fire neurons. *PLoS computational biology*, 8(4):e1002478.

Land, P. W., Blas, A. L. d., and Reddy, N. (1995). Immunocytochemical localization of gabaa receptors in rat somatosensory cortex and effects of tactile deprivation. *Somatosensory & motor research*, 12(2):127–141.

Lapicque, L. (1907). Recherches quantitatives sur l'excitation électrique des nerfs traitée comme une polarisation. *J. Physiol. Pathol. Gen*, 9(1):620–635.

Latham, P., Richmond, B., Nelson, P., and Nirenberg, S. (2000). Intrinsic dynamics in neuronal networks. i. theory. *Journal of Neurophysiology*, 83(2):808–827.

Leung, L. S. and Yu, H.-W. (1998). Theta-frequency resonance in hippocampal ca1 neurons in vitro demonstrated by sinusoidal current injection. *Journal of Neurophysiology*, 79(3):1592–1596.

Levy, R., Hutchison, W. D., Lozano, A. M., and Dostrovsky, J. O. (2000). High-frequency synchronization of neuronal activity in the subthalamic nucleus of parkinsonian patients with limb tremor. *The Journal of neuroscience*, 20(20):7766–7775.

Lewis, C., Bosman, C., and Fries, P. (2015a). Recording of brain activity across spatial scales. *Current opinion in neurobiology*, 32:68–77.

Lewis, L. D., Voigts, J., Flores, F. J., Schmitt, L. I., Wilson, M. A., Halassa, M. M., and Brown, E. N. (2015b). Thalamic reticular nucleus induces fast and local modulation of arousal state. *eLife*, page e08760.

Li, D. and Zhou, C. (2011). Organization of Anti-Phase Synchronization Pattern in Neural Networks: What are the Key Factors? *Front. Syst. Neurosci.*, 5(100):doi: 10.3389/fnsys.2011.00100.

Liley, D. T., Cadusch, P. J., and Dafilis, M. P. (2002). A spatially continuous mean field theory of electrocortical activity. *Network: Computation in Neural Systems*, 13(1):67–113.

Limousin, P., Pollak, P., Benazzouz, A., Hoffmann, D., Le Bas, J., Perret, J., Benabid, A., and Broussolle, E. (1995). Effect on parkinsonian signs and symptoms of bilateral subthalamic nucleus stimulation. *The Lancet*, 345(8942):91–95.

Lindén, H., Hagen, E., Leski, S., Norheim, E. S., Pettersen, K. H., and Einevoll, G. T. (2013). Lfpy: a tool for biophysical simulation of extracellular potentials generated by detailed model neurons. *Frontiers in neuroinformatics*, 7.

Liu, X. B. and Jones, E. G. (1999). Predominance of corticothalamic synaptic inputs to thalamic reticular nucleus neurons in the rat. *The Journal of comparative neurology*, 414(1):67–79.

Livingstone, M. S. and Hubel, D. H. (1981). Effects of sleep and arousal on the processing of visual information in the cat. *Nature*, 291(5816):554–561.

Llinás, R. and Jahnsen, H. (1982). Electrophysiology of mammalian thalamic neurones in vitro. *Nature*, 297(5865):406–408.

Llinas, R. and Ribary, U. (1993). Coherent 40-hz oscillation characterizes dream state in humans. *Proceedings of the National Academy of Sciences*, 90(5):2078–2081.

Llinas, R., Ribary, U., Contreras, D., and Pedroarena, C. (1998). The neuronal basis for consciousness. *Philosophical Transactions of the Royal Society B: Biological Sciences*, 353(1377):1841–1849.

Llinás, R. R. and Paré, D. (1991). Of dreaming and wakefulness. *Neuroscience*, 44(3):521–535.

Lubenov, E. V. and Siapas, A. G. (2009). Hippocampal theta oscillations are travelling waves. *Nature*, 459(7246):534–539.

Lyons, K. E. and Pahwa, R. (2008). Deep brain stimulation and tremor. *Neurotherapeutics*, 5(2):331–338.

Magri, C., Whittingstall, K., Singh, V., Logothetis, N., and Panzeri, S. (2009). A toolbox for the fast information analysis of multiple-site lfp, eeg and spike train recordings. *BMC Neurosci.*, 10(1):81.

Malagarriga, D., Villa, A. E., Garcia-Ojalvo, J., and Pons, A. J. (2015). Mesoscopic segregation of excitation and inhibition in a brain network model. *PLOS Comput Biol*, 11(2):e1004007.

Markov, N., Ercsey-Ravasz, M., Gomes, A. R., Lamy, C., Magrou, L., Vezoli, J., Misery, P., Falchier, A., Quilodran, R., Gariel, M., et al. (2012). A weighted and directed interareal connectivity matrix for macaque cerebral cortex. *Cerebral Cortex*, page bhs270.

Markram, H., Lübke, J., Frotscher, M., and Sakmann, B. (1997). Regulation of synaptic efficacy by coincidence of postsynaptic aps and epsps. *Science*, 275(5297):213–215.

Markram, H., Toledo-Rodriguez, M., Wang, Y., Gupta, A., Silberberg, G., and Wu, C. (2004). Interneurons of the neocortical inhibitory system. *Nat. Rev. Neurosci.*, 5(10):793–807.

Massimini, M., Ferrarelli, F., Esser, S. K., Riedner, B. A., Huber, R., Murphy, M., Peterson, M. J., and Tononi, G. (2007). Triggering sleep slow waves by transcranial magnetic stimulation. *Proceedings of the National Academy of Sciences*, 104(20):8496–8501.

Maynard, E. M., Nordhausen, C. T., and Normann, R. A. (1997). The utah intracortical electrode array: a recording structure for potential brain-computer interfaces. *Electroencephalography and clinical neurophysiology*, 102(3):228–239.

Mazzoni, A., Lindén, H., Cuntz, H., Lansner, A., Panzeri, S., and Einevoll, G. T. (2015). Computing the local field potential (lfp) from integrate-and-fire network models. *PLoS Comput Biol*, 11(12):e1004584.

Mazzoni, A., Panzeri, S., Logothetis, N. K., and Brunel, N. (2008). Encoding of naturalistic stimuli by local field potential spectra in networks of excitatory and inhibitory neurons. *PLoS Comput Biol*, 4(12)(12):e1000239. doi: 10.1371/journal.pcbi.1000239.

McAlonan, K., Cavanaugh, J., and Wurtz, R. H. (2008). Guarding the gateway to cortex with attention in visual thalamus. *Nature*, 456(7220):391–394.

McCormick, D. A. (1992). Neurotransmitter actions in the thalamus and cerebral cortex and their role in neuromodulation of thalamocortical activity. *Progress in neurobiology*, 39(4):337–388.

McIntosh, A. R. (2000). Towards a network theory of cognition. *Neural Netw*, 13(8-9):861–870.

McIntyre, C. C., Grill, W. M., Sherman, D. L., and Thakor, N. V. (2004). Cellular effects of deep brain stimulation: model-based analysis of activation and inhibition. *Journal of neurophysiology*, 91(4):1457–1469.

Mesulam, M.-M. (1990). Large scale neurocognitive networks and distributed processing for attention. *Annals of neurology*, 28(5).

Minderhoud, J. M. (1971). An anatomical study of the efferent connections of the thalamic reticular nucleus. *Experimental Brain Research*, 112:435–446.

Mirollo, R. E. and Strogatz, S. H. (1990). Synchronization of pulse-coupled biological oscillators. *SIAM Journal on Applied Mathematics*, 50(6):1645–1662.

Montez, T., Poil, S.-S., Jones, B. F., Manshanden, I., Verbunt, J. P., van Dijk, B. W., Brussaard, A. B., van Ooyen, A., Stam, C. J., Scheltens, P., et al. (2009). Altered temporal correlations in parietal alpha and prefrontal theta oscillations in early-stage alzheimer disease. *Proceedings of the National Academy of Sciences*, 106(5):1614–1619.

Montgomery, S. M. and Buzsáki, G. (2007). Gamma oscillations dynamically couple hippocampal ca3 and ca1 regions during memory task performance. *Proceedings of the National Academy of Sciences*, 104(36):14495–14500.

Montgomery, S. M., Sirota, A., and Buzsáki, G. (2008). Theta and gamma coordination of hippocampal networks during waking and rapid eye movement sleep. *The Journal of Neuroscience*, 28(26):6731–6741.

Moran, R., Pinotsis, D. A., and Friston, K. (2013). Neural masses and fields in dynamic causal modeling. *Frontiers in computational neuroscience*, 7.

Morison, R. and Bassett, D. (1945). Electrical activity of the thalamus and basal ganglia in decorticate cats. *Journal of Neurophysiology*, 8(5):309–314.

Mountcastle, V. B. (1957). Modality and topographic properties of single neurons of cat's somatic sensory cortex. *Journal of neurophysiology*, 20(4):408–434.

Muller, L. and Destexhe, A. (2012). Propagating waves in thalamus, cortex and the thalamocortical system: experiments and models. *Journal of Physiology-Paris*, 106(5):222–238.

Muller, L., Reynaud, A., Chavane, F., and Destexhe, A. (2014). The stimulus-evoked population response in visual cortex of awake monkey is a propagating wave. *Nature communications*, 5.

Naud, R., Marcille, N., Clopath, C., and Gerstner, W. (2008). Firing patterns in the adaptive exponential integrate-and-fire model. *Biological cybernetics*, 99(4-5):335–347.

Nauhaus, I., Busse, L., Carandini, M., and Ringach, D. L. (2009). Stimulus contrast modulates functional connectivity in visual cortex. *Nature neuroscience*, 12(1):70–76.

Nauhaus, I., Busse, L., Ringach, D. L., and Carandini, M. (2012). Robustness of traveling waves in ongoing activity of visual cortex. *The Journal of Neuroscience*, 32(9):3088–3094.

Nelson, M. and Rinzel, J. (1998). The hodgkin—huxley model. In *The Book of GENESIS*, pages 29–49. Springer.

Neuenschwander, S. and Singer, W. (1996). Long-range synchronization of oscillatory light responses in the cat retina and lateral geniculate nucleus. *Nature*, 379(6567):728–733.

O'Keefe, J. (1976). Place Units in the Hippocampus of the Freely Moving Rat. *Experimental Neurology*, 51(1):78–109.

O'Keefe, J. and Nadel, L. (1978). *The hippocampus as a cognitive map*, volume 3. Clarendon Press Oxford.

O'Keefe, J. and Recce, M. L. (1993). Phase relationship between hippocampal place units and the EEG theta rhythm. *Hippocampus*, 3(3):317–330.

Osan, R. and Ermentrout, B. (2002). The evolution of synaptically generated waves in one-and two-dimensional domains. *Physica D: Nonlinear Phenomena*, 163(3):217–235.

Pais-Vieira, M., Kunicki, C., Tseng, P.-H., Martin, J., Lebedev, M., and Nicolelis, M. A. (2015). Cortical and thalamic contributions to response dynamics across layers of the primary somatosensory cortex during tactile discrimination. *Journal of neurophysiology*, 114(3):1652–1676.

Panzeri, S. and Treves, A. (1996). Analytical estimates of limited sampling biases in different information measures. *Network*, 7(7):87–107.

Penfield, W. and Jasper, H. (1954). Epilepsy and the functional anatomy of the human brain.

Perez-Orive, J., Mazor, O., Turner, G., Cassenaer, S., Wilson, R., and Laurent, G. (2002). Oscillations and sparsening of odor representations in the mushroom body. *Science*, 297:359–365.

Phillips, W. A. and Silverstein, S. M. (2003). Convergence of biological and psychological perspectives on cognitive coordination in schizophrenia. *Behavioral and Brain Sciences*, 26(01):65–82.

Phillips, W. A. and Singer, W. (1997). In search of common foundations for cortical computation. *Behavioral and Brain Sciences*, 20(04):657–683.

Pikovsky, A., Rosenblum, M., and Kurths, J. (2003). *Synchronization: A Universal Concept in Nonlinear Sciences*. Cambridge University Press.

Pinto, D. J. and Ermentrout, G. B. (2001). Spatially structured activity in synaptically coupled neuronal networks: I. traveling fronts and pulses. *SIAM journal on Applied Mathematics*, 62(1):206–225.

Pinto, D. J., Patrick, S. L., Huang, W. C., and Connors, B. W. (2005). Initiation, propagation, and termination of epileptiform activity in rodent neocortex in vitro involve distinct mechanisms. *The Journal of neuroscience*, 25(36):8131–8140.

Pons, A., Cantero, J. L., Atienza, M., and Garcia-Ojalvo, J. (2010). Relating structural and functional anomalous connectivity in the aging brain via neural mass modeling. *Neuroimage*, 52(3):848–861.

Potjans, T. C. and Diesmann, M. (2014). The cell-type specific cortical microcircuit: relating structure and activity in a full-scale spiking network model. *Cerebral cortex*, 24(3):785–806.

Prechtl, J., Cohen, L., Pesaran, B., Mitra, P., and Kleinfeld, D. (1997). Visual stimuli induce waves of electrical activity in turtle cortex. *Proceedings of the National Academy of Sciences*, 94(14):7621–7626.

Price, C. J. and Friston, K. J. (2005). Functional ontologies for cognition: the systematic definition of structure and function. *Cognitive Neuropsychology*, 22(3-4):262–275.

Quian Quiroga, R. and Panzeri, S. (2009). Extracting information from neuronal populations: information theory and decoding approaches. *Nat. Rev. Neurosci.*, 10(3):173–85.

Rabinovich, M. I., Afraimovich, V. S., Bick, C., and Varona, P. (2012). Information flow dynamics in the brain. *Physics of Life Reviews*, 9(1):51–73.

Rall, W. (1967). Distinguishing theoretical synaptic potentials computed for different soma-dendritic distributions of synaptic input. *Journal of neurophysiology*, 30(5):1138–1168.

Reimer, A., Hubka, P., Engel, A. K., and Kral, A. (2010). Fast propagating waves within the rodent auditory cortex. *Cerebral Cortex*, page bhq073.

Reinhold, K., Lien, A. D., and Scanziani, M. (2015). Distinct recurrent versus afferent dynamics in cortical visual processing. *Nat Neurosci*, 18(12):1789–97.

Rennie, C. J., WRIGHT, J. J., and ROBINSON, P. A. (2000). Mechanisms of cortical electrical activity and emergence of gamma rhythm. *Journal of Theoretical Biology*, 205(1):17–35.

Ribary, U., Ioannides, A., Singh, K. D., Hasson, R., Bolton, J., Lado, F., Mogilner, A., and Llinas, R. (1991). Magnetic field tomography of coherent thalamocortical 40-hz oscillations in humans. *Proceedings of the National Academy of Sciences*, 88(24):11037–11041.

Richardson, M. J., Brunel, N., and Hakim, V. (2003). From subthreshold to firing-rate resonance. *Journal of neurophysiology*, 89(5):2538–2554.

Ringo, J., Doty, R., Demeter, S., and Simard, P. (1994). Time is the essence: A conjecture that hemispheric specialization arises from interhemispheric conduction delay. *Cereb Cortex*, 4:331–343.

Ritz, R. and Sejnowski, T. J. (1997). Synchronous oscillatory activity in sensory systems: new vistas on mechanisms. *Current Opinion in Neurobiology*, 7(4):536–546.

Rodrigues, S., Chizhov, A. V., Marten, F., and Terry, J. R. (2010). Mappings between a macroscopic neural-mass model and a reduced conductance-based model. *Biological cybernetics*, 102(5):361–371.

Rodriguez, E., George, N., Lachaux, J.-P., Martinerie, J., Renault, B., and Varela, F. J. (1999). Perception's shadow: long-distance synchronization of human brain activity. *Nature*, 397(6718):430–433.

Roelfsema, P., Engel, A., Konig, A., and Singer, W. (1997). Visuomotor integration is associated with the zero time-lag synchronization among cortical areas. *Nature*, 385:157–161.

Roskies, A. L. (1999). The binding problem. *Neuron*, 24(1):7–9.

Rubenstein, J. and Merzenich, M. (2003). Model of autism: increased ratio of excitation/inhibition in key neural systems. *Genes, Brain and Behavior*, 2(5):255–267.

Rubino, D., Robbins, K. A., and Hatsopoulos, N. G. (2006). Propagating waves mediate information transfer in the motor cortex. *Nature neuroscience*, 9(12):1549–1557.

Salami, M., Itami, C., Tsumoto, T., and Kimura, F. (2003). Change of conduction velocity by regional myelination yields constant latency irrespective of distance between thalamus and cortex. *Proceedings of the National Academy of Sciences*, 100(10):6174–6179.

Salinas, E. and Sejnowski, T. J. (2001). Correlated neuronal activity and the flow of neural information. *Nature Reviews Neuroscience*, 2(8):539–550.

Salmelin, R. and Kujala, J. (2006). Neural representation of language: activation versus long-range connectivity. *Trends in cognitive sciences*, 10(11):519–525.

Samengo, I., Mato, G., Elijah, D. H., Schreiber, S., and Montemurro, M. A. (2013). Linking dynamical and functional properties of intrinsically bursting neurons. *Journal of computational neuroscience*, 35(2):213–230.

Sanchez-Vives, M. V. and McCormick, D. A. (2000). Cellular and network mechanisms of rhythmic recurrent activity in neocortex. *Nature neuroscience*, 3(10):1027–1034.

Sancristóbal, B., Vicente, R., and Garcia-Ojalvo, J. (2014). Role of frequency mismatch in neuronal communication through coherence. *Journal of computational neuroscience*, 37(2):193–208.

Sancristóbal, B., Vicente, R., Sancho, J. M., and Garcia-Ojalvo, J. (2013). Emergent bimodal firing patterns implement different encoding strategies during gamma-band oscillations. *Frontiers in Computational Neuroscience*, 7:18.

Schnitzler, A. and Gross, J. (2005). Normal and pathological oscillatory communication in the brain. *Nature reviews. Neuroscience*, 6(4):285–96.

Schoffelen, J.-M., Oostenveld, R., and Fries, P. (2005). Neuronal Coherence as a Mechanism of Effective Corticospinal Interaction. *Science*, 308(5718):111–113.

Schoffelen, J.-M., Poort, J., Oostenveld, R., and Fries, P. (2011). Selective movement preparation is subserved by selective increases in corticomuscular gamma-band coherence. *The Journal of Neuroscience*, 31(18):6750–6758.

Schwartz, A. (2015). The promise of neurotechnology. *Science*, 350(6256):11–11.

Schyns, P. G., Thut, G., and Gross, J. (2011). Cracking the Code of Oscillatory Activity. *PLoS Biology*, 9(5):e1001064.

Servello, D., Porta, M., Sassi, M., Brambilla, A., and Robertson, M. M. (2008). Deep brain stimulation in 18 patients with severe gilles de la tourette syndrome refractory to treatment: the surgery and stimulation. *Journal of Neurology, Neurosurgery & Psychiatry*, 79(2):136–142.

Shadlen, M. N. and Movshon, J. A. (1999). Synchrony Unbound: Review A Critical Evaluation of the Temporal Binding Hypothesis. *Neuron*, 24:67–77.

Sherman, S. M. (2001). Tonic and burst firing: Dual modes of thalamocortical relay. *Trends in Neurosciences*, 24(2):122–126.

Sherman, S. M. (2006). Thalamus. *Scholarpedia*, 1(9):1583.

Sherman, S. M. and Guillery, R. W. (2002). The role of the thalamus in the flow of information to the cortex. *Philosophical transactions of the Royal Society of London. Series B, Biological sciences*, 357(November):1695–1708.

Shipp, S. (2003a). The functional logic of cortico–pulvinar connections. *Philosophical Transactions of the Royal Society of London B: Biological Sciences*, 358(1438):1605–1624.

Shipp, S. (2003b). The functional logic of cortico-pulvinar connections. *Philos Trans R Soc Lond B Biol Sci*, 358(1438):1605–24.

Shoham, D., Glaser, D. E., Arieli, A., Kenet, T., Wijnbergen, C., Toledo, Y., Hildesheim, R., and Grinvald, A. (1999). Imaging cortical dynamics at high spatial and temporal resolution with novel blue voltage-sensitive dyes. *Neuron*, 24(4):791–802.

Siegel, M., Körding, K. P., and König, P. (2000). Integrating top-down and bottom-up sensory processing by somato-dendritic interactions. *J Comput Neurosci*, 8(2):161–73.

Siegle, J. H., Pritchett, D. L., and Moore, C. I. (2014). Gamma-range synchronization of fast-spiking interneurons can enhance detection of tactile stimuli. *Nature neuroscience*, 17(10):1371–1379.

Sik, A., Penttonen, M., Ylinen, A., and Buzsáki, G. (1995). Hippocampal ca1 interneurons: an in vivo intracellular labeling study. *The Journal of neuroscience*, 15(10):6651–6665.

Singer, W. (1999). Neuronal synchrony: a versatile code for the definition of relations? *Neuron*, 24(1).

Singer, W. and Gray, C. M. (1995). Visual Feature Integration and the Temporal Correlation Hypothesis. *Annual Review of Neuroscience*, 18(1):555–586.

Slovin, H., Arieli, A., Hildesheim, R., and Grinvald, A. (2002). Long-term voltage-sensitive dye imaging reveals cortical dynamics in behaving monkeys. *Journal of neurophysiology*, 88(6):3421–3438.

Smith, G. D., Cox, C. L., Sherman, M. S., and Rinzel, J. (2001). A firing-rate model of spike-frequency adaptation in sinusoidally-driven thalamocortical relay neurons. *Thalamus & Related Systems*, 1(02):135–156.

Soriano, J., Rodríguez Martínez, M., Tlusty, T., and Moses, E. (2008). Development of input connections in neural cultures. *Proc Natl Acad Sci U S A*, 105(37):13758–63.

Sotero, R. C., Trujillo-Barreto, N. J., Iturria-Medina, Y., Carbonell, F., and Jimenez, J. C. (2007). Realistically coupled neural mass models can generate eeg rhythms. *Neural computation*, 19(2):478–512.

Spiegler, A., Knösche, T. R., Schwab, K., Haueisen, J., and Atay, F. M. (2011). Modeling brain resonance phenomena using a neural mass model. *PLoS Comput Biol*, 7(12):e1002298.

Spira, M. E. and Hai, A. (2013). Multi-electrode array technologies for neuroscience and cardiology. *Nature nanotechnology*, 8(2):83–94.

Sporns, O., Honey, C. J., and Kötter, R. (2007). Identification and classification of hubs in brain networks. *PLoS ONE*, 2(10).

Stam, C., Jones, B., Nolte, G., Breakspear, M., and Scheltens, P. (2007). Small-world networks and functional connectivity in alzheimer's disease. *Cerebral cortex*, 17(1):92–99.

Stein, R. B. (1967). Some models of neuronal variability. *Biophysical journal*, 7(1):37.

Stepanyants, A., Hirsch, J. A., Martinez, L. M., Kisvárday, Z. F., Ferecskó, A. S., and Chklovskii, D. B. (2008). Local potential connectivity in cat primary visual cortex. *Cerebral Cortex*, 18(1):13–28.

Steriade, M. (2003). *Neuronal Substrates of Sleep and Epilepsy*. Cambridge University Press.

Steriade, M. (2006). Grouping of brain rhythms in corticothalamic systems. *Neuroscience*, 137(4):1087–1106.

Steriade, M. and Deschenes, M. (1984). The thalamus as a neuronal oscillator. *Brain Research Reviews*, 8(1):1–63.

Steriade, M. and McCarley, R. W. (2005). *Brain Control of Wakefulness and Sleep*. Springer US, Boston, MA.

Steriade, M., McCormick, D. A., and Sejnowski, T. J. (1993). Thalamocortical oscillations in the sleeping and aroused brain. *Science*, 262:679–85.

Sterratt, D., Graham, B., Gillies, A., and Willshaw, D. (2011). *Principles of computational modelling in neuroscience*. Cambridge University Press.

Steyn-Ross, M. L., Steyn-Ross, D. A., Sleigh, J. W., and Liley, D. (1999). Theoretical electroencephalogram stationary spectrum for a white-noise-driven cortex: evidence for a general anesthetic-induced phase transition. *Physical Review E*, 60(6):7299.

Stopfer, M., Bhagavan, S., Smith, B. H., and Laurent, G. (1997). Impaired odour discrimination on desynchronization of odour-encoding neural assemblies. *Nature*, 390(6655):70–74.

Stroh, A., Adelsberger, H., Groh, A., Rühlmann, C., Fischer, S., Schierloh, A., Deisseroth, K., and Konnerth, A. (2013). Making waves: initiation and propagation of corticothalamic ca 2+ waves in vivo. *Neuron*, 77(6):1136–1150.

Takahashi, K., Saleh, M., Penn, R. D., and Hatsopoulos, N. (2011). Propagating waves in human motor cortex. *Frontiers in human neuroscience*, 5:40.

Tallon-Baudry, C., Mandon, S., Freiwald, W. A., and Kreiter, A. K. (2004). Oscillatory Synchrony in the Monkey Temporal Lobe Correlates with Performance in a Visual Short-term Memory Task. *Cereb. Cortex*, 14(7):713–720.

Taschenberger, H., Leão, R. M., Rowland, K. C., Spirou, G. A., and von Gersdorff, H. (2002). Optimizing synaptic architecture and efficiency for high-frequency transmission. *Neuron*, 36(6):1127–1143.

Tasker, R. R. (1998). Deep brain stimulation is preferable to thalamotomy for tremor suppression. *Surgical neurology*, 49(2):145–153.

Theyel, B. B., Llano, D. a., and Sherman, S. M. (2010). The corticothalamocortical circuit drives higher-order cortex in the mouse. *Nat. Neurosci.*, 13(1):84–8.

Tiesinga, P., Fellous, J.-M., and Sejnowski, T. J. (2008). Regulation of spike timing in visual cortical circuits. *Nature reviews neuroscience*, 9(2):97–107.

Tiesinga, P. H. and Sejnowski, T. J. (2004). Rapid temporal modulation of synchrony by competition in cortical interneuron networks. *Neural computation*, 16(2):251–275.

Timofeev, I., Grenier, F., Bazhenov, M., Sejnowski, T., and Steriade, M. (2000). Origin of slow cortical oscillations in deafferented cortical slabs. *Cerebral Cortex*, 10(12):1185–1199.

Toral, R. and Colet, P. (2014). *Stochastic numerical methods: an introduction for students and scientists*. John Wiley & Sons.

Touboul, J. and Brette, R. (2008). Dynamics and bifurcations of the adaptive exponential integrate-and-fire model. *Biological cybernetics*, 99(4-5):319–334.

Traub, R., Jefferys, J., and Miles, R. (1993). Analysis of the propagation of disinhibition-induced after-discharges along the guinea-pig hippocampal slice in vitro. *The Journal of physiology*, 472:267.

Traub, R. D., Bibbig, A., LeBeau, F. E., Buhl, E. H., and Whittington, M. A. (2004). Cellular mechanisms of neuronal population oscillations in the hippocampus in vitro. *Annu. Rev. Neurosci.*, 27:247–278.

Traub, R. D., Whittington, M. A., Stanford, I. M., and Jefferys, J. G. R. (1996). A mechanism for generation of long-range synchronous fast oscillations in the cortex. *Nature*, 383(6601):621–624.

Tuckwell, H. C. (2005). *Introduction to theoretical neurobiology: volume 2, nonlinear and stochastic theories*, volume 8. Cambridge University Press.

Uhlhaas, P. and Singer, W. (2006). Neural Synchrony in Brain Disorders: Relevance for Cognitive Dysfunctions and Pathophysiology. *Neuron*, 52(1):155–168.

Uhlhaas, P. J., Pipa, G., Lima, B., Melloni, L., Neuenschwander, S., Nikolić, D., and Singer, W. (2009). Neural synchrony in cortical networks: history, concept and current status. *Frontiers in integrative neuroscience*, 3.

van Elswijk, G., Maij, F., Schoffelen, J.-M., Overeem, S., Stegeman, D. F., and Fries, P. (2010). Corticospinal beta-band synchronization entails rhythmic gain modulation. *The Journal of Neuroscience*, 30(12):4481–4488.

van Pelt, J. and van Ooyen, A. (2013). Estimating neuronal connectivity from axonal and dendritic density fields. *Front Comput Neurosci*, 7:160.

Van Vreeswijk, C., Abbott, L. F., and Ermentrout, G. B. (1994). When inhibition not excitation synchronizes neural firing. *Journal of computational neuroscience*, 1(4):313–321.

Vanderwolf, C. H. (1969). Hippocampal electrical activity and voluntary movement in the rat. *Electroencephalography and clinical neurophysiology*, 26(4):407–418.

Varela, F., Lachaux, J. P., Rodriguez, E., and Martinerie, J. (2001). The Brainweb: Phase synchronization and large-scale integration. *Nature Reviews: Neuroscience*, 2:229–239.

Varela, F. J. (1995). Resonant cell assemblies: a new approach to cognitive functions and neuronal synchrony. *Biological research*, 28(1):81–95.

Velazquez, J. L. P. and Carlen, P. L. (2000). Gap junctions, synchrony and seizures. *Trends in neurosciences*, 23(2):68–74.

Vicente, R., Gollo, L., Mirasso, C., Fischer, I., and Pipa, G. (2008). Dynamical relaying can yield zero time lag neuronal synchrony despite long conduction delays. *Proc Natl Acad Sci U S A*, 105(44):17157–17162.

Victor, J. D. (2006). Approaches to information-theoretic analysis of neural activity. *Biol. Theory*, 1:302–316.

Viriyopase, A., Bojak, I., Zeitler, M., and Gielen, S. (2012). When Long-Range Zero-Lag Synchronization is Feasible in Cortical Networks. *Front Comput Neurosci*, 6(49)(49):doi: 10.3389/fncom.2012.00049.

von Krosigk, M., Bal, T., and McCormick, D. (1993a). Cellular mechanisms of a synchronized oscillation in the thalamus. *Science*, 261(5119):361–364.

von Krosigk, M., Bal, T., and McCormick, D. A. (1993b). Cellular mechanisms of a synchronized oscillation in the thalamus. *Science*, 261(5119):361–364.

Von Stein, A., Chiang, C., and König, P. (2000). Top-down processing mediated by interareal synchronization. *Proceedings of the National Academy of Sciences*, 97(26):14748–14753.

Von Stein, A. and Sarnthein, J. (2000). Different frequencies for different scales of cortical integration: from local gamma to long range alpha/theta synchronization. *International journal of psychophysiology*, 38(3):301–313.

Wang, X.-J. (2010a). Neurophysiological and Computational Principles of Cortical Rhythms in Cognition. *Physiological Reviews*, 90(3):1195–1268.

Wang, X.-J. (2010b). Neurophysiological and computational principles of cortical rhythms in cognition. *Physiological reviews*, 90(3):1195–1268.

Ward, L. (2003). Synchronous neural oscillations and cognitive processes. *Trends in Cognitive Sciences*, 7(12):553–559.

Watt, A. J., Cuntz, H., Mori, M., Nusser, Z., Sjöström, P. J., and Häusser, M. (2009). Traveling waves in developing cerebellar cortex mediated by asymmetrical purkinje cell connectivity. *Nature neuroscience*, 12(4):463–473.

Watts, D. J. and Strogatz, S. H. (1998). Collective dynamics of 'small-world' networks. *Nature*, 393(6684):440–2.

Wehr, M. and Laurent, G. (1996). Odour encoding by temporal sequences of firing in. *Nature*, 384:14.

Wester, J. C. and Contreras, D. (2012). Columnar interactions determine horizontal propagation of recurrent network activity in neocortex. *The Journal of Neuroscience*, 32(16):5454–5471.

Willis, A. M., Slater, B. J., Gribkova, E. D., and Llano, D. A. (2015). Open-loop organization of thalamic reticular nucleus and dorsal thalamus: A computational model. *Journal of neurophysiology*, 114(4):2353–2367.

Wimmer, K., Compte, A., Roxin, A., Peixoto, D., Renart, A., and de la Rocha, J. (2015). Sensory integration dynamics in a hierarchical network explains choice probabilities in cortical area MT. *Nature communications*, 6.

Winson, J. (1972). Interspecies differences in the occurrence of theta. *Behavioral Biology*, 7(4):479–487.

Witte, R. S., Rousche, P. J., and Kipke, D. R. (2007). Fast wave propagation in auditory cortex of an awake cat using a chronic microelectrode array. *Journal of neural engineering*, 4(2):68.

Womelsdorf, T., Fries, P., Mitra, P. P., and Desimone, R. (2006). Gamma-band synchronization in visual cortex predicts speed of change detection. *Nature*, 439(7077):733–6.

Womelsdorf, T., Schoffelen, J.-M., Oostenveld, R., Singer, W., Desimone, R., Engel, A. K., and Fries, P. (2007). Modulation of neuronal interactions through neuronal synchronization. *Science*, 316(5831):1609–12.

Woodman, M. M. and Jirsa, V. K. (2013). Emergent dynamics from spiking neuron networks through symmetry breaking of connectivity. *PloS one*, 8(5):e64339.

Wright, J. and Liley, D. (1996). Dynamics of the brain at global and microscopic scales: Neural networks and the eeg. *Behavioral and Brain Sciences*, 19(02):285–295.

Wu, J.-Y., Huang, X., and Zhang, C. (2008). Propagating waves of activity in the neocortex: what they are, what they do. *The Neuroscientist*, 14(5):487–502.

Xu, W., Huang, X., Takagaki, K., and Wu, J.-y. (2007). Compression and reflection of visually evoked cortical waves. *Neuron*, 55(1):119–129.

Zandvakili, A. and Kohn, A. (2015). Coordinated neuronal activity enhances corticocortical communication. *Neuron*, 87(4):827–839.

Zanos, T. P., Mineault, P. J., Nasiotis, K. T., Guitton, D., and Pack, C. C. (2015). A sensorimotor role for traveling waves in primate visual cortex. *Neuron*, 85(3):615–627.

Zhang, H. and Jacobs, J. (2015). Traveling theta waves in the human hippocampus. *The Journal of Neuroscience*, 35(36):12477–12487.